# Optimal Black-Start Restoration of Low-Inertia Networks Enabled by Innovative Estimation and Control Methods for Grid-Forming Converters

PhD Thesis

Mohamed Abouyehia

Department of Electrical and Electronic Engineering

University of Strathclyde, Glasgow

June 2026

# Copyright

# Acknowledgments

I would like to sincerely thank my supervisor, **Prof. Khaled Ahmed**, for his continuous guidance, support, and encouragement throughout this research. His advice and willingness to share his knowledge have greatly shaped this thesis.

I am also very grateful to **Yasmine Abouelseoud**, **Agustí Egea-Àlvarez**, and **Ayman S. Abdel-Khalik** for their helpful feedback, valuable suggestions, and kind support at important stages of this work. I would also like to thank the members of the Power Electronics, Drives & Energy Conversion (PEDEC) research group for creating a friendly and supportive research environment.

I gratefully acknowledge the financial support provided by the Energy Technology Partnership (ETP) and ScottishPower Energy Networks for funding this research. Their investment in advancing power systems research has been instrumental in enabling this work.

I am deeply grateful to my **parents** and my **wife**. Their patience, love, and constant prayers have been my greatest source of strength throughout this journey.

# Abstract

The progressive displacement of synchronous generation by converter-interfaced resources is fundamentally transforming the dynamic behaviour of modern power systems. As conventional synchronous generators are decommissioned, the rotational inertia, electromechanical damping, fault current contribution, and inherent synchronising capability that have historically underpinned grid stability are systematically diminished. Grid-forming converters have emerged as the foremost enabling technology for sustaining stable operation under these conditions. However, a critical gap persists in understanding how converter-level estimation and control capabilities can be formally embedded within system-level operational decision-making. This challenge is particularly pronounced during black-start restoration following a complete or partial blackout. This thesis addresses this gap by developing novel estimation and control methods for grid-forming converters and demonstrating their integration within an optimal black-start restoration framework for converter-dominated low-inertia distribution networks.

In the estimation domain, this thesis addresses the two most critical parameters governing the dynamic security of low-inertia power systems, namely inertia and frequency. For inertia estimation, the first method introduces a wavelet transform-based approach operating in the time-frequency domain. A closed-form relationship between wavelet coefficient magnitudes and the physical inertia constant is established and validated through hardware-in-the-loop experiments under realistic noisy measurement conditions. The second method introduces an integral-based reformulation of the swing equation that simultaneously captures aggregate and spatially distributed inertia. This formulation accurately identifies inertially weak zones across the network. For frequency estimation, two novel methods are proposed. The first exploits the oscillatory behaviour of the Park–Clarke transformation under frequency deviation conditions. A cross-product formulation of normalised voltage components is developed that enables near-instantaneous frequency extraction. The second method extends this principle through fractional-order derivative calculus. The amplitude of the fractional derivative encodes the frequency deviation in a manner that permits direct algebraic recovery of the system frequency. Experimental validation demonstrates superior dynamic response and improved estimation accuracy compared with leading phase-locked loop (PLL) methods.

In the control domain, this thesis addresses two fundamental challenges facing grid-forming converters in low-inertia networks, namely transient damping performance and voltage

quality under unbalanced conditions. The first contribution introduces a fractional-order derivative-based feedforward damping loop that augments the conventional droop controller. The auxiliary loop provides continuously tuneable transient damping while remaining inherently inactive at steady state. Significant reductions in active power overshoot and settling time are achieved under step load conditions. The second contribution addresses voltage unbalance through a novel Expectation-Maximisation algorithm integrated with a Kalman filter. A new time-varying measurement matrix is derived that represents the second-order harmonic coupling between sequence components. An integrated controller simultaneously suppresses negative-sequence and zero-sequence voltages within the positive-sequence grid-forming architecture. The unbalance suppression framework is complemented by a data-driven Prony-based stability assessment method that evaluates system stability directly from time-domain measurements. Experimental validation on a laboratory-scale converter confirms that the proposed controller effectively reduces the voltage unbalance factor to within the limits mandated by the GB Grid Code.

To bridge the gap between converter-level intelligence and system-level operational decision-making, a mixed-integer linear programming formulation is developed for optimal black-start restoration in converter-dominated distribution networks. The objective function minimises the total customer damage cost, which inherently drives the restoration towards the shortest feasible makespan. The optimisation is applied to a standard distribution test system with multiple grid-forming and grid-following converters. Estimation and control outputs from all preceding contributions are embedded within the optimisation through confidence factors that parameterise the usable value of each physical quantity as perceived by the restoration optimiser. Inertia estimation scales the available system kinetic energy at each restoration step and enforces a RoCoF ceiling that limits the permissible load pickup. Frequency estimation accuracy narrows the guard margin on frequency constraints and unlocks additional feasible load pickup capacity. Effective damping relaxes the frequency nadir constraint and permits larger load increments within the same frequency headroom. Unbalance suppression efficiency prevents derating of available sources and makes more power available for load pickup. The formulation demonstrates that the proposed estimation and control enhancements yield measurable improvements in restoration speed, transient security, and economic efficiency compared with conventional methods. Collectively, these results confirm that grid-forming converters equipped with the proposed estimation and control methods can serve as the primary enablers of black-start restoration.

# List of Abbreviations

| Abbreviation | Full Form |
|---|---|
| ADN | Active Distribution Network |
| ARMAX | Autoregressive Moving Average with Exogenous Input |
| BS | Black Start |
| CDF | Customer Damage Function |
| CDSC | Cascaded Delayed Signal Cancellation |
| CDSC-PLL | Cascaded Delayed Signal Cancellation Phase-Locked Loop |
| CHiL | Control Hardware-in-the-Loop |
| CIG | Converter-Interfaced Generator |
| CWT | Continuous Wavelet Transform |
| DDSRF | Decoupled Double Synchronous Reference Frame |
| DDSRF-PLL | Decoupled Double Synchronous Reference Frame Phase-Locked Loop |
| DG | Distributed Generator |
| DSC | Delayed Signal Cancellation |
| DSP | Digital Signal Processor |
| DSOGI-PLL | Dual Second-Order Generalised Integrator Phase-Locked Loop |
| D-STATCOM | Distribution Static Synchronous Compensator |
| DVR | Dynamic Voltage Restorer |
| EM | Expectation–Maximisation Algorithm |
| EM–K | Expectation–Maximisation-Enhanced Kalman Filter |
| ESEM | Enhanced Stability Estimation Method |
| FCS-MPCC | Finite Control Set Model Predictive Current Control |
| FF-PLL | Feed-Forward Phase-Locked Loop |
| FOD | Fractional-Order Damping |
| FREM | Fast Response Estimation Method |
| GB | Great Britain |
| GFL | Grid-Following (Converter Control Mode) |
| GFM | Grid-Forming (Converter Control Mode) |
| GL | Grünwald–Letnikov |
| GUI | Graphical User Interface |
| IEEE | Institute of Electrical and Electronics Engineers |
| LC | Inductor–Capacitor Filter |
| LB | Lower Bound |
| LP | Linear Programming |
| LPF | Low-Pass Filter |
| MaxAE | Maximum Absolute Error |

| **Abbreviation** | **Full Form** |
|---|---|
| MILP | Mixed-Integer Linear Programme |
| MSE | Mean Squared Error |
| MVAr | Megavolt-Ampere Reactive |
| MW | Megawatt |
| NBS | Non-Black-Start |
| NPC | Neutral-Point-Clamped |
| NSR | Noise-to-Signal Ratio |
| PCC | Point of Common Coupling |
| PI | Proportional–Integral Controller |
| PLL | Phase-Locked Loop |
| PMU | Phasor Measurement Unit |
| PSS | Power System Stabiliser |
| p.u. | Per Unit |
| PWM | Pulse-Width Modulation |
| P–f | Active Power–Frequency Loop |
| P–ω | Active Power–Frequency Droop |
| Q–V | Reactive Power–Voltage Droop |
| R-L | Riemann–Liouville |
| RMS | Root Mean Square |
| RMSE | Root Mean Square Error |
| RoCoF | Rate of Change of Frequency |
| S/H | Sample and Hold |
| SG | Synchronous Generator |
| SNR | Signal-to-Noise Ratio |
| SOGI-QSG | Second-Order Generalised Integrator Quadrature Signal Generator |
| SPWM | Sinusoidal Pulse-Width Modulation |
| SRF-PLL | Synchronous Reference Frame Phase-Locked Loop |
| STATCOM | Static Synchronous Compensator |
| THD | Total Harmonic Distortion |
| UB | Upper Bound |
| UBF | Voltage Unbalance Factor |
| $UBF_2\%$ | Negative-Sequence Voltage Unbalance Factor |
| $UBF_0\%$ | Zero-Sequence Voltage Unbalance Factor |

# List of Symbols

| Symbol | Definition |
|---|---|
| **Latin Letters Uppercase** | |
| $A$ | (i) State transition matrix; (ii) Amplitude of the $i$-th Prony mode ($A_i$) |
| $A_{eq}, B_{eq}$ | Equality-constraint coefficient matrices (MILP) |
| $A_{in}, B_{in}$ | Inequality-constraint coefficient matrices (MILP) |
| $A_m$ | Measured peak amplitude of the fractional-derivative output |
| $B$ | (i) Noise bandwidth of band-limited noise process; (ii) Set of buses |
| $B_H, B_N$ | Effective harmonic/high-frequency measurement noise bandwidths |
| $C, C_k$ | Observation (measurement) matrix; subscript $k$ denotes time-varying form |
| $C_{dc}$ | DC-link capacitance |
| $C_f$ | Filter capacitance |
| $D$ | (i) Damping coefficient; (ii) Unbalance input perturbation; (iii) Set of loads |
| $D^{\alpha}$ | Fractional derivative operator of order $\alpha$ |
| $E[\cdot]$ | Expectation operator |
| $\mathcal{F}\{\cdot\}$ | Fourier transform operator |
| $F_{k\|k-1}$ | Prior (predicted) error covariance matrix |
| $F_{k\|k}$ | Posterior (updated) error covariance matrix |
| $G$ | Set of distributed generators |
| $G_{BS}$ | Subset of black-start-capable generators |
| $G_{GFM}$ | Subset of grid-forming converters |
| $G_{NBS}$ | Subset of non-black-start generators, $G \setminus G_{BS}$ |
| $H$ | Inertia constant (general) |
| $H_c(t)$ | Cumulative integral inertia estimator |
| $H_f$ | Frequency-domain inertia index |
| $H_i$ | Complex residue of the $i$-th Prony mode |
| $\mathcal{I}(t)$ | Instantaneous integrand of the integral-based estimator |
| $I_{g,\text{rated}}$ | Rated per-phase current of the converter $g$ |
| $K_k$ | Kalman gain matrix at time step $k$ |
| $K_g$ | Baseline frequency-droop coefficient of the generator $g$ |
| $\bar{K}_g$ | Effective damping coefficient (incorporating $\delta_{\text{FOD}}$) |
| $L$ | Set of branches |
| $L_f$ | Converter-side filter inductance |
| $M$ | (i) Measurement noise covariance matrix; (ii) Big-$M$ constant (MILP) |
| $N$ | (i) Memory/window length; (ii) Butterworth filter order; (iii) Buffer size |
| $P$ | Measured active power |

| Symbol | Definition |
|---|---|
| $P_g^{\max}$ | Maximum (nameplate) active-power capacity of the generator $g$ |
| $\bar{P}_g^{\max}$ | Effective maximum active-power capacity (derated) |
| $P_g^{\text{start}}$ | Startup power consumption of the generator $g$ |
| $P_{g,t}^{DG}$ | Active-power output of the generator $g$ at time $t$ |
| $P_{g,t}^{R}$ | Active-power reserve of the generator $g$ at time $t$ |
| $P_{L,k}$ | Active-power demand of the load $k$ |
| $P_{l,t}^{line}$ | Active-power flow on the branch $l$ at time $t$ |
| $P_s(\alpha, \Delta\omega)$ | Signal power after fractional differentiation |
| $P_\eta(\alpha, B)$ | Noise power after fractional differentiation |
| $Q$ | Measured reactive power |
| $Q_g^{\max}, Q_g^{\min}$ | Maximum/minimum reactive-power limits of the generator $g$ |
| $\bar{Q}_g^{\max}, \bar{Q}_g^{\min}$ | Effective (derated) reactive-power limits |
| $Q_{g,t}^{DG}$ | Reactive-power output of the generator $g$ at time $t$ |
| $Q_{L,k}$ | Reactive-power demand of the load $k$ |
| $Q_{l,t}^{line}$ | Reactive-power flow on the branch $l$ at time $t$ |
| $R_f$ | Filter resistance |
| $R_g$ | Active-power ramp rate of the generator $g$ |
| $S$ | (i) Transient strength coefficient; (ii) Set of customer sectors |
| $S_k$ | Innovation covariance matrix at time step $k$ |
| $S_{\text{base}}$ | System-based apparent power |
| $S_g$ | Apparent-power rating of the generator $g$ |
| $S_l^{\max}$ | Apparent-power thermal rating of the branch $l$ |
| $S_\eta(f)$ | Power spectral density of noise process $\eta(t)$ |
| $SNR_{\text{in}}, SNR_{\text{out}}$ | Input/output signal-to-noise ratio |
| $T$ | (i) Fundamental period; (ii) Full discrete time horizon $\{0, \dots, T_{BS}\}$ |
| $T_1$ | Time steps excluding initial state $T \setminus \{0\}$ |
| $T_{BS}$ | Total number of permissible restoration time steps |
| $T_{dq}(\theta)$ | Park–Clarke transformation matrix |
| $T_s$ | Sampling period |
| $T_S$ | Settling time |
| $U_{b,t}$ | Squared voltage magnitude at the bus $b$ at time $t$ |
| $U_{\max}, U_{\min}$ | Squared upper/lower voltage limits |
| $V_{abc}$ | Three-phase voltage vector |
| $V_d, V_q$ | Direct-axis and quadrature-axis voltage components |
| $V_m$ | Peak phase voltage amplitude |

| Symbol | Definition |
|---|---|
| $V_{pcc}$ | PCC voltage magnitude |
| $V^{+}, V^{-}$ | Positive-/negative-sequence voltage component |
| $WT_f(a, b)$ | Continuous wavelet transform coefficient at scale $a$, translation $b$ |
| $X$ | Set of unobserved (latent) states |
| $Y$ | Set of observed measurements |
| $Z$ | (i) MILP objective function value; (ii) Volt-ampere base; (iii) Grid impedance |
| $Z^{*}_{MILP}$ | Optimal objective value of MILP |

**Latin Letters Lowercase**

| | |
|---|---|
| $a$ | Scale parameter (CWT) |
| $b$ | (i) Translation parameter (CWT); (ii) Right-hand side value (big-$M$); (iii) Bus at which load $k$ is located |
| $c, d$ | Cost coefficient vectors (MILP) |
| $f$ | Frequency |
| $f_c$ | Butterworth filter cutoff frequency |
| $\dot{f}(t)$ | Time derivative of system frequency (RoCoF) |
| $\dot{f}_{\max}$ | Physical RoCoF withstand limit |
| $f_i$ | Modal oscillation frequency of the $i$-th Prony mode |
| $f_s$ | Sampling frequency |
| $f_s^{CDF}(\cdot)$ | Customer damage function for sector $s$ |
| $fr(l), to(l)$ | Sending-end/receiving-end bus of the branch $l$ |
| $k$ | (i) Discrete time-step index; (ii) Area number index |
| $k_{p,d}^{-}, k_{i,d}^{-}$ | Proportional/integral gains, negative-sequence d-axis PI |
| $k_{p,q}^{-}, k_{i,q}^{-}$ | Proportional/integral gains, negative-sequence q-axis PI |
| $k_{p,d}^{0}, k_{i,d}^{0}$ | Proportional/integral gains, zero-sequence d-axis PI |
| $k_{p,q}^{0}, k_{i,q}^{0}$ | Proportional/integral gains, zero-sequence q-axis PI |
| $m_{abc}$ | Total three-phase modulation command |
| $m_{abc}^{+}$ | Positive-sequence modulation index (abc frame) |
| $m_{abc}^{-}$ | Negative-sequence modulation index (abc frame) |
| $m_0$ | Zero-sequence modulation index |
| $m_g$ | The bus on which the generator $g$ is connected |
| $n$ | (i) State vector dimension/Prony model order; (ii) Discrete sample index |
| $p$ | Dimension of the measurement vector |
| $p(Y \mid \theta)$ | Marginal likelihood of observations given parameters |
| $p(Y, X \mid \theta)$ | Complete-data likelihood |
| $s$ | (i) Laplace variable; (ii) Customer sector to which load $k$ belongs |

| Symbol | Definition |
|---|---|
| $s(t)$ | Noisy signal model for normalised d-axis component |
| $t_g^{DG}$ | Startup time of the generator $g$ |
| $t_i$ | $i$-th duration breakpoint in the customer damage function |
| $t_{line}$ | Branch restoration (switching) time |
| $u_{b,t}^{bus}$ | Restoration status of the bus $b$ at time $t$ ($1 =$ energised) |
| $u_{g,t}^{DG}$ | Restoration status of the generator $g$ at time $t$ ($1 =$ online) |
| $u_{k,t}^{Load}$ | Restoration status of the load $k$ at time $t$ ($1 =$ restored) |
| $u_{l,t}^{line}$ | Restoration status of the branch $l$ at time $t$ ($1 =$ closed) |
| $v_{PCC,0^{\perp}}(t)$ | Orthogonal (quarter-period delayed) zero-sequence component |
| $w_k$ | Process noise vector at time step $k$ |
| $x$ | Vector of continuous decision variables (MILP) |
| $x_k$ | State vector at time step $k$ |
| $\hat{x}_{k\|k-1}$ | Prior (predicted) state estimate at step $k$ |
| $\hat{x}_{k\|k}$ | Posterior (updated) state estimate at step $k$ |
| $x_{\min}, x_{\max}$ | Lower/upper bounds of continuous variable (big-$M$) |
| $z$ | Vector of binary decision variables (MILP) |
| $z^{-1}$ | Unit delay operator |

**Greek Letters**

| | |
|---|---|
| $\alpha$ | (i) Fractional derivative order; (ii) Active-power reserve requirement |
| $\alpha_{\text{opt}}$ | Optimal fractional order minimising the NSR |
| $\beta$ | Process noise covariance matrix |
| $\gamma_g$ | Converter derating factor due to negative-sequence current, $1/(1+\rho_g)$ |
| $\Gamma(z)$ | Gamma function |
| $\delta$ | (i) Rotor angle; (ii) Power angle (between $\vec{V}_{pcc}$ and $\vec{V}_g$) |
| $\delta_{\text{FOD}}$ | FOD damping enhancement factor (settling-time ratio minus one) |
| $\Delta\delta$ | Small perturbation of the power angle about $\delta_0$ |
| $\Delta f$ | Frequency deviation |
| $\varepsilon_m$ | Additive amplitude measurement perturbation |
| $\epsilon$ | (i) Small regularisation constant |
| $\epsilon_H$ | Maximum relative inertia estimation error |
| $\epsilon_R$ | Relative RoCoF estimation error |
| $\epsilon_k$ | Innovation (measurement residual) at time step $k$ |
| $\zeta_i$ | Damping ratio of the $i$-th Prony mode |
| $\eta(t)$ | Additive zero-mean noise process |
| $\eta_H$ | Inertia estimation confidence factor, $1/(1+\epsilon_H)$ |

| Symbol | Definition |
|---|---|
| $\theta$ | (i) EM parameter vector (ii) Angular position of rotating reference frame |
| $\lambda_i$ | Continuous-time pole of the $i$-th Prony mode |
| $\mu_R$ | RoCoF-detection confidence factor, $1-\epsilon_R$ |
| $\xi$ | SNR preservation factor |
| $\rho_g$ | Negative-sequence current ratio of converter $g$, $I_g^-/I_g^+$ |
| $\sigma_i$ | Damping coefficient of the $i$-th Prony mode |
| $\sigma_{\hat{d}}^2$ | Variance of the signal component of $\hat{d}[n]$ |
| $\sigma_\eta^2$ | Variance of the additive measurement noise |
| $\psi(t)$ | Mother wavelet function |
| $\omega$ | Angular frequency |
| $\omega_i$ | Imaginary part of the $i$-th Prony continuous-time pole |
| $\omega_{\mathrm{ref}}$ | Reference angular frequency for the Park–Clarke transformation |

**Special Notations**

| | |
|---|---|
| $*$ | Convolution operation |
| $(\cdot)^*$ | Complex conjugation |
| $(\cdot)^T$ | Matrix or vector transpose |
| $\arg(\cdot)$ | Argument (phase angle) of a complex number |
| $\ln(\cdot)$ | Natural logarithm |
| $\mathrm{rect}(t)$ | Unit rectangular pulse function |
| $\mathrm{sinc}(x)$ | $\sin(x)/x$ |
| $\mathcal{N}(0,\Sigma)$ | Zero-mean Gaussian distribution with covariance $\Sigma$ |
| $0^+$ | Instantly after a disturbance |

**Number Sets**

| | |
|---|---|
| $\mathbb{C}$ | Set of complex numbers |
| $\mathbb{R}$ | Set of real numbers |
| $\mathbb{Z}^+$ | Set of positive integers |

**Table of Contents**

# Chapter 1 Introduction

## 1.1 Background

Reliable and secure operation of an interconnected power system requires continuous balance between generation and demand [1]. Any sustained imbalance appears as a deviation of system frequency from its nominal value and, if not corrected promptly, may trigger protective relay operations that disconnect generation or load. For more than a century, this balance has been supported by synchronous generators (SGs), whose electromechanical dynamics provide an immediate stabilising response and have formed the basis of grid codes and protection coordination. The ongoing energy transition is changing this foundation, as conventional synchronous plants are progressively being replaced by converter-interfaced renewable generation that does not inherently exhibit the same dynamic characteristics [2]. The effects of this transition extend across all operating timescales, from the immediate inertial response following a disturbance to the restoration of an entire network after a widespread blackout. Although this transition affects all operating timescales, this thesis examines the most demanding case, black-start restoration after a complete blackout, where insufficient inertia, inadequate damping, poor frequency measurement fidelity, and degraded voltage quality manifest simultaneously and at their most severe. The central problem addressed in this thesis is how to enable converter-interfaced generation to reliably perform black-start restoration without relying on synchronous generators, while overcoming these combined challenges. The following subsections examine three connected aspects of this problem and establish the motivation for the research.

### 1.1.1 The Displacement of Synchronous Generation and the Decline of System Inertia

The conventional power system architecture shown in Figure 1.1 is built around large centralised synchronous generators. Hydroelectric and thermal plants provide bulk generation at high voltage, and power flows in one direction through transmission and distribution networks to end consumers. In this structure, synchronous generators serve not only as energy sources but also as the providers of four inherent stability services. These are: (i) rotational inertia from stored rotor kinetic energy that resists frequency changes during power imbalances, (ii) electromechanical damping from damper windings, (iii) synchronous torque that maintains phase coherence through rotor–stator electromagnetic coupling, and

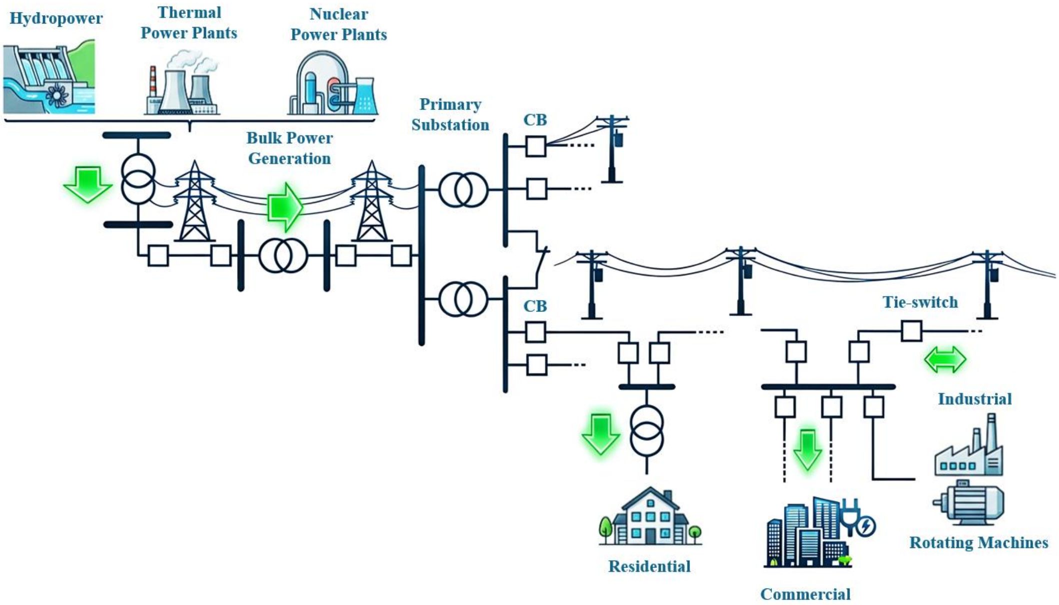


**Figure 1.1:** Conventional power system with centralised generation.

(iv) fault current capability made possible by low sub-transient reactance, which supplies the high currents needed for proper relay operation. Together, these four services form the physical basis of power system stability, protection, and control.

Figure 1.2 shows how this basis is changing. In the modern power system, power flow is increasingly bidirectional, while wind farms, battery storage systems, and other distributed resources continue to displace the synchronous fleet. Because these resources are connected through power electronic converters rather than directly coupled rotating machines, they do not inherently provide the same four services. Dedicated control strategies, most notably grid-forming converter architectures, can emulate several of these services. However, the fidelity of this emulation depends critically on the estimation and control methods employed within the converter, particularly under the extreme conditions encountered during black-start restoration, which constitutes the central focus of this thesis.

Among the four services, the decline of rotational inertia carries the most immediate consequences for frequency stability. For a given power imbalance, the initial rate of change of frequency (RoCoF) is inversely proportional to the total system inertia. The RoCoF at the onset of a disturbance is theoretically determined directly from the swing equation, $\frac{df}{dt} = -\frac{f_0 \Delta P}{2H}$, where $f_0$ is the nominal frequency, $\Delta P$ is the active power imbalance in per unit, and H is the inertia constant in seconds. However, in practice, the UK Grid Code assesses RoCoF

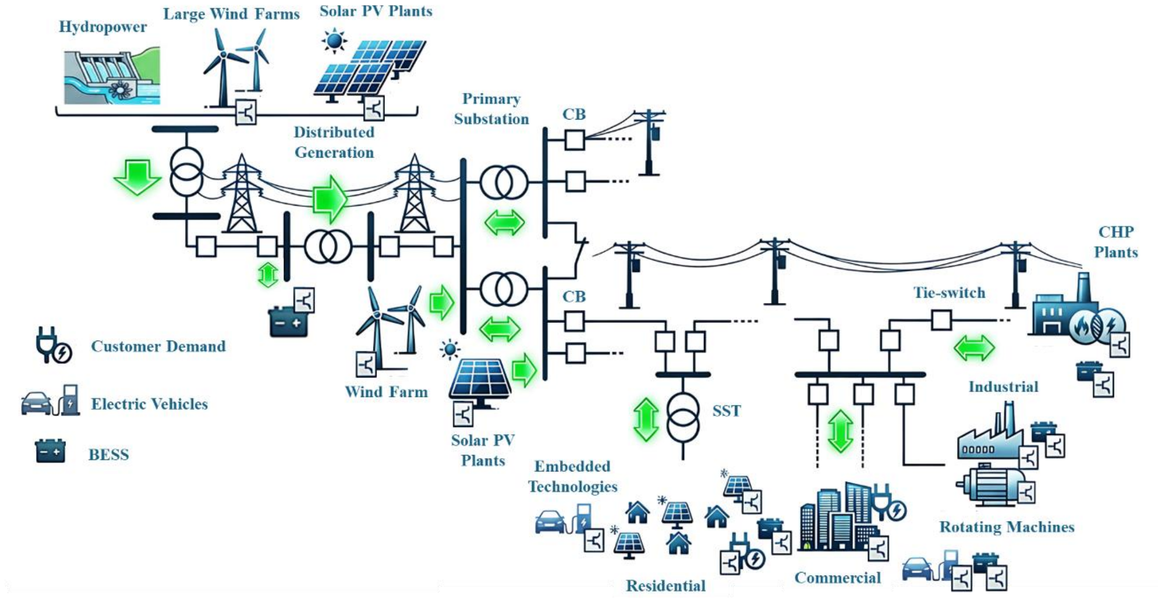


**Figure 1.2:** Modern power system with converter-interfaced generation.

over a 500 ms rolling measurement window [3]. Reducing the inertia to one-third of its original value increases the rate at which frequency deviates from its nominal value by a factor of three. Figure 1.3 demonstrates this relationship through two systems subjected to an identical disturbance. The high-inertia system exhibits a moderate RoCoF and a shallow frequency nadir, while the low-inertia system exhibits a RoCoF approximately three times steeper and a deeper nadir. The time available for corrective action contracts accordingly. Moreover, the reduction in electromechanical damping compounds the inertia deficit. Not only does the frequency deviate faster in a low-inertia system, but the oscillatory response

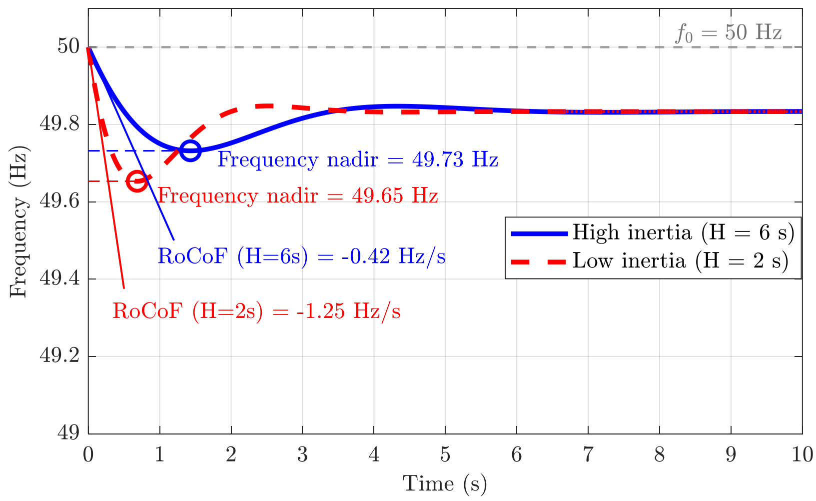


**Figure 1.3:** Frequency response of high and low-inertia systems to identical disturbance.

following a disturbance is less well-damped, which leads to larger power overshoots and longer settling times before a new equilibrium is reached.

These effects are no longer hypothetical. Figure 1.4 presents the projected duration curve of the system inertia constant for the Great Britain power system under increasing converter-based resource penetration. The 2030 scenario already indicates a notable reduction from the historical norm of approximately five to six seconds, while the 2040 scenario reveals that the inertia constant is expected to fall below one second for approximately twenty percent of the year [4]. Under such conditions, all four stability services that SGs have traditionally provided must be sourced from alternative technologies if secure system operation is to be maintained.

Real events have already shown the consequences of low-inertia operation in power systems worldwide. On 28 September 2016, the South Australian power system experienced a complete blackout [5]. At the time, wind generation supplied a large share of local demand and system inertia was low. A sequence of severe storm-related faults triggered the protection in multiple wind turbines, which caused them to disconnect from the grid. The remaining synchronous generation could not stop the frequency from falling. Around 850,000 customers lost supply. The Australian Energy Market Operator identified low system inertia as a key factor in the speed and severity of the blackout.

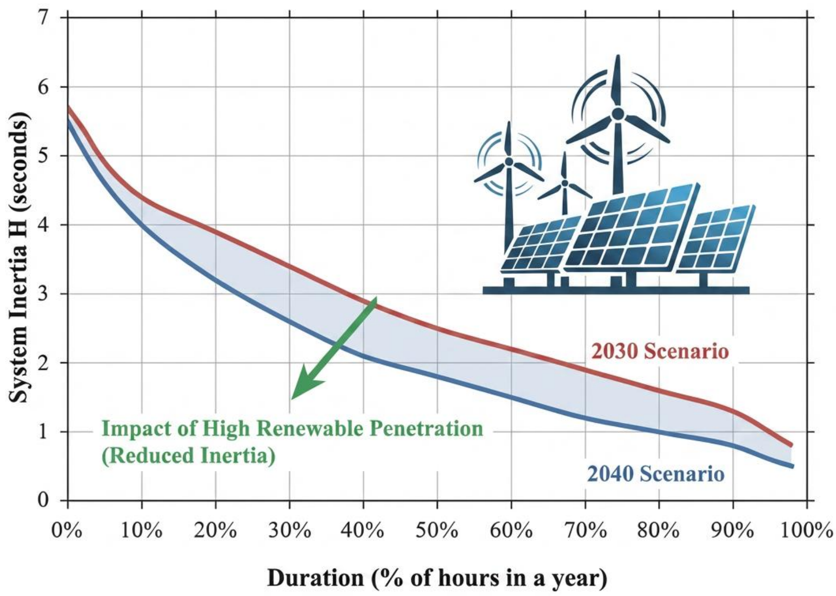


**Figure 1.4:** Projected duration curve of the system inertia constant for Great Britain under increasing converter-based resource penetration [4].

On 9 August 2019, Great Britain experienced a major frequency disturbance. The Hornsea offshore wind farm and the Little Barford gas plant both tripped within seconds of each other, and the system lost approximately 1,528 MW of generation [6]. System frequency fell to 48.8 Hz. Automatic load shedding disconnected approximately one million customers, and rail services across England were disrupted. The post-event investigation identified low synchronous inertia as a contributing factor to the depth of the frequency drop.

In Ireland, low inertia has become a live operational constraint. EirGrid integrated minimum system inertia and maximum rate of change of frequency metrics into its generation scheduling process as early as November 2014. This ensures that the mix of generators committed to run at any given time maintains adequate inertia levels on the system. This confirms that low-inertia operation is not a future risk but a present operational challenge already requiring active management solutions [7].

### 1.1.2 Grid-Forming Converters as the Enabling Technology

The challenges introduced by the displacement of SGs have motivated the power systems research community to develop converter control architectures capable of replicating the stability services that SGs formerly provided. Two fundamentally different control philosophies have emerged, broadly classified as grid-following and grid-forming [8].

A grid-following converter operates on the assumption that a stable voltage waveform already exists at its point of connection. It measures the terminal voltage, extracts the phase angle through a phase-locked loop, and injects current into the network to track an externally determined power reference. This approach functions reliably when the network contains sufficient synchronous generation to maintain a stiff voltage and frequency reference. However, as the synchronous fleet contracts and the system becomes electrically weaker, the phase-locked loop becomes unstable. Under such conditions, interactions between the phase-locked loop dynamics and the weak network impedance can produce sustained oscillations and loss of synchronism. In a black-start scenario, where no voltage reference exists at all, a following converter is by definition unable to operate because there is no grid to follow [9].

In contrast, a grid-forming converter does not require an external voltage reference. Instead, it establishes the voltage magnitude and frequency at its terminals autonomously. Other devices connected to the same network then synchronise to the voltage waveform that the grid-forming converter has created. This fundamental reversal of causality, from following an existing voltage to creating one, is what makes grid-forming control indispensable in converter-dominated and zero-inertia conditions, and particularly during black-start restoration, where the converter must energise a dead network without external support [10].

The ability of a grid-forming converter to emulate the stability services formerly provided by SGs does not, however, guarantee that these services are delivered with sufficient accuracy or speed under all operating conditions. Two real-world projects have demonstrated this capability in practice. In Great Britain, grid-forming battery energy storage systems were contracted to provide synthetic inertia and voltage stability services to the transmission network [11]. In South Australia, a large-scale battery storage system was operated in grid-forming mode, which confirmed that converter-based storage can emulate the voltage and frequency support characteristics of synchronous generators [12]. The fidelity of each emulated service is fundamentally determined by the effectiveness of the estimation algorithms and control loops embedded within the converter. These algorithms and control loops face their most severe test during black-start restoration, which is examined in the following subsection.

### 1.1.3 Black-Start Restoration in Converter-Dominated Networks

The estimation and control challenges discussed above reach their greatest severity during black-start restoration, yet grid-forming converters remain viable resources capable of energising a dead network. The Great Britain Grid Code formally recognises this capability by stipulating that any plant owner contracted to provide a black-start service must demonstrate grid-forming functionality as a prerequisite for service provision [13]. Practical validation of converter-led black-start has also been achieved at the Dersalloch onshore wind farm in Scotland, where a dead network was successfully energised in grid-forming mode [14]. However, black-start restoration with converters remains a significant challenge. Four technical challenges arise simultaneously during this process, as illustrated in Figure 1.5.

- **Challenge 1 (Inertia Uncertainty):** In the early restoration stages, only one or two grid-forming converters may be online and form a small, low-inertia electrical island. Each load pickup produces a steep frequency transient governed by the virtual inertia of the converter rather than by the large rotating mass of a synchronous generator. Accurate real-time inertia estimation is therefore essential for determining safe load-step sizes; overestimation risks a frequency deviation that trips protection and halts

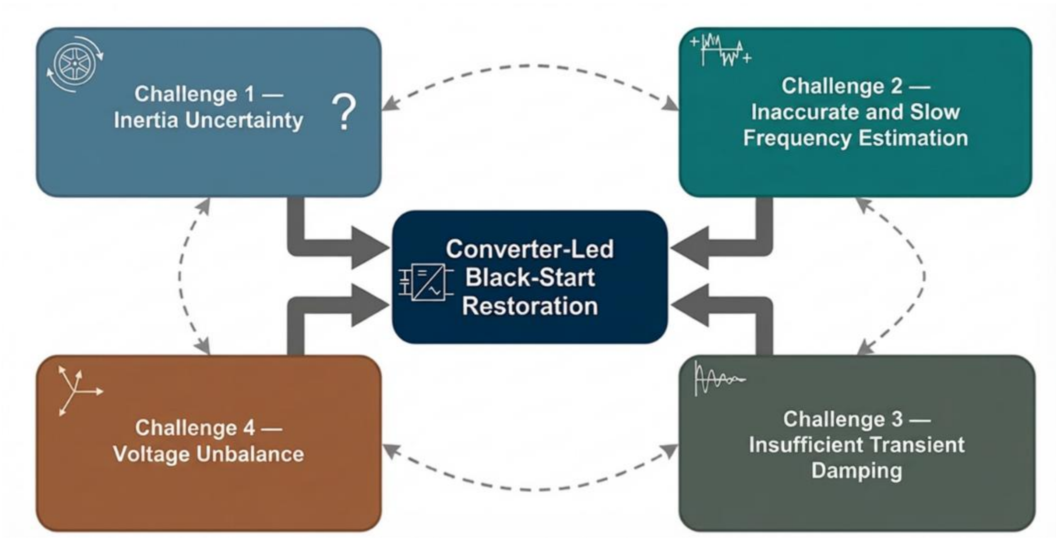


**Figure 1.5:** Technical challenges encountered during converter-led black-start restoration.

restoration, whereas underestimation prolongs the process through unnecessarily conservative load steps.

- **Challenge 2 (Inaccurate and Slow Frequency Estimation):** Accurate and fast frequency information is critical during restoration because the frequency constraints that govern safe load pickup must be evaluated using the actual network frequency. Inaccurate or delayed frequency information may cause the restoration controller to violate a binding constraint or impose excessive conservatism that delays demand recovery.
- **Challenge 3 (Insufficient Transient Damping):** If the low-inertia island formed during black-start is lightly damped, frequency oscillations and power overshoots following each load pickup event will persist. Each restoration step requires the previous transient to be adequately settled before the next switching action can proceed; a lightly damped system prolongs this settling time and directly delays the restoration sequence. The converter providing black-start must therefore deliver sufficient damping to ensure stable restoration.
- **Challenge 4 (Voltage Unbalance):** Balanced three-phase conditions cannot be guaranteed during sequential demand reconnection, because load pickup may include unbalanced loads that produce negative-sequence voltage components. The resulting unbalance degrades power quality and may exceed the voltage unbalance factor limit prescribed by the GB Grid Code. Negative-sequence components also degrade

voltage and frequency regulation through second-harmonic oscillations in the synchronous reference frame.

Reliable converter-led restoration, therefore, requires that all four challenges be addressed concurrently at the converter control level.

## 1.2 Research Aim, Objectives and Contributions

### 1.2.1 Research Aim

The aim of this thesis is to develop novel estimation and control methods for grid-forming converters that address the four technical challenges identified above, and to demonstrate that the formal integration of the outputs of these methods within an optimal restoration framework yields measurably faster, more secure, and more economical black-start restoration of converter-dominated low-inertia networks.

### 1.2.2 Research Objectives

To achieve this aim, five specific research objectives are defined and organised into three complementary domains: estimation, control, and system-level integration. The estimation domain develops real-time knowledge of system inertia and network frequency (addressing Challenges 1 and 2). The control domain enhances the transient performance and voltage quality of the grid-forming converter during restoration (addressing Challenges 3 and 4). The system integration domain embeds the outputs of all estimation and control methods within an optimal restoration decision framework.

#### 1.2.2.1 Estimation Domain Objectives

- **Objective 1:** To develop rapid, accurate, and numerically stable methods for estimating the inertia of converter-dominated low-inertia networks (addressing Challenge 1).
- **Objective 2:** To develop rapid and accurate algebraic methods for system frequency estimation within a sub-cycle timescale, free from the inherent convergence delays of feedback-based tracking loops (addressing Challenge 2).

#### 1.2.2.2 Control Domain Objectives

- **Objective 3:** To design a supplementary damping controller for the grid-forming converter that suppresses active power oscillations during transient events, is inherently inactive during steady-state operation, and offers a continuously tunable damping characteristic (addressing Challenge 3).

- **Objective 4:** To develop a voltage unbalance decoupling and suppression framework for the grid-forming converter that reduces unbalance to within grid code limits and adapts automatically to variable noise conditions (addressing Challenge 4).

### 1.2.3 System Integration Objective

- **Objective 5:** To formulate an optimal black-start restoration model for a converter-dominated low-inertia distribution network that formally embeds the outputs of Objectives 1–4 as constraint parameters, and to demonstrate that this integration yields measurably faster, more secure, and more economical restoration compared with conventional approaches.

Together, these five objectives span the full path from converter-level signal estimation, through enhanced converter control design, to system-level operational optimisation.

### 1.2.4 Research Contributions

Seven original contributions are made to achieve the five objectives stated above.

- **Contribution 1 — Wavelet-based inertia estimation in the frequency domain (Objective 1):** A frequency-domain inertia index is formally defined for the first time from the ratio of peak wavelet coefficients extracted from measured active power and angular frequency signals. A closed-form analytical proof establishes that this index is exactly proportional to the conventional inertia constant. Numerical differentiation is replaced entirely with wavelet coefficient magnitudes. This removes the noise amplification and division-by-zero instabilities that undermine all derivative-based estimators.
- **Contribution 2 — Integral-based inertia estimation in the time-domain (Objective 1):** The swing equation is transformed through an exact algebraic procedure into a derivative-free integral identity. The unknown inertia constant appears in this identity as a provably exact proportionality factor of a cumulative integral computed from measured power and frequency deviations alone. This is the first estimator that simultaneously captures two physically distinct forms of information. The converged value is exactly proportional to the true inertia constant.

The transient trajectory before convergence reveals how rapidly and strongly each generator contributes to frequency stabilisation after a disturbance.

- **Contribution 3 — Integer-order derivative-based frequency estimation (Objective 2):** The Park–Clarke transformation produces an oscillatory output when the reference frequency is deliberately set to differ from the actual system frequency. A cross-product formulation is derived from this property that algebraically cancels all instantaneous trigonometric dependencies. The result is an expression that equals the frequency deviation at every time instant without the need for filters, iteration, or signal smoothing. Under noise-free simulation conditions, the method tracks step changes, ramps, sinusoidal oscillations, and phase perturbations with at most one sample of delay. Phase-locked loop methods require multiple oscillation cycles to reach the same result.
- **Contribution 4 — Fractional-order derivative-based frequency estimation (Objective 2):** The noise-accuracy trade-off that limits the integer-order derivative methods is dissolved through the use of a derivative of non-integer tuneable order. The frequency deviation appears directly in the output amplitude through a power-law relationship whose exponent is the tuneable order parameter. From this property, the frequency is recovered through a single logarithmic inversion and no feedback loop is needed at any stage. A noise analysis rooted in spectral theory is derived that partitions the full parameter design space into three distinct behavioural regions. From this analysis, a closed-form expression for the optimal non-integer order that minimises the noise-to-signal ratio in mixed-noise environments is produced. The proposed method demonstrates superior accuracy and faster response under both rapid and slow frequency changes compared with recent phase-locked loop methods.
- **Contribution 5 — Fractional-order feedforward damping for grid-forming converters (Objective 3):** A supplementary damping loop based on a non-integer-order derivative of the incremental active power change is contributed. It is formally proved through equilibrium point analysis that this loop does not alter the steady-state operating point. Continuously tunable transient damping is therefore achieved through the non-integer order parameter without any penalty to steady-state frequency regulation or power sharing accuracy. This combination of steady-state preservation and continuously tunable damping is absent from all existing supplementary damping methods.

- **Contribution 6 — Dynamic Expectation-Maximisation-Based Kalman Decoupling Method for Voltage Unbalance Suppression in Grid-Forming Converters (Objective 4):** A voltage unbalance compensation and decoupling framework is developed for grid-forming converters. A novel time-varying observation structure is derived that explicitly encodes the second-harmonic coupling between positive-sequence and negative-sequence voltage components directly into the Kalman filter measurement model. This structural encoding enables the filter to isolate only the measurement content that cannot be explained by the known coupling physics. The filter update then distributes this unexplained content across the sequence state variables with minimum variance. The Expectation–Maximisation algorithm removes the requirement for manual noise covariance tuning and makes the proposed method adaptive to weak grids, an advantage lacking in existing methods. It is therefore self-calibrating under variable and unpredictable noise environments.
- **Contribution 7 — Faster, secure, and economical black-start restoration through integrated converter estimation and control intelligence (Objective 5):** A mixed-integer linear programming formulation for optimal black-start restoration of converter-dominated distribution networks is developed. The outputs of Contributions 1 to 6 are embedded within the formulation through four confidence factors that formally translate the accuracy of each proposed estimation and control method into the constraint parameters of the restoration optimiser. The inertia estimation accuracy scales the available generation headroom. The frequency estimation precision tightens the rate-of-change-of-frequency margin. The damping performance relaxes the frequency deviation constraint. The unbalance suppression effectiveness restores the full rated capacity of the converter. This formal translation establishes for the first time that black-start restoration quality is a continuous and quantifiable function of converter-level estimation and control performance rather than a binary feasibility condition.

Together, these seven contributions achieve the research objectives, as summarised in Figure 1.6.

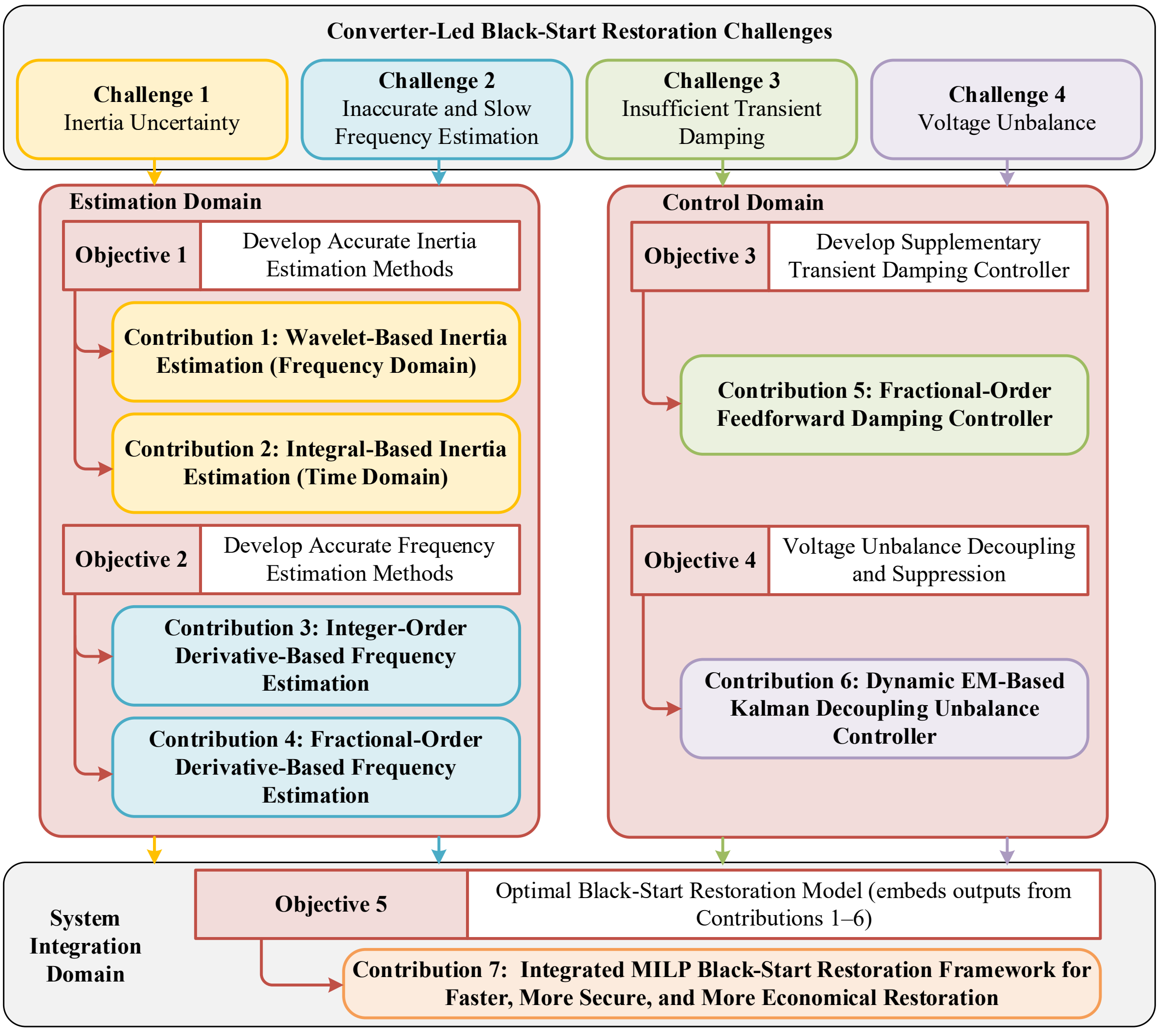


**Figure 1.6:** Mapping of black-start challenges to research objectives and contributions.

## 1.3 List of Publications

- **Journal Papers**

1. **M. Abouyehia**, A. Egea-Àlvarez, S. S. Aphale and K. H. Ahmed, "Novel Frequency-Domain Inertia Mapping and Estimation in Power Systems Using Wavelet Analysis," *IEEE Transactions on Power Systems*, vol. 40, no. 3, pp. 2557–2567, May 2025.

2. **M. Abouyehia**, A. Egea-Àlvarez and K. H. Ahmed, "Evaluating Inertia Estimation Methods in Low-Inertia Power Systems: A Comprehensive Review with Analytic Hierarchy Process-Based Ranking," *Renewable and Sustainable Energy Reviews*, vol. 217, 115794, 2025.

3. **M. Abouyehia**, A. Egea-Àlvarez and K. H. Ahmed, "A Novel Fractional-Order Derivative-Based Method for Frequency Estimation in Low-Inertia Future Grids,"

*IEEE Transactions on Industrial Electronics*, vol. 73, no. 3, pp. 4989–5001, March 2026.

4. **M. Abouyehia**, A. Egea-Àlvarez, A. S. Abdel-Khalik and K. H. Ahmed, "Novel Dynamic Expectation-Maximization-Based Kalman Decoupling Method for Unbalance Controller in Grid-Forming Converters," *IEEE Transactions on Control Systems Technology*, **conditionally accepted for publication**, 2026.
5. A. Colak, **M. Abouyehia** and K. Ahmed, "Novel Hierarchical Energy Management System for Enhanced Black Start Capabilities at Distribution and Transmission Networks," *Energies*, vol. 17, no. 11, 2605, 2024.
6. A. Colak, **M. Abouyehia** and K. Ahmed, "Novel Dynamic Inertia Damping Enhancement of Droop Control for Grid-Forming Converters," *IET Power Electronics*, vol. 19, no. 1, e70219, 2026.

- **Conference Papers**

7. **M. Abouyehia**, Y. N. Abdelaziz, A. Egea-Àlvarez and K. H. Ahmed, "Integral-Based Inertia Estimation Method for Power Systems with High Renewable Integration," *9th IEEE Workshop on the Electronic Grid (eGRID)*, Santa Fe, NM, USA, 2024.
8. **M. Abouyehia**, R. Nasser, A. Egea-Àlvarez and K. H. Ahmed, "Derivative-Based Method for High-Speed Frequency Estimation in Low-Inertia Future Grids," *10th IEEE Workshop on the Electronic Grid (eGRID)*, Glasgow, United Kingdom, 2025.
9. **M. Abouyehia**, A. Colak, R. Nasser, A. Egea-Àlvarez and K. H. Ahmed, "A Novel Fractional-Order Damping Control Method for Enhancing Synchronization in Grid-Forming Converters," *13th International Conference on Smart Grid (icSmartGrid)*, Glasgow, United Kingdom, 2025.
10. A. Colak, **M. Abouyehia** and K. Ahmed, "Resilience and Frequency Control in Low-Inertia Power Systems: Challenges and Solutions," *13th International Conference on Renewable Energy Research and Applications (ICRERA)*, Nagasaki, Japan, 2024.

## 1.4 Thesis Organisation

The remainder of this thesis is organised as follows.

**Chapter 2** reviews the literature in five technical areas relevant to this thesis. These areas include inertia estimation, frequency estimation, damping control for grid-forming converters, voltage unbalance detection and compensation, and black-start restoration optimisation. It classifies the main methods, explains their principles, and identifies their limitations.

**Chapter 3** presents the mathematical foundations used throughout the thesis. These include the Fourier transform, continuous wavelet transform, fractional-order calculus, the discrete-time Kalman filter, the Expectation–Maximisation algorithm, Prony analysis, and mixed-integer linear programming.

**Chapter 4** addresses inertia uncertainty through two novel derivative-free inertia estimation methods. The first employs the continuous wavelet transform to extract transient strengths from active power and angular frequency signals, defines a frequency-domain inertia index from the ratio of peak wavelet coefficients, and derives a closed-form mapping to the time-domain inertia constant. The second reformulates the swing equation into an integral identity that avoids numerical instabilities and produces a continuous running estimate characterising both dynamic inertia response and inertia constants across network areas. The chapter validates the first method through control hardware-in-the-loop experiments and the second through simulations.

**Chapter 5** addresses inaccurate and slow frequency estimation using two novel methods that exploit the oscillatory behaviour of the Park–Clarke transformation under a deliberate reference-frequency offset. The first develops a cross-product formulation where trigonometric terms cancel to yield the frequency deviation algebraically at every instant. The second uses a tunable fractional-order derivative that encodes frequency deviation into the output amplitude and permits recovery through logarithmic inversion with intrinsic noise rejection. The chapter validates the first method through simulations and the second through hardware experiments on a grid emulator.

**Chapter 6** addresses insufficient transient damping and voltage unbalance through two novel control methods for grid-forming converters. The first introduces a fractional-order feedforward damping loop that is inherently inactive at steady state and provides continuously tunable transient damping. The second employs an Expectation–Maximisation-enhanced Kalman filter that encodes second-harmonic coupling between sequence components, followed by dedicated controllers that suppress negative-sequence and zero-sequence voltages. The chapter evaluates the damping method through simulations and the unbalance method through hardware experiments.

**Chapter 7** develops a mixed-integer linear programming formulation for optimal black-start restoration that minimises total customer outage cost subject to constraints on network topology, generator capacity, power balance, voltage, and frequency stability. The outputs of the preceding chapters are embedded through four confidence factors that translate estimation accuracy and control performance into tunable constraint parameters to govern generation headroom and frequency margins. The chapter applies the formulation to a modified IEEE 33-bus distribution system and compares conventional methods against proposed methods.

**Chapter 8** summarises the main conclusions and outlines directions for future research.

# Chapter 2 Literature Review

The progressive displacement of synchronous generation by converter-interfaced sources is diminishing the rotational inertia and electromechanical damping of modern power systems [15, 16], and identifies four technical challenges during restoration. This chapter reviews the existing literature relevant to each challenge and identifies the research gaps that the thesis contributions address. The review spans five technical domains organised from converter-level estimation and control to system-level restoration optimisation, namely inertia estimation, frequency estimation, transient damping control, voltage unbalance compensation, and black-start restoration optimisation.

## 2.1 Inertia Estimation Methods

The initial RoCoF, evaluated within approximately the first 500 ms following an active power imbalance before governor action and damping responses become significant, is inversely proportional to the total inertia of all online synchronous machines [17]. Accurate real-time inertia knowledge is therefore essential for safe load pickup during restoration. The comprehensive review in [18] classified inertia estimation methods into six categories. Table 2.1 summarises these categories with their principal limitations. The six categories span a spectrum from physics-based to data-driven approaches. The dominant standard approach is the analytical swing-equation method, in which measured RoCoF and active power imbalance are substituted directly into the swing equation to compute inertia. The remaining categories build on or depart from this foundation. For instance, adaptive methods extend the standard approach with correction terms for load dynamics or sliding-window averaging. Statistical methods identify inertia from historical measurement patterns. Model-assisted methods use auxiliary hardware or Kalman estimators combined with a system model. Machine learning methods learn frequency–inertia relationships from labelled training data. Frequency-domain methods extract spectral parameters to form a smoothed RoCoF for subsequent use in the swing equation.

In terms of estimation speed, analytical and frequency-domain methods provide estimates within one to two cycles. Adaptive and statistical methods are slower due to data windowing. Kalman filter methods converge relatively fast but depend on model accuracy, while machine learning methods operate in near real time after training but rely on data quality.

**Table 2.1:** Classification of inertia estimation methods.

| Category | Representative Methods | Operating Mechanism | Principal Limitation | Ref. |
|---|---|---|---|---|
| **Analytical** | Swing equation-based methods. Polynomial approximation. | Uses frequency and power in the swing equation to estimate inertia. Polynomial fitting smooths oscillations before estimation. Some formulations can avoid division by zero and estimate damping. | Differentiation amplifies noise. Polynomial fitting needs long data windows. In these methods, accuracy depends on PMU placement. | [19-21] |
| **Adaptive** | Swing equation with frequency-voltage dynamic correction. Sliding window. | Adds a voltage-dependent load model to the swing equation. Uses averaging windows on PMU power and RoCoF data to estimate inertia. | Requires a known load model. Accuracy degrades with fewer PMUs. Window size trades robustness against accuracy. | [22, 23] |
| **Statistical** | Switching Markov Gaussian Model. Autoregressive Moving Average with Exogenous Input. | Learns historical frequency with inertia patterns and updates inertia online. Fits post-disturbance active power and frequency data to estimate local inertia. | Needs retraining and periodic calibration. Needs a clear disturbance window, good synchronised measurements, and sufficient power change. | [24, 25] |
| **Model-Assisted** | Closed-loop micro perturbation identification. Adaptive unscented Kalman filter estimation. | Injects a small designed probing signal and identifies equivalent inertia from the system response. Estimates the inertia online from rotor speed and power measurements. | Closed-loop micro perturbation identification needs probing hardware and sufficient signal quality. Kalman filter accuracy depends on the fidelity of the measurements or the system model. | [26, 27] |
| **Machine Learning** | Convolutional neural network. Residual neural network. Long-recurrent convolutional network. | Trained offline on labelled frequency and voltage measurements with known inertia. Provides fast online estimation after deployment. | Needs large, diverse training data. Generalises poorly to unseen device types or operating conditions. Sensitive to PMU placement. | [28-30] |
| **Frequency Domain** | Interpolated discrete Fourier transform with Kalman filtering. | Interpolated discrete Fourier transform extracts signal parameters. Kalman filtering provides a smoothed RoCoF. The result can then be used in the swing equation to estimate inertia. | Does not estimate inertia directly. Needs accurate knowledge of power imbalance. | [31] |

Existing inertia estimation methods still face several persistent limitations as follows:

- Most methods estimate inertia from RoCoF, which requires differentiating the measured frequency. This amplifies noise and can cause numerical instability. Time-domain solutions, such as polynomial fitting, increase complexity.
- Current methods produce a single inertia value at one instant after a disturbance. They do not capture how the inertial response evolves over the transient or how it varies with the disturbance location and severity.
- Most swing-equation-based methods ignore damping, which is generally valid for synchronous generators during the initial response. However, converters have stronger damping effects that can distort inertia estimation. Therefore, estimating inertia rapidly before the damping response remains a major challenge.

The standard swing-equation method fails on all three counts: differentiation noise corrupts the RoCoF signal, a single-point estimate cannot track how the inertial response evolves over the transient, and the neglect of converter damping biases the estimate as converter penetration increases. These limitations highlight the need for a rapid, robust inertia estimation method for restoration that avoids noisy frequency differentiation, tracks transient inertial response, and remains reliable under large converter damping. Chapter 4 addresses these specific failures by proposing methods that avoid frequency differentiation entirely and produce a continuous inertia profile robust to converter damping.

## 2.2 Frequency Estimation Methods

Accurate and fast frequency estimation is essential for both the inertia estimation methods that require the time derivative of frequency, and the restoration optimisation, where the rate of change of frequency and frequency nadir constraints must be evaluated in real time. Any delay, bias, or noise in the frequency estimate propagates into inertia estimates and degrades restoration decisions. Phase-locked loop (PLL) methods constitute the dominant approach to frequency estimation in power systems [32, 33]. Among PLL variants, the synchronous reference frame PLL (SRF-PLL) is the most widely deployed baseline method against which all other approaches are benchmarked. Table 2.2 summarises the main categories of frequency estimation methods with their principal limitations. Although the second-order generalised integrator frequency-locked loop (SOGI-FLL) shares the fundamental feedback principle of PLL methods and can be considered a closely related approach, it is categorised

**Table 2.2:** Classification of frequency estimation methods.

| Category | Representative Methods | Operating Mechanism | Principal Limitation | Ref. |
|---|---|---|---|---|
| **Standard PLL** | Synchronous reference frame PLL. Feed-forward PLL. | Uses a PI controller to force the q-axis voltage to zero and estimate frequency. The feed-forward form reduces steady-state error during frequency changes. | Sensitive to severe voltage unbalance. The conventional variant has a steady-state tracking error proportional to RoCoF. | [32-34] |
| **Harmonic-Filtering PLL** | Dual second-order generalised integrator PLL (DSOGI-PLL). Cascaded delayed signal cancellation PLL. Cascaded delayed signal cancellation with frequency detector. | Uses pre-filtering stages to reject harmonics and unbalance before frequency estimation. The frequency detector variant replaces the PLL loop with direct algebraic frequency calculation. | Standard DSOGI-PLL has slow convergence and frequency overshoot. Wider harmonic rejection needs more cascaded operators, which roughly increases response time. | [35-37] |
| **Fractional-Order PLL** | Fractional-order synchronous reference frame PLL. | Replaces the integrator with fractional-order operators to provide more tuning freedom. | Requires approximation for fractional integration, which increases computational complexity. | [38] |
| **Kalman Filter** | Extended Kalman filter. Linear Kalman filter with frequency-locked loop. | Estimates voltage or frequency as state variables using recursive prediction and correction. | Requires covariance tuning. The extended Kalman filter accuracy degrades for longer sampling horizons and requires an accurate model for linearisation. | [39, 40] |
| **Frequency-Locked Loop** | Second-order generalised integrator frequency-locked loop. Second-order generalised integrator frequency-locked loop with damping ratio adaptation. | Uses a second-order generalised integrator and a frequency-locked loop for direct frequency estimation. The adaptive variant adjusts the damping ratio online. | Settling time depends on the damping ratio and the nominal frequency, which causes a trade-off between speed and filtering. The adaptive version improves this, but still needs trial-and-error tuning. | [41] |

separately here because it estimates frequency directly through an error-driven frequency adaptation loop without an explicit phase-tracking integration stage.

Existing frequency estimation methods still face several persistent limitations as follows:

- All PLL-based methods use integral control action to track the phase angle, which inherently introduces dynamic delay [32]. The conventional synchronous reference frame PLL (SRF-PLL) is a type-II system that produces a steady-state tracking error proportional to the rate of frequency change during acceleration and deceleration [34].
- Methods that incorporate pre-filters for harmonic rejection necessarily slow the response further. The dual second-order generalised integrator PLL (DSOGI-PLL) has a large convergence time and suffers from overshoot [35]. In cascaded delayed signal cancellation methods, wider harmonic coverage approximately increases the response time [36, 37]. In the second-order generalised integrator frequency-locked loop (SOGI-FLL), stronger filtering capability directly slows the dynamic response [41].
- Non-PLL alternatives, specifically Kalman filter-based methods (linear and extended variants) and algebraic frequency-shift filtering, require either careful parameter tuning or a prolonged period of stable, unchanging grid conditions to converge to accurate estimates. The linear Kalman filter requires trial-and-error tuning of covariance matrices [40]. The extended Kalman filter estimation quality needs a sufficient period of steady-state operation before estimation noise diminishes [39]. The frequency-shift filtering method assumes that the frequency fluctuates only slightly around the nominal value [42].

The standard SRF-PLL fails on all three counts: its integral control action introduces inherent dynamic delay, its type-II structure produces steady-state tracking error proportional to RoCoF, and adding pre-filters for noise rejection slows the response further. These are fundamental limitations of the feedback loop structure shared by all standard PLL and FLL variants. These limitations highlight the need for a frequency estimation method for restoration that eliminates feedback-loop convergence delays, provides robust noise rejection without sacrificing dynamic response, and remains reliable under the steep RoCoF conditions encountered during black-start. Chapter 5 addresses these specific failures by proposing methods that are rapid and robust to noise.

## 2.3 Damping Control for Grid-Forming Converters

In synchronous machines, damper windings produce a torque opposing rotor speed deviations and are critical for stable operation [43]. Grid-forming converters lack physical damper windings, so damping must be explicitly designed into the control structure. The droop controller is the most common method for grid-forming converter control; however, the low-pass filter in the standard droop formulation delays convergence of the converter frequency toward the grid frequency, which produces phase angle errors that drive active power oscillations [44]. During restoration, each load pickup requires the previous transient to settle first, so light damping directly prolongs the restoration sequence. The analysis in [45] classified damping methods into those applied in the active power–frequency loop, those in the voltage magnitude loop, and those exploiting DC-link capacitor dynamics. Table 2.3 summarises these categories with their principal limitations.

Existing methods face several persistent limitations as follows:

- Many active power–frequency loop damping methods inadvertently alter the steady-state operating point. Moreover, using the estimated frequency for damping introduces frequency estimator dynamics that can cause instability in weak grids [45].
- Derivative-based damping terms amplify high-frequency measurement noise and switching harmonics [46] and restrict the achievable damping bandwidth in practice.
- Most damping methods, namely, frequency-difference, derivative, and power-feedforward, require access to virtual angular frequency generated within the power-frequency control loop. These damping methods are not efficient when inertia is realised through the DC-link capacitor [45]. Only voltage-amplitude and DC-link dynamics methods remain applicable in such configurations.
- Integer-order differential damping methods provide a fixed dynamic structure with no intermediate behaviour between proportional action and full differentiation. No existing method offers a continuously adjustable damping characteristic that can be shaped between these two extremes.

These limitations highlight the need for a damping method that offers fast dynamic response, continuously adjustable damping characteristics, preservation of the steady-state operating point, and immunity to derivative-induced noise amplification. The two standard approaches

**Table 2.3:** Classification of damping control methods for grid-forming converters.

| Category | Operating Mechanism | Principal Limitation | Ref. |
|---|---|---|---|
| **Frequency-difference damping (P–f loop)** | Adds a term based on the difference between the grid-forming converter (GFM) frequency and a reference frequency to the active power–frequency loop. The reference may be nominal or PLL-measured frequency. | Using measured frequency adds PLL dynamics that may cause instability in weak grids. Using nominal frequency shifts the steady-state operating point. | [45, 47, 48] |
| **Derivative-based damping (P–f loop)** | Generates a damping signal from the derivative of GFM frequency or active power, filtered to suppress noise. | Derivative action amplifies measurement noise and switching harmonics. Designing the filter to provide strong damping without degrading inertial response remains challenging. | [45, 46, 49] |
| **Power-feedforward and virtual resistance damping (P–f loop)** | Adds a damping signal proportional to the input–output power difference, or virtual resistance without frequency measurement; however, this can raise output impedance and, in weak grids or poor tuning, amplify power oscillations. | The active power–frequency loop is inaccessible in converters where inertia is implemented through a DC-link capacitor. Virtual resistance increases the apparent impedance and may affect power transfer capability. | [45, 50] |
| **PSS-inspired voltage injection (Q–V loop)** | A filtered signal from the virtual angular frequency of GFM is injected into the voltage magnitude reference, similar to a power system stabiliser. | Requires precise filter tuning. Has limited damping effect near zero power output, where the power–angle sensitivity is highest. | [45, 51] |
| **DC-link dynamics matching control (DC-link loop)** | Maps DC-link capacitor voltage dynamics to the AC-side frequency reference via a transfer function parameterised by inertia and damping coefficients. The resulting power-frequency relationship is equivalent to the swing equation, where the damping and inertia coefficients directly emulate the electromechanical damping and inertia constants. | The damping is highly dependent on controller tuning, and improper selection of the damping parameter can lead to oscillatory behaviour or insufficient damping. In particular, the damping must be carefully coordinated with the inertia setting to maintain stability and acceptable dynamic performance. | [52, 53] |

in literature, namely frequency difference damping and derivative-based damping, do not meet these requirements. Chapter 6 addresses these issues using a fractional-order derivative feedforward loop with a tunable order between zero and one applied to incremental active power. This approach naturally goes to zero at steady state and reduces noise amplification compared to integer order derivatives.

## 2.4 Voltage Unbalance Detection and Compensation

During black-start load reconnection, balanced three-phase conditions cannot be guaranteed because feeder sections may carry asymmetric loads. In the positive-sequence synchronous reference frame, voltage unbalance creates second-harmonic oscillations through coupling between positive and negative sequence components [33, 54]. Standard PI controllers remove steady-state error only for DC signals and cannot suppress these oscillations. Grid codes, therefore, limit voltage unbalance to 2% at the point of common coupling [55]. Under unbalanced conditions, unequal phase currents force the grid-forming converter to derate its aggregate power output to keep individual phase currents within rated limits. Effective voltage unbalance detection and compensation are therefore essential for maintaining grid code compliance and avoiding unnecessary capacity derating. Existing methods identified in Table 2.4 can be broadly grouped into hardware-based and control-based solutions.

- Hardware-based methods, including distribution static synchronous compensators (D-STATCOM), static synchronous compensators (STATCOM), and dynamic voltage restorers (DVR), require extra power electronics hardware, added cost, and installation/coordination effort.

Control-based methods avoid extra hardware but introduce their own trade-offs:

- Sequence-separation methods such as the dual decoupled synchronous reference frame PLL (DDSRF-PLL) and the second-order generalised integrator quadrature signal generator (SOGI-QSG) depend on filter tuning, which creates a compromise between disturbance rejection and dynamic response [33, 54, 56, 57].
- Optimisation-based methods such as finite control set model predictive current control (FCS-MPCC) require high computation and accurate system models, which may be difficult during restoration [58].

**Table 2.4:** Classification of voltage unbalance detection and compensation methods.

| Methods | Operating Mechanism | Principal Limitation | Ref. |
|---|---|---|---|
| **Distribution Static Synchronous Compensator (D-STATCOM). STATCOM with a virtual resistor.** | Injects controlled positive- and negative-sequence currents at the point of common coupling. The virtual resistor variant suppresses negative-sequence voltage by balancing virtual branch currents. | Requires extra power-electronic hardware, cost, and installation coordination. | [59, 60] |
| **Dynamic Voltage Restorer (DVR)** | Injects a compensating series voltage through a coupling transformer between the source and the load. | Requires additional series hardware. Accurate tuning is also required. | [61] |
| **Sequence-Selective Virtual Impedance** | Adds software-defined impedance to the converter voltage loop. A negative-sequence virtual inductance compensates the negative-sequence voltage drop across the physical filter inductance. | The virtual inductance design is constrained by the physical filter inductance. Stability is sensitive to impedance choice. | [62] |
| **Finite Control Set Model Predictive Current Control (FCS-MPCC)** | Evaluates candidate switching states at each sampling instant and selects the one that minimises a multi-objective cost function, typically including current tracking, DC-link capacitor voltage balancing, and active damping. | Computational burden is high and increases with converter complexity and the number of switching states. | [58] |
| **Decoupled Double Synchronous Reference Frame Phase-Locked Loop (DDSRF-PLL)** | Transforms the three-phase voltage into two counter-rotating synchronous reference frames. A cross-feedback network removes double-frequency oscillations caused by positive- and negative-sequence coupling, and a low-pass filter extracts the sequence components. | Low-voltage and high-unbalance conditions may cause instability. Filter bandwidth trades disturbance rejection for response speed. | [33, 54] |
| **Second-Order Generalised Integrator Quadrature Signal Generator (SOGI-QSG)** | Generates orthogonal in-phase and quadrature signals from measured αβ-frame voltages using a resonant structure tuned to the fundamental frequency; sequence components are then derived algebraically. | Performance depends strongly on tuning. Poor tuning can cause a slower response or reduced harmonic rejection. | [56, 57] |

- Virtual impedance methods avoid extra hardware by reshaping converter output impedance in software, but their stability depends strongly on impedance selection and coordination with filter and droop parameters [62].

These limitations highlight the need for a voltage unbalance detection and compensation method for grid-forming converters during black-start restoration that achieves robust sequence separation under low-voltage and high-unbalance conditions and adapts to time-varying weak-grid impedance environments. The two standard methods in the literature, namely DDSRF-PLL and SOGI-QSG, do not meet these requirements. Chapter 6 addresses these issues using an expectation maximisation enhanced Kalman filter that explicitly models inter-sequence coupling and updates noise covariances online so it remains adaptive and works across a wide range of unbalance levels.

## 2.5 Black-Start Restoration Optimisation

Power system restoration following a complete or partial blackout is a complex multi-stage problem that requires coordinated scheduling of generators, transmission lines, and loads [63, 64]. The restoration process is usually divided into three phases. The first is a system assessment, in which operators identify the available resources. The second is system restoration, in which black-start generators are started, and the main transmission network is energised. The third is load restoration, where customer loads are gradually reconnected [63, 65]. During black-start, the system must satisfy operational constraints such as active and reactive power balance, and frequency/voltage limits [65, 66]. The following subsections review optimisation methods for black-start restoration and then explain why their performance depends strongly on accurate converter estimation and control.

### 2.5.1 Optimisation Approaches for Black-Start Restoration

Various optimisation approaches have been proposed for black-start restoration in power systems, each reflecting a trade-off between optimality, computational effort, and scalability to large networks. Rule-based and graph-theoretic methods are simple and fast but do not ensure optimal restoration paths. Meta-heuristic methods such as genetic algorithms and particle swarm optimisation improve solution quality but require higher computation time. Dynamic programming can guarantee optimal solutions, but it becomes impractical for large systems due to rapid growth in problem size. Mixed-integer linear programming methods provide a structured framework with optimality guarantees and can represent switching actions, though they depend on accurate linear models. Stochastic extensions further incorporate renewable uncertainty but increase complexity. These trade-offs are summarised in Table 2.5. These methods typically aim to minimise restoration time and generation cost, while ensuring system stability, maintaining voltage and frequency within limits, and maximising load pickup during the restoration process.

Among these approaches, MILP-based optimisation is the most widely adopted for two reasons. First, it naturally represents binary restoration decisions, which are common in black-start, such as the on/off status of circuit breakers [67]. Second, piecewise linearisation allows MILP to represent common nonlinear relationships efficiently, so commercial branch-and-bound solvers can find the global optimum [67-70]. These features make MILP-based optimisation a well-established and effective formulation for black-start restoration.

**Table 2.5:** Classification of optimisation approaches for black-start restoration.

| Optimisation Approach | Advantage | Ref. |
|---|---|---|
| **Rule-based expert systems** | Easy to implement because the restoration steps follow operator experience and predefined rules. | [64, 71, 72] |
| **Meta-heuristic optimisation** | Suitable for large and complex restoration problems where exact methods are too slow. | [73] |
| **Distributed and multi-agent-based optimisation** | Distributes restoration decisions across network areas. Improves scalability, reduces reliance on a central controller, and avoids full network knowledge. | [70, 74] |
| **Dynamic programming-based optimisation** | Evaluates possible system states at each stage and guarantees the best solution, but the computational burden increases rapidly with problem size. | [67] |
| **Mixed-integer linear programming (MILP) based optimisation** | Guarantees the global optimum with high computational efficiency and can directly model on/off decisions. | [67-69] |
| **Graph-theoretic optimisation** | Represents the network as a graph and quickly identifies suitable restoration paths based on network connectivity and restoration priorities. | [75] |
| **Stochastic MILP-based optimisation** | Considers wind and solar uncertainty, so the restoration plan remains feasible under forecast errors. | [69] |

### 2.5.2 Dependence of Restoration Optimisation on Converter Estimation and Control Quality

The optimisation approaches reviewed in the previous subsection provide effective frameworks for restoration decision-making. However, each must enforce physical constraints at every restoration step, and the required parameters must be obtained from the power system. In a conventional power system built around synchronous generators, these parameters are inherent physical properties of the rotating machines. The inertia constant is fixed by the rotor mass and speed, the system frequency is a direct measurement of the rotor angular velocity, damping is provided physically by damper windings, and voltage is established by stator-rotor electromagnetic coupling [65, 66]. These quantities are stable, well characterised, and can be treated as reliable known inputs to any restoration optimiser.

In a converter-dominated low-inertia network, these quantities are produced by estimation and control algorithms within the converter [66, 70, 76]. Inertia is virtual rather than physical, frequency is estimated, damping is provided by control loops, and voltage quality depends on converter regulation and unbalance compensation. As a result, the effectiveness of the restoration optimiser depends on the accuracy of these estimations and control methods.

Regarding inertia estimation and safe load-step sizing, the maximum load that can be connected at each restoration step depends on the available system inertia [67, 69]. If the inertia estimate is too high, the optimiser may allow a load step that exceeds the true system capability, which causes a frequency drop and possible under-frequency protection operation. If the inertia estimate is too low, the optimiser may choose unnecessarily small load steps, which slows the restoration process. Therefore, accurate inertia information directly affects whether load pickup is safe and efficient.

Regarding frequency estimation and constraint evaluation, the RoCoF and frequency nadir constraints for each load pickup must be evaluated from the actual system frequency [65, 67]. If the frequency estimate is slow, the optimiser may permit the next switching action before the previous transient is correctly assessed. If the estimate is noisy or biased, the optimiser may receive a distorted view of the system state, which can cause missed constraint violations or unnecessary blocking of restoration actions. These constraints cannot be neglected during black-start restoration. Grid codes specify minimum frequency limits below which disconnection is required to protect equipment. In addition, generators must withstand limited rates of change of frequency, as excessive variations can trigger protection systems or lead to loss of synchronism. Therefore, the speed and accuracy of frequency estimation directly affect the reliability of restoration.

Regarding transient damping and restoration speed, the system experiences active power oscillations after each load pickup or switching event, and these oscillations must settle before the next action can proceed [66]. If the grid-forming converter provides insufficient damping, the oscillations last longer, which increases the minimum interval between restoration steps. Therefore, the damping performance of the converter directly affects the total restoration time.

Regarding voltage unbalance and available generation capacity, sequential load reconnection may introduce single-phase or unbalanced loads that produce negative-sequence voltage components [76, 77]. If the converter control does not suppress these components effectively, the voltage unbalance factor may exceed grid code limits. The converter may then need to reduce its output to keep phase currents within rated limits, which reduces the generation capacity available for the next restoration steps. Therefore, voltage unbalance compensation directly affects the available generation headroom during restoration.

In summary, black-start restoration in converter-dominated networks is not only an optimisation problem but also a measurement and control problem. The optimisation method provides the decision framework, but the accuracy, speed, and robustness of converter-level estimation and control determine whether restoration is successful, fast, and secure, or whether it is delayed by protection trips, conservative decisions, or grid code violations. This motivates the integration of the converter-level methods developed in this thesis, namely, inertia estimation, frequency estimation, transient damping control, and voltage unbalance compensation, into an MILP-based restoration optimisation framework.

# Chapter 3 Mathematical Foundations for Estimation, Control, and Optimisation

This chapter establishes the mathematical preliminaries upon which the contributions of Chapters 4–7 are built. Seven topics are presented. The Fourier transform and the continuous wavelet transform provide the time–frequency analysis foundations for the inertia estimation method developed in Chapter 4. Fractional-order calculus underpins both the frequency estimation approach of Chapter 5 and the damping controller designed in Chapter 6. The discrete-time Kalman filter and the Expectation–Maximisation algorithm supply the recursive estimation framework employed in Chapter 6. Prony analysis provides the modal extraction technique used in the stability assessment of Chapter 6. Finally, mixed-integer linear programming provides the optimisation formulation adopted for the restoration scheduling problem addressed in Chapter 7. Each tool is presented in its general mathematical form, with emphasis on the properties most relevant to subsequent chapters.

## 3.1 Fourier Transform

The Fourier transform, employed in the estimation domain of this thesis, decomposes a time-domain signal into its constituent frequency components [78]. For a function $g(t)$, the Fourier transform is defined as

$$G(f) = \int_{-\infty}^{\infty} g(t)\ e^{-j2\pi f t}\, dt \tag{3.1}$$

where $f$ denotes frequency in hertz and $j = \sqrt{-1}$. The inverse Fourier transform recovers the original signal, as follows:

$$g(t) = \int_{-\infty}^{\infty} G(f)\ e^{j2\pi f t}\, df \tag{3.2}$$

The existence of $G(f)$ requires that $g(t)$ be absolutely integrable [78].

### 3.1.1 Fundamental Properties of the Fourier Transform

Four properties of the Fourier transform are used extensively in the analytical derivations of this thesis, as follows:

- Linearity: For constants $a, b \in \mathbb{C}$ and functions $g_1(t)$ and $g_2(t)$, the Fourier transform satisfies

$$\mathcal{F}\{a\, g_1(t) + b\, g_2(t)\} = a\, G_1(f) + b\, \mathrm{G}_2(f) \tag{3.3}$$

- Convolution theorem: The Fourier transform of the convolution of two functions is equal to the pointwise product of their Fourier transforms:

$$\mathcal{F}\{g_1 * g_2\}(f) = G_1(f) \cdot G_2(f) \tag{3.4}$$

- Time scaling: For a real constant $a \neq 0$, the Fourier transform satisfies

$$\mathcal{F}\{g(at)\} = \frac{1}{|a|} G\left(\frac{f}{a}\right) \tag{3.5}$$

  Thus, contraction in time ($|a| > 1$) leads to expansion in frequency, and vice versa.

- Time shifting: A delay of $t_0$ seconds introduces a linear phase shift in the frequency:

$$\mathcal{F}\{g(t - t_0)\} = e^{-j2\pi f t_0}\, G(f) \tag{3.6}$$

### 3.1.2 Fourier Transform of Rectangular Pulse

The rectangular pulse function appears frequently in the analytical developments throughout this thesis, and its Fourier transform is therefore stated here for later reference.

The unit rectangular pulse rect $(t)$, defined as unity for $|\ t\ | \leq \frac{1}{2}$ and zero otherwise, possesses the Fourier transform [79],

$$\mathcal{F}\{\mathrm{rect}\,(t)\} = \mathrm{sinc}\,(\pi f) \tag{3.7}$$

where $\mathrm{sinc}\,(x) \coloneqq \sin\,(x)/x$ for $x \neq 0$ and $\mathrm{sinc}\,(0) = 1$. Using the time-scaling property in (3.5) and the time-shifting property in (3.6), a rectangular pulse of width $\Delta t$ centred at $t_0$, written as,

$$\mathrm{rect}_{\,\Delta t}(t - t_0) = \mathrm{rect}\left(\frac{t - t_0}{\Delta t}\right), \tag{3.8}$$

has the Fourier transform

$$\mathcal{F}\{\mathrm{rect}_{\,\Delta t}(t - t_0)\} = \frac{\sin\,(\pi f \Delta t)}{\pi f}\, e^{-j2\pi f t_0} \tag{3.9}$$

## 3.2 Continuous Wavelet Transform

The continuous wavelet transform (CWT), also employed in the estimation domain, is a time–frequency analysis method that examines how the spectral content of a signal evolves over time. Unlike the Fourier transform, which integrates over the entire time axis and thereby discards temporal information, the CWT preserves both time and frequency localisation by comparing the signal with shifted and scaled copies of a reference function called the mother wavelet [80].

### 3.2.1 Definition and Scale–Translation Parameters

The CWT of a finite-energy signal $g(t)$ with respect to a mother wavelet $\psi(t)$ is defined as

$$WT_g(a, b) = \frac{1}{\sqrt{|a|}} \int_{-\infty}^{\infty} g(t)\psi^* \left(\frac{t-b}{a}\right) dt \tag{3.10}$$

where $a \in \mathbb{R} \setminus \{0\}$ is the scale parameter, $b \in \mathbb{R}$ is the translation parameter, and the superscript $^*$ denotes complex conjugation.

The scale parameter $a$ controls the time–frequency trade-off. Large values of $|a|$ stretch the wavelet in time, which narrows its frequency bandwidth and yields high frequency resolution at the expense of time resolution. Small values of $|a|$ compress the wavelet in time, which broadens its frequency bandwidth and yields high time resolution at the expense of frequency resolution. The translation parameter $b$ slides the wavelet along the time axis. At each position $b$, the convolution integral in (3.10) measures the local similarity between the signal and the wavelet. Positions where the wavelet aligns closely with a transient produce large magnitudes, and positions where no transient is present produce small magnitudes.

### 3.2.2 Common Mother Wavelets

Several families of mother wavelets $\psi(t)$ are widely used and can be classified as either real-valued or complex-valued [81], as illustrated in Figure 3.1.

Real-valued wavelets, such as the Mexican Hat and the Derivative of Gaussian, yield coefficients that carry only amplitude information. These wavelets are well-suited to edge detection. Complex-valued wavelets, such as the Gabor wavelet, produce coefficients that contain both amplitude and phase information.

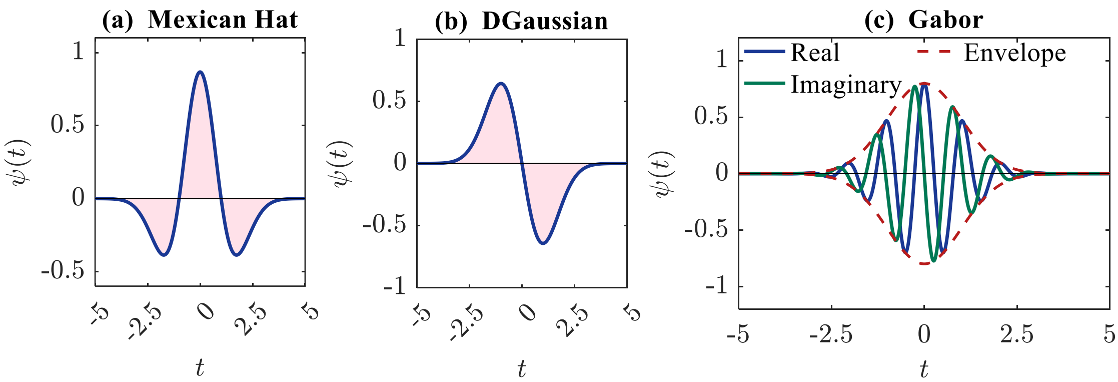


**Figure 3.1:** Different types of wavelet functions $\psi(t)$: (a) Mexican Hat (real), (b) DGaussian (real), and (c) Gabor (complex).

This additional information makes them particularly effective for analysing transient events and especially suitable for the applications considered in this thesis. The Gabor wavelet is defined as

$$\psi(t) = \sqrt{\frac{2}{\pi}}\ e^{-j\omega_0 t}\ e^{-t^2/2} \tag{3.11}$$

where $\omega_0$ is the central frequency parameter. A valid mother wavelet should satisfy the admissibility condition, which requires that the wavelet possess zero mean:

$$\int_{-\infty}^{\infty} \psi(t)\, dt = 0 \tag{3.12}$$

For the Gabor wavelet, the admissibility condition is satisfied when $\omega_0 > 6$ [82].

## 3.3 Fractional-Order Calculus

Classical calculus, whose generalisation underpins both the estimation and control domains of this thesis, restricts the order of differentiation and integration to integer values: the first derivative $f'(t)$, the second derivative $f''(t)$, and so forth. Fractional-order calculus generalises these operations by permitting the order to assume any real value $\alpha$. For a fractional order $0 < \alpha < 1$, the operator $D^\alpha$ produces a result that lies between the original function ($\alpha = 0$) and its first derivative ($\alpha = 1$). This intermediate behaviour introduces a continuous design parameter that is absent in integer-order formulations. Although several definitions of fractional derivatives have been proposed, only the Riemann–Liouville definition and the Grünwald–Letnikov discrete approximation are considered in this thesis.

### 3.3.1 The Gamma Function

Most fractional derivative definitions depend on the Gamma function, which generalises the factorial to non-integer arguments. It is defined for $z > 0$ as [83]:

$$\Gamma(z) = \int_0^{\infty} t^{z-1}\ e^{-t}\, dt \tag{3.13}$$

The Gamma function satisfies the recurrence $\Gamma(z+1) = z \cdot \Gamma(z)$, and for positive integers it reduces to the factorial: $\Gamma(n) = (n-1)!$ for $n \in \mathbb{Z}^+$.

### 3.3.2 The Riemann–Liouville Fractional Derivative

The Riemann–Liouville (R-L) fractional derivative of order $\alpha > 0$ for a function $g(t)$ is [84]:

$$\mathcal{D}^\alpha g(t) = \frac{1}{\Gamma(n-\alpha)} \frac{d^n}{dt^n} \int_{-\infty}^{t} \frac{g(\tau)}{(t-\tau)^{\alpha-n+1}}\, d\tau \tag{3.14}$$

where $n \in \mathbb{Z}^+$ is the smallest integer greater than $\alpha$. For the case of primary interest in this thesis, where $0 < \alpha < 1$, the integer $n = 1$, and the definition reduces to:

$$\mathcal{D}^\alpha g(t) = \frac{1}{\Gamma(1-\alpha)} \frac{d}{dt} \int_{-\infty}^{t} \frac{g(\tau)}{(t-\tau)^\alpha}\, d\tau \tag{3.15}$$

### 3.3.3 Fractional Derivatives of Sinusoidal Functions

For sinusoidal signals, the R-L definition yields the following closed-form expressions [84]:

$$\mathcal{D}^\alpha[\sin(\omega t)] = \omega^\alpha \sin\left(\omega t + \frac{\pi}{2}\alpha\right) \tag{3.16}$$

$$\mathcal{D}^\alpha[\cos(\omega t)] = \omega^\alpha \cos\left(\omega t + \frac{\pi}{2}\alpha\right) \tag{3.17}$$

where $\omega$ represents the angular frequency of the sinusoidal signal. These results reveal two effects of the fractional derivative on sinusoidal signals. The amplitude is scaled by the factor $\omega^\alpha$, which depends on both the signal frequency $\omega$ and the fractional order $\alpha$. For $\alpha = 1$, this factor reduces to $\omega$, and the classical result that differentiation scales a sinusoid by its frequency is recovered. The phase is shifted by $(\pi/2)\alpha$ radians. For $\alpha = 1$, the shift equals $\pi/2$, which is the 90° phase advance of classical differentiation. The effect of fractional differentiation on a sinusoidal signal is illustrated in Figure 3.2.

### 3.3.4 Frequency-Domain Representation of Fractional Derivative

For a function $g(t)$ with the Fourier transform $G(f)$, the Fourier transform of the R-L fractional derivative is [85].

$$\mathcal{F}\{\mathcal{D}^\alpha g(t)\} = (j2\pi f)^\alpha G(f) \tag{3.18}$$

The factor $(j\pi f)^\alpha$ is the transfer function of the fractional derivative operator. This expression shows that the fractional derivative acts as a frequency-dependent gain. For $\alpha = 1$, the gain increases linearly with frequency, which is the well-known high-pass characteristic of first-order differentiation. For $0 < \alpha < 1$, the gain increases at the sub-linear

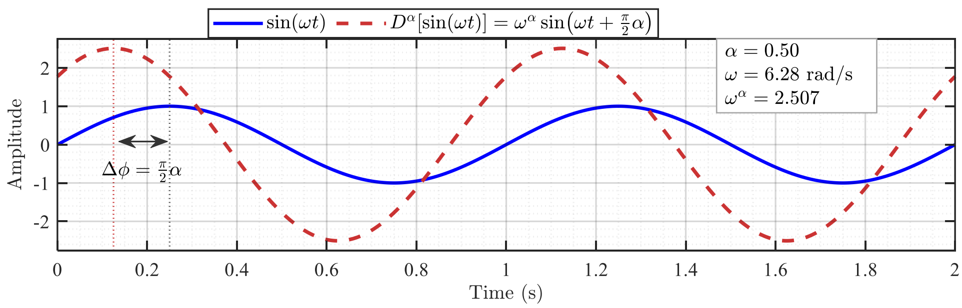


**Figure 3.2:** Illustration of the effect of fractional differentiation on a sinusoidal signal.

rate $f^{\alpha}$, which provides strictly less amplification at every frequency than first-order differentiation. This property is advantageous in reducing noise sensitivity.

### 3.3.5 Discrete-Time Approximation via the Grünwald–Letnikov Formula

The Grünwald–Letnikov definition provides a direct route to the discrete-time implementation of the fractional derivative. It approximates the fractional derivative through a weighted sum of past samples [86]:

$$D^{\alpha}g(t) \approx \frac{1}{h^{\alpha}}\sum_{k=0}^{N} w_k^{(\alpha)}\, g(t-kh) \tag{3.19}$$

where $h$ is the sampling interval, $N$ is the number of retained historical samples (the memory length), and the weights $w_k^{(\alpha)}$ are computed recursively as

$$w_0^{(\alpha)} = 1, w_k^{(\alpha)} = \left(1 - \frac{1+\alpha}{k}\right) w_{k-1}^{(\alpha)}, \quad k = 1,2,\dots,N \tag{3.20}$$

The recursive computation of the weights avoids the explicit evaluation of Gamma functions and is numerically efficient. Each weight $w_k^{(\alpha)}$ corresponds to the generalised binomial coefficient $(-1)^{\mathrm{k}}\binom{\alpha}{k}$. Moreover, the memory length $N$ determines the trade-off between computational cost and approximation accuracy. Larger values of $N$ improve the fidelity of the approximation by retaining more of the historical signal, but each additional sample increases the computational burden at every time step.

## 3.4 Discrete-Time Kalman Filter

The Kalman filter, central to the control domain of this thesis, is a recursive state estimation algorithm that produces the minimum-variance linear unbiased estimate of the internal state of a dynamic system from a sequence of noisy measurements [87]. Its principal advantage lies in its recursive structure, where at each time step only the current measurement and the previous estimate are required.

### 3.4.1 Discrete State-Space Model

The filter operates on a linear discrete-time state-space model of the form

$$x_k = A\, x_{k-1} + w_{k-1} \tag{3.21}$$

$$y_k = C_k x_k + v_k \tag{3.22}$$

In this formulation, $x_k \in \mathbb{R}^n$ is the state vector at time step $k$, $y_k \in \mathbb{R}^p$ is the measurement vector, $A \in \mathbb{R}^{n\times n}$ is the state transition matrix, and $C_k \in \mathbb{R}^{p\times n}$ is the observation matrix. The subscript $k$ on the observation matrix indicates that it may vary with time; when $C_k$ is constant, it is written simply as $C$. The vectors $w_k \in \mathbb{R}^n$ and $v_k \in \mathbb{R}^p$ represent process noise and measurement noise, respectively. Both noise processes are assumed to be zero-mean, white, and mutually uncorrelated Gaussian sequences:

$$w_k \sim \mathcal{N}(0, \beta), v_k \sim \mathcal{N}(0, M) \tag{3.23}$$

where $\beta \succeq 0$ is the process noise covariance and $M \succ 0$ is the measurement noise covariance.

### 3.4.2 Prediction and Update Recursion

The Kalman filter alternates between a prediction step, which propagates the state estimate forward through the dynamic model, and an update step, which corrects the prediction using the current measurement. This recursion process is illustrated in Figure 3.3. In the application considered in this thesis, the control input is zero, and therefore the input term is omitted. Given the posterior state estimate $\hat{x}_{k-1|k-1}$ and its covariance $F_{k-1|k-1}$ at time step $k-1$, the prediction step yields the prior state estimate and covariance,

$$\hat{x}_{k|k-1} = A\,\hat{x}_{k-1|k-1} \tag{3.24}$$

$$F_{k|k-1} = A\,F_{k-1|k-1}\,A^T + \beta \tag{3.25}$$

The difference between the actual measurement and the predicted measurement is commonly referred to as the innovation and is defined as

$$\epsilon_k = y_k - C_k \hat{x}_{k|k-1} \tag{3.26}$$

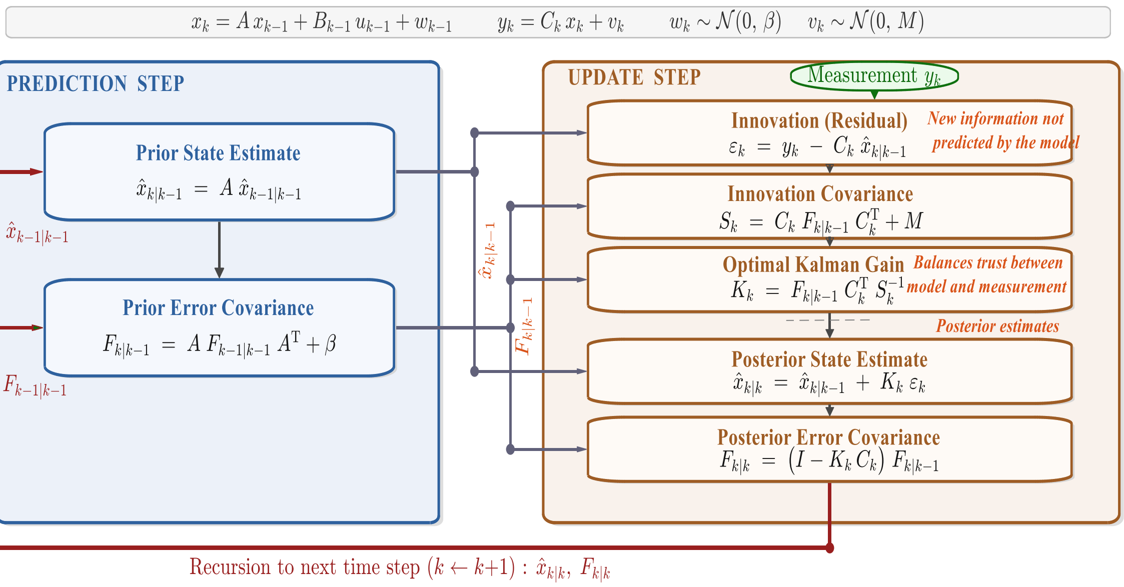


**Figure 3.3:** Block diagram of the discrete-time Kalman filter recursion.

The innovation represents the information content of the new measurement, the component that cannot be predicted from the model and the previous estimate. Its covariance is

$$S_k = C_k F_{k|k-1} \, C_k^T + M \tag{3.27}$$

The optimal gain matrix, which minimises the trace of the posterior error covariance, is

$$K_k = F_{k|k-1} \, C_k^T S_k^{-1} \tag{3.28}$$

The gain represents a compromise between trust in the model prediction and trust in the measurement. When the measurement noise covariance $M$ is large relative to the predicted state covariance $F_{k|k-1}$, the gain is small, and the filter relies predominantly on the model. When $M$ is small, the gain is large, and the filter tracks the measurement closely. The posterior state estimate (update step) and covariance are then obtained as

$$\hat{x}_{k|k} = \hat{x}_{k|k-1} + K_k \, \epsilon_k \tag{3.29}$$

$$F_{k|k} = (I - K_k \, C_k) \, F_{k|k-1} \tag{3.30}$$

The posterior estimate in (3.29) is formed by adding a correction that is proportional to the innovation and scaled by the Kalman gain. The role of the innovation is central when the observation matrix encodes a known coupling or interference structure. In such cases, the predicted measurement $C_k \hat{x}_{k|k-1}$ accounts for the expected interference based on the current state estimates. The innovation, therefore, isolates only the component of the measurement that cannot be explained by the known structure. The Kalman gain then distributes this unexplained component across the state variables in proportion to the current uncertainty.

### 3.4.3 Sensitivity to Covariance Misspecification

In practice, $\beta$ and $M$ are rarely known exactly, and misspecification leads to inaccurate estimates. If $\beta$ is set too small, the filter places excessive trust in the model, which causes the estimate to respond sluggishly to genuine state changes. If $M$ is set too small, the filter places excessive trust in the measurements, and the estimate becomes contaminated by measurement noise. This sensitivity motivates the use of data-driven methods for covariance estimation, such as the Expectation–Maximisation algorithm presented in the following section.

## 3.5 The Expectation–Maximisation Algorithm

The Expectation–Maximisation (EM) algorithm, also employed in the control domain, is an iterative procedure for maximum-likelihood estimation of unknown parameters in probabilistic models that involve latent variables [88]. In the context of state estimation, the latent variables are the true system states $\{x_k\}$, the observed data are the measurements $\{y_k\}$, and the unknowns are $\theta = \{\beta, M\}$.

### 3.5.1 General Formulation

Let $Y = \{y_1, y_2, \dots, y_N\}$ denote the set of $N$ observed measurements, and let $X = \{x_1, x_2, \dots, x_N\}$ denote the corresponding unobserved states. The objective of the EM algorithm is to estimate the parameter vector $\theta$ by maximising the marginal log-likelihood $\ln p(Y \mid \theta)$. Direct maximisation of this quantity is difficult. To circumvent this difficulty, EM replaces the original problem with the maximisation of an auxiliary function [89]

$$Q(\theta \mid \theta^{(i)}) = \mathbb{E}_{X|Y,\theta^{(i)}}[\ln p(Y, X \mid \theta)], \tag{3.31}$$

where $\theta^{(i)}$ is the parameter estimate at iteration $i$. This function is the expected complete-data log-likelihood, evaluated with respect to the posterior distribution of the hidden states conditioned on the observations and the current parameter estimate. The EM algorithm then alternates between the following two steps:

- **The E-step** computes the posterior distribution $p(X \mid Y, \theta^{(i)})$, and uses it to evaluate $Q(\theta|\theta^{(i)})$. For a linear Gaussian state-space model, this is done by applying a Kalman smoother over the $N$-sample window using the current values of $\beta^{(i)}$ and $M^{(i)}$.
- **The M-step** updates the parameter estimate by maximising the auxiliary function:

$$\theta^{(i+1)} = \arg\max_{\theta} Q(\theta \mid \theta^{(i)}). \tag{3.32}$$

### 3.5.2 Closed-Form Updates for Gaussian State-Space Models

For the linear Gaussian state-space model in (3.21)–(3.22), the M-step admits closed-form updates. Let $\hat{x}_k$ denote the state estimate at time step $k$ obtained in the E-step. The updated covariance matrices are given by

$$\beta^{(i+1)} = \frac{1}{N-1}\sum_{k=2}^{N}(\hat{x}_k - A\hat{x}_{k-1})(\hat{x}_k - A\hat{x}_{k-1})^T + \epsilon I, \tag{3.33}$$

$$M^{(i+1)} = \frac{1}{N}\sum_{k=1}^{N}(y_k - C_k\hat{x}_k)(y_k - C_k\hat{x}_k)^T + \epsilon I, \tag{3.34}$$

where $\epsilon I$ is a small regularisation term, with $\epsilon \ll 1$, included to preserve positive definiteness and improve numerical stability during the Kalman gain computation in (3.28).

### 3.5.3 Role of the window length N

The window length $N$ determines the trade-off between estimation accuracy and adaptation speed. A smaller window enables faster tracking of changes in the noise environment, but the resulting covariance estimates are more sensitive to statistical fluctuations. A larger window improves estimation reliability by averaging over more samples, but may reduce responsiveness to rapid changes.

## 3.6 Prony Analysis

Prony analysis, used for stability validation in the control domain, is a parametric signal modelling technique that represents a discrete-time signal as a finite sum of damped complex exponentials. Each component is characterised by an amplitude, phase, frequency, and damping coefficient. Unlike Fourier-based methods, which describe signal content exclusively in terms of frequency, Prony analysis simultaneously identifies both the oscillation frequency and the damping rate of each modal component. This dual characterisation makes the method suitable for stability assessment, where the decay or growth of oscillatory modes determines the stability of the system [90].

### 3.6.1 Damped Exponential Signal Model

Consider a signal $y(k)$ sampled at $T_s$ seconds. Prony analysis approximates this signal as

$$y(k) = \sum_{i=1}^{n} H_i \; z_i^k, \qquad k = 0, 1, \ldots, N-1 \tag{3.35}$$

where $N$ is the total number of samples, $n$ is the model order (the number of exponential modes), $H_i = A_i \, e^{j\phi_i} \in \mathbb{C}$ is the complex residue of the $i$-th mode with amplitude $A_i$ and the initial phase $\phi_i$, and $z_i \in \mathbb{C}$ is the discrete-time eigenvalue. The eigenvalue is related to the continuous-time pole $\lambda_i$ through

$$z_i = e^{(\sigma_i + j\,2\pi f_i)\,T_s} = e^{\lambda_i T_s} \tag{3.36}$$

where $f_i$ is the modal oscillation frequency in hertz and $\sigma_i$ is the damping coefficient in nepers per second. The continuous-time modal parameters are recovered from the discrete-time eigenvalues by inverting (3.36)

$$\sigma_i = \frac{\ln\, |\, z_i \,|}{T_s}, f_i = \frac{\arg\,(z_i)}{2\pi\, T_s} \tag{3.37}$$

The damping ratio associated with each mode is

$$\zeta_i = \frac{-\sigma_i}{\sqrt{\sigma_i^2 + (2\pi f_i)^2}} \tag{3.38}$$

To validate the accuracy of the Prony method, a test signal composed of three damped sinusoidal modes is constructed and analysed with model order $n = 2M = 6$, where $M$ is the number of sinusoidal modes. As shown in Figure 3.4(a), the Prony reconstruction $\hat{y}(t)$ is visually indistinguishable from the original signal $y(t)$. The pointwise error in Figure 3.4(b)

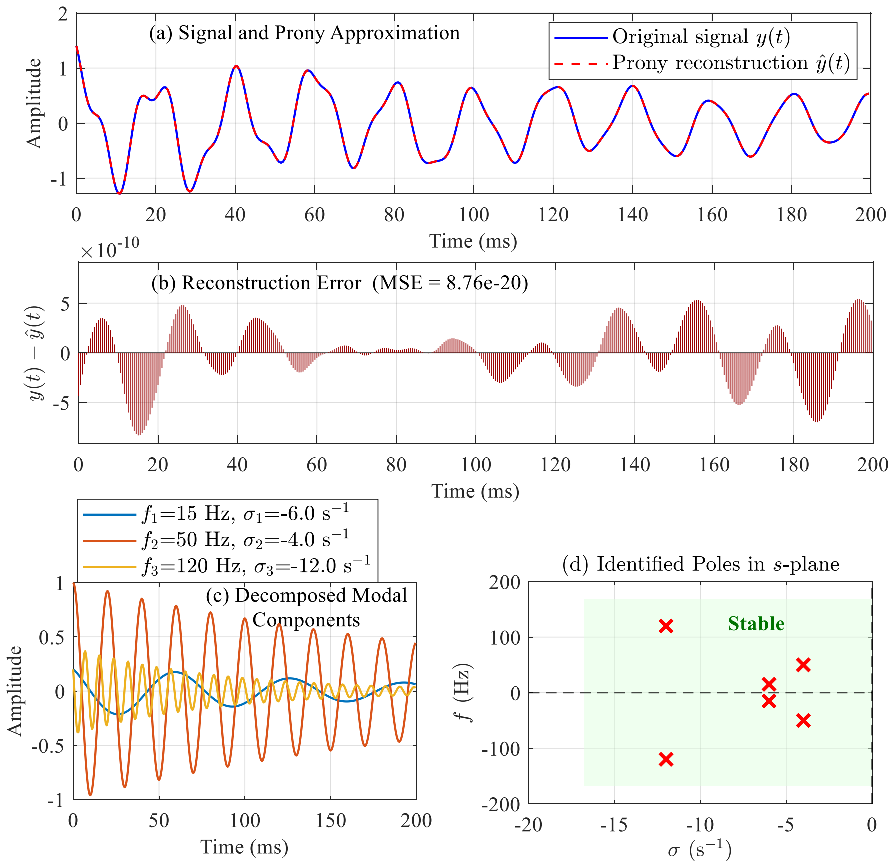


**Figure 3.4:** Prony analysis applied to a measured signal: (a) the original signal y(t) and its Prony reconstruction $\hat{y}(t)$, (b) the pointwise reconstruction error, (c) the three decomposed modal components, and (d) the identified continuous-time poles in the s-plane.

confirms that the residual is at machine-precision level, and demonstrates that Prony analysis provides an exact decomposition when the correct model order is selected. The three recovered modal components, depicted in Figure 3.4(c), match their true counterparts in frequency and damping rate. The corresponding continuous-time poles, plotted in Figure 3.4(d), reside entirely in the stable (left) half of the $s$-plane. This accuracy underpins the use of Prony analysis in the subsequent sections to extract stability-critical oscillatory modes from the PCC voltage response of the grid-forming converter.

## 3.7 Mixed-Integer Linear Programming

Mixed-integer linear programming (MILP), the foundation of the optimisation domain, is a mathematical optimisation framework for problems that involve both continuous and discrete decision variables, subject to linear constraints and a linear objective function [91]. The inclusion of integer (typically binary) variables enables the representation of logical decisions such as the on/off commitment of a unit or the open/closed status of a switch.

### 3.7.1 Standard Formulation for MILP

A mixed-integer linear program in standard form is written as

$$\min_{\mathrm{x,\,z}} \mathcal{Z} = \mathrm{c}^{\mathrm{T}}\mathrm{x} + \mathrm{d}^{\mathrm{T}}\mathrm{z} \tag{3.39}$$

subject to

$$\mathrm{A_{eq}}\,\mathrm{x} + \mathrm{B_{eq}}\,\mathrm{z} = \mathrm{b_{eq}} \tag{3.40}$$

$$\mathrm{A_{in}}\,\mathrm{x} + \mathrm{B_{in}}\,\mathrm{z} \leq \mathrm{b_{in}} \tag{3.41}$$

$$\mathrm{x} \geq 0, \mathrm{z} \in \{0,1\} \tag{3.42}$$

where $\mathcal{Z}$ is the objective function, $\mathrm{x} \in \mathbb{R}^n$ is the vector of continuous decision variables, $\mathrm{z} \in \{0,1\}^m$ is the vector of binary decision variables, c and $d$ are cost coefficient vectors, and the matrices $A_{\mathrm{eq}}$, $B_{\mathrm{eq}}$, $A_{\mathrm{in}}$, $B_{\mathrm{in}}$ and vectors $b_{\mathrm{eq}}$, $b_{\mathrm{in}}$ encode the equality and inequality constraints. In the restoration scheduling problem of Chapter 7, x represents continuous quantities such as generator active power output and ramp rates, while z encodes discrete commitment decisions such as unit energisation sequence and switching actions; both are solved simultaneously within a single optimisation. The exact optimal solution is obtained via the branch-and-bound algorithm, where LP relaxation serves solely to compute bounding values that guide the search, as discussed in the next sections.

### 3.7.2 LP Relaxation and Bounds

The LP relaxation of a MILP is obtained by replacing the integrality constraint $\mathbf{z} \in \{0,1\}^m$ with the continuous relaxation $0 \leq \mathbf{z} \leq 1$. The resulting problem is a standard linear program and can be solved efficiently by conventional methods such as the simplex method. Because the LP relaxation enlarges the feasible set by admitting fractional values of $z$, its optimal objective value cannot exceed the MILP optimum in a minimisation problem:

$$\mathcal{Z}^*_{\mathrm{LP}} \leq \mathcal{Z}^*_{\mathrm{MILP}} \tag{3.43}$$

The LP relaxation, therefore, provides a lower bound on the optimal MILP objective. Conversely, any feasible integer solution provides an upper bound, since it represents a valid but potentially suboptimal candidate. This lower-bounding property of the LP relaxation is fundamental to the branch-and-bound algorithm discussed next, where LP relaxations are solved repeatedly to guide the search for the optimal integer solution.

### 3.7.3 Branch-and-Bound Algorithm

The dominant exact solution method for MILP is the branch-and-bound algorithm, which systematically explores the solution space by constructing a search tree. The procedure is summarised in Figure 3.5 and described below. The algorithm begins by solving the LP relaxation at the root node, in which all integrality requirements are temporarily removed. If the resulting solution already satisfies every integrality constraint, it is optimal for the original MILP, and the process terminates immediately. Otherwise, the LP objective value is recorded as the initial lower bound (LB) and the upper bound (UB) is set to positive infinity. The algorithm then enters the iteration loop shown in the shaded region. A variable $z_j$ whose relaxed value is fractional is selected, and two child nodes are created by fixing $z_j = 0$ and $z_j = 1$, respectively. The LP relaxation is solved at each child node, and one of four outcomes determines what happens next. If the LP relaxation is infeasible, no integer-feasible point can

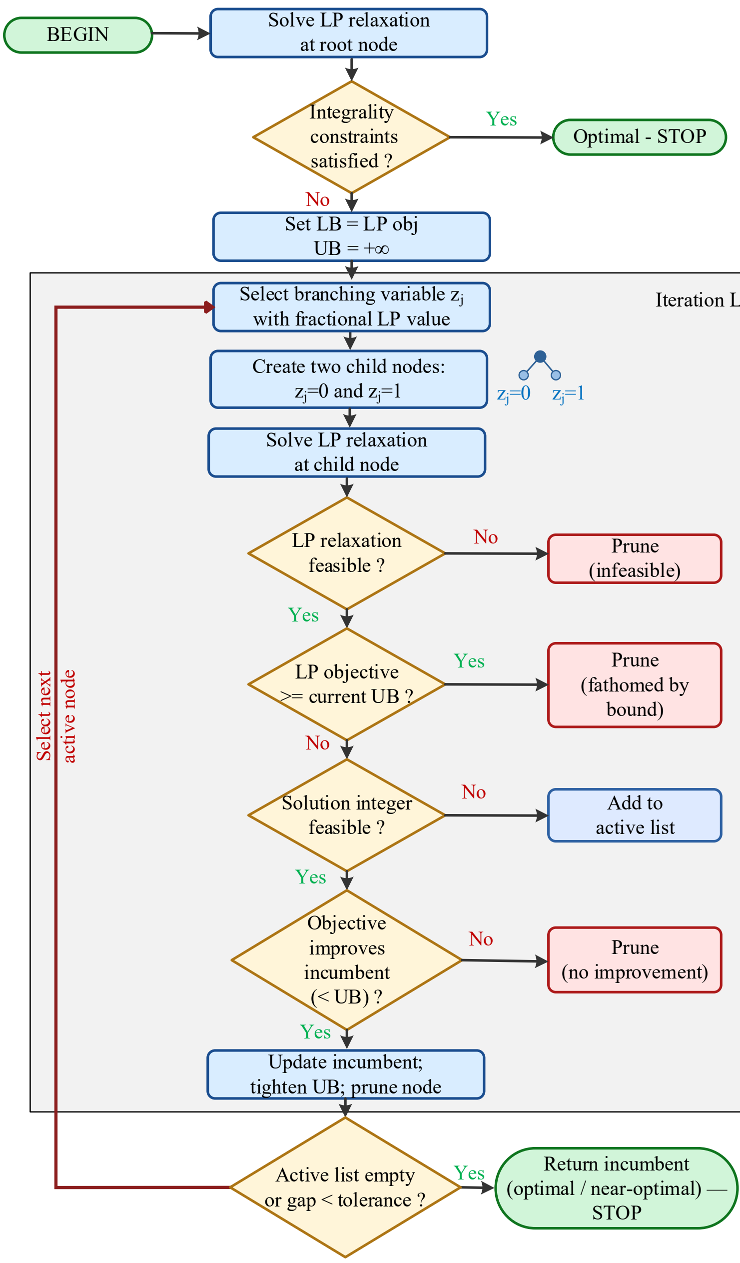


**Figure 3.5:** Flowchart of the branch-and-bound algorithm.

exist in that branch, and the node is pruned. If the LP objective is greater than or equal to the current UB, no descendant of that node can improve upon the best known solution, and the node is likewise pruned. If the LP solution violates at least one integrality constraint yet its objective remains below the UB, the node is added to the active list for further branching. Finally, if the solution satisfies all integrality constraints and its objective is strictly less than the current UB, the incumbent solution is updated, the UB is tightened, and the node is pruned. After processing a node, the algorithm selects the next node from the active list and repeats. The algorithm terminates when the active list is empty.

### 3.7.4 Conditional Constraints via the Big-M Method

Many practical optimisation problems require that a continuous variable be permitted to take nonzero values only when a binary variable is activated. This conditional relationship is represented in linear form through the big-M method. Let $x$ be a continuous variable with bounds $x^{\min}$ and $x^{\max}$, and let $z \in \{0,1\}$ be a binary activation variable. The constraint that $x$ must be zero when $z = 0$ and may lie within $[x^{\min}, x^{\max}]$ when $z = 1$ is expressed as

$$x^{\min} z \leq x \leq x^{\max} z \tag{3.44}$$

When $z = 0$, both bounds collapse to zero and force $x = 0$. When $z = 1$, the bounds expand to the original range $[x^{\min}, x^{\max}]$. The binary variable $z$ therefore acts as a switch that activates or deactivates the continuous variable. A more general form arises when the relationship to be enforced is an equality that should hold only when a binary variable is active. Let $f(x) = b$ be an equality constraint that should be imposed when $z = 1$ and relaxed when $z = 0$. This is modelled as

$$-M(1 - z) \leq f(x) - b \leq M(1 - z) \tag{3.45}$$

where $M$ is a large positive constant. When $z = 1$, the constraint reduces to $f(x) = b$. When $z = 0$, the bounds expand to $[-M, M]$.

## 3.8 Summary

This chapter established the seven mathematical tools that underpin the contributions of Chapters 4–7. The Fourier transform characterises the global frequency content of a signal, while the continuous wavelet transform resolves how that content evolves in time. Fractional-order calculus generalises differentiation to non-integer orders and offers a continuous design parameter between a signal and its first derivative. The discrete-time Kalman filter delivers optimal recursive state estimation, and the Expectation–Maximisation algorithm removes the need for manual tuning of the noise covariance matrices on which the filter relies. Prony analysis recovers oscillation frequencies and damping rates from measured signals for parametric stability assessment. Mixed-integer linear programming provides the optimisation framework for problems that combine continuous and binary decision variables under linear constraints. Each tool is applied in its respective chapter to address a specific estimation, control, or optimisation problem in low-inertia power systems. It is noted that these mathematical foundations are equally established in high-inertia systems, but they become more critical here due to the reduced stabilising margins that characterise converter-dominated grids.

# Chapter 4 Novel Inertia Estimation Methods for Power Systems with High Renewable Integration

Synchronous generators contribute rotational kinetic energy to the power system through the physical coupling between their rotating mass and the electrical network. This stored energy, quantified by the inertia constant H, governs the rate at which the system frequency changes in response to a power imbalance. As synchronous machines are replaced by converter-interfaced resources that possess no inherent rotational inertia, the aggregate system inertia diminishes [92]. The consequence is steeper post-disturbance RoCoF, lower frequency nadirs, and heightened susceptibility to cascading failures.

Inertia awareness becomes particularly critical during black-start restoration. As grid-forming converters sequentially energise sections of the network, the restoration controller must determine at each stage whether the available inertia (both physical and synthetic) can absorb the frequency transient that the next load pickup will produce [93]. An overestimate of inertia may cause frequency deviations sufficient to trigger protective relay operations and abort the restoration sequence. An underestimate leads to unnecessarily conservative load pickup and delays the return to normal service.

Despite the advancements in the methods surveyed in the literature review, significant challenges remain in inertia estimation. These unresolved challenges underscore the need for an accurate, computationally efficient, and robust estimation method. This chapter addresses this need by presenting two complementary novel methods: a wavelet transform-based method that operates in the time–frequency domain and an integral-based method that operates in the time domain. Both methods fundamentally avoid derivative calculations, thereby eliminating the numerical instabilities in conventional estimation methods.

## 4.1 Wavelet-Based Inertia Estimation

This section develops the first of two derivative-free inertia estimation methods proposed in this thesis. The method employs the continuous wavelet transform (CWT), introduced in Section 3.2, to extract transient strengths from measured active power and angular frequency signals without numerical differentiation. Then, a novel frequency inertia index $H_f$, is derived from these transient strengths, and its exact mathematical relationship to the conventional time-domain inertia constant $H_t$, is established.

### 4.1.1 Transient Detection and Quantification Capability

The CWT, defined in (3.10) with the complex Gabor wavelet in (3.11), provides simultaneous time and frequency localisation. At each translation b, the inner product between the signal and the shifted, scaled wavelet quantifies their local similarity. Large coefficient magnitudes indicate alignment with a transient event; small magnitudes indicate quiescent behaviour. The complex Gabor wavelet, illustrated in Figure 3.1(c), is selected for this method because its amplitude and phase information enable accurate timing and quantification of transient events. Figure 4.1 demonstrates this capability through an illustrative example. A step function u(t) with initial value 4 experiences two transient events: a decrease of $\Delta u = 1$ at t = 0.3 s and a decrease of $\Delta u = 2$ at t = 0.6 s, as shown in Figure 4.1(a). The CWT is applied to u(t) with the Gabor wavelet. The resulting coefficient magnitudes $|\mathcal{WT}_{u(t)}(a,b)|$, shown in Figure 4.1(b), exhibit two distinct peaks located precisely at t = 0.3 s and t = 0.6 s. The peak at t = 0.6 s (magnitude 0.334) is exactly twice

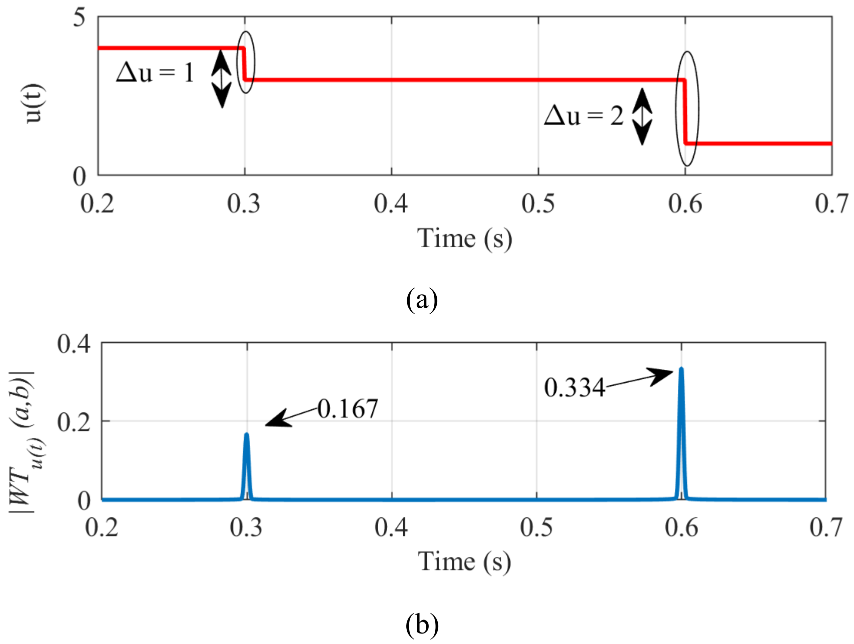


**Figure 4.1:** Wavelet transform applied to transient detection. (a) Step function u(t) with transient events at t = 0.3 s ($\Delta u = 1$) and t = 0.6 s ($\Delta u = 2$). (b) Coefficient magnitudes $|\mathcal{WT}_{u(t)}(a,b)|$ with peaks of 0.167 and 0.334 at the corresponding transient times.

the peak at t = 0.3 s (magnitude 0.167), which mirrors the 2:1 ratio of transient strengths in the time domain.

Two properties are evident from this example. First, the CWT localises transient events in time through the positions of its peak coefficients. Second, the magnitudes of these peaks are directly proportional to the transient strengths. These two properties are exploited in the following subsections to formulate a derivative-free inertia estimation method that relies on time–frequency representation rather than numerical differentiation. Because this formulation replaces numerical differentiation with wavelet coefficient magnitudes, the method is inherently robust to measurement noise.

### 4.1.2 The Swing Equation and Time-Domain Inertia

The inertia constant $H$ governs rotor dynamics through the following swing equation:

$$\frac{2HZ}{\omega_0}\frac{d^2\delta}{dt^2} = \Delta P \tag{4.1}$$

where $\frac{d^2\delta}{dt^2}$ denotes the acceleration of rotor angle $\delta$ over time, $\Delta P$ is the active power imbalance, $Z$ is the volt-ampere (VA) base and $\omega_0$ is the rated angular frequency of the rotor. Additionally, the rotor angle acceleration relates to the angular frequency deviation through

$$\frac{d^2\delta}{dt^2} = \omega_0\frac{d\overline{\Delta\omega_r}}{dt} \tag{4.2}$$

where $\omega_r$ denotes the angular frequency of the rotor and the bar notation denotes per-unit quantities with respect to $Z$ and $\omega_0$. Substitution of (4.2) into (4.1) yields the per-unit form:

$$2H\frac{d\overline{\Delta\omega_r}}{dt} = \overline{\Delta \mathrm{P}} \tag{4.3}$$

The corresponding transfer function representation is shown in Figure 4.2, where the inertia block $1/(2H)$ relates the power imbalance to the rate of change of angular frequency, and the integrator $1/s$ produces the angular frequency deviation. One key observation is that the inertia constant manifests during transient periods. Therefore, integration of both sides of (4.3) over the transient interval $[t_1,\, t_1 + \Delta t]$ produces

$$H_t = \frac{\int_{t_1}^{t_1+\Delta t}\overline{\Delta p}\,dt}{2\overline{\Delta\omega_r}} \tag{4.4}$$

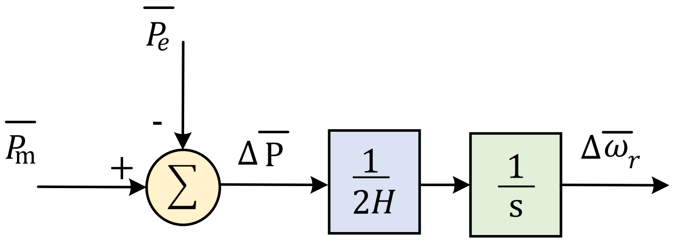


**Figure 4.2:** Transfer function loop for the inertia constant.

where $t_1$ is the instant at which the transient occurs and $\Delta t$ is the transient duration. The subscript t specifies that this value is derived from time-domain analysis.

### 4.1.3 The Frequency Inertia Index

Direct evaluation of (4.4) requires precise identification of the transient duration $\Delta t$ and accurate determination of the transient per unit values of $\Delta\bar{P}$ and $\Delta\bar{\omega}_r$. Both requirements are difficult to satisfy under noisy measurement conditions. The CWT offers an alternative path, as demonstrated in Section 4.1.1, as the peak wavelet coefficients capture transient strengths directly, which avoids extracting transient parameters from the time domain.

To establish the time–frequency formulation, the integral and the factor 0.5 in (4.4) are temporarily removed, and the time-domain inertia is expressed as the simplified ratio:

$$\widetilde{H}_t = \frac{\overline{\Delta p}}{\overline{\Delta \omega_r}} \tag{4.5}$$

where $\widetilde{H}_t$ denotes the simplified inertia ratio obtained by removing the integral and the factor 0.5 from (4.4). The CWT defined in (3.10) with the Gabor wavelet in (3.11) is then applied separately to the measured per-unit active power $\bar{p}(t)$ and angular frequency $\bar{\omega}_r(t)$:

$$\mathcal{WT}_{p(\mathrm{t})}(a,b) = \frac{1}{\sqrt{|a|}}\sqrt{\frac{2}{\pi}}\int_{-\infty}^{\infty} \bar{p}(t)\, e^{i\omega_0\left(\frac{t-b}{a}\right)} e^{\frac{-\left(\frac{t-b}{a}\right)^2}{2}} dt \tag{4.6}$$

$$\mathcal{WT}_{\omega(t)}(a,b) = \frac{1}{\sqrt{|a|}}\sqrt{\frac{2}{\pi}}\int_{-\infty}^{\infty} \bar{\omega}_r\,(t)\, e^{i\omega_0\left(\frac{t-b}{a}\right)}\, e^{-\frac{\left(\frac{t-b}{a}\right)^2}{2}}\, dt \tag{4.7}$$

The transient strengths $\Delta\bar{P}$ and $\Delta\bar{\omega}_r$ correspond to the maximum absolute values of the continuous wavelet transform coefficients $\mathcal{WT}_{p(\mathrm{t})}(a,b)$ and $\mathcal{WT}_{\omega(t)}(a,b)$ defined in (4.6) and (4.7), denoted as $\max_{a,b} |\mathcal{WT}_{p(\mathrm{t})}(a,b)|$ and $\max_{a,b} |\mathcal{WT}_{\omega(t)}(a,b)|$, respectively. The frequency inertia index is therefore defined as

$$H_f = \frac{\max\limits_{a,b}\left|\mathcal{WT}_{p(\mathrm{t})}(a,b)\right|}{\max\limits_{a,b}\left|\mathcal{WT}_{\omega(t)}(a,b)\right|} \tag{4.8}$$

The subscript $f$ indicates that this quantity is derived from time–frequency analysis. Because the integral action and the factor 0.5 in (4.4) have been omitted, $H_f$ does not equal $H_t$ directly. However, the two quantities are related through a constant proportionality, and the precise mapping is established in the following subsection.

### 4.1.4 Mapping Between Hf and Ht

The transfer function in Figure 4.2 is simulated in MATLAB for several values of $H_t$. A step change from 1 pu to 0.5 pu is applied to the per-unit electrical power $\bar{P}_e$, the angular frequency response $\Delta\overline{\omega_r}(t)$ is recorded, and both signals are processed through (4.6) and (4.7), and $H_f$ is computed from (4.8). The results are presented in Table 4.1.

**Table 4.1:** Comparison between the exact $H_t$ and the frequency inertia index $H_f$.

| **Exact value ($H_t$)** | $\max_{a,b}\lvert\mathcal{WT}_{p(t)}(a,b)\rvert$ | $\max_{a,b}\lvert\mathcal{WT}_{\omega(t)}(a,b)\rvert$ | **Estimated $H_f$** | $\frac{H_t}{H_f}$ |
|---|---|---|---|---|
| **0.1** | 3.17 | 1.9574e-03 | 1.6195e+03 | 6.1747e-05 |
| **1** | 3.17 | 1.9574e-04 | 1.6195e+04 | 6.1747e-05 |
| **5** | 3.17 | 3.9149e-05 | 8.0973e+04 | 6.1749e-05 |
| **10** | 3.17 | 1.9574e-05 | 1.6195e+05 | 6.1747e-05 |
| **100** | 3.17 | 1.9574e-06 | 1.6195e+06 | 6.1747e-05 |

Three observations follow from Table 4.1:

- $H_t$ and $H_f$ maintain a constant proportional relationship. A change in $H_t$ by a given factor produces an identical factor change in $H_f$.
- The ratio $H_t/H_f$ is constant at $6.1747 \times 10^{-5}$. The analytical derivation below proves that this value equals $2(\Delta t)^2/\pi$, where $\Delta t$ is the transient period identified by the CWT.
- The value of $H_f$ is independent of the step change magnitude, which is consistent with the physical nature of the inertia constant.

The analytical derivation of the ratio $H_t/H_f$ follows from observing that the integral over the transient period in the numerator of (4.4) computes the area under $\Delta\bar{P}(t)$ over a window of width $\Delta t$. This operation is equivalent to convolving $\Delta\bar{P}(t)$ with a rectangular pulse of width $\Delta t$, as defined in (3.8).

$$y(t) = \int_{t_1}^{t_1+\Delta t} \overline{\Delta p}\, dt \equiv \overline{\Delta p}(t) * rect_{\Delta t}(t) \tag{4.9}$$

where $*$ denotes the convolution operation. This equivalence holds when the rectangular pulse aligns with the transient at $t_1$.

The proposed method identifies the maximum frequency component at the transient instant through the CWT. This requires the frequency-domain representations of the rectangular pulse and the Gaussian envelope of the Gabor wavelet separately, whose spectra are then combined through the convolution theorem. The Fourier transform of the scaled and shifted rectangular pulse follows directly from (3.9) with $t_0 = t_1$. The Gaussian envelope $e^{-t^2/2}$ in the Gabor wavelet (3.11) acts as a damping factor during the CWT computation. In the frequency domain, this Gaussian damping function, denoted $Damp_{WT}(t)$, transforms to:

$$\mathcal{F}\big(Damp_{WT}(t)\big) = \sqrt{2\pi} * \sqrt{\frac{2}{\pi}}\, e^{-\frac{(2\pi f-\,\omega_0)^2}{2}} \tag{4.10}$$

The damping term is scaled by $\Delta t$ to align with the rectangular pulse width. Application of the time-scaling property in (3.5) produces

$$\mathcal{F}\left(Damp_{WT}\left(\frac{t}{\Delta t}\right)\right) = 2\Delta t\ e^{-\frac{(2\pi\Delta t\, f-\omega_0)^2}{2}} \tag{4.11}$$

The frequency spectrum of the rectangular pulse modulated by the wavelet damping is the product of (3.9) and (4.11), in accordance with the convolution theorem in (3.4):

$$\mathcal{F}\left(Damp_{WT}\left(\frac{t}{\Delta t}\right) * rect_{\Delta t}(t-t_1)\right) = \\ 2\Delta t\ e^{-\frac{(2\pi\Delta t\, f-\omega_0)^2}{2}}\ \frac{\sin(\pi f\Delta t)}{\pi f} e^{-j2\pi f t_1} = \frac{2\Delta t}{\pi f}\sin(\pi f\Delta t)\, e^{-\frac{(2\pi f\Delta t-\omega_0)^2}{2}}\ e^{-j2\pi f t_1} \tag{4.12}$$

The maximum contribution from this expression is $2\Delta t/(\pi f)$, which occurs at $f = 1/(2\Delta t)$ where the sine term equals unity. The maximum wavelet coefficient of the rectangular pulse is therefore

$$\max_{a,b} |\mathcal{W}\mathrm{T}_{\mathrm{rect}(t)}(a,b)| = \frac{4(\Delta t)^2}{\pi} \tag{4.13}$$

The time-domain inertia in (4.4) is now expressed entirely in terms of wavelet coefficients. The numerator acquires the factor from (4.13) to account for the integral action, and the denominator retains the factor of 2:

$$H_t = \frac{\int_{t_1}^{t_1+\Delta t} \overline{\Delta p}\, dt}{2\overline{\Delta\omega_r}} = \frac{\max\limits_{a,b}\left|\mathcal{W}\mathrm{T}_{p(\mathrm{t})}(a,b)\right| \times \frac{4(\Delta \mathrm{t})^2}{\pi}}{2 \times \max\limits_{a,b}\left|\mathcal{W}\mathrm{T}_{\omega(\mathrm{t})}(a,b)\right|} = H_f \times \frac{2(\Delta \mathrm{t})^2}{\pi} \tag{4.14}$$

Equation (4.14) establishes the complete mathematical bridge between the frequency inertia index and the time-domain inertia constant. The transient period $\Delta t$ is determined directly from the CWT, and the scalar factor $2(\Delta t)^2/\pi$ accounts for the integral action and the factor 0.5 that were omitted in the definition of $H_f$. This result confirms the constant ratio $H_t/H_f = 6.1747 \times 10^{-5}$ observed in Table 4.1 for the identified transient period.

### 4.1.5 Proposed Inertia Estimation Algorithm

The mathematical framework established in the preceding subsections is now assembled into a practical estimation algorithm. The frequency inertia index $H_f$ defined in (4.8) and its mapping to the time-domain inertia $H_t$ through (4.14) form the analytical core of the method. The mapping is necessary because $H_f$ is defined without the integral and the factor 0.5 present in (4.4) and therefore does not directly equal the physical inertia constant $H_t$. This subsection presents the step-by-step procedure for inertia estimation in both standalone single-machine systems and interconnected multi-area power systems.

#### 4.1.5.1 Standalone Single-Machine Network

The estimation procedure for a single machine, whether a synchronous generator or a converter-interfaced generator, is summarised in Figure 4.3 and proceeds as follows:

- **Step 1 (Wavelet construction):** The Gabor wavelet in (3.11) is constructed at multiple scales. Each scale corresponds to a specific frequency, which enables the CWT to resolve transient content across a range of frequencies.
- **Step 2 (Signal acquisition):** The per-unit active power $\bar{p}(t)$ and angular frequency $\bar{\omega}(t)$ are measured at the machine bus.
- **Step 3 (Wavelet analysis):** The CWT is applied separately to $\bar{p}(t)$ and $\bar{\omega}(t)$ through (4.6) and (4.7). At each scale a and time shift b, the wavelet is correlated with the measured signal, and the resulting coefficients capture both the time localisation and frequency content of transient events.

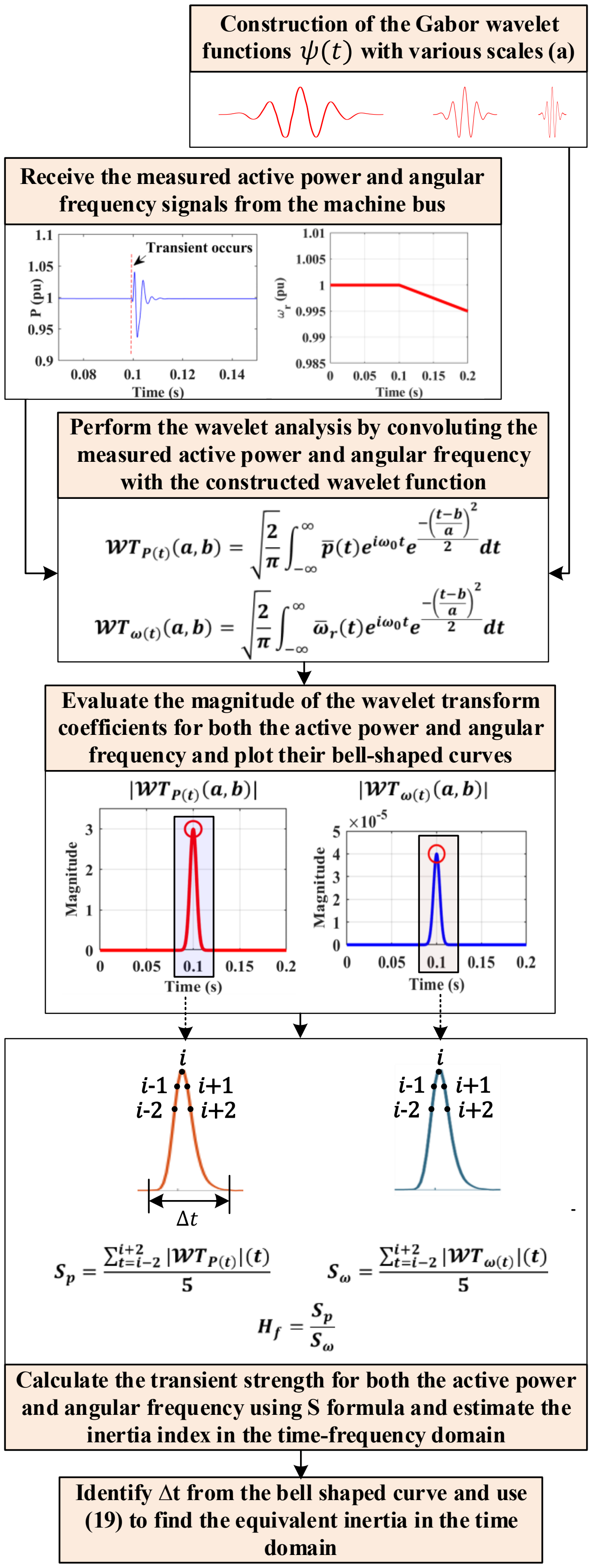


**Figure 4.3:** Transient detection and strength measurement by wavelet coefficient analysis, where the transient affects both active power and frequency signals.

- **Step 4 (Transient detection and strength evaluation):** The coefficient magnitudes are examined across all scales and translations. The dominant scale $a$ is identified as the scale at which the global maximum occurs. At this scale, the coefficient magnitude profile as a function of translation b forms a bell-shaped curve centred at the transient instant, as illustrated in Figure 4.3. To improve robustness against measurement noise, the transient strength is computed not from the single peak value alone but from an average over a neighbourhood of the peak. Specifically, the strength coefficient S for a signal $x(t)$ is defined as

$$S = \frac{\sum_{t=i-2}^{t=i+2} |W\, T_{f(t)}|(t)}{5} \tag{4.15}$$

where $i$ is the index of the peak coefficient. This averaging mitigates the influence of isolated outliers and provides a more robust measure of transient intensity.

- **Step 5 (Frequency inertia index computation):** The strength coefficient in (4.15) is evaluated for both the active power signal ($S_p$) and the angular frequency signal ($S_\omega$). The frequency inertia index is then obtained as $H_f = S_p/S_\omega$.
- **Step 6 (Time-domain mapping):** The transient duration $\Delta t$ is identified from the temporal width of the bell-shaped curve in the time–frequency coefficient profile. The time-domain inertia constant is recovered through (4.14) as $H_t = H_f \times 2(\Delta t)^2/\pi$.

#### 4.1.5.2 Interconnected Multi-Area Networks

Different areas have different inertia constants due to uneven renewable displacement, so each area should be estimated independently to reveal the spatial inertia distribution. The method requires no network model or topology knowledge; each PMU uses only its own two local signals, so mesh or multi-terminal complexity does not affect the algorithm. Therefore, a notable advantage of the proposed method is that it requires only two measurement signals per area, namely, active power and angular frequency. This property makes the method scalable to large interconnected networks with minimal instrumentation overhead. In contrast, derivative-based methods require accurate RoCoF computation. Figure 4.4 illustrates the general architecture for a multi-area power system. A phasor measurement unit (PMU) placed at the generator bus of each area collects the active power and angular frequency data. The CWT is then applied to both signals from each area through (4.6) and (4.7), and the transient strengths $S_p^k$ and $S_\omega^k$ are evaluated for each area $k$. The equivalent inertia constant for the area $k$ is obtained as

$$H_{eq}^k = \frac{S_p^k}{S_\omega^k} \times \frac{2(\Delta t^k)^2}{\pi} \tag{4.16}$$

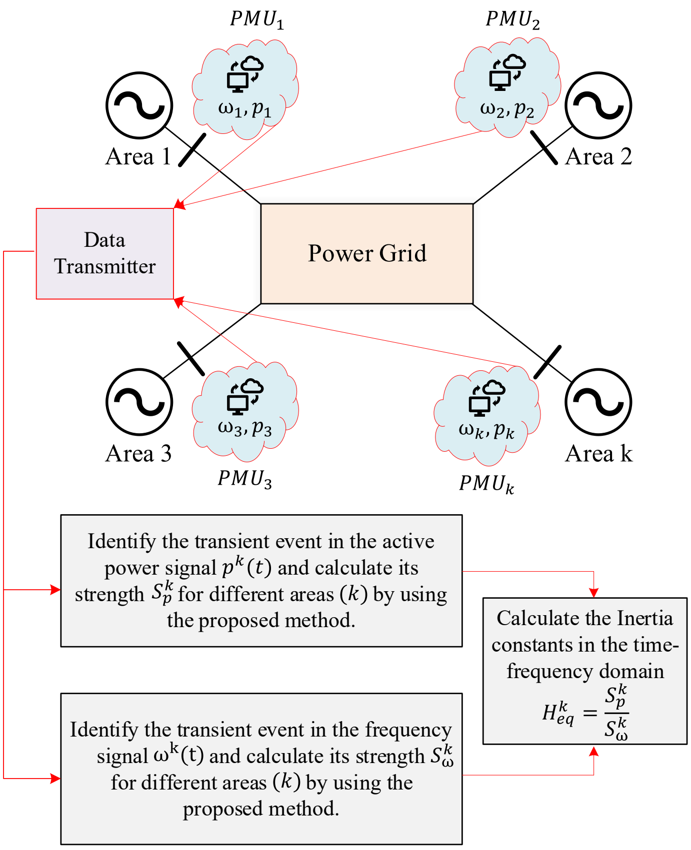


**Figure 4.4:** Proposed inertia estimation method for a multi-area power system.

where $k$ denotes the area number and $\Delta t^k$ is the transient duration of the area $k$. The transient in active power and angular frequency is identified from the peak of the CWT coefficient magnitude, where the bell-shaped curve localises the disturbance in time. Figure 4.5 presents an example network, a modified version of the IEEE 9-bus system, which comprises three areas: Area 1 with synchronous generator G1 at bus 1, Area 2 with synchronous generator G2 at bus 2, and Area 3 with a converter-interfaced generator. This system will be used to validate the proposed inertia estimation method. Fast-acting control loops that respond within the 20 ms estimation window modify $\Delta\bar{P}(t)$ before analysis is complete, and cause the estimated transient strength to reflect a mixture of inertial and control responses rather than pure inertia. Moreover, CWT bandpass filtering reduces high-frequency noise, but the disturbance must be large enough so the wavelet peak is above the noise floor. Otherwise, noise can distort the peak and reduce estimation accuracy.

## 4.2 Control Hardware-in-the-Loop Validation

The estimation algorithm developed in Section 4.1 is validated through control hardware-in-the-loop (CHiL) experiments on the modified IEEE 9-bus system depicted in Figure 4.5. The

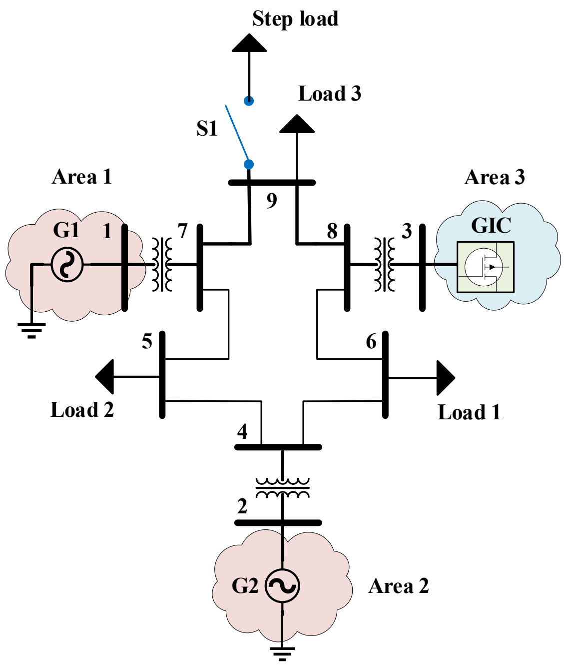


**Figure 4.5:** IEEE modified 9-bus system.

system parameters are listed in Table 4.2. As described in the preceding section, the standard IEEE 9-bus system comprises three interconnected areas with three synchronous generators; however, the generator at Area 3 has been replaced with a converter-interfaced generator (CIG), as shown in Figure 4.5. This configuration enables a comprehensive assessment of the proposed method with both traditional synchronous generators and non-synchronous converter-interfaced sources. The system-level components, namely, transformers, generators, transmission lines, loads, and buses, are implemented within the PLECS platform, which executes on a real-time platform comprising four ARM Cortex-A53 cores at 1.5 GHz. The proposed estimation algorithm is executed on a 150 MHz DSP (TMS320F28379D). The simulation provides active power output of the generators connected at buses 1, 2, and 3, and the corresponding angular frequency at those generator terminals.

**Table 4.2:** System parameters for the IEEE 9-bus test system.

| Parameter | Definition | Value |
|---|---|---|
| $P_n^{G1}, P_n^{G2}, P_n^{GIC}$ | Nominal power for G1, G2 and CIG | 200 MVA each |
| $\omega_n$ | Nominal grid angular frequency | 2π ×50 rad/s |
| $V_n$ | Nominal grid voltage | 230 kV |
| $P_1, Q_1$ | Active and reactive power for load 1 | 140 MW, 30 MVAR |
| $P_2, Q_2$ | Active and reactive power for load 2 | 135 MW, 50 MVAR |
| $P_3, Q_3$ | Active and reactive power for load 3 | 100 MW, 35 MVAR |
| $H_{G1}, H_{G2}, H_{CIG}$ | Inertia constant for G1, G2 and CIG | 3.7 s each |
| $D_{G1}, D_{G2}, D_{CIG}$ | Damping coefficients for G1, G2, G1G | 0.05, 0.05, 20 pu |

These signals are transmitted through analogy output channels to the DSP, which analyses the transient content and identifies the inertia of each area following the procedure in Section 4.1.5. The experimental setup is shown in Figure 4.6. The proposed method is validated under two cases, namely uniform inertia distribution and non-uniform inertia distribution. The CHiL implementation demonstrates that the proposed method operates in real time using measured signals, thereby validating its practical implementation beyond offline simulation; the wavelet transform is implemented directly through discrete convolution with the Gabor kernel across selected scales.

### 4.2.1 Uniform Inertia Distribution

This case study assumes that the three areas have identical inertia constant with a value of 3.7 s. To assess the inertia response, a purely active 40 MW load step is applied to bus 9 at t = 0.1 s by closing the switch S1 in Figure 4.5. Compared with the smallest pre-existing load of 100 MW (Table 4.2), this 40 MW step represents a moderate disturbance and highlights the method’s effectiveness under realistic conditions such as step loading during black-start restoration. The selected disturbance magnitude represents approximately 10–40% of individual load levels in the test system, which ensures a sufficient signal-to-noise ratio for accurate frequency estimation; smaller disturbances may be masked by measurement noise. However, as measurement noise is reduced, smaller disturbance magnitudes can also be used while still maintaining accurate estimation.

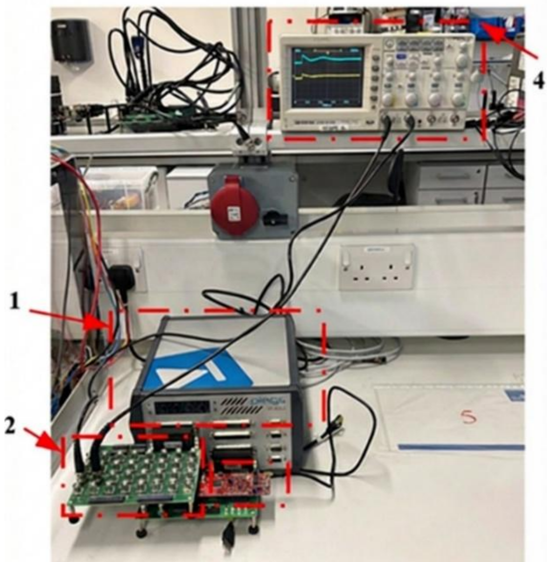


**Figure 4.6:** Control hardware-in-the-loop validation setup: (1) PLECS RT simulator, (2) input/output interface, (3) DSP (TMS320F28379D), and (4) oscilloscope.

Figure 4.7(a) shows the angular frequency measured at buses 1, 2, and 3. The angular frequency decreases following the load increase, and the rate of decline reflects the inertia of each area. Figure 4.7(b) depicts the corresponding active power measurements. These signals are then processed through the wavelet-based estimation procedure of Section 4.1.5. Figure 4.7(c) and Figure 4.7(d) present the fine-scale wavelet coefficients for the angular frequency and active power, respectively. The prominent spike in coefficient magnitude at approximately t = 0.1 s confirms the transient event. The CWT for active power and angular frequency uses the same time shift parameter, so both identify the same disturbance instant. This ensures the peaks occur at the same time.

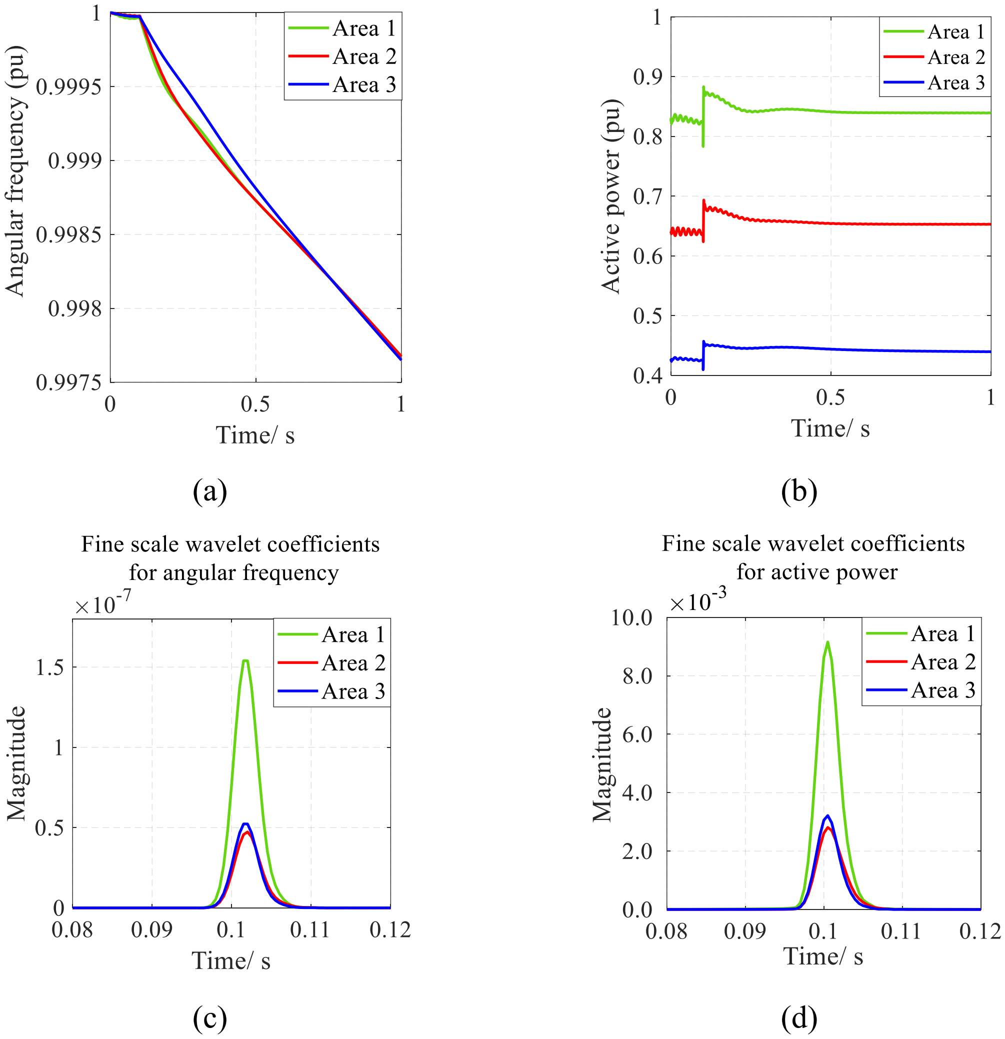


**Figure 4.7:** Wavelet analysis for uniform inertia: (a) angular frequency responses from buses 1, 2, and 3; (b) active power responses; (c) fine-scale wavelet coefficients for angular frequency; (d) fine-scale wavelet coefficients for active power.

The transient strength is determined by averaging five points around the peak, as prescribed by (4.15). Table 4.3 presents the transient strengths for active power ($S_p^1, S_p^2, S_p^3$) and angular frequency ($S_\omega^1, S_\omega^2, S_\omega^3$), together with the estimated inertia obtained through (4.16) with $\Delta t = 0.01$ s. The actual inertia values and relative errors are also reported.

**Table 4.3:** Transient strength and estimated inertia for uniform inertia distribution.

| Transient strength | | Estimated inertia | Actual inertia ($\boldsymbol{H_t^i}$) | Relative error (%) |
|---|---|---|---|---|
| $\boldsymbol{S_p^1}$ | 9.1E-03 | 3.761 | 3.7 | 1.64% |
| $\boldsymbol{S_\omega^1}$ | 1.54E-07 | | | |
| $\boldsymbol{S_p^2}$ | 2.89E-03 | 3.889 | 3.7 | 5.11% |
| $\boldsymbol{S_\omega^2}$ | 4.73E-08 | | | |
| $\boldsymbol{S_p^3}$ | 3.1E-03 | 3.773 | 3.7 | 1.97% |
| $\boldsymbol{S_\omega^3}$ | 5.23E-08 | | | |

The errors are small across all three areas. Area 2 exhibits the largest relative error of 5.11%, which is attributable to the greater electrical distance between the disturbance location (bus 9) and the generator bus of Area 2. This larger distance increases network impedance, which weakens and spreads the transient signal during propagation. As a result, the CWT captures a reduced and broadened peak, and this leads to lower estimation accuracy.

### 4.2.2 Non-Uniform Inertia Distribution with Measurement Noise

This case study assigns different inertia values: 10 s for G1 and 3.7 s for both G2 and the CIG. The objective is to verify whether the proposed method can distinguish these differences. Furthermore, the PMU measurements are corrupted with Gaussian white noise at a signal-to-noise ratio of 60 dB, a level commonly observed in synchrophasor measurements at transmission levels [94]. The same purely active 40 MW load disturbance is applied at bus 9 at t = 0.1 s.

Figure 4.8(a) shows the angular frequency data from each area bus. Because Area 1 has the highest inertia, its frequency declines at a slower rate. Figure 4.8(b) illustrates the active power sharing among the three generators following the disturbance. The irregular fluctuations visible in both plots reflect the additive Gaussian noise on the measurements. The wavelet analysis is applied as prescribed in Section 4.1.5. Figure 4.8(c) and Figure 4.8(d) present the fine-scale wavelet coefficients for angular frequency and active power,

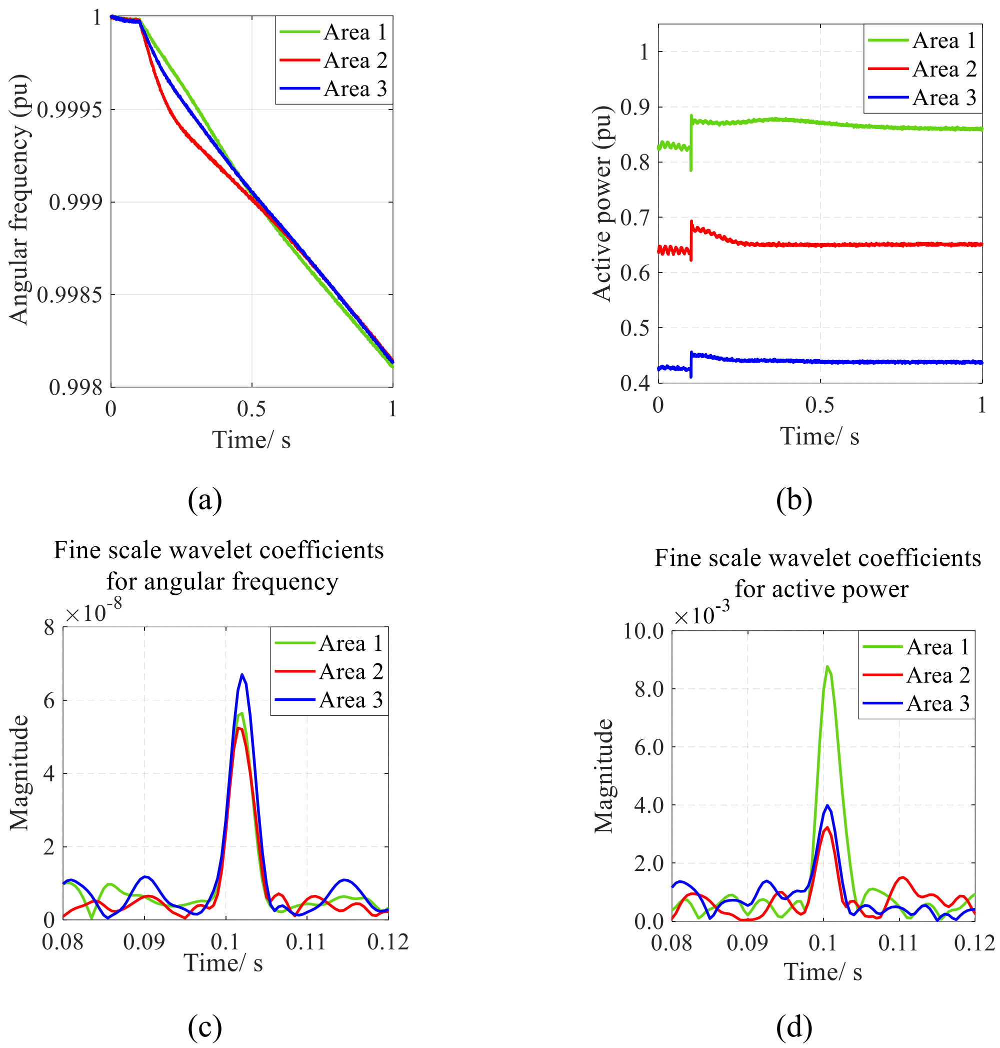


**Figure 4.8:** Wavelet analysis for non-uniform inertia with noise: (a) angular frequency responses; (b) active power responses; (c) fine-scale wavelet coefficients for angular frequency; (d) fine-scale wavelet coefficients for active power.

respectively. The transient event at t = 0.1 s is clearly identified. The elevated inertia of Area 1 is reflected in the reduced strength of $S_{\omega}^{1}$ compared with its counterpart in Section 4.2.1, since higher inertia constrains the rate of speed deviation, thereby producing a smaller wavelet coefficient peak. Table 4.4 presents the estimated time-domain inertia across the three areas in the non-uniform inertia distribution case, obtained through (4.16) with $\Delta t =$ 0.01 s. The relative errors of 1.88%, 6.05%, and 2.18% for Areas 1, 2, and 3, respectively, demonstrate that the proposed method maintains accuracy despite the presence of measurement noise.

**Table 4.4:** Transient strength and estimated inertia for non-uniform inertia distribution with noise.

| Transient strength | | Estimated inertia | Actual inertia ($H_t^i$) | Relative error (%) |
|---|---|---|---|---|
| $S_p^1$ | 8.77E-03 | 10.188 | 10 | 1.88% |
| $S_\omega^1$ | 5.48E-08 | | | |
| $S_p^2$ | 3.23E-03 | 3.924 | 3.7 | 6.05% |
| $S_\omega^2$ | 5.24E-08 | | | |
| $S_p^3$ | 3.98E-03 | 3.781 | 3.7 | 2.18% |
| $S_\omega^3$ | 6.70E-08 | | | |

### 4.2.3 Comparative Assessment

The proposed method is compared with two established techniques in MATLAB, and replicates the same conditions as Section 4.2.2. The signals are sampled at 100 kHz, which yields 2000 samples within the 20 ms estimation window used for wavelet analysis. A longer observation window of 0.2 s is used to capture the full transient response. The fast response estimation method (FREM), based on (4.3), and the enhanced stability estimation method (ESEM) [19] are selected as benchmarks. The comparison evaluates accuracy, numerical stability, and noise resilience for the estimation of Area 1 inertia. Figure 4.9 shows the estimated inertia trajectories for Area 1 under the three methods. The FREM responds within 40 ms but exhibits significant oscillations around the actual value, which indicates low numerical stability and poor noise rejection, and results in an unbounded relative error. The ESEM achieves higher numerical stability with a bounded relative error of $\pm$10%, but its 200 ms response time is considerably slower, and its noise rejection remains limited. The proposed method achieves a response time of approximately 20 ms with high numerical stability and noise rejection. Its bounded relative error of $\pm$1.88% is the lowest among the three methods. Table 4.5 summarises the comparison results across the three methods.

**Table 4.5:** Comparative analysis of inertia estimation methods.

| Method | Estimation Speed | Numerical Stability | Noise Resistance | Steady-State error |
|---|---|---|---|---|
| **FREM** | Fast (40 ms) | Low | Low | Not bounded |
| **ESEM** | Slow (200 ms) | High | Medium | ±10% |
| **Proposed method** | Very fast (20 ms) | High | High | ±1.88% |

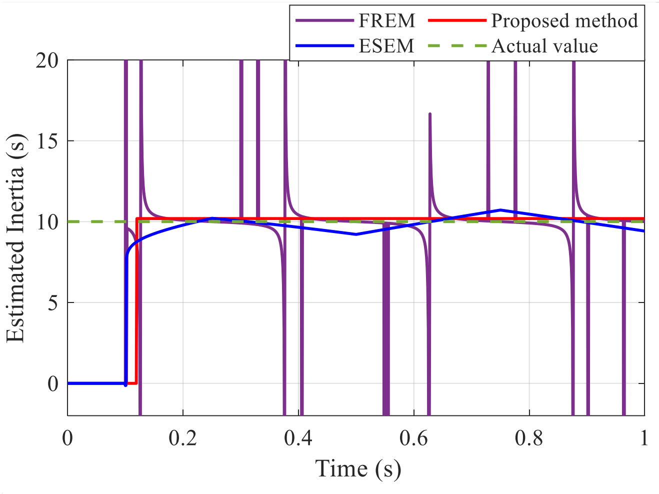


**Figure 4.9:** Comparative analysis: FREM, ESEM, and the proposed wavelet-based method for inertia estimation of Area 1 under noisy conditions.

It should be noted that the plotted trajectories in Figure 4.9 represent the dynamic behaviour of the estimators rather than changes in the physical inertia, which remains constant; variations in the curves reflect estimator convergence speed and noise sensitivity. Moreover, unlike recursive least squares methods, which require an explicit model structure and parameter tuning, the proposed method is model-free and avoids these requirements.

### 4.2.4 Sensitivity to the Damping Coefficient

As noted in Section 4.1.2, the damping term is excluded from the estimation formulation. This assumption relies on the rapid ≈ 20 ms operational timeframe of the proposed method, during which the system response is predominantly governed by inertia. This subsection quantifies the condition under which this assumption remains valid.

The swing equation including damping is $2H\frac{d\overline{\Delta\omega_r}}{dt} + D\overline{\Delta\omega_r} = \overline{\Delta \mathrm{P}}$, whose solution for $\overline{\Delta\omega_r}(0) = 0$ gives $\overline{\Delta\omega_r}$ as a function of time.

$$\overline{\Delta\omega_r}(t) = \frac{\overline{\Delta \mathrm{P}}}{D}\left(1 - e^{-\frac{D}{2H}t}\right) \tag{4.17}$$

where $D$ is the damping coefficient. For small values of $t$ during the initial transient phase, the exponential function admits the first-order Taylor approximation $e^{-x} \approx 1 - x$, which yields

$$\overline{\Delta\omega_r}(t) \approx \frac{\overline{\Delta \mathrm{P}}}{2H}t \tag{4.18}$$

This confirms that the early response is dominated by inertia with negligible damping contribution, which matches the undamped solution ($\overline{\Delta\omega_r}(t) = \frac{\overline{\Delta \mathrm{P}}}{2H}t$). To quantify the negligibility condition at t = 0.02 s (operational timeframe of the proposed method), the approximation gives

$$e^{-\frac{D}{2H}\times 0.02} \approx 1 - \frac{D}{2H} \times 0.02 \tag{4.19}$$

For the damping term to remain negligible, the second term must be much less than unity ($\frac{0.01D}{H} \ll 1$), which simplifies to

$$D \ll 100H \tag{4.20}$$

This constraint is well satisfied by the typical damping coefficients of conventional synchronous machines and CIG designs [95], as listed in Table 4.2. The proposed method, therefore, remains reliable under practical operating conditions. Moreover, for GFM, the virtual inertia and damping are programmable, and the constraint D ≪ 100H can be guaranteed by design parameter selection. However, for GFM configurations with high virtual damping, the ratio D/100H increases noticeably and introduces estimation error. Separately, for optimal performance in complex interconnected systems, measurements should be acquired as close as possible to the area of interest, whether near synchronous machines or converter-interfaced sources. In the IEEE 9-bus system, this principle is satisfied by the placement of measurements at buses 1, 2, and 3.

## 4.3 Proposed Integral-Based Inertia Estimation Method

The wavelet-based method of Sections 4.1.1–4.1.5 achieves high accuracy and noise immunity but requires computing wavelet coefficients across multiple scales, which may be unnecessarily complex when a simpler approach suffices. In practice, real-time CWT requires appropriate scale selection and the use of scales that are less affected by noise. This section introduces a second, complementary method that operates entirely in the time domain by replacing both the wavelet transform and derivative calculations with integration.

As discussed in Section 4.1.1, estimation of inertia from the conventional swing equation (4.3) requires the time derivative of angular frequency, which amplifies measurement noise and creates division-by-zero instabilities under steady-state conditions. The wavelet-based method resolves these issues in the time-frequency domain. The integral-based method presented here provides an alternative solution in the time domain and avoids derivatives entirely through reformulation by integration. In addition to this derivative-free property, the method offers a further capability: a continuous running estimate of the full post-disturbance inertia response. This estimate characterises both the inertia constant and the inertia dynamics simultaneously, rather than producing a single-point estimate for each event.

### 4.3.1 Derivation of the Integral Formulation from the Swing Equation

The integral formulation is derived from the per-unit swing equation (4.3) through exact algebraic and calculus operations. The only approximation is the neglect of damping under the constraint $D \ll 100H$ established in (4.20). Starting from (4.3),

$$2H \frac{d\overline{\Delta\omega_r}}{dt} = \overline{\Delta \mathrm{P}} \tag{4.21}$$

Both sides are divided by $[\overline{\Delta\omega_r}(t)]^2$, valid for all t where $\overline{\Delta\omega_r}(t) \neq 0$ (conditions established in Section 4.3.3:

$$\frac{2H}{[\overline{\Delta\omega_r}]^2} \frac{d(\overline{\Delta\omega_r})}{dt} = \frac{\overline{\Delta \mathrm{P}}}{[\overline{\Delta\omega_r}]^2} \tag{4.22}$$

The left-hand side can be recognised as an exact total derivative by applying the chain rule to $-1/\overline{\Delta\omega_r}(t)$:

$$\frac{d}{dt}\left(\frac{-1}{\overline{\Delta\omega_r}}\right) = -(-1)[\overline{\Delta\omega_r}]^{-2} \frac{d\overline{\Delta\omega_r}}{dt} = \frac{1}{[\overline{\Delta\omega_r}]^2} \frac{d\overline{\Delta\omega_r}}{dt} \tag{4.23}$$

Substituting (4.23) into (4.22) and absorbing the time-invariant 2H inside the derivative gives

$$\frac{d}{dt}\left(\frac{-2H}{\overline{\Delta\omega_r}}\right) = \frac{\overline{\Delta \mathrm{P}}}{[\overline{\Delta\omega_r}]^2} \tag{4.24}$$

Equation (4.24) is an exact reformulation of (4.21) in which the left-hand side is a total derivative and the right-hand side depends only on the measurable signals $\overline{\Delta \mathrm{P}}$ and $\overline{\Delta\omega_r}$. Integrating both sides from $t_1$ to t, where $t_1 > t_0$ is chosen such that $\overline{\Delta\omega_r}(t_1) \neq 0$ (Section 4.3.3), and applying the fundamental theorem of calculus yields

$$\frac{-2H}{\overline{\Delta\omega_r}(t)} + \frac{2H}{\overline{\Delta\omega_r}(t_1)} = \int_{t_1}^{t} \frac{\overline{\Delta \mathrm{P}}(\tau)}{[\overline{\Delta\omega_r}(\tau)]^2}\, d\tau \tag{4.25}$$

Factoring $2H$ produces the closed-form identity:

$$2H\left[\frac{1}{\overline{\Delta\omega_r}(t_1)} - \frac{1}{\overline{\Delta\omega_r}(t)}\right] = \int_{t_1}^{t} \frac{\overline{\Delta \mathrm{P}}(\tau)}{[\overline{\Delta\omega_r}(\tau)]^2}\, d\tau \tag{4.26}$$

Equation (4.26) is the central result, an exact, derivative-free identity relating H to a definite integral of two measured signals. Moreover, it eliminates both noise amplification and division-by-zero instabilities.

### 4.3.2 Cumulative Integral Estimator

The identity in (4.26) motivates the definition of a cumulative estimator. The instantaneous integrand is

$$\mathcal{I}(t) \triangleq \frac{\overline{\Delta \mathrm{P}}(t)}{[\overline{\Delta\omega_r}(t)]^2} \tag{4.27}$$

and the cumulative integral estimator is

$$H_c(t) \triangleq \int_{t_1}^{t} \mathcal{I}(\tau)\, d\tau = \int_{t_1}^{t} \frac{\overline{\Delta \mathrm{P}}(\tau)}{[\overline{\Delta\omega_r}(\tau)]^2}\, d\tau \tag{4.28}$$

For multi-area networks, the estimator is applied independently at each generator bus in area k:

$$H_c^k(t) = \int_{t_1}^{t} \frac{\overline{\Delta \mathrm{P}}_{(k)}(\tau)}{\left[\overline{\Delta\omega_r}_{(k)}(\tau)\right]^2}\, d\tau \tag{4.29}$$

where $\overline{\Delta \mathrm{P}}_{(k)}$ and $\overline{\Delta\omega_r}_{(k)}$ are the per-unit deviations measured at the generator bus of area k. From (4.26), the exact relationship between $H_c(t)$ and the true inertia constant is

$$H_c(t) = 2H\left[\frac{1}{\overline{\Delta\omega_r}(t_1)} - \frac{1}{\overline{\Delta\omega_r}(t)}\right] \tag{4.30}$$

Equation (4.30) shows that $H_c(t)$ is exactly proportional to H at every instant $t > t_1$, with the proportionality factor computed entirely from measured frequency data. Importantly, the method evaluates $H_c(t)$ directly from (4.29) rather than extracting H from (4.30), since the latter would require dividing by a proportionality factor that approaches zero when $\overline{\Delta\omega_r}(t) \approx \overline{\Delta\omega_r}(t_1)$. This design avoids any division that could introduce numerical instability. The formulation in (4.29) and (4.30) possesses four key properties:

- **Property 1 (Derivative-free computation):** The integrand requires only $\overline{\Delta \mathrm{P}}(\tau)$ and $[\overline{\Delta\omega_r}(\tau)]^2$; no time derivative of any measured signal appears, which eliminates noise amplification and division-by-zero instabilities.

- **Property 2 (Inherent noise attenuation):** Integration provides natural low-pass filtering and attenuates high-frequency noise through accumulation.
- **Property 3 (Continuous running estimate):** Evaluating (4.29) at successive time steps yields a continuous trajectory $H_c(t)$ that retains the full dynamic information of the inertial response. From (4.30), this transient profile is governed by the evolving proportionality factor, which stabilises as $\overline{\Delta\omega_r}(t)$ reaches its post-disturbance steady state $\overline{\Delta\omega_r}_{ss}$. At convergence, $H_c$ approaches $2H\left[\frac{1}{\overline{\Delta\omega_r}(t_1)} - \frac{1}{\overline{\Delta\omega_r}(t)}\right]$. The transient profile, therefore, reveals the dynamic inertia response of each generator (how rapidly and strongly it contributes to frequency stabilisation) while the converged value is proportional to H. This dual characterisation of transient dynamics and steady-state inertia constitutes a significant advancement over methods that estimate only the inertia constant.
- **Property 4 (Proportional tracking for relative inertia identification):** For generators measured under the same disturbance, the ratios of converged $H_c$ values correspond to the ratios of actual inertia constants and enable quantitative identification of inertially strong and weak areas.

Based on these properties, this study recommends relying on $H_c(t)$ directly rather than attempting to extract H. Since $H_c(t)$ is exactly proportional to H; it preserves relative inertia information across areas. In many practical applications, the primary requirement is not the absolute inertia constant but rather the relative inertia distribution to identify weak areas. The quantity $H_c(t)$ fulfils this requirement without numerical issues, provided the conditions in Section 4.3.3 are satisfied.

### 4.3.3 Numerical Stability Conditions

The only potential instability source is the integrand $\mathcal{J}(t)$, which becomes unbounded as $\overline{\Delta\omega_r}(t) \rightarrow 0$. Two conditions ensure $H_c(t)$ remains well-defined:

- **Condition 1 (Non-zero initial deviation) :** The lower limit $t_1$ satisfies $t_1 > t_0$ and $|\overline{\Delta\omega_r}(t_1)| \geq \epsilon$, where $t_0$ is the disturbance onset time and $\epsilon > 0$ is a small threshold. Integration begins only after the frequency has deviated sufficiently from nominal.

- **Condition 2 (Bounded integrand):** Throughout $[t_1, t]$, the deviation satisfies $|\overline{\Delta\omega_r}(\tau)| \geq \epsilon > 0,\ \forall\, \tau \in [t_1, t]$, where $\varepsilon$ is the same threshold defined in Condition 1, to ensure $\mathcal{J}(t)$ remains bounded.

Both conditions are physically justified. Following a sudden load change at $t_0$, the frequency deviation initially increases monotonically from zero and remains bounded away from zero during the inertial response, before primary frequency control arrests the frequency decline and establishes a new steady-state offset. In practice, $t_1$ is the first instant after $t_0$ at which $|\overline{\Delta\omega_r}|$ exceeds $\varepsilon$, and $t$ is selected within the interval for which the deviation remains non-zero.

### 4.3.4 Implementation Procedure

The implementation is illustrated in Figure 4.10 and proceeds as follows for each area k.

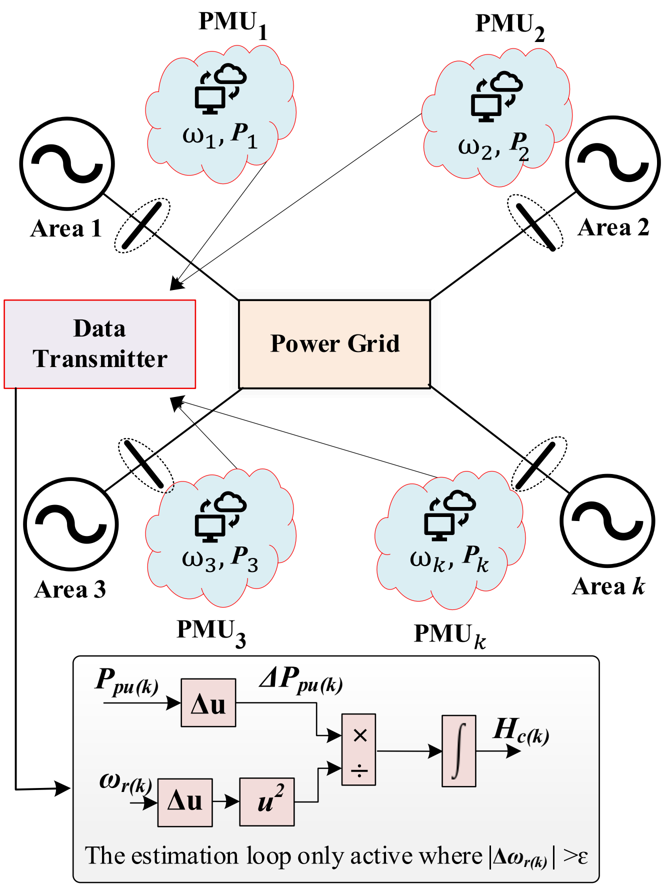


**Figure 4.10:** Framework of the proposed integral-based inertia estimation algorithm.

- **Step 1:** Measure the per-unit active power $\bar{p}_{(k)}(t)$ and angular frequency $\bar{\omega}_{r(k)}(t)$ at the generator bus of area k, using PMUs. These are the same signals required by the wavelet-based method in Section 4.1.5.
- **Step 2:** Compute the deviations $\overline{\Delta \mathrm{P}}_{(k)}(t)$ and $\overline{\Delta\omega_{r}}_{(k)}(t)$. If $|\overline{\Delta\omega_{r}}_{(k)}(t)| \geq \epsilon$, evaluate $\mathcal{J}(t)$ using (4.27); otherwise, set $\mathcal{J}(t) = 0$ to enforce the guard condition of Section 4.3.3.
- **Step 3:** At each subsequent time step $t > t_1$, compute the cumulative integral $H_{c(k)}(t) = \int_{t_1}^{t} \mathcal{J}_{(k)}(\tau)\, d\tau$ using (4.29). The resulting profiles are compared across areas to identify relative inertia strengths through Property 4.

## 4.4 Validation of the Integral-Based Inertia Estimation Method

The integral-based method is validated on the same IEEE 9-bus hybrid system used for the wavelet-based method, as shown in Figure 4.5. The network comprises two synchronous generators (G1 and G2) at buses 1 and 2 and one converter-interfaced generator (CIG) at bus 3. The nominal ratings ($P_n^{G1} = P_n^{G2} = P_n^{CIG} = 200$ MW, $V_n = 230$ kV, $\omega_n = 2\pi \times 50$ rad/s) remain as specified in Table 4.2. Several parameters are modified from Table 4.2 to evaluate capabilities specific to the integral-based method. The load profile is set to 90 MW / 30 MVAR (Load 1), 125 MW / 50 MVAR (Load 2), and 100 MW / 35 MVAR (Load 3). The inertia constant of G2 is set to $H_{G2} = 10$ s, while G1 and the CIG retain $H_{G1} = H_{CIG} = 3.7$ s, which establishes a non-uniform inertia distribution. The damping coefficients are $D_{G1} = D_{G2} = 0.05$ pu and $D_{CIG} = 10$ pu. These modifications, particularly the non-uniform inertia distribution and the elevated CIG damping, serve two purposes: to evaluate the method's ability to distinguish generators with different inertia constants, and to reveal qualitative differences between physical and virtual inertia responses. All simulations are conducted in MATLAB/Simulink. A 9.5% step load increase (30 MW) is applied at three distinct bus locations across three case studies: bus 5, bus 9, and bus 6 (Figure 4.5). The use of three disturbance locations enables evaluation of how the spatial relationship between disturbance and generator influences the estimated dynamic inertia response.

### 4.4.1 Case Study 1: Disturbance at Bus 5

The step load is applied at bus 5 at t = 0.1 s. Figure 4.11 presents $H_c(t)$ computed from (4.29) for all three generators. The response comprises two distinct regions: a transient region immediately after the disturbance that reflects inertia dynamics, and a steady-state region where the estimates converge to values proportional to the true inertia constants.

At steady state, the estimates for G1 and the CIG converge to approximately equal values consistent with $H_{G1} = H_{CIG} = 3.7$s. A small deviation appears in the CIG estimate due to its high damping coefficient ($D_{CIG} = 10$ pu versus $D_{G1} = D_{G2} = 0.05$ pu); this effect is examined in Section 4.4.4. The G2 estimate is approximately 2.7 times that of G1 and the CIG, which matches the true ratio, $H_{G2}/H_{G1} = 10/3.7 \approx 2.7$. This agreement confirms that the method accurately preserves relative inertia through its proportional tracking property.

The transient response reveals that, because the disturbance at bus 5 is electrically closest to G2 and G2 possesses the largest inertia constant ($H_{G2} = 10$ s), it exhibits the most pronounced inertia contribution and plays the dominant role in frequency stabilisation. The small steady-state offset in the CIG estimate is due to its higher damping, which introduces bias compared to synchronous generators. This effect is analysed in Subsection 4.4.4. The estimator provides useful inertia information within the first tens of milliseconds. Full convergence provides accurate relative inertia between areas and occurs once the frequency stabilises, typically within 0.5 to 1 s. Convergence is identified when the rate of change of the estimate ($H_c(t)$) becomes small.

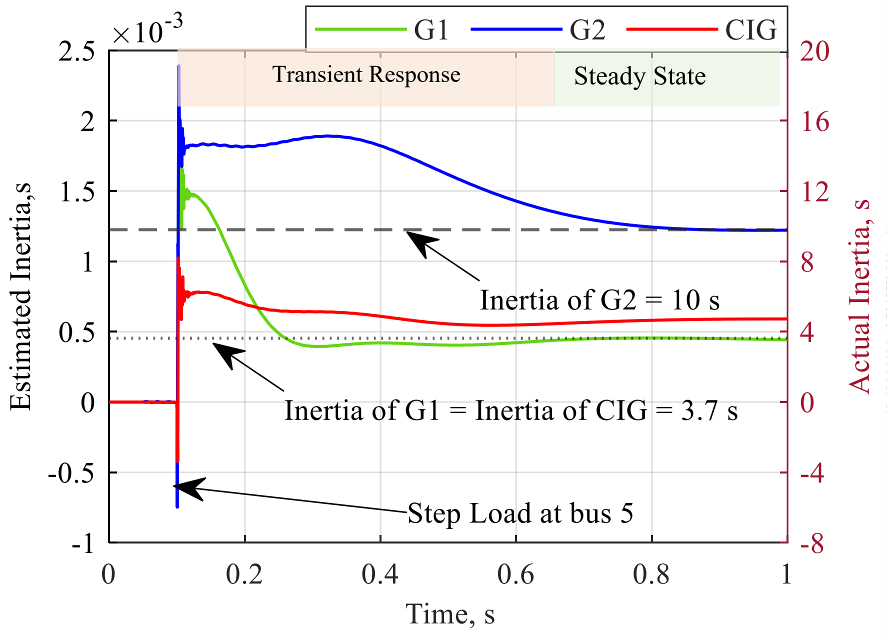


**Figure 4.11:** Estimated inertia response $H_c(t)$ for G1, G2, and the CIG following a 9.5% step load disturbance at bus 5.

### 4.4.2 Case Study 2: Disturbance at Bus 9

Figure 4.12 presents the estimated inertia responses when the step load is applied at bus 9 at $t = 0.1$ s. The steady-state results remain consistent with Case Study 1, G1 and the CIG converge to the same proportional level corresponding to $H_{G1} = H_{CIG} = 3.7$ s, and G2 maintains a value approximately 2.7 times higher. This consistency demonstrates robustness to disturbance location, as the inferred inertia ratios remain invariant.

The transient response, however, reveals a shift in dynamic contribution. Bus 9 is electrically closer to G1 and the CIG, which leads to higher transient peaks in their responses compared to Case Study 1. Although G2 still contributes significantly due to its larger inertia constant, G1 responds more strongly and rapidly because of its proximity. The CIG, despite identical nominal inertia to G1, exhibits a slower response that reflects the controlled nature of its virtual inertia.

### 4.4.3 Case Study 3: Disturbance at Bus 6

Figure 4.13 presents the results when the step load is applied at bus 6 at t = 0.1 s. G2 again exhibits the most substantial overall inertia response due to its large inertia constant and relative proximity to the disturbance. Both G1 and the CIG contribute meaningfully;

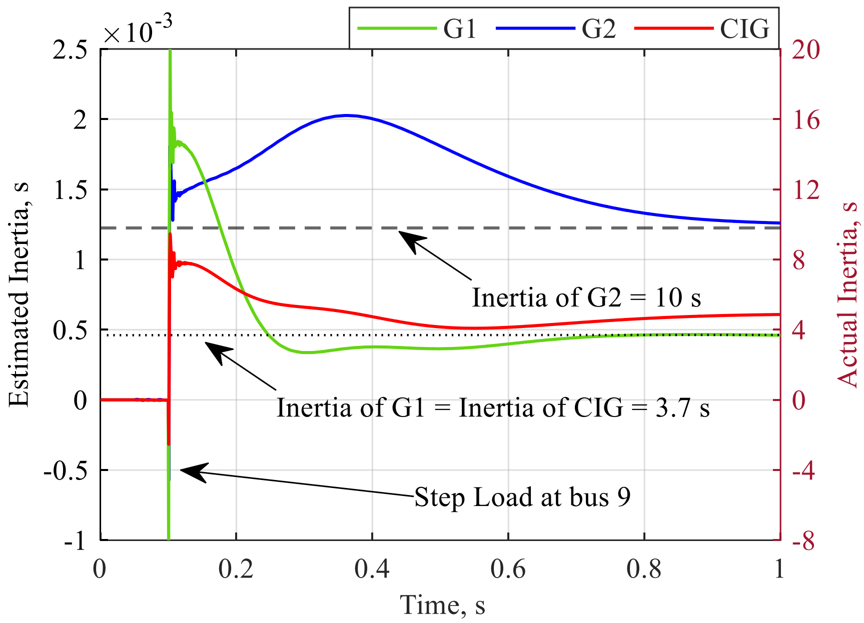


**Figure 4.12:** Estimated inertia response $H_c(t)$ for G1, G2, and the CIG following a 9.5% step load disturbance at bus 9.

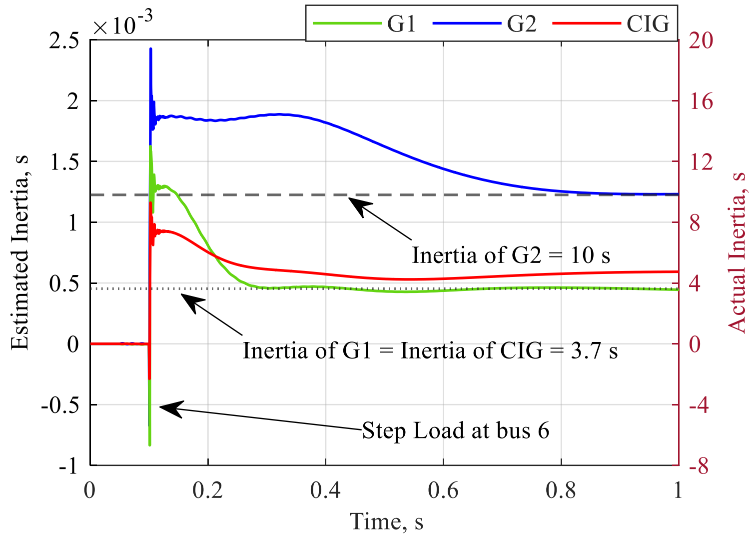


**Figure 4.13:** Estimated inertia response $H_c(t)$ for G1, G2, and the CIG following a 9.5% step load disturbance at bus 6.

however, G1 responds more rapidly than the CIG even when it is not closest to the disturbance. This difference reflects the inherently faster physical inertia response of synchronous machines, whose stored kinetic energy is instantaneously coupled to the grid.

Across all three case studies, the CIG achieves a steady-state inertia contribution comparable in magnitude to G1 but shows less dominant transient behaviour. The consistency of steady-state estimates across all disturbance locations further confirms the robustness of the proposed method.

### 4.4.4 Sensitivity to the Damping Coefficient

A notable feature across Sections 4.4.1–4.4.3 is the discrepancy between the estimated inertia of the CIG and that of G1, despite their identical actual inertia constants ($H_{G1} = H_{CIG} = 3.7$ s). This discrepancy, consistently more pronounced for the CIG (see Figure 4.12 and Figure 4.13), is primarily attributed to its high virtual damping coefficient ($D_{CIG} = 10$ pu versus $D_{G1} = D_{G2} = 0.05$ pu). Recall that the integral formulation neglects damping effects. For the CIG, the damping to inertia ratio is significantly higher than that of synchronous generators. This elevated damping introduces a bias in the integral formulation and reduces estimation accuracy.

Figure 4.14 illustrates this effect by progressively increasing the CIG damping coefficient from 10 pu to 40 pu. As the damping increases through 10, 20, 30, and 40 pu, the steady-state $H_c$ value deviates further from the true value of $H_{CIG}$ = 3.7 s. The estimation error grows monotonically with damping, which confirms that the proposed method is most accurate for systems with relatively low damping, consistent with the theoretical requirement of (4.20). Potential mitigation strategies for this error include incorporating a known or identified damping coefficient D into the formulation by considering the complete swing equation with damping in (4.21) or restricting the method to generators satisfying a small D/100H ratio.

## 4.5 Summary

This chapter has presented two novel methods for estimating the inertia constant H in power systems with converter integration. Both methods are motivated by the critical need for accurate inertia awareness during power system restoration. The wavelet-based method employs the continuous wavelet transform with the complex Gabor wavelet to analyse transient events in the time-frequency domain. Validation through control hardware-in-the-loop experiments on the IEEE 9-bus hybrid system yielded estimation errors of 1.64%, 5.11%, and 1.97% for areas 1, 2, and 3 under uniform inertia distribution, and errors of

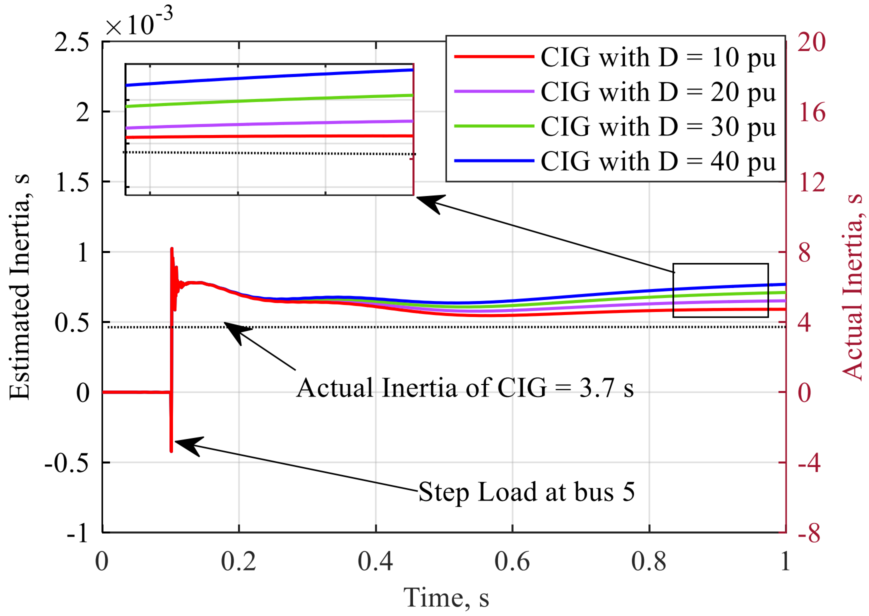


**Figure 4.14:** Impact of increasing the CIG damping coefficient from 10 pu to 40 pu on the estimated inertia response $H_c(t)$.

1.88%, 6.05%, and 2.18% under non-uniform inertia distribution with 60 dB Gaussian white noise. The integral-based method reformulates the swing equation into a derivative-free, time-domain integral formula through a systematic mathematical procedure. Validation on the same IEEE 9-bus system demonstrated consistent proportional estimation across three disturbance locations (Case Studies 1–3). The running estimate further revealed how the virtual inertia response of converter-interfaced generators differs qualitatively from the physical inertia response of synchronous machines, since the CIG exhibited less dominant transient behaviour despite identical steady-state inertia constants.

Both methods share the fundamental advantages of being derivative-free and of requiring only active power and angular frequency measurements from PMUs. Their respective strengths are complementary:

- The wavelet-based method is suited for rapid, absolute-value inertia assessment during real-time monitoring.
- The integral-based method provides dual characterisation of inertia. It captures not only the proportional inertia estimate $H_c$ but also the transient dynamics of the inertia response. Through analysis of these dynamics, the method identifies dominant generators during transient events and determines how electrical proximity to the disturbance influences their response. Although each generator uses local measurements, the response differs because power redistribution is governed by network impedance, so generators closer to the disturbance experience larger $\overline{\Delta \mathrm{P}}$ and faster $\overline{\Delta\omega_r}$ which leads to distinct $H_c(t)$ profiles. It therefore highlights areas with stronger or weaker inertia support and supports a more informed understanding of the grid dynamic response. The continuous $H_c(t)$ trajectory shows which generators respond first and most strongly and allows direct comparison of relative inertia contributions across areas.

# Chapter 5 Novel Frequency Estimation Methods for Power Systems with High Renewable Integration

Accurate and rapid frequency estimation is fundamental to power system monitoring, protection, and control. Existing frequency estimation methods surveyed in Chapter 3 suffer from three persistent limitations: sensitivity to harmonic distortion, inherent delays that compromise responsiveness to rapid frequency changes, and computational complexity that hinders real-time embedded implementation. No existing method simultaneously achieves harmonic immunity, near-instantaneous response, and low computational complexity. This chapter addresses these limitations through two complementary novel methods. Both of which exploit the oscillatory behaviour of the dq-frame components under frequency deviation conditions:

- The integer-order estimation method employs integer-order derivatives of the normalised dq components combined with a cross-product formulation to achieve algebraically exact, near-instantaneous frequency extraction.
- The fractional-order estimation method extends this principle through fractional-order calculus, where the amplitude of the fractional derivative encodes the frequency deviation and a tunable fractional order provides intrinsic control over noise sensitivity.

Both methods fundamentally avoid the integral control action of PLL-based approaches and thereby eliminate the dynamic delays that limit conventional methods.

## 5.1 The dq-Frame Oscillation Principle

Both frequency estimation methods presented in this chapter share a common foundational principle that exploits the oscillatory behaviour of the Park–Clarke transformation under frequency deviation conditions. This section establishes the mathematical framework underpinning both methods.

### 5.1.1 Three-Phase Voltage Representation

Consider a balanced three-phase voltage system with instantaneous phase voltages:

$$V_{abc}(t) = \begin{bmatrix} V_a(t) \\ V_b(t) \\ V_c(t) \end{bmatrix} = V_m \begin{bmatrix} \sin(\omega_{\text{act}} t) \\ \sin(\omega_{\text{act}} t - 2\pi/3) \\ \sin(\omega_{\text{act}} t + 2\pi/3) \end{bmatrix} \tag{5.1}$$

where $V_m$ is the peak phase voltage amplitude and $\omega_{\text{act}}$ is the actual angular frequency. Under nominal steady-state conditions, $\omega_{\text{act}} = 2\pi \times 50$ rad/s. Following a disturbance, $\omega_{\text{act}}$ deviates from its nominal value and evolves as a function of time.

### 5.1.2 Park–Clarke Transformation and Frequency Encoding

The Park–Clarke transformation maps $V_{abc}(t)$ into orthogonal components in a rotating dq:

$$\mathbf{T}_{dq}(\theta) = \frac{2}{3} \begin{bmatrix} \cos(\theta) & \cos\left(\theta - \frac{2\pi}{3}\right) & \cos\left(\theta + \frac{2\pi}{3}\right) \\ \sin(\theta) & \sin\left(\theta - \frac{2\pi}{3}\right) & \sin\left(\theta + \frac{2\pi}{3}\right) \end{bmatrix} \tag{5.2}$$

where $\theta = \int \omega_{\text{ref}}\, dt$ is the angular position of the rotating reference frame synchronised to a predefined reference frequency $\omega_{\text{ref}}$. The dq components $V_{dq}(t) \in \mathbb{R}^2$ are:

$$V_{dq}(t) = \begin{bmatrix} V_d(t) \\ V_q(t) \end{bmatrix} = \mathbf{T}_{dq}(\theta)\, V_{abc}(t) \tag{5.3}$$

When $\omega_{\text{ref}} = \omega_{\text{act}}$, the reference frame rotates in exact synchronism with the three-phase voltages, and the dq components reduce to static dc values. When a frequency mismatch exists, an angular frequency deviation arises:

$$\Delta\omega = \omega_{\text{act}} - \omega_{\text{ref}} \tag{5.4}$$

Substituting into (5.3) and applying standard trigonometric identities, the dq components become oscillatory functions of $\Delta\omega$:

$$\begin{bmatrix} V_d(t) \\ V_q(t) \end{bmatrix} = V_m \begin{bmatrix} \sin(\Delta\omega\, t) \\ \cos(\Delta\omega\, t) \end{bmatrix} \tag{5.5}$$

Equation (5.5) reveals the fundamental encoding principle that underpins both estimation methods. The unknown frequency deviation $\Delta\omega$ is encoded into the oscillation frequency of the $dq$ components. The $d$-axis and $q$-axis components oscillate as orthogonal sinusoids at frequency $\Delta\omega$ and maintain a 90° phase relationship at all times. Some conventional frequency estimation computes $\theta$ through the arctangent of $\alpha\beta$ components and differentiates it, which introduces phase unwrapping issues, and numerical sensitivity near zero crossings. In contrast, the proposed method directly extracts frequency from dq-frame oscillations using algebraic operations, thereby avoiding angle computation and eliminating phase discontinuities.

Figure 5.1 illustrates this principle under three conditions. In Scenario 1, $\omega_{\text{ref}} = \omega_{\text{act}}$, which yields $\Delta\omega = 0$ and static dq values. In Scenario 2, a 10 Hz mismatch produces dq oscillations at 10 Hz. In Scenario 3, a 20 Hz mismatch produces oscillations at 20 Hz. This confirms that the dq oscillation frequency is directly and exclusively determined by the frequency deviation. If $\Delta\omega$ can be accurately estimated from the oscillatory dq signals, the actual system frequency is immediately recovered as:

$$\omega_{\text{act}} = \Delta\omega + \omega_{\text{ref}} \tag{5.6}$$

### 5.1.3 Amplitude Normalisation

The components in (5.5) are directly proportional to $V_m$. Variations in $V_m$ due to voltage sags, swells, or flicker would therefore compromise estimation accuracy. To eliminate this dependency, a normalisation step is applied where $d(t) = V_d(t)$ and $q(t) = V_q(t)$ denote the unnormalised dq components from (5.5). The normalised components are defined as:

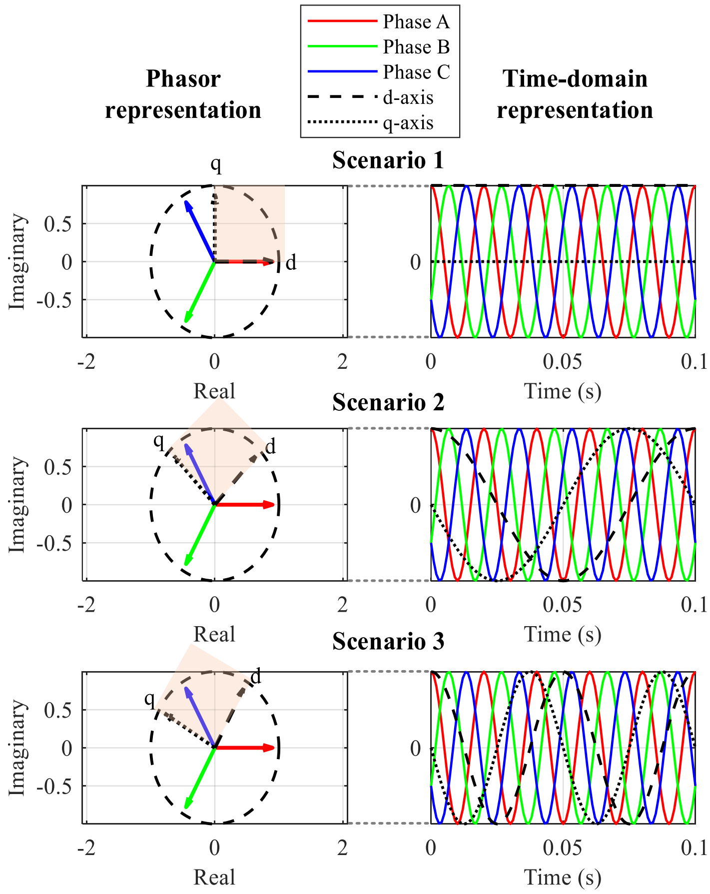


**Figure 5.1:** Phasor and time-domain representations of abc and dq coordinates under frequency mismatches: (1) no mismatch, (2) 10 Hz, and (3) 20 Hz.

$$\begin{bmatrix} \hat{d}(t) \\ \hat{q}(t) \end{bmatrix} = \frac{V_m}{\sqrt{d^2(t) + q^2(t)}} \begin{bmatrix} \sin(\Delta\omega\, t) \\ \cos(\Delta\omega\, t) \end{bmatrix} = \begin{bmatrix} \sin(\Delta\omega\, t) \\ \cos(\Delta\omega\, t) \end{bmatrix} \tag{5.7}$$

where $\sqrt{d^2(t) + q^2(t)} = V_m$ under balanced conditions. The normalised components $\hat{d}(t)$ and $\hat{q}(t)$ are unit-amplitude sinusoids depending exclusively on $\Delta\omega$. This ensures insensitivity to voltage magnitude changes, which is critical during black-start restoration, where voltages vary significantly as network sections are sequentially energised.

### 5.1.4 Reference Frequency Selection

The choice of $\omega_{\mathrm{ref}}$ determines the dq oscillation frequency and influences several aspects of estimator performance.

- Setting $\omega_{\mathrm{ref}}$ equal to the nominal system frequency results in dq oscillations only when a deviation is present. The resulting small $\Delta\omega$ under normal conditions limits the estimator update rate and reduces the signal-to-noise ratio, as a low-frequency oscillation embedded in broadband noise is inherently more difficult to extract.
- Setting $\omega_{\mathrm{ref}}$ significantly below the nominal frequency increases $\Delta\omega$ and produces higher-frequency dq oscillations. This offers a higher estimator update rate enabling more frequent frequency estimates. However, $\Delta\omega$ cannot be increased arbitrarily, as it is constrained by the sampling frequency $f_s$ to preserve numerical accuracy and prevent aliasing. Specific guidelines for optimal selection of $\omega_{\mathrm{ref}}$ are discussed in the respective method sections.

The derivation of (5.5) assumes $\omega_{\mathrm{act}} > \omega_{\mathrm{ref}}$ and therefore $\Delta\omega > 0$. In practice, the estimator must correctly interpret the sign of the deviation and allow $\Delta\omega$ to take either sign in (5.4), so that $\omega_{\mathrm{act}} = \omega_{\mathrm{ref}} + \Delta\omega$ holds for both $\omega_{\mathrm{act}} > \omega_{\mathrm{ref}}$ and $\omega_{\mathrm{act}} < \omega_{\mathrm{ref}}$. Cases in which $\Delta\omega = 0$ must also be excluded, since the $dq$ signals become constant, and the derivative-based estimator loses its oscillatory input.

## 5.2 Integer-Order Derivative-Based Frequency Estimation Method

Having established in Section 5.1 that the normalised dq components encode the unknown frequency deviation $\Delta\omega$ into their oscillation frequency, this section develops the integer-order derivative-based estimation method. The method exploits the deterministic relationship between the first-order derivative of a sinusoidal signal and its frequency to achieve exact, near-instantaneous frequency extraction with a latency of one sampling period, through a cross-product formulation.

### 5.2.1 Cross-Product Frequency Extraction

The normalised dq components established in (5.7) are recalled:

$$\hat{d}(t) = \sin(\Delta\omega\, t)$$
$$\hat{q}(t) = \cos(\Delta\omega\, t) \tag{5.8}$$

where $\Delta\omega$ is assumed constant over the observation interval. The generalisation to time-varying $\Delta\omega$ (t) is discussed at the end of this subsection.

The first-order time derivatives of these components are obtained by direct differentiation:

$$\dot{\hat{d}}(t) = \frac{d}{dt}[\sin(\Delta\omega\, t)] = \Delta\omega\cos(\Delta\omega\, t)$$
$$\dot{\hat{q}}(t) = \frac{d}{dt}[\cos(\Delta\omega\, t)] = -\Delta\omega\sin(\Delta\omega\, t) \tag{5.9}$$

where $\dot{\hat{d}}(t)$ and $\dot{\hat{q}}(t)$ denote the first-order time derivatives of $\hat{d}(t)$ and $\hat{q}(t)$, respectively. It is immediately apparent from (5.9) that the unknown frequency deviation $\Delta\omega$ appears as a multiplicative factor in the amplitude of each derivative. This observation forms the basis of the extraction strategy. If $\Delta\omega$ can be isolated from these expressions, the actual system frequency is recovered through (5.6). However, extracting $\Delta\omega$ from either expression in (5.9) individually requires knowledge of the instantaneous value of the trigonometric function at the same time instant, which reintroduces a division operation that becomes numerically unstable at the zero crossings of the respective trigonometric function. Specifically, recovering $\Delta\omega$ from the d-axis alone in (5.9) requires dividing by cos $(\Delta\omega t)$, which vanishes at $t = (2k+1)\pi/2\Delta\omega$ for integer k. To circumvent this difficulty, a cross-product formulation is developed that eliminates the trigonometric dependence entirely.

The cross-product is constructed by combining the normalised dq components and their derivatives:

$$C(t) = \hat{q}(t)\,\dot{\hat{d}}(t) - \hat{d}(t)\,\dot{\hat{q}}(t) \tag{5.10}$$

Substituting (5.8) and (5.9) into (5.10) yields:

$$\mathcal{C}(t) = \cos(\Delta\omega\, t) \cdot \Delta\omega \cos(\Delta\omega\, t) - \sin(\Delta\omega\, t) \cdot (-\Delta\omega \sin(\Delta\omega\, t)) \tag{5.11}$$

Expanding:

$$\mathcal{C}(t) = \Delta\omega \cos^2(\Delta\omega\, t) + \Delta\omega \sin^2(\Delta\omega\, t) \tag{5.12}$$

Applying the Pythagorean trigonometric identity $\sin^2(\theta) + \cos^2(\theta) = 1$:

$$\mathcal{C}(t) = \Delta\omega[\cos^2(\Delta\omega\, t) + \sin^2(\Delta\omega\, t)] = \Delta\omega \tag{5.13}$$

Equation (5.13) constitutes the central result of the integer-order method. The cross-product $\mathcal{C}(t)$ is identically equal to the frequency deviation $\Delta\omega$ at every time instant, independent of the instantaneous phase argument. This result generalises to time-varying frequency deviations: if $\Delta\omega(t)$ varies slowly relative to the sampling rate, $\mathcal{C}(t) = \Delta\omega(t)$ at each instant. This result holds exactly under the assumptions of balanced three-phase voltages and the absence of noise and harmonic distortion. The algebraic exactness of (5.13) implies that a single evaluation of the cross-product at any arbitrary time instant is theoretically sufficient to determine $\Delta\omega$ without averaging, filtering, or iterative convergence. The practical limitations imposed by measurement noise on this theoretically exact result are quantified later in this section.

Having obtained $\Delta\omega$ from (5.13), the actual angular frequency of the system is recovered by direct application of (5.6):

$$\widehat{\omega}_{\text{act}} = \mathcal{C}(t) + \omega_{\text{ref}} \tag{5.14}$$

and the corresponding frequency in hertz:

$$\hat{f}_{\text{act}} = \frac{\widehat{\omega}_{\text{act}}}{2\pi} = \frac{\mathcal{C}(t) + \omega_{\text{ref}}}{2\pi} \tag{5.15}$$

### 5.2.2 Discrete-Time Implementation

In practical implementation, the continuous-time derivatives in (5.9) must be approximated using discrete-time difference operations. Consider that the normalised dq components are sampled at discrete time instants $t_n = nT_s$, where $T_s = 1/f_s$ is the sampling period and $f_s$ is the sampling frequency. The sampled signals are denoted $\hat{d}[n] = \hat{d}(nT_s)$ and $\hat{q}[n] = \hat{q}(nT_s)$.

The first-order backward difference approximation to the continuous-time derivative is:

$$\dot{\hat{d}}[n] \approx \frac{\hat{d}[n] - \hat{d}[n-1]}{T_s}$$
$$\dot{\hat{q}}[n] \approx \frac{\hat{q}[n] - \hat{q}[n-1]}{T_s} \tag{5.16}$$

The discrete-time cross-product is then computed as:

$$\mathcal{C}[n] = \hat{q}[n]\,\dot{\hat{d}}[n] - \hat{d}[n]\,\dot{\hat{q}}[n] \tag{5.17}$$

and the estimated frequency at each sample is:

$$\widehat{\omega}_{\mathrm{act}}[n] = \mathcal{C}[n] + \omega_{\mathrm{ref}} \tag{5.18}$$

The backward difference approximation introduces a truncation error of order $\mathcal{O}(T_s)$, which diminishes as the sampling frequency increases. Higher-order finite difference approximations, such as the central difference:

$$\dot{\hat{d}}[n] \approx \frac{\hat{d}[n+1] - \hat{d}[n-1]}{2T_s} \tag{5.19}$$

reduce the truncation error to $\mathcal{O}(T_s^2)$ but introduce a one-sample look-ahead requirement that may not be acceptable in real-time applications where causal implementation is mandatory. For the implementation presented in this chapter, the backward difference approximation (5.16) is adopted due to its causal nature and minimal computational requirements.

The computational burden of the cross-product computation and frequency recovery at each sample instant is very low. The backward-difference derivative approximation requires two subtraction operations, followed by two divisions by $T_s$ to obtain the discrete-time derivatives $\dot{\hat{d}}[n]$ and $\dot{\hat{q}}[n]$. The cross-product computation in (5.17) then requires two multiplication operations, followed by one subtraction to evaluate their difference. Finally, one additional addition is required to add the known reference frequency $\omega_{\mathrm{ref}}$ and obtain $\widehat{\omega}_{\mathrm{act}}[n]$. In total, these stages require eight arithmetic operations per sample, which is significantly lower than that of conventional methods. These characteristics make the integer-order estimator attractive for applications requiring fast and lightweight frequency estimation, especially in restoration and black-start scenarios where robust operation and rapid execution are essential.

### 5.2.3 Noise Sensitivity Analysis

The algebraic exactness established in (5.13) holds under ideal conditions, where the normalised dq components are pure sinusoidal signals. In practice, however, the measured three-phase voltages are inevitably corrupted by noise originating from measurement transducers and power electronic switching. This noise propagates through the Park–Clarke transformation and the normalisation step into the dq components, yields signals of the form:

$$\hat{d}_{\text{noisy}}[n] = \hat{d}[n] + \eta_d[n]$$
$$\hat{q}_{\text{noisy}}[n] = \hat{q}[n] + \eta_q[n] \tag{5.20}$$

where $\eta_d[n]$ and $\eta_q[n]$ represent additive noise components on the d-axis and q-axis, respectively. The first-order backward difference of the noisy d-axis signal is:

$$\dot{\hat{d}}_{\text{noisy}}[n] = \frac{\hat{d}_{\text{noisy}}[n] - \hat{d}_{\text{noisy}}[n-1]}{T_s} = \dot{\hat{d}}[n] + \frac{\eta_d[n] - \eta_d[n-1]}{T_s} \tag{5.21}$$

The second term in (5.21) represents the differentiated noise. If the noise $\eta_d[n]$ is modelled as a wide-sense stationary random process with power spectral density $S_\eta(f)$, then the differentiation operation, which corresponds to multiplication by $j2\pi f$ in the frequency domain, amplifies the noise power spectral density by a factor of $(2\pi f)^2$. This high-frequency amplification is a well-known and fundamental property of differentiation.

To quantify the noise amplification, consider the signal-to-noise ratio (SNR) at the output of the differentiator. Let the input SNR be defined as:

$$\text{SNR}_{\text{in}} = \frac{\sigma_{\hat{d}}^2}{\sigma_\eta^2} \tag{5.22}$$

where $\sigma_{\hat{d}}^2$ denotes the variance of the signal component of $\hat{d}[n]$ and $\sigma_\eta^2$ denotes the variance of the additive measurement noise. The backward difference operation produces an output whose signal component has variance $\Delta\omega^2\, \sigma_{\hat{d}}^2$ (since differentiation scales a sinusoid of frequency $\Delta\omega$ by the factor $\Delta\omega$), while the noise component has variance $2\sigma_\eta^2/T_s^2$ (since the difference of two uncorrelated noise samples doubles the variance, and division by $T_s$ amplifies it by $1/T_s^2$). The output SNR is therefore:

$$\mathrm{SNR_{out}} = \frac{\Delta\omega^2 \sigma_{\hat{d}}^2}{2\sigma_\eta^2 / T_s^2} = \frac{\Delta\omega^2 T_s^2}{2} \cdot \mathrm{SNR_{in}} \tag{5.23}$$

where the factor of 2 in the denominator arises from the assumption that $\eta_d[n]$ and $\eta_d[n-1]$ are uncorrelated samples of the noise process. The ratio of output SNR to input SNR defines the preservation factor:

$$\mathcal{P} = \frac{\mathrm{SNR_{out}}}{\mathrm{SNR_{in}}} = \frac{\Delta\omega^2 T_s^2}{2} \tag{5.24}$$

Equation (5.24) reveals two important dependencies. First, the output SNR degrades as the sampling period $T_s$ decreases, because a shorter sampling interval reduces the signal change between consecutive samples while the noise magnitude remains unchanged, and causes the noise to dominate the finite difference. Second, the output SNR degrades as the frequency deviation $\Delta\omega$ decreases, because a smaller $\Delta\omega$ causes the normalised dq components to vary more slowly, and reduces the signal content in the derivative toward zero while the differentiation noise remains constant. In the limiting case $\Delta\omega \to 0$, the dq components become dc signals, their derivatives vanish, and the output consists of amplified noise.

This analysis quantitatively explains why the raw cross-product estimate exhibits significant noise-induced fluctuations in practical implementations. The noise amplification inherent in integer-order differentiation represents the principal limitation of the method as presented in this section. Two complementary strategies are developed in subsequent sections to address this limitation. The first strategy, presented in Section 5.3, introduces a Butterworth low-pass filtering stage to attenuate the high-frequency noise components amplified by the differentiation operation, at the cost of introducing a controlled amount of estimation delay. The second strategy, presented in Section 5.5, replaces the integer-order derivative with a fractional-order derivative, which provides intrinsic control over the degree of noise amplification through the fractional-order parameter $\alpha$.

## 5.3 Enhanced Integer-Order Method with Butterworth Low-Pass Filtering

Section 5.2.3 established that the integer-order differentiation operation amplifies high-frequency noise. This section develops a filtering enhancement that attenuates the noise-induced fluctuations while preserving the essential frequency information embedded in the cross-product signal.

### 5.3.1 Butterworth Filter Design and Implementation

The schematic of the complete enhanced estimator, shown in Figure 5.2, reveals that the Butterworth low-pass filter is applied to the discrete-time dq components before the backward difference and cross-product operations. This pre-differentiation placement is critical as it smooths the dq sequences before the backward difference is computed. Therefore, the high-frequency noise content identified in (5.21) is attenuated before it can be amplified by the factor $1/T_s$ inherent in the differentiation operation. The discrete-time signal processing chain operates as follows: The sampled three-phase voltage $V_{abc}[n]$ is transformed into the $dq$ reference frame using $\omega_{\mathrm{ref}}$, normalised by the voltage magnitude as in (5.7), filtered through a discrete-time Butterworth low-pass filter, differentiated through the backward difference method, and subsequently processed using the cross-product formulation to obtain the estimated actual frequency.

$$\hat{f}_{\mathrm{act}}[n] = \frac{\Delta\hat{\omega}[n] + \omega_{\mathrm{ref}}}{2\pi} \tag{5.25}$$

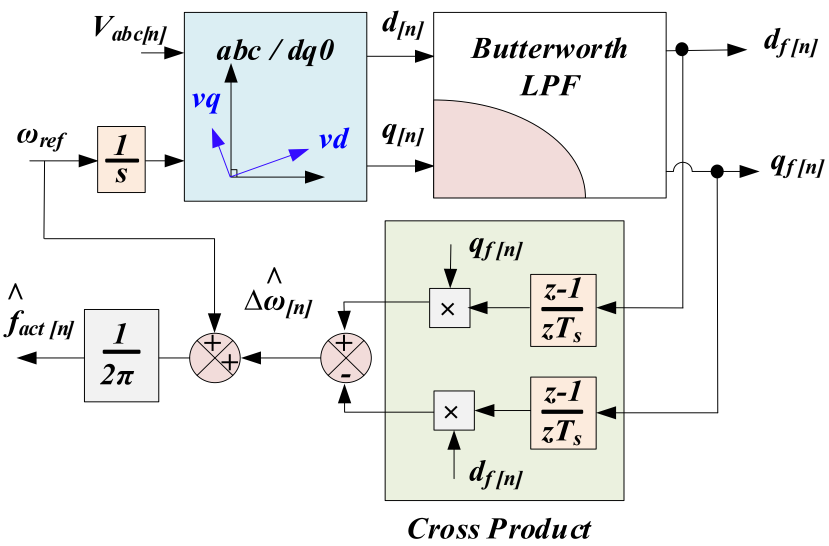


**Figure 5.2:** Schematic diagram of the proposed frequency estimation method for three-phase signals.

The discrete-time implementation of the first-order Butterworth low-pass filter is obtained by applying the bilinear (Tustin) transformation to the first-order continuous-time prototype. The resulting discrete-time transfer function is:

$$H(z) = \frac{b_0 + b_1\, z^{-1}}{1 + a_1\, z^{-1}} \tag{5.26}$$

where the filter coefficients are given by:

$$\begin{aligned} b_0 = b_1 &= \frac{\omega_c\, T_s}{2 + \omega_c\, T_s} \\ a_1 &= \frac{\omega_c\, T_s - 2}{2 + \omega_c\, T_s} \end{aligned} \tag{5.27}$$

and $\omega_c$ is the desired cutoff angular frequency. The corresponding difference equation, which is implemented directly in the discrete-time processing chain, is:

$$\begin{aligned} \hat{d}_f[n] &= b_0\, \hat{d}_{\text{noisy}}[n] + b_1\, \hat{d}_{\text{noisy}}[n-1] - a_1\, \hat{d}_f[n-1] \\ \hat{q}_f[n] &= b_0\, \hat{q}_{\text{noisy}}[n] + b_1\, \hat{q}_{\text{noisy}}[n-1] - a_1\, \hat{q}_f[n-1] \end{aligned} \tag{5.28}$$

where $\hat{d}_{\text{noisy}}[n]$ and $\hat{q}_{\text{noisy}}[n]$ are the noisy normalised dq components. Equation (5.28) shows that each filtered output sample requires only the current and previous input samples and the previous filtered output. The cutoff frequency $\omega_c$ must be chosen to separate the useful $dq$ oscillation at $\Delta\omega = \omega_{\text{act}} - \omega_{\text{ref}}$ from the measurement noise band. The useful frequency content in the $dq$ frame typically lies between 0 Hz and a few tens of hertz, which depends on the magnitude of the frequency deviation. The measurement noise, by contrast, usually occupies much higher frequencies. Accordingly, the cutoff frequency is set to $\omega_c = 2\pi \times 70$ rad/s, which preserves the useful $dq$-domain frequency-deviation information while providing strong attenuation of high-frequency noise. To quantify this attenuation, the discrete-time frequency response of $H(z)$ is evaluated on the unit circle at $z = e^{j\Omega}$, where $\Omega = \omega T_s$ is the digital frequency. For a noise frequency of $f_n = 10{,}000$ Hz and a sampling interval of $T_s = 1\ \mu$s, the magnitude response is:

$$|H(e^{j\,2\pi f_n T_s})| = \frac{|\ b_0 + b_1\, e^{-j\,2\pi f_n T_s}\ |}{|\ 1 + a_1\, e^{-j\,2\pi f_n T_s}\ |} \approx 0.007 \tag{5.29}$$

This represents approximately 99.3% attenuation of the noise amplitude at 10 kHz (equivalently, 99.995% attenuation of the noise power). Since the frequency response is monotonically decreasing, even greater attenuation is achieved at higher frequencies. The filter gain at the useful signal frequencies (below 70 Hz) remains close to unity.

### 5.3.2 Influence of Reference Frequency and Filter Order on Estimation Accuracy

The reference frequency $\omega_{\text{ref}}$ constitutes a design degree of freedom that directly influences the effectiveness of the Butterworth filter. Setting $\omega_{\text{ref}}$ to zero produces dq frame oscillations at the full source frequency ($\Delta\omega = 2\pi \times 50$ rad/s). In this case, the useful signal frequency is relatively high and approaches the noise band, which makes spectral separation more difficult and requires a higher cutoff frequency that admits more noise. Conversely, setting $\omega_{\text{ref}}$ slightly below the source frequency results in lower-frequency oscillations in the dq frame. For instance, if $\omega_{\text{ref}}$ corresponds to 49 Hz, and the actual frequency is 50 Hz, the dq components oscillate at only $\Delta\omega = 2\pi \times 1$ rad/s. Similarly, choosing $\omega_{\text{ref}}$ = 51 Hz yields $\Delta\omega$ = $-2\pi \times 1$ rad/s. In both cases, the estimator operates correctly, but the sign of $\Delta\omega$ must be preserved. This creates a large spectral gap between the 1 Hz useful signal and the kilohertz noise band, and allows the Butterworth filter to attenuate the noise very effectively without any distortion of the signal of interest.

Therefore, $\omega_{\text{ref}}$ is strategically chosen between 0 and near $\omega_{\text{act}}$ to optimise noise resistance. Higher values of $\omega_{\text{ref}}$ are preferred in noisy environments to maximise spectral separation, while lower values are acceptable in quieter environments where less filtering is needed and the full speed advantage of the unfiltered method can be exploited. Figure 5.3 presents a parametric study of the root mean square error (RMSE) between the actual frequency and the estimated frequency as a function of both the reference frequency $\omega_{\text{ref}}$ and the Butterworth filter order N. This surface plot reveals two trends that are essential for practical design.

Regarding the effect of reference frequency, as $\omega_{\text{ref}}$ increases, the RMSE decreases monotonically. This confirms the spectral separation argument, a higher $\omega_{\text{ref}}$ produces lower-frequency dq oscillations, which increases the distance between the useful signal and the noise band and allows the Butterworth filter to operate more effectively. Moreover, the RMSE increases when the Butterworth filter order exceeds one. This occurs because higher-

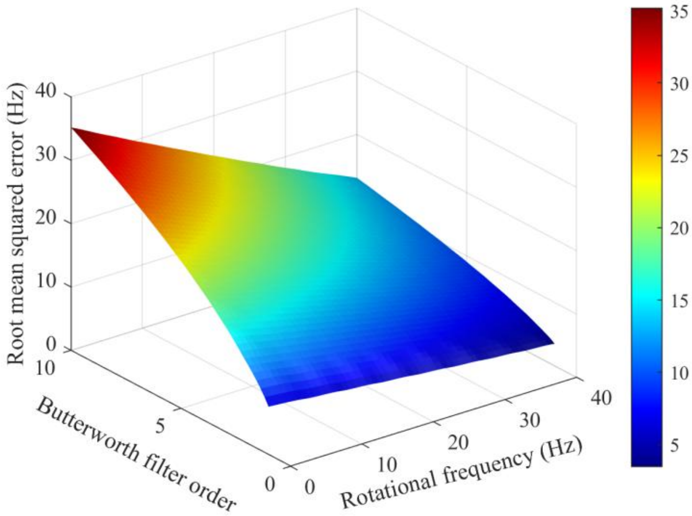


**Figure 5.3:** Impact of reference frequency of dq transformation and Butterworth filter order on frequency estimation accuracy (RMSE).

order discrete-time filters introduce extra phase shift and steeper phase variation near the passband edge. This increases group delay and introduces additional latency in the estimation. The cross-product frequency estimator relies on algebraic cancellation. The added delay degrades the accuracy of the instantaneous frequency estimate. This leads to an increase in the RMSE of $\widehat{\Delta\omega}[n]$ and outweighs the benefit of improved noise attenuation. Based on these findings, a first-order Butterworth filter with cutoff frequency $f_c = 70\ Hz$ is adopted for all subsequent implementations. The reference frequency $\omega_{ref}$ is selected close to the expected system frequency to maximise spectral separation between the useful dq oscillation and the measurement noise band.

## 5.4 Simulation Validation of the Integer-Order Method

This section validates the integer-order method through discrete-time simulations implemented in MATLAB/Simulink. The proposed method is compared against the conventional SRF-PLL under a comprehensive set of signal disturbances across two scenarios, namely, a noise-free environment with the filter deactivated and a noisy environment with the first-order Butterworth filter activated. SRF-PLL is implemented in MATLAB/Simulink with parameters optimised using the Response Optimizer toolbox. This includes tuning of loop filters to ensure fair comparison. The three-phase test signal $V_{abc}[n]$ subjects the estimator to all practically relevant disturbance types within a single simulation run. The disturbance schedule encompasses rapid frequency changes during 0.10–0.20 s, a ramp frequency change from 0.25 to 0.40 s, sinusoidal frequency oscillations between 0.45 and 0.55 s, step frequency changes during 0.60–0.70 s and 1.10–1.15 s, sinusoidal magnitude variation from 0.80 to 0.90 s, and phase shifts between 0.95 and 1.15 s.

### 5.4.1 Noise-Free Environment

In this scenario, the Butterworth filter is deactivated, and the estimator operates using only the backward difference and cross-product operations. Figure 5.4 presents the results. During rapid frequency changes between 0.10 and 0.20 s, the proposed method captures the variation

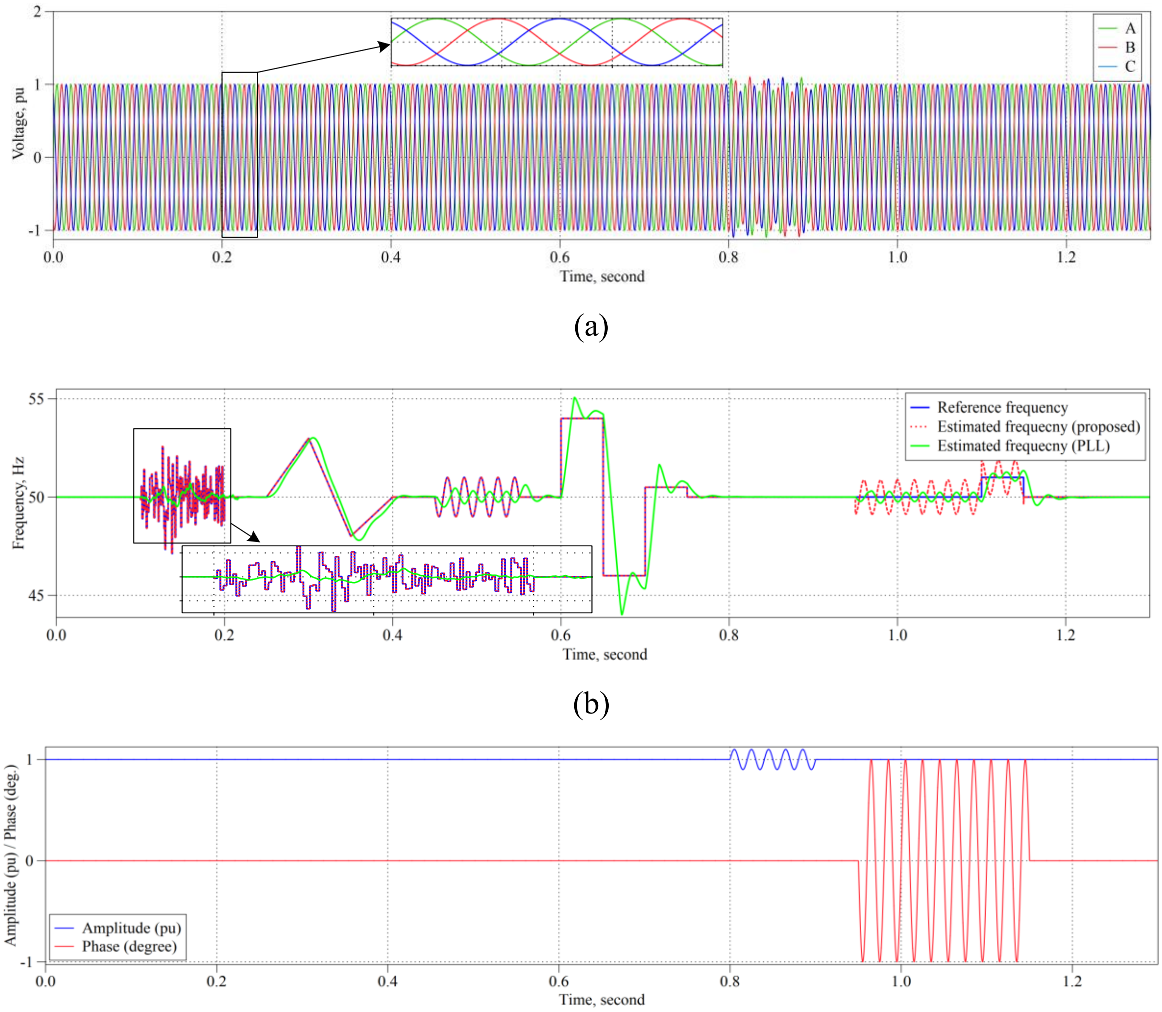


(a)

(b)

(c)

**Figure 5.4:** Simulation results in the noise-free environment: (a) abc per-unit signal, (b) actual frequency versus estimated frequency for the proposed method and the PLL, and (c) magnitude and phase profiles of the original abc signal.

almost immediately, with a maximum delay of one sample $T_s$, whereas the PLL introduces a visible lag due to the integral action of its PI controller. Throughout the ramp interval from 0.25 to 0.40 s, the proposed method tracks the ramp with at most one-sample delay, while the PLL exhibits a persistent lag. The sinusoidal oscillations between 0.45 and 0.55 s further highlight this distinction; the proposed method tracks the oscillations with no observable phase lag, while the PLL introduces approximately 90° of phase lag (a characteristic that can cause damping problems in control systems that rely on PLL-based frequency feedback). The step changes during 0.60–0.70 s and 1.10–1.15 s are detected within one sample by the proposed method, whereas the PLL requires several cycles to converge. During the magnitude variation from 0.80 to 0.90 s, neither method is affected, which confirms that the normalisation in (5.7) successfully decouples amplitude from the frequency estimate. The phase shifts between 0.95 and 1.15 s reveal that the proposed method accurately reflects the relationship $f = \frac{1}{2\pi}\frac{d\theta}{dt}$, while the PLL introduces additional detection delay.

### 5.4.2 Noisy Environment

White Gaussian noise is added to the abc signal to simulate practical measurement noise from instrumentation such as PMUs. The first-order Butterworth filter with $f_c = 70$ Hz is activated, and the filtered dq sequences are used in the cross-product computation. Figure 5.5 presents the results. The filter introduces a modest delay relative to the unfiltered case, as expected from its group delay, yet the proposed method remains consistently faster than the PLL across all disturbance types. These results expose the core limitation that motivates the remainder of this chapter. The noise–accuracy trade-off in the integer-order method is managed by an external filter with fixed parameters that offers no mechanism to continuously tune the balance between noise rejection and tracking speed. The fractional-order extension, introduced in Section 5.5 provides an alternative approach by embedding this trade-off within the differentiation operator through the tunable order $\alpha$.

## 5.5 Fractional-Order Derivative-Based Frequency Estimation

The integer-order method developed in Sections 5.2–5.3 achieves near-instantaneous frequency extraction through a cross-product formulation. However, the noise sensitivity analysis of Section 5.2.3 revealed a fundamental limitation. The first-order backward difference amplifies high-frequency noise by a factor proportional to $1/T_s$, and the

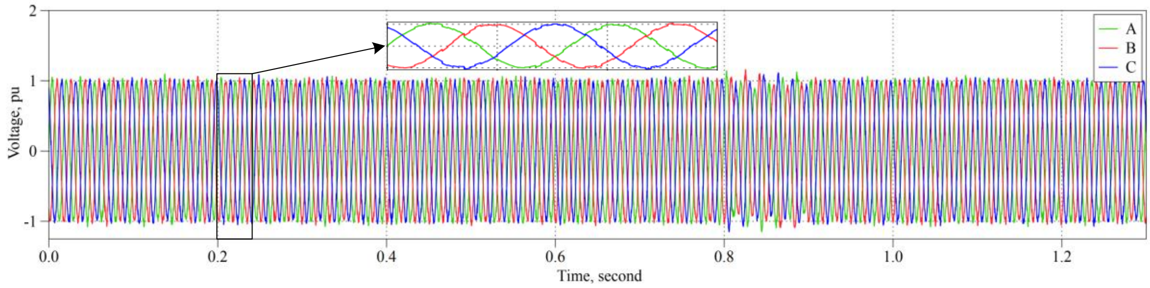


(a)

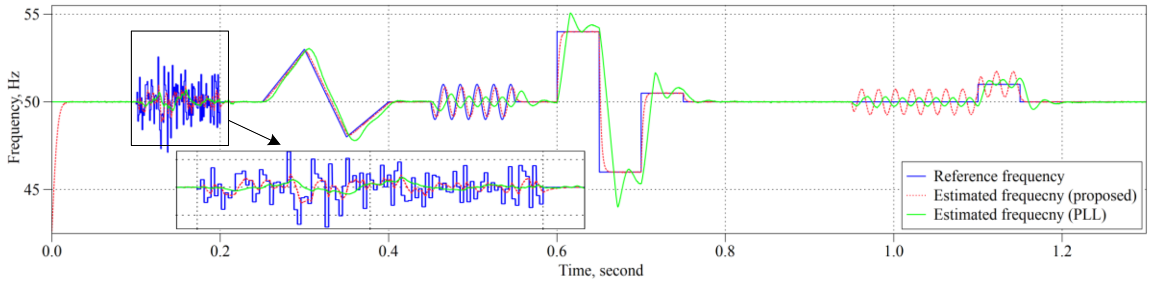


(b)

**Figure 5.5:** Noisy environment simulation results: (a) noisy abc per-unit signal, and (b) actual versus estimated frequency for the proposed method and the PLL.

Butterworth filter introduced in Section 5.3 addresses this only through an external post-processing stage with fixed parameters. This fixed-parameter design offers no mechanism for continuous adaptation to changing noise conditions. Fractional-order calculus provides an alternative approach that embeds the noise–accuracy trade-off directly within the differentiation operator through the tunable order $\alpha$.

The mathematical foundations of fractional-order calculus, including the Gamma function, the Riemann–Liouville definition, and the Grünwald–Letnikov discrete approximation, are established in Section 3.3. Two properties from that development are central to the method proposed in this section. The fractional derivatives of sinusoidal functions given by (3.16) and (3.17) reveal that the operator $D^{\alpha}$ scales the amplitude by $\omega^{\alpha}$ and shifts the phase by $\left(\frac{\pi}{2}\right)\alpha$ radians. For $\alpha < 1$, the amplitude scaling $\omega^{\alpha}$ is strictly less than the factor $\omega$ produced by integer-order differentiation when $\omega > 1$, and reduces the amplification of high-frequency noise compared to the integer-order case. The phase shift is proportionally reduced below $\pi/2$, yet the orthogonality between sine and cosine components is preserved, since both experience identical shifts. The frequency-domain representation in (3.18) confirms that the fractional derivative acts as a frequency-dependent gain with sub-linear growth rate $f^{\alpha}$ for $0 < \alpha < 1$, and ensures strictly less amplification at every frequency than first-order differentiation. Together, these properties establish that the unknown frequency $\omega$ is encoded in the amplitude scaling factor $\omega^{\alpha}$ of the fractional derivative output and can therefore be recovered algebraically.

### 5.5.1 Analytical Formulation

The normalised dq components established in (5.7) are $\hat{d}(t) = \sin(\Delta\omega\, t)$ and $\hat{q}(t) = \cos(\Delta\omega\, t)$, where $\Delta\omega = \omega_{\mathrm{act}} - \omega_{\mathrm{ref}}$ is the unknown frequency deviation. Application of the fractional derivative of order $\alpha$ to these components, through (3.16) and (3.17) with $\omega = \Delta\omega$, yields

$$\mathcal{D}^{\alpha}\begin{bmatrix}\hat{d}(t)\\ \hat{q}(t)\end{bmatrix} = (\Delta\omega)^{\alpha}\begin{bmatrix}\sin\left(\Delta\omega\, t+\frac{\pi}{2}\alpha\right)\\ \cos\left(\Delta\omega\, t+\frac{\pi}{2}\alpha\right)\end{bmatrix} \tag{5.30}$$

Equation (5.30) constitutes the central analytical result that distinguishes the fractional-order method from the integer-order method of Section 5.2. In the integer-order case ($\alpha = 1$), the derivatives in (5.9) produce signals with amplitudes scaled by $\Delta\omega$, and the cross-product formulation of (5.10) is required to eliminate the time-dependent trigonometric terms. In the fractional-order case ($0 < \alpha < 1$), the amplitude scaling factor is $(\Delta\omega)^{\alpha}$, and this amplitude can be extracted directly without a cross-product operation.

The key insight is that the amplitude of the fractional derivative output encodes the frequency deviation $\Delta\omega$ through the power-law relationship $A_m = (\Delta\omega)^{\alpha}$, where $A_m$ denotes the measured amplitude.

The amplitude $A_m$ is defined as the peak magnitude of the $\hat{d}$-component fractional derivative:

$$A_m = \max\,\left|\mathcal{D}^{\alpha}\left[\hat{d}(t)\right]\right| = (\Delta\omega)^{\alpha} \tag{5.31}$$

Due to the orthogonality between sine and cosine preserved in (5.30), the maximum of $D^{\alpha}\hat{d}(t)$ occurs precisely at the zero-crossing instants of $D^{\alpha}\hat{q}(t)$, and vice versa. This orthogonality provides a natural triggering mechanism for amplitude measurement. The zero crossings of the $\hat{q}$-component fractional derivative serve as the instants at which the $\hat{d}$-component fractional derivative achieves its peak value.

Taking the natural logarithm of both sides of (5.31) yields a linear relationship:

$$\ln(A_m) = \alpha \ln(\Delta\omega) \tag{5.32}$$

Rearrangement gives the frequency deviation explicitly as:

$$\Delta\omega = e^{\frac{\ln(A_m)}{\alpha}} \tag{5.33}$$

The actual system frequency is then recovered through (5.6) as $\omega_{\text{act}} = \Delta\omega + \omega_{\text{ref}}$, and the corresponding frequency in hertz is:

$$f_{\text{act}} = \frac{\omega_{\text{act}}}{2\pi} \tag{5.34}$$

The estimation requires only the measurement of $A_m$ at zero-crossing instants, the logarithmic inversion in (5.33), and the addition of $\omega_{\text{ref}}$. This feedforward algebraic structure is fundamentally distinct from the closed-loop tracking architecture of PLL-based methods and accounts for the fast dynamic response of the proposed estimator.

### 5.5.2 Implementation Architecture

Figure 5.6 illustrates the complete block diagram of the proposed method. The three-phase voltage $V_{abc}$ is first transformed into the rotating dq frame through the Park–Clarke transformation with reference frequency $\omega_{\text{ref}}$. The dq components are then normalised to unit-amplitude signals $\hat{d}(t)$ and $\hat{q}(t)$ through (5.7) and subsequently processed by the fractional-order derivative operator $D^{\alpha}(\cdot)$.

A sample-and-hold mechanism captures $A_m$ from the $\hat{d}$-component fractional derivative upon receipt of a trigger signal generated at zero-crossing events of the $\hat{q}$-component fractional derivative. The zero-crossing detector and sample-and-hold block ensure accurate amplitude measurement at the correct phase-synchronised instant under practical sampling constraints. Once $A_m$ is acquired, (5.33) is applied to estimate $\Delta\omega$, and the result is added to $\omega_{\text{ref}}$ to obtain $\omega_{\text{act}}$ through (5.6). Under unbalanced conditions, a positive-sequence extractor is applied to the input abc voltage prior to the estimation process.

### 5.5.3 Role of the Tunable Parameters

The proposed method contains two tunable parameters, namely, the fractional order $\alpha$ and the reference frequency $\omega_{\text{ref}}$, each governing a distinct aspect of estimator performance.

- **The reference frequency $\boldsymbol{\omega_{\text{ref}}}$** controls the estimation update rate. The oscillation frequency of the dq components, $\Delta\omega = \omega_{\text{act}} - \omega_{\text{ref}}$, determines the update rate, with

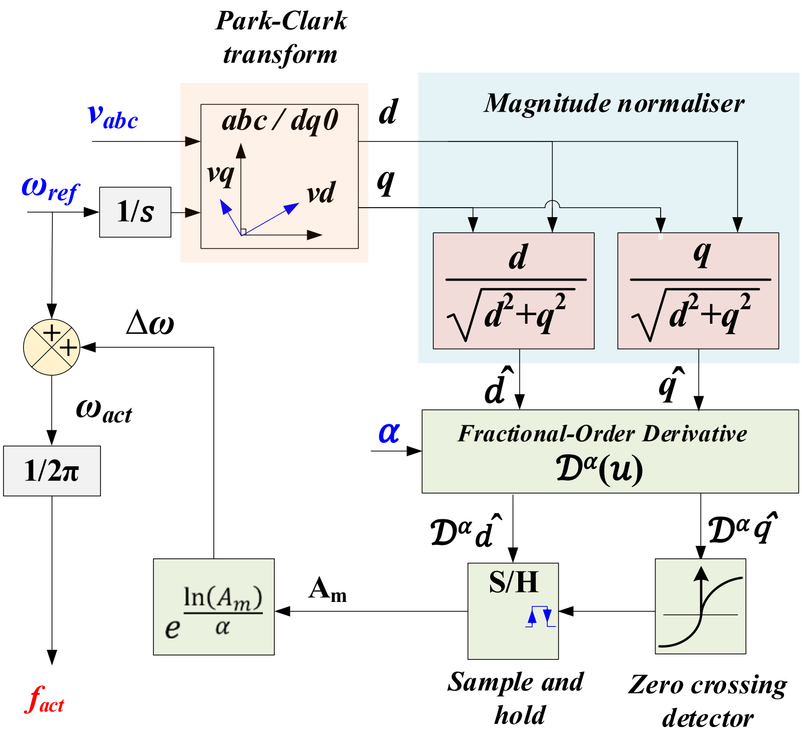


**Figure 5.6:** Block diagram of the proposed fractional-order derivative-based frequency estimation method.

updates occurring at twice the oscillation frequency because amplitude peaks arise at both the maxima and minima of the sinusoidal waveform. A lower reference frequency increases $\Delta\omega$ and produces more frequent updates. For an actual frequency of 50 Hz and a reference of 40 Hz, the oscillation frequency is 10 Hz and updates occur at 20 Hz (one every 50 ms). In low-inertia systems that require higher update rates, a negative reference frequency can be employed; a reference of -50 Hz yields an oscillation frequency of 100 Hz and updates occur at 200 Hz (one every 5 ms). The reference can be decreased further to achieve near-continuous estimation. This tunability enables the method to be tailored to each application, namely, low-inertia systems benefit from frequent updates that track rapid frequency variations, while high-inertia systems can reduce the update rate to optimise computational efficiency.

- **The fractional order $\boldsymbol{\alpha}$** controls noise sensitivity. As established in (3.16) and (3.17), the fractional derivative scales the amplitude of a component at frequency $\omega$ by $\omega^\alpha$. For $\alpha < 1$, this scaling is less aggressive than the factor $\omega$ from integer-order differentiation and results in reduced amplification of high-frequency noise. Smaller values of $\alpha$ provide less aggressive noise amplification, while larger values provide higher sensitivity to frequency changes and improved robustness against amplitude measurement inaccuracies. The detailed analysis of these trade-offs and systematic guidelines for optimal selection of $\alpha$ and $\omega_{\text{ref}}$ are presented in Section 5.6.

## 5.6 Noise Analysis, Stability, and Parameter Selection

The fractional-order frequency estimator of Section 5.5 introduces two tunable parameters, $\alpha$ and $\omega_{\text{ref}}$. The optimal selection of these parameters requires a quantitative understanding of how the fractional derivative operator transforms realistic signal disturbances, how measurement inaccuracies propagate through the logarithmic inversion of (5.33), and how the discrete-time implementation constrains the admissible parameter range. This section develops the necessary analytical framework for parameter selection. Subsections 5.6.1–5.6.4 examine the spectral interaction between the fractional derivative and noisy signals, and establish a noise-to-signal ratio expression and a classification of operating regions. Subsection 5.6.5 analyses estimation sensitivity through perturbation theory, and Subsection 5.6.6 validates the analytical predictions empirically. Subsections 5.6.7–5.6.9 translate these results into systematic parameter selection guidelines for representative power system environments.

### 5.6.1 Noisy Signal Model and Differentiated Signal Power

The normalised $\hat{d}$-axis component from (5.7) is augmented with an additive noise term to model realistic signal corruption:

$$g(t) = \sin(\Delta\omega\, t) + \eta(t), t \in \mathbb{R} \tag{5.35}$$

where the first term represents the ideal normalised $\hat{d}$-component oscillating at the frequency deviation $\Delta\omega = \omega_{\text{act}} - \omega_{\text{ref}}$, and $\eta(t)$ denotes a zero-mean stochastic process with power spectral density (PSD) $S_\eta(f)$. This term encompasses measurement noise from voltage sensors and quantisation effects from analogue-to-digital conversion. The objective of the subsequent analysis is to quantify, for each value of $\alpha$, the relative power of the noise component compared to the signal component after fractional differentiation.

The fractional derivative of the sinusoidal component, established in (5.30), yields a sinusoid with amplitude $(\Delta\omega)^\alpha$. Its time-averaged power is:

$$P_s(\alpha, \Delta\omega) = \frac{1}{2}(\Delta\omega)^{2\alpha} \tag{5.36}$$

The signal power increases monotonically with both $\alpha$ and $\Delta\omega$, which confirms that larger frequency deviations and higher $\alpha$ produce stronger signals after differentiation.

### 5.6.2 Spectral Transformation of the Noise Component

The frequency-domain representation of the fractional derivative established in (3.18) yields $\mathcal{F}\{D^\alpha \eta(t)\} = (j2\pi f)^\alpha\, \mathcal{F}\{\eta(t)\}$, where the magnitude of the transfer function is $(2\pi f)^\alpha$. Taking the squared magnitude gives the PSD of the differentiated noise:

$$S_{D^\alpha \eta}(f) = (2\pi f)^{2\alpha}\, S_\eta(f) \tag{5.37}$$

Equation (5.37) establishes that the fractional derivative applies a frequency-dependent gain $(2\pi f)^{2\alpha}$ to the noise spectrum. Three properties follow directly. First, the gain increases monotonically with frequency, so high-frequency components are amplified more strongly than low-frequency components. Second, for $\alpha < 1$, the gain $(2\pi f)^{2\alpha}$ is strictly less than $(2\pi f)^2$ at every frequency, which provides intrinsic noise suppression relative to integer-order differentiation. Third, reducing $\alpha$ continuously reduces the gain at all frequencies, with the limit $\alpha \to 0$ recovering the identity operator with no noise amplification.

### 5.6.3 Noise-to-Signal Ratio

To obtain a scalar measure of the noise impact, $\eta(t)$ is modelled as a band-limited process with flat PSD $S_\eta(f) = S_0$ for $f \in [0, B]$, where B is the noise bandwidth. This flat-spectrum assumption provides a tractable model representative of broadband measurement noise in practical power system instrumentation. The total noise power after fractional differentiation is obtained by integrating (5.37):

$$P_\eta(\alpha, B) = \int_0^{2\pi B} (2\pi f)^{2\alpha}\, S_0\, d\omega = \frac{S_0\,(2\pi B)^{2\alpha+1}}{2\alpha + 1} \tag{5.38}$$

The noise-to-signal ratio (NSR), defined as the ratio of total noise power to signal power, is:

$$\mathrm{NSR}(\alpha, B, \Delta\omega) = \frac{P_\eta(\alpha, B)}{P_s(\alpha, \Delta\omega)} = \frac{2S_0\,(2\pi B)^{2\alpha+1}}{(2\alpha + 1)(\Delta\omega)^{2\alpha}} \tag{5.39}$$

Equation (5.39) is the fundamental expression governing the noise performance of the estimator. The NSR is inversely proportional to $(\Delta\omega)^{2\alpha}$, so increasing $\Delta\omega$ always improves signal-to-noise performance. The NSR is directly proportional to $(2\pi B)^{2\alpha+1}$, so wider noise bandwidths degrade performance. The dependence on $\alpha$ is inherently nonlinear, as $\alpha$ appears in three distinct locations, in the numerator through $(2\pi B)^{2\alpha+1}$, in the denominator through $(\Delta\omega)^{2\alpha}$, and in the denominator through $(2\alpha+1)$. The combined effect of these terms determines whether increasing $\alpha$ improves or degrades the NSR for a given combination of B and $\Delta\omega$.

### 5.6.4 Classification of NSR Behaviour Regions

The nonlinear dependence of the NSR on $\alpha$ requires systematic classification of the parameter space $(B, \Delta\omega)$. Computing the partial derivative $\partial\,\mathrm{NSR}/\,\partial\alpha$ and examining its sign within $\alpha \in [0,1]$ partitions the parameter space into three distinct regions, illustrated in Figure 5.7.

- **Region 1** (pink area): the NSR decreases monotonically as $\alpha$ increases. This corresponds to conditions where B is small relative to $\Delta\omega$, characteristic of harmonic-rich environments with negligible high-frequency noise. The dominant effect of increasing $\alpha$ is to amplify the signal more than the noise, because the signal frequency $\Delta\omega$ lies well above the noise bandwidth. The optimal strategy is to select $\alpha$ as large as possible.

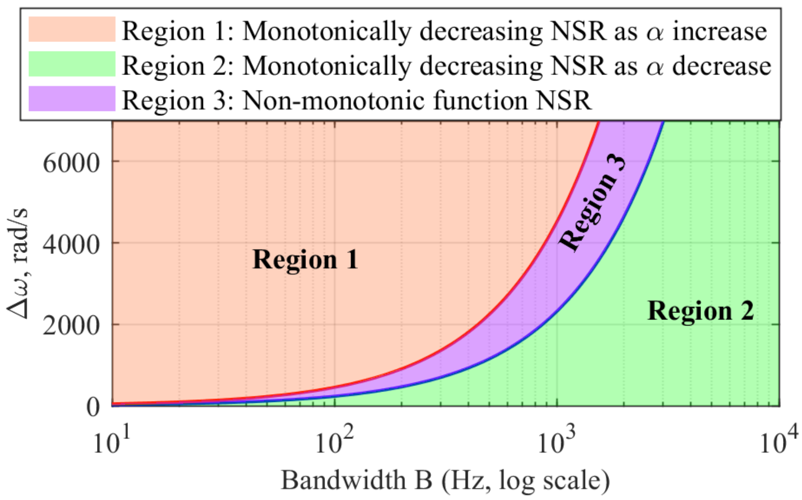


**Figure 5.7:** Regions of NSR behaviour as a function of bandwidth B and frequency deviation $\Delta\omega$, showing monotonic and non-monotonic areas for $\alpha \in [0,1]$.

- **Region 2** (green area): the NSR decreases monotonically as $\alpha$ decreases. This corresponds to conditions where B is large relative to $\Delta\omega$, characteristic of environments dominated by high-frequency measurement noise (4–100 kHz). Increasing $\alpha$ amplifies the high-frequency noise components more rapidly than the signal, and results in net degradation. The optimal strategy is to select $\alpha$ as small as possible, subject to the stability constraints of Subsection 5.6.5.
- **Region 3** (purple area): the NSR exhibits non-monotonic behaviour, initially decreasing as $\alpha$ increases from zero, and reaching a minimum at an intermediate value, then increasing as $\alpha$ approaches unity. This arises in mixed-noise environments where both low-frequency harmonics and high-frequency measurement noise are present simultaneously. The optimal fractional order that minimises the NSR is obtained by setting $\partial\,\mathrm{NSR}/\,\partial\alpha = 0$:

$$\alpha_{\text{optimal (Region 3)}} = \frac{1}{2}\left(\frac{1}{\ln\left(\frac{2\pi B}{\Delta\omega}\right)} - 1\right) \tag{5.40}$$

Figure 5.8 illustrates the three qualitatively distinct NSR behaviours. In Figure 5.8(a), the NSR has a clear minimum at an intermediate $\alpha$, which corresponds to a mixed-noise environment (Region 3). In Figure 5.8(b), the NSR decreases monotonically with increasing $\alpha$ (Region 1). In Figure 5.8(c), the NSR increases monotonically with $\alpha$ (Region 2).

### 5.6.5 Perturbation-Based Stability Analysis

The noise analysis of Subsections 5.6.1–5.6.4 characterises the spectral transformation of signal and noise components. However, the estimation accuracy also depends on how measurement inaccuracies in the amplitude $A_m$ propagate through the nonlinear logarithmic inversion of (5.33). These inaccuracies arise from residual noise, finite-precision arithmetic, timing errors in zero-crossing detection, and quantisation effects, and are collectively modelled as a small additive perturbation $\varepsilon_m$ applied to the ideal amplitude:

$$A'_m = A_m + \varepsilon_m = (\Delta\omega)^{\alpha} + \varepsilon_m \tag{5.41}$$

where $|\varepsilon_m| \ll (\Delta\omega)^{\alpha}$. Applying a first-order Taylor expansion of $\ln(A'_m)$ around $A_m$ and using the identity $\ln(\Delta\omega)^{\alpha} = \alpha\ln(\Delta\omega)$, yields:

$$\ln(A'_m) \approx \alpha \ln(\Delta\omega) + \frac{\varepsilon_m}{(\Delta\omega)^{\alpha}} \tag{5.42}$$

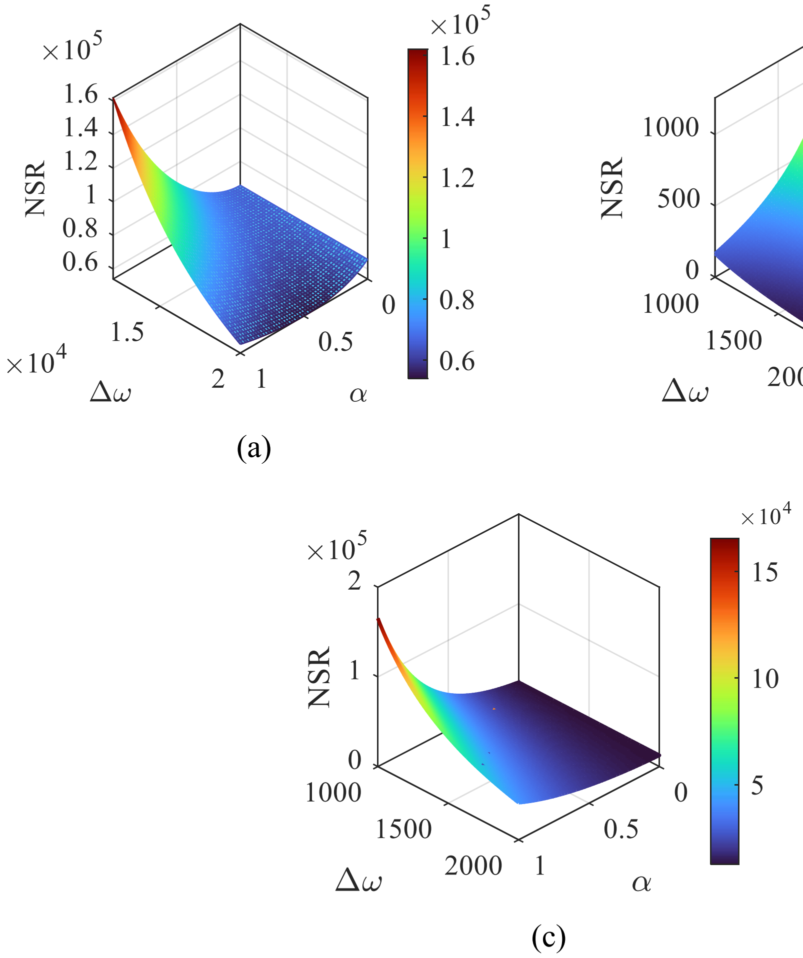


**Figure 5.8:** Variations in NSR behaviour with $\alpha$: (a) non-monotonic (Region 3), (b) monotonically decreasing with $\alpha$ (Region 1), and (c) monotonically increasing with $\alpha$ (Region 2).

Substituting (5.42) into the frequency estimation formula (5.33) gives the perturbed estimate:

$$\Delta\omega' = e^{\frac{1}{\alpha}\left(\alpha\ln(\Delta\omega)+\frac{\varepsilon_m}{(\Delta\omega)^{\alpha}}\right)} = e^{\ln(\Delta\omega)+\frac{\varepsilon_m}{\alpha(\Delta\omega)^{\alpha}}} \tag{5.43}$$

For small perturbations satisfying $\varepsilon_m/(\Delta\omega)^{\alpha} \ll 1$, that approximates the exponential as $e^x \approx 1 + x$ gives:

$$\Delta\omega' \approx \Delta\omega\left(1+\frac{\varepsilon_m}{\alpha(\Delta\omega)^{\alpha}}\right) \tag{5.44}$$

The relative estimation error is therefore:

$$\frac{\Delta\omega' - \Delta\omega}{\Delta\omega} \approx \frac{\varepsilon_m}{\alpha(\Delta\omega)^{\alpha}} \tag{5.45}$$

For the estimator to remain stable, this relative error must be small, requiring:

$$\varepsilon_m \ll \alpha(\Delta\omega)^{\alpha} \tag{5.46}$$

Equation (5.46) is the formal stability condition. Increasing $\Delta\omega$ enhances robustness because $(\Delta\omega)^{\alpha}$ grows with $\Delta\omega$, which makes the relative impact of a fixed $\varepsilon_m$ proportionally smaller. Increasing $\alpha$ also enhances robustness through two mechanisms, the linear prefactor $\alpha$ increases, and the term $(\Delta\omega)^{\alpha}$ increases for $\Delta\omega > 1$ (always satisfied in practice). Based on numerical evaluation and empirical validation, the practical design criterion is:

$$\frac{\varepsilon_m}{\alpha(\Delta\omega)^{\alpha}} \leq 10^{-2} \tag{5.47}$$

### 5.6.6 Empirical Validation of the Analytical Results

Figure 5.9 demonstrates the combined effects of $\alpha$ and $\Delta\omega$ on noise resistance and presents results for $\alpha \in \{0.1, 0.5, 0.9\}$ at two frequency deviations ($\Delta\omega = 2\pi \times 10$ rad/s and $\Delta\omega =$

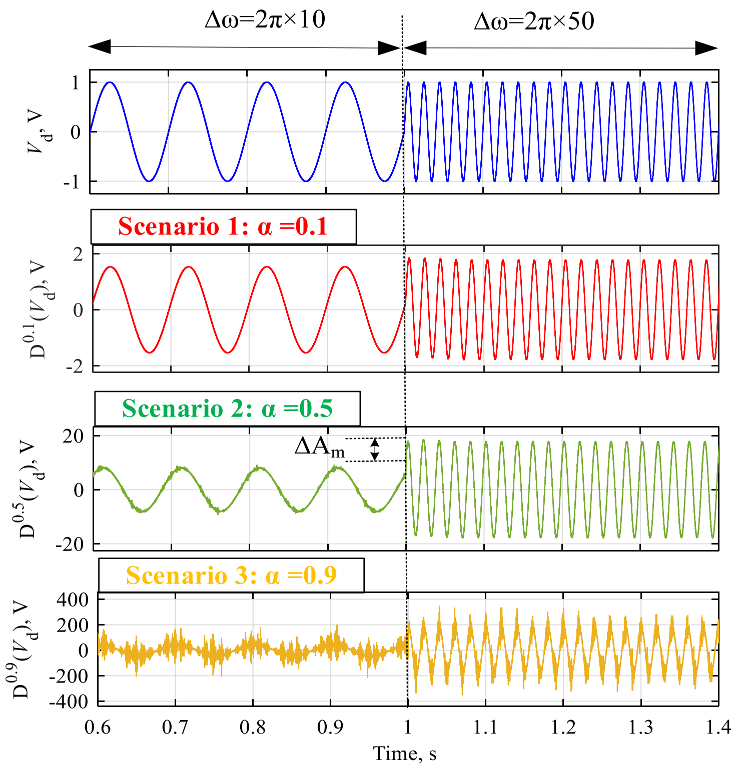


**Figure 5.9:** Impact of fractional derivative order $\alpha$ and frequency deviation $\Delta\omega$ on the $\hat{d}$-component's noise resistance.

$2\pi \times 50$ rad/s). The $\hat{d}$-axis component is corrupted by measurement noise with a bandwidth up to 100 kHz and amplitude inaccuracy $\varepsilon_m = \pm 0.01$ V.

This experiment evaluates how the fractional order $\alpha$ and frequency deviation $\Delta\omega$ influence noise robustness and amplitude scaling under controlled noise conditions. The results confirm all analytical predictions. As $\Delta\omega$ increases, the amplitude $A_m = (\Delta\omega)^\alpha$ increases for all $\alpha$ values, and reduces the relative impact of $\varepsilon_m$ as predicted by (5.45). For fixed $\Delta\omega$, the amplitude increases markedly with $\alpha$, from the order of units at $\alpha = 0.1$ to hundreds at $\alpha = 0.9$, and improves robustness to additive errors. Regarding noise sensitivity, $\alpha = 0.1$ produces minimal noise corruption in the differentiated signal, whereas noise influence becomes progressively more pronounced at $\alpha = 0.5$ and $\alpha = 0.9$, consistent with the spectral gain $(2\pi f)^{2\alpha}$ of (5.37). When $\Delta\omega$ increases from $2\pi \times 10$ to $2\pi \times 50$, noise resistance improves for both $\alpha = 0.5$ and $\alpha = 0.9$, though residual effects persist at $\alpha = 0.9$. For the selected parameters, the operating point falls within Region 2 of Figure 5.7, where the NSR decreases with decreasing $\alpha$. This result confirms the theoretical predictions of (5.39).

### 5.6.7 Sampling and Update Rate Constraints

The preceding analysis demonstrates that increasing $\Delta\omega$ benefits both noise rejection and estimation robustness. However, the Grünwald–Letnikov discretisation requires a sufficient number of samples per cycle of the dq-component oscillation. While the Nyquist criterion requires only two samples per cycle, the weighted summation structure of the Grünwald–Letnikov formula demands significantly more to achieve acceptable truncation error. A conservative guideline, validated through experimental results, requires at least 20 samples per cycle, which yields:

$$\Delta\omega < \pi f_s / 10 \tag{5.48}$$

where $f_s$ is the sampling frequency. For $f_s = 10$ kHz, this gives $\Delta\omega_{\max} \approx 3142$ rad/s ($\approx$500 Hz). In a 50 Hz system where $\omega_{\text{act}} \approx 314$ rad/s, the reference frequency must satisfy $\omega_{\text{ref}} > 314 - 3142 \approx -2828$ rad/s. This confirms that the negative reference frequencies introduced in Section 5.5.3 are practically achievable within the sampling constraint, and that the available design space for $\omega_{\text{ref}}$ extends well into the negative frequency range.

The update rate is determined by the zero-crossing trigger mechanism. Since two trigger events occur per oscillation cycle of the $\hat{q}$-component fractional derivative, the update period is $T_{\text{update}} = \pi/\Delta\omega$, which corresponds to $2\Delta\omega/(2\pi)$ estimates per second. This relationship enables direct specification of a target update rate: for example, an update rate of 700 Hz requires $\Delta\omega = 700\pi \approx 2199$ rad/s, corresponding to $\omega_{\text{ref}} = 2\pi(50 - 350) = -2\pi \times 300$ rad/s, which lies comfortably within the permissible range.

### 5.6.8 Scenario-Based Parameter Selection

The analytical results of Subsections 5.6.1–5.6.7 provide the foundation for systematic parameter selection. Three representative operating environments are considered.

**Scenario 1 (Harmonic-rich environment with negligible high-frequency noise):** In systems with significant nonlinear loads and effective filters attenuating components above 1 kHz, the effective noise bandwidth B remains narrow, and the operating point falls within Region 1 of Figure 5.7. Both the NSR and the stability condition improve with increasing $\alpha$, so no trade-off exists. Values of $\alpha \geq 0.6$ are recommended. The designer must verify that no residual high-frequency content is present, as even small amounts of broadband noise can be amplified significantly at large $\alpha$, as demonstrated in Figure 5.9.

**Scenario 2 (High-frequency noise dominant with negligible harmonics):** In systems with clean waveforms but broadband measurement noise extending from several kilohertz to 100 kHz, the operating point falls within Region 2. Noise suppression demands the smallest possible $\alpha$, while the stability condition (5.46) demands that $\alpha$ remain sufficiently large. To illustrate this bound, for $\Delta\omega = 3142$ rad/s and $\varepsilon_m = \pm 0.01\text{V}$, $\alpha = 0.2$ yields a stability ratio of $0.01/(0.2 \times 3142^{0.2}) = 0.01/1.034 \approx 0.0097$, marginally satisfying (5.47). However, $\alpha = 0.1$ yields $0.01/(0.1 \times 3142^{0.1}) = 0.01/0.227 \approx 0.044$, which exceeds the threshold by a factor of four. The minimum admissible order for this configuration is therefore $\alpha_{\min} = 0.2$, which underscores the importance of evaluating the stability and noise objectives jointly.

**Scenario 3 (Mixed-noise environment):** The most realistic condition involves both harmonic distortion and high-frequency noise simultaneously. It is recommended to design for operation in Region 3 of Figure 5.7, which permits the greatest design flexibility. A systematic four-step procedure is recommended:

- **Step 1:** Identify the effective noise bandwidth $B_H$ and locate the maximum $\Delta\omega$ that keeps the operating point within Region 3, by entering Figure 5.7 at $B_H$ on the horizontal axis and moving vertically until intersecting the Region 1–Region 3 boundary.
- **Step 2:** Compute $\alpha_{\text{opt}}$ using (5.40) with the effective noise bandwidth $B_H$ and the selected $\Delta\omega$.
- **Step 3:** If $\alpha_{\text{opt}} > 0.5$, the high-frequency noise amplification may become significant, and the designer should reduce $\Delta\omega$ incrementally and recompute $\alpha_{\text{opt}}$ until the condition $\alpha_{\text{opt}} < 0.5$ is satisfied. This iterative reduction trades a small amount of update rate and signal amplitude for improved noise rejection.
- **Step 4:** Verify the stability condition (5.47). If it is unsatisfied, apply a low-pass filter to the input signal to suppress the high-frequency noise. Once this noise is eliminated, the effective bandwidth $B_H$ decreases, the operating point shifts toward Region 1, and larger values of $\Delta\omega$ and $\alpha$ can be employed per Scenario 1.

### 5.6.9 Design Example and Real-Time Considerations

The four-step procedure presented in Subsection 5.6.8 is evaluated under conditions representative of the experimental setup described in Section 5.7. Specifically, the setup includes harmonics up to the 13th order ($B_H \approx 650\,\text{Hz}$), high-frequency noise with bandwidth $B_N \approx 100\,\text{kHz}$, amplitude inaccuracy of $\varepsilon_m = \pm 0.01$ V, a sampling frequency of $f_s = 10\,\text{kHz}$, and a nominal system frequency of 50 Hz.

In Step 1, entering Figure 5.7 at $B_H = 650$ Hz yields an initial maximum deviation of $\Delta\omega \approx 2\pi \times 450$ rad/s ($\approx 2827$ rad/s). In Step 2, substituting into (5.40) yields $\alpha_{\text{opt}} \approx 0.85$. In Step 3, since 0.85 > 0.5, $\Delta\omega$ is reduced incrementally. For instance, $\Delta\omega = 2\pi \times 400$ gives $\alpha_{\text{opt}} \approx 0.5$ (borderline); a further reduction to $\Delta\omega = 2\pi \times 350 \approx 2199$ rad/s gives $\alpha_{\text{opt}} \approx 0.3$, which satisfies the condition comfortably. In Step 4, computing $(2199)^{0.3} \approx 10.06$, the stability ratio becomes $0.01/(0.3 \times 10.06) = 0.0033$, well below the $10^{-2}$ threshold with a margin exceeding a factor of three. The final design parameters are $\alpha = 0.3$ and $\omega_{\text{ref}} = 2\pi(50 - 350) = -2\pi \times 300$ rad/s, corresponding to a reference frequency of -300 Hz. This configuration yields an update rate of approximately 700 Hz.

## 5.7 Hardware Validation and Experimental Results

The proposed fractional-order frequency estimation method is validated on the real-time hardware platform shown in Figure 5.10. The CINERGIA programmable grid emulator provides precise control over grid voltage magnitude, phase, and frequency. Three-phase voltage signals from the emulator pass through measurement sensors with a noise bandwidth of approximately 100 kHz before connection to a dSPACE real-time simulator, on which the proposed algorithm is implemented. Estimated frequency values are displayed on the dSPACE graphical user interface and logged for post-processing. The three-phase voltage signals are scaled to $\pm 10\ V$ input range for the dSPACE ADC, with a sampling frequency of 10 kHz and 16-bit resolution.

Three recent PLL-based methods serve as benchmarks, namely, the feed-forward PLL (FF-PLL) [96], the dual second-order generalised integrator PLL (DSOGI-PLL) [35], and the cascaded delayed signal cancellation PLL (CDSC-PLL) [97]. Optimal parameters for all benchmarks are obtained through MATLAB's Response Optimizer toolbox in Simulink to ensure fair comparison. The proposed method uses the parameters identified through the

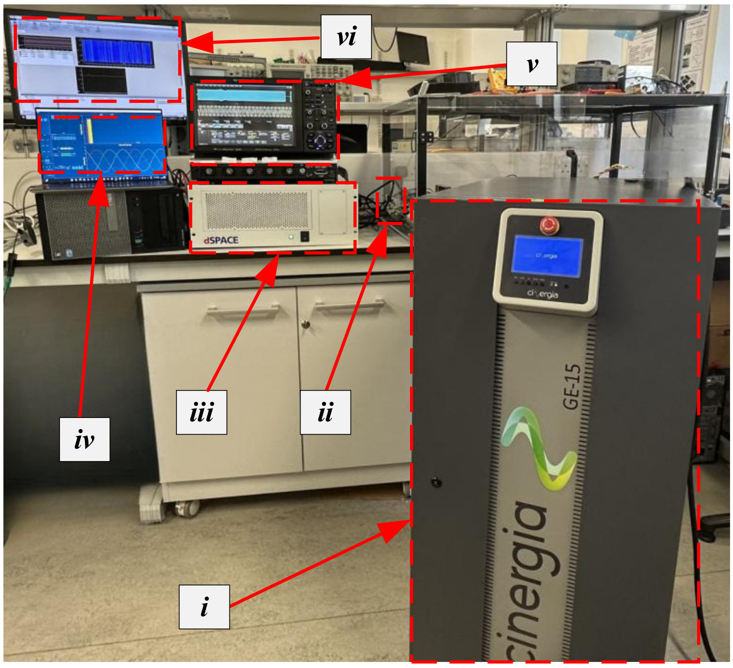


**Figure 5.10:** Hardware implementation setup: (i) CINERGIA grid emulator; (ii) voltage sensors; (iii) dSPACE real-time simulator; (iv) emulator GUI; (v) oscilloscope; (vi) dSPACE GUI.

design procedure of Section 5.6.9 ($\alpha = 0.3$ and $\omega_{\text{ref}} = -2\pi \times 300$ rad/s). Six experimental scenarios are conducted under harmonic distortion levels that conform to European standards, as specified in Table 5.1.

Performance is quantified through three metrics, namely, the maximum absolute error (MaxAE), the root mean square error (RMSE), and the settling time ($T_S$), defined as the duration for the estimate to stabilise within 1% of its steady-state value.

**Table 5.1:** Harmonic components as a percentage of fundamental, per European Standard.

| Harmonic components | | | | | | THD |
|---|---|---|---|---|---|---|
| 3rd | 5th | 7th | 9th | 11th | 13th | 10.46% |
| 5% | 6% | 5% | 1.5% | 3.5% | 3% | |

### 5.7.1 Scenario 1: Fast Frequency Dynamics with Low-Order Harmonics

This scenario evaluates performance under rapid frequency variation. A step from 50 Hz to 52 Hz is applied at t = 1 s at a rate of 200 Hz/s, which approximates a near-instantaneous transition representative of severe transients in low-inertia systems. Figure 5.11(a) shows the three-phase line voltages at 10.46% THD, and Figure 5.11(b) presents the frequency estimation errors.

The proposed method achieves a settling time of 118 ms, a 9.9% improvement over the FF-PLL (131 ms), 47.6% over the DSOGI-PLL (225 ms), and 48% over the CDSC-PLL (227 ms). The substantial margins over the DSOGI-PLL and CDSC-PLL reflect the fundamental advantage of derivative-based estimation over integral-based PLL architectures, which require multiple oscillation cycles for feedback-loop convergence.

The proposed method achieves a peak error of 1.896 Hz, lower than that of the FF-PLL (1.979 Hz) by 4.2%, the DSOGI-PLL (1.977 Hz) by 4.1%, and the CDSC-PLL (1.984 Hz) by 4.4%. The RMSE is 0.491 Hz, compared with 0.615 Hz (FF-PLL), 0.591 Hz (DSOGI-PLL), and 0.622 Hz (CDSC-PLL), for improvements of 20.2%, 16.9%, and 21.1%, respectively.

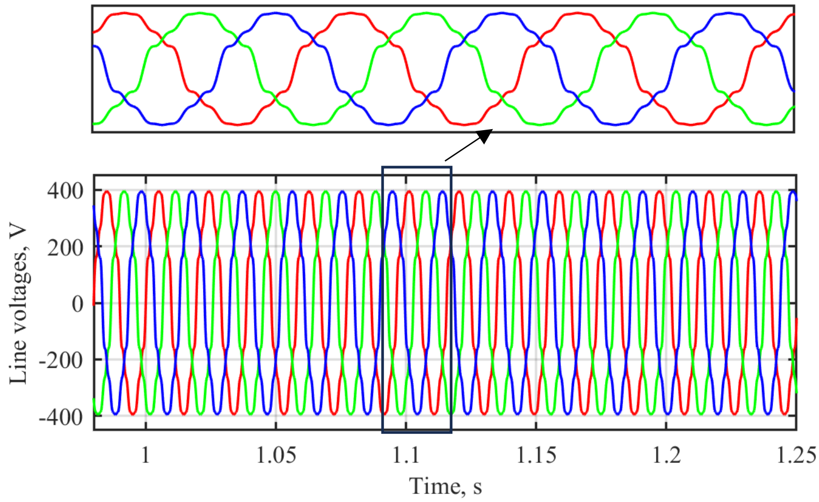


(a)

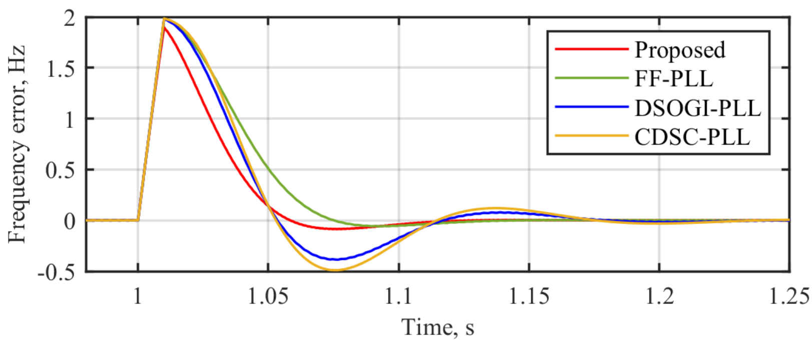


(b)

**Figure 5.11:** Scenario 1: (a) three-phase line voltages at 10.46% THD; (b) frequency estimation errors.

### 5.7.2 Scenario 2: Fast Frequency Dynamics with High-Frequency Noise

The same 50-to-52 Hz step at 200 Hz/s is applied, but low-order harmonics are replaced by high-frequency noise in the 2–5 kHz range. This scenario isolates estimator behaviour under broadband measurement noise and directly validates the noise rejection analysis of the preceding sections. Figure 5.12(a) shows the distorted voltages and Figure 5.12(b) the estimation errors. The proposed method maintains RMSE, peak error, and settling time values consistent with those of Scenario 1. This confirms the robustness of the selected parameters ($\alpha = 0.3$, $\Delta\omega = 2\pi \times 350$ rad/s). The FF-PLL and DSOGI-PLL exhibit sustained oscillations of approximately 0.01 Hz peak-to-peak, because their harmonic rejection strategies are optimised for low-order harmonics and are less effective against broadband disturbances.

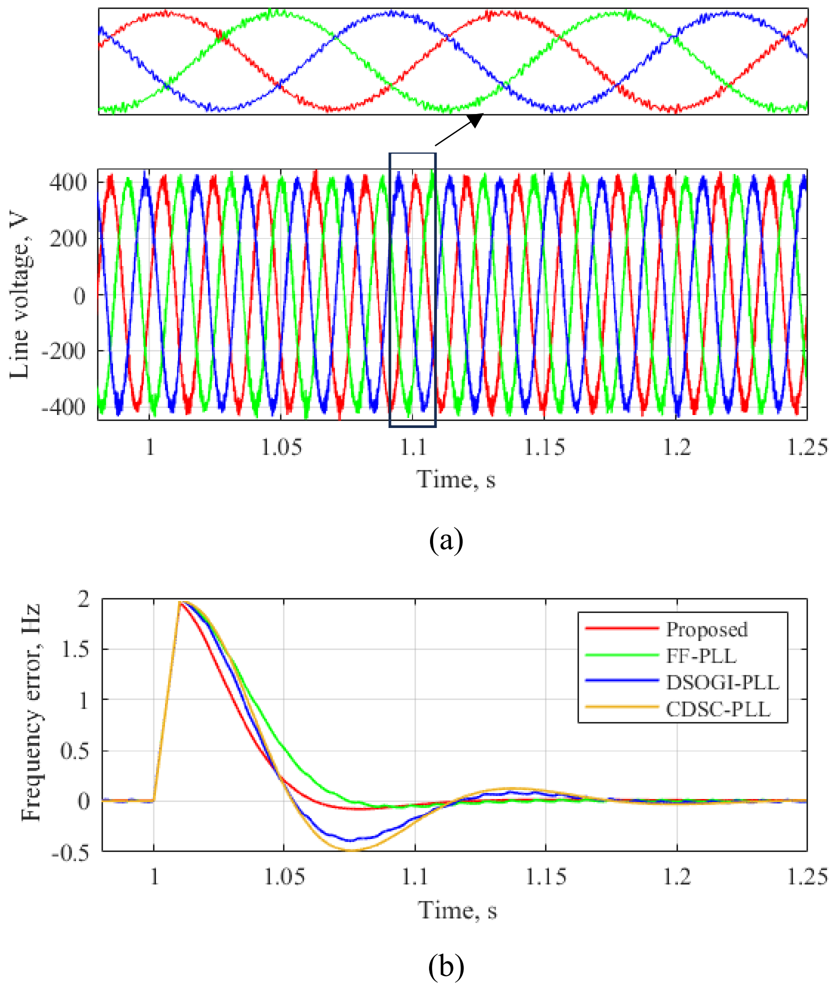


**Figure 5.12:** Scenario 2: (a) three-phase voltages with high-frequency noise; (b) frequency estimation errors.

Both the CDSC-PLL and the proposed method demonstrate strong immunity to high-frequency distortion and maintain stable tracking throughout the transient.

### 5.7.3 Scenario 3: Slow Frequency Dynamics with Low-Order Harmonics

This scenario assesses performance under slow dynamics. The frequency ramps down at 0.5 Hz/s from t = 5 s to t = 6 s, reaches a minimum, and ramps back at the same rate from t = 6 s to t = 7 s, with THD at 10.46%. Figure 5.13(a) shows the estimated frequencies and Figure 5.13(b) the estimation errors.

The proposed method achieves a settling time of 124.5 ms, faster than the FF-PLL (134.2 ms) by 7.2%, the DSOGI-PLL (286.2 ms) by 56.5%, and the CDSC-PLL (292.3 ms) by 57.4%. The peak error is 0.0078 Hz, a reduction of 55.4% relative to the FF-PLL (0.0175

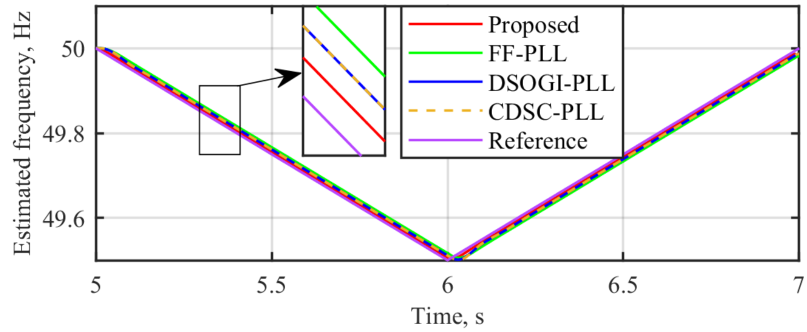


(a)

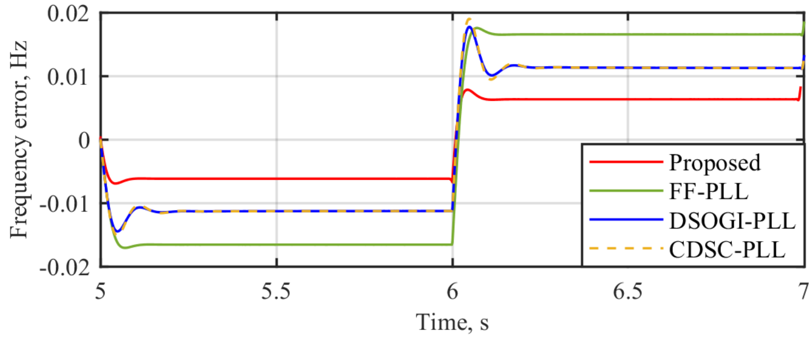


(b)

**Figure 5.13:** Scenario 3: (a) frequency estimation responses; (b) estimation errors.

Hz), 55.9% relative to the DSOGI-PLL (0.0177 Hz), and 58.9% relative to the CDSC-PLL (0.0190 Hz). The RMSE is 0.0063 Hz, compared with 0.0163 Hz (FF-PLL), 0.0114 Hz (DSOGI-PLL), and 0.0114 Hz (CDSC-PLL), for improvements of 61.4%, 44.7%, and 44.7% respectively.

These margins, particularly the 61.4% RMSE reduction over the FF-PLL, demonstrate that the proposed method excels under moderate dynamics where sustained tracking accuracy is critical. The proposed fast, non-iterative method reduces sustained steady-state tracking error that PLL methods experience during prolonged frequency excursions.

### 5.7.4 Scenario 4: Magnitude and Phase Variations with Harmonics

This scenario evaluates robustness under voltage magnitude disturbances and phase perturbations representative of dips, swells, and flicker. Figure 5.14(a) shows the three-phase

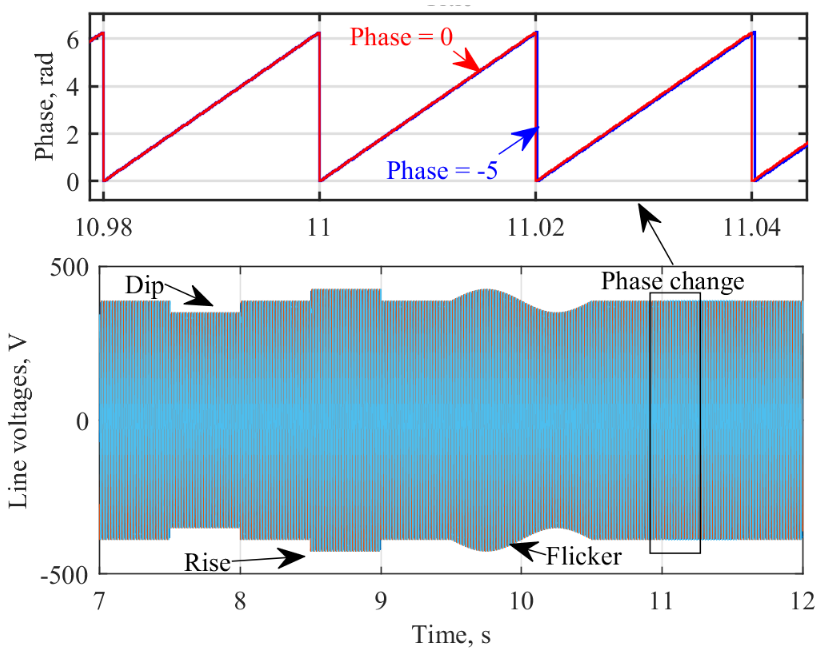


(a)

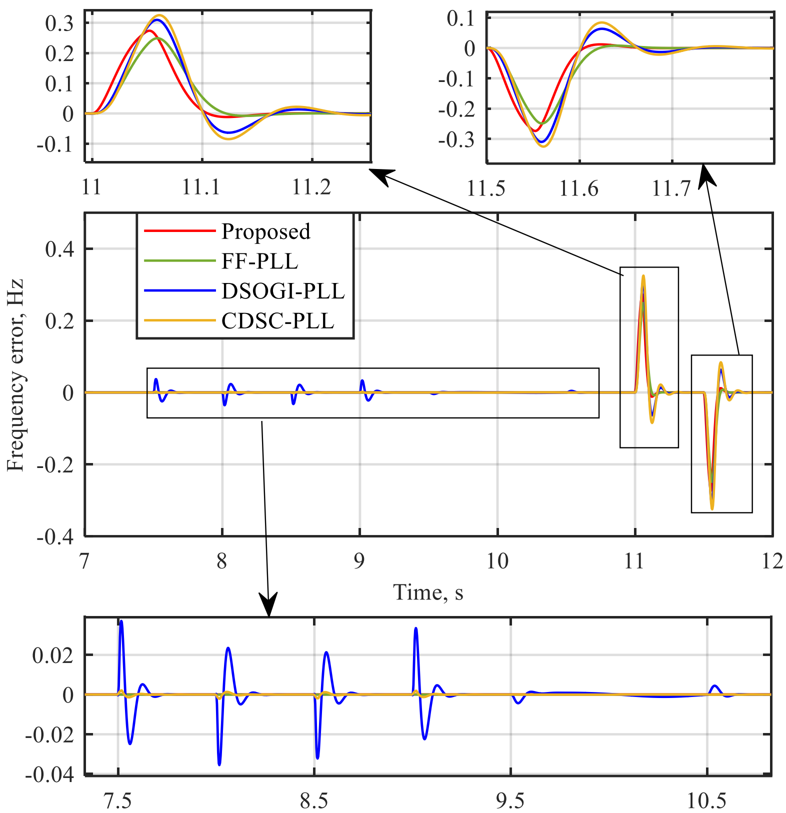


(b)

**Figure 5.14:** Scenario 4: (a) three-phase voltages with inset phase measurement; (b) frequency estimation errors.

voltages under the following sequence, a 10% dip at t = 7.5 s for 0.5 s, a 10% rise at t = 8.5 s for 0.5 s, a 1 Hz flicker with 10% modulation, a -5° phase shift at t = 11 s, and a +5° phase shift at t = 11.5 s, both at 100°/s. The inset of Figure 5.14(a) shows the phase in radians alongside the nominal zero reference. Figure 5.14(b) presents the estimation errors.

During dip, rise, and flicker events, the proposed method and the FF-PLL both achieve zero peak error and zero RMSE. This confirms that the normalisation block achieves perfect decoupling between magnitude variations and frequency estimation. The DSOGI-PLL performs the worst with a 0.04 Hz peak error and a 0.01 Hz RMSE; the CDSC-PLL shows intermediate performance with a 0.002 Hz peak error and a 0.0005 Hz RMSE.

The phase perturbation results are particularly significant. The relationship between phase change and instantaneous frequency deviation is $\Delta f = \Delta\varphi/(360 \cdot \Delta t)$, where $\Delta\varphi$ is in degrees and $\Delta t$ in seconds. For the -5° shift at t = 11 s over 0.05 s, the theoretical deviation is 0.2778 Hz. The proposed method estimates 0.2737 Hz at 1.47% error, compared with the FF-PLL at 0.2488 Hz (10.43% error), the DSOGI-PLL at 0.3096 Hz (11.44%), and the CDSC-PLL at 0.3251 Hz (17.02%). This capacity to capture phase-induced frequency dynamics within the first cycle of a transient is critical for reliable inertia estimation in low-inertia power systems.

### 5.7.5 Scenario 5: Severe Fault Conditions

A three-phase fault reduces all line voltages to near zero at t = 2 s for 200 ms. Figure 5.15(a) shows the voltages and Figure 5.15(b) the estimation errors.

The proposed method correctly identifies the terminal frequency as near zero during the fault, with zero error throughout the fault period. After fault clearance, the estimate returns to 50 Hz with a settling time of 113.57 ms. The FF-PLL also detects the zero-frequency condition but settles in 146.1 ms (the proposed method is 22.3% faster). The proposed method achieves a peak error of 51.49 Hz versus 53.36 Hz for the FF-PLL (3.5% improvement) and an RMSE of 14.26 Hz versus 20.49 Hz (30.4% reduction). These errors directly influence RoCoF estimation and frequency-based protection thresholds during black-start. Reduced RMSE prevents false triggering of protection mechanisms. The DSOGI-PLL and CDSC-PLL fail to detect the zero-frequency condition entirely and maintain output estimates near 50 Hz despite the absence of an input signal. The proposed method avoids this failure mode through its open-loop, measurement-driven architecture.

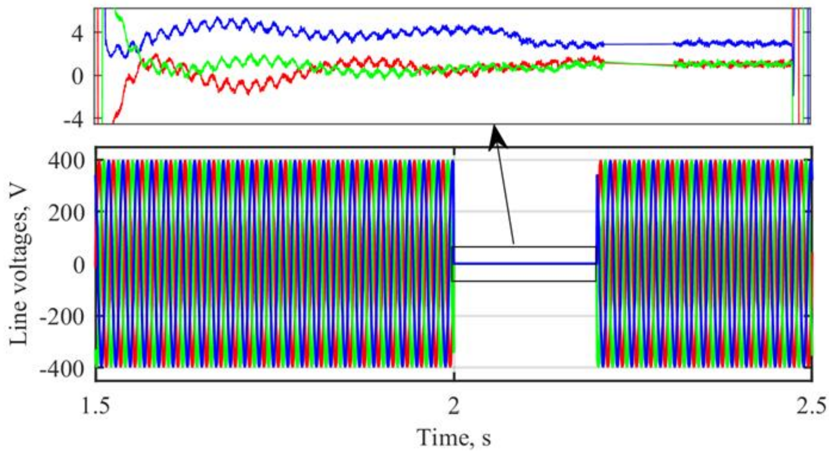


(a)

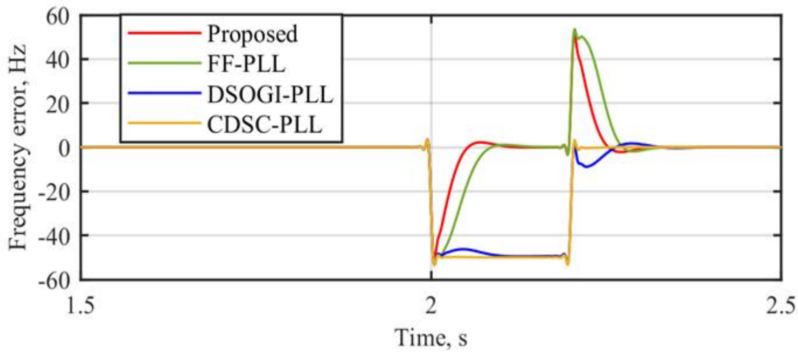


(b)

**Figure 5.15:** Scenario 5: (a) three-phase voltages; (b) frequency estimation errors.

When the input voltage collapses, the dq-component oscillation ceases, and the frequency estimate correctly reflects the absence of signal.

### 5.7.6 Scenario 6: Unbalanced Conditions

DC offsets of 0.05, 0.10, and 0.15 per unit are added to phases a, b, and c, respectively, at t = 2 s. Figure 5.16(a) shows the voltages. Figure 5.16(b) presents errors without positive-sequence extraction (PSE), and Figure 5.16(c) shows errors with PSE applied.

Without PSE, the proposed method exhibits sustained oscillations of 0.11 Hz, compared with 0.02 Hz (FF-PLL), 0.04 Hz (DSOGI-PLL), and zero (CDSC-PLL). The larger oscillation of the proposed method results from the direct sensitivity of its open-loop structure to negative-sequence components, which produce additional oscillations at unexpected frequencies in the dq frame.

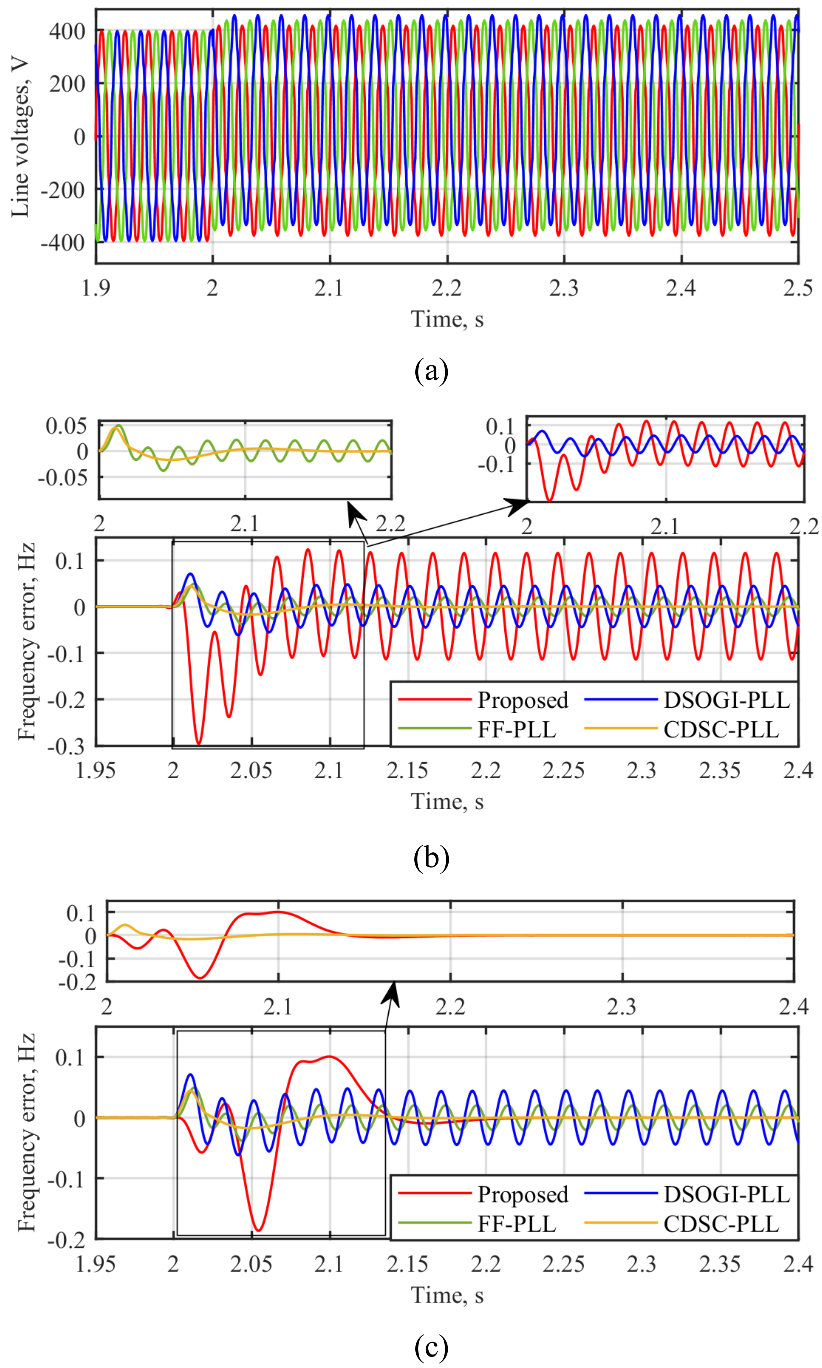


**Figure 5.16:** Scenario 6: (a) voltages with DC offsets; (b) errors without PSE; (c) errors with PSE.

A positive-sequence extraction stage based on delayed signal cancellation (DSC) is therefore integrated upstream of the fractional derivative computation. As Figure 5.16(c) confirms, the sustained oscillations are eliminated entirely. Under these conditions, the proposed method achieves comparable steady-state accuracy to the FF-PLL and DSOGI-PLL, although a slightly higher transient peak error is observed. The CDSC-PLL retains a slight advantage, as the upstream DSC stage introduces additional processing delay in the proposed method.

### 5.7.7 Computational Time Analysis

The computational cost of the proposed method is dominated by the fractional-order derivative, implemented through the Grünwald–Letnikov approximation discussed in Section 3.3.5. The buffer size (the number of retained historical samples) governs both accuracy and cost. All methods are simulated concurrently in MATLAB/Simulink Performance Advisor over 10 repetitions for buffer sizes from 50 to 500. Figure 5.17(a) shows each method's share of computational time, and Figure 5.17(b) provides the internal breakdown of the proposed method.

For buffer sizes between 50 and 250, the proposed method exhibits the lowest computational load at 12.07%, followed by the FF-PLL (12.34%), the DSOGI-PLL (29.22%), and the CDSC-PLL (46.35%). Beyond 250, the fractional derivative cost rises and eventually

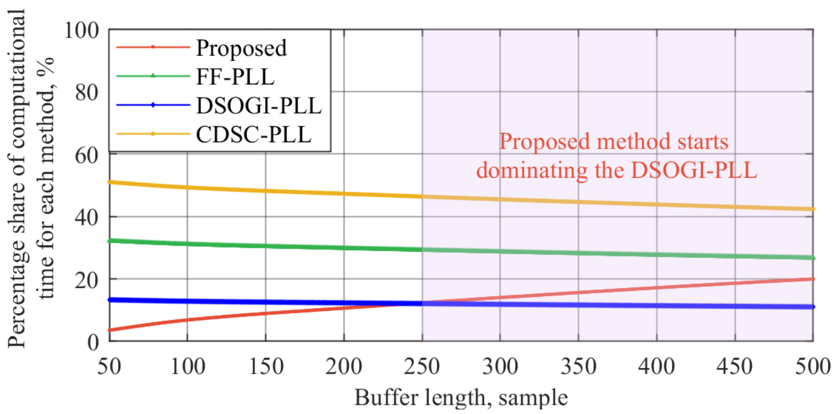


(a)

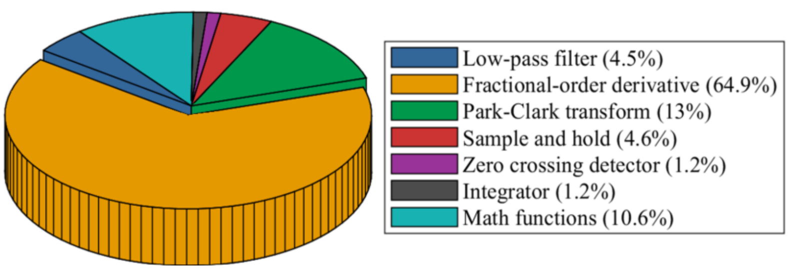


(b)

**Figure 5.17:** Computational analysis: (a) percentage time share per method versus buffer size; (b) internal component contributions of the proposed method.

surpasses that of the DSOGI-PLL. For 50 Hz applications, a buffer of 250 samples or fewer maintains accuracy with full computational advantage. Within the proposed method, the fractional derivative accounts for 64.9% of the total burden, the Park–Clarke transformation for 13%, mathematical functions for 10.6%, the low-pass filter for 4.5%, sample-and-hold for 4.6%, the zero-crossing detector for 1.2%, and the integrator for 1.2%.

Table 5.2 summarises comparative performance across all scenarios; bracketed percentages indicate relative improvement of the proposed method over each benchmark. The six scenarios collectively demonstrate consistent performance improvements of the proposed method.

## 5.8 Summary

This chapter developed two novel frequency estimation methods for low-inertia power systems, both of which exploit the oscillatory behaviour of normalised dq-frame components that arises when the Park-transform reference frequency is deliberately offset from the true grid frequency. Unlike conventional PLL-based approaches that rely on integral action, the proposed methods employ derivative-based algebraic operations to extract the frequency and thereby eliminate the dynamic delays inherent to integral actions.

The integer-order method achieves algebraically exact frequency extraction through a cross-product formulation requiring only eight arithmetic operations per sample. Although near-instantaneous under ideal conditions, the method's reliance on differentiation amplifies high-frequency noise and necessitates an external Butterworth filter to manage the noise–accuracy trade-off, which motivated the development of the fractional-order alternative.

The fractional-order method addresses this limitation by replacing the integer-order derivative with a tunable fractional-order derivative of order $\alpha \in (0,1)$. The fractional derivative amplitude encodes frequency deviation through the power-law relationship $A_m = (\Delta\omega)^{\alpha}$, which then enables direct algebraic recovery of the system frequency. Two tunable parameters ($\alpha$ and $\omega_{\text{ref}}$) provide largely decoupled control over noise sensitivity and estimation update rate, respectively.

The integer-order method remains attractive for ultra-fast, low-noise environments due to its minimal computational cost, whereas the fractional-order method is preferred in noisy

**Table 5.2:** Relative performance of benchmark methods compared with the proposed method.

| Scenario | Metric | Proposed | FF-PLL | DSOGI-PLL | CDSC-PLL |
|---|---|---|---|---|---|
| **Fast frequency dynamics** | RMSE (Hz) | 0.491 | 0.615 (20.2%) | 0.591 (16.9%) | 0.622 (21.1%) |
| | MaxAE (Hz) | 1.896 | 1.979 (4.2%) | 1.977 (4.1%) | 1.984 (4.4%) |
| | $T_S$ (ms) | 118 | 131 (9.9%) | 225 (47.6%) | 227 (48.0%) |
| **Slow frequency dynamics** | RMSE (Hz) | 0.0063 | 0.0163 (61.4%) | 0.0114 (44.7%) | 0.0114 (44.7%) |
| | MaxAE (Hz) | 0.0078 | 0.0175 (55.4%) | 0.0177 (55.9%) | 0.0190 (58.9%) |
| | $T_S$ (ms) | 124.5 | 134.2 (7.2%) | 286.2 (56.5%) | 292.3 (57.4%) |
| **Magnitude and phase variations** | RMSE at magnitude variations (Hz) | 0 | 0 | 0.010 | 0.0005 |
| | MaxAE at magnitude variations (Hz) | 0 | 0 | 0.040 | 0.002 |
| | Phase-induced frequency detection error (%) | 1.47% | 10.43% | 11.44% | 17.02% |
| **Severe fault condition** | RMSE (Hz) | 14.26 | 20.49 (30.4%) | N/A | N/A |
| | MaxAE (Hz) | 51.49 | 53.36 (3.5%) | N/A | N/A |
| | $T_S$ (ms) | 113.57 | 146.1 (22.3%) | N/A | N/A |
| **Unbalanced condition** | Sustained oscillation without PSE (Hz) | 0.11 | 0.02 | 0.04 | 0 |
| | Sustained oscillation with PSE (Hz) | 0 | 0.02 | 0.04 | 0 |
| **Computational time** | % time at buffer size of 250 samples | 12.07% | 12.34% | 29.22% | 46.35% |

conditions where robustness is critical, at the expense of slightly higher computational complexity.

Experimental validation across six scenarios on a CINERGIA grid emulator and dSPACE real-time platform demonstrated consistent performance improvements of the fractional-order method over three advanced PLL benchmarks (FF-PLL, DSOGI-PLL, CDSC-PLL). Settling times improved by 7–57%, RMSE reduced by up to 61.4%, phase-induced frequency detection achieved 1.47% error compared with 10–17% for PLL methods, and operational continuity and valid frequency tracking were maintained during severe faults where DSOGI-PLL and CDSC-PLL failed to produce estimates entirely. The method also achieved the lowest computational cost at a buffer size of 250 samples.

Within the broader thesis framework, the frequency estimation methods developed here provide the foundational measurement layer for the inertia estimation (Chapter 4) and restoration optimisation (Chapter 7) chapters. The sub-cycle response capability and tunable update rate ensure frequency measurements are available with the accuracy and speed required for reliable inertia estimation. Furthermore, the RoCoF and frequency nadir constraints enforced within the black-start restoration optimisation formulation developed in Chapter 7 depend on real-time frequency measurements of sufficient accuracy and speed.

When used in derivative-based control (RoCoF estimation), the low-latency nature of the proposed methods improves responsiveness. However, noise amplification must be carefully managed, particularly for small $\Delta\omega$.

# Chapter 6 Innovative Control Methods for Grid-Forming Converters During Power System Restoration

The preceding chapters established the measurement layer for grid-forming converter operation during restoration. Accurate estimation alone, however, is insufficient; the estimated signals must be acted upon by control algorithms that address the unique challenges of a converter that serves as the sole voltage and frequency reference in a low-inertia restoration network. Two challenges are particularly critical: transient damping following each load pickup event, and voltage unbalance compensation as asymmetric loads are sequentially reconnected.

This chapter addresses both challenges. The transient damping problem is solved through a fractional-order derivative-based feedforward damping loop that augments the conventional droop controller. The unbalance problem is solved through an Expectation–Maximisation-enhanced Kalman filter, built upon the frameworks in Sections 3.4 and 3.5. The proposed filter constructs a novel time-varying measurement matrix that encodes the inter-sequence coupling introduced by unbalanced loads, thereby enabling adaptive sequence separation and subsequent unbalance suppression.

## 6.1 Fractional-Order Active Power Damping

This section develops a fractional-order feedforward damping loop that augments the conventional droop controller to suppress active power oscillations during transients.

### 6.1.1 Conventional Droop Control and Its Inherent Trade-Off

In standard grid-forming converter control architectures, the internal frequency reference $\omega$ is regulated through a droop-based active power–frequency loop. The measured active power $P$ is compared with a reference setpoint $P_{\text{set}}$, and the resulting deviation is scaled by a droop coefficient $m_p$ and processed through a first-order low-pass filter with cut-off frequency $\omega_c$. The internal angular frequency is

$$\omega = \omega_{\text{set}} - \underbrace{\frac{\omega_c}{s + \omega_c}(P - P_{\text{set}})\, m_p}_{\Delta\omega} \tag{6.1}$$

where $\omega_{\text{set}}$ is the nominal angular frequency and $\Delta\omega$ is the dynamic frequency deviation. The low-pass filter attenuates switching harmonics while it introduces a first-order lag. This low-pass nature, however, creates a fundamental limitation during rapid transient events. The filter delays the convergence of $\omega$ toward the actual grid frequency $\omega_g$, which produces a phase angle error $\delta = \int (\omega - \omega_g)\, dt$ that drives active power oscillations. This effect becomes more pronounced under weak-grid conditions, where high grid impedance reduces the synchronising power coefficient and weakens the coupling between power angle and active power, which leads to increased oscillatory behaviour. A lower droop gain $m_p$ or filter bandwidth $\omega_c$ improves transient responsiveness but degrades steady-state regulation accuracy or noise immunity, respectively. No independent degree of freedom therefore exists within the conventional droop architecture to enhance transient damping without a corresponding penalty in steady-state performance or noise rejection.

### 6.1.2 Proposed Fractional-Order Feedforward Damping Loop

To resolve this trade-off, an auxiliary feedforward loop based on the fractional-order derivative of the incremental power change $\Delta P$ is proposed. The signal $\Delta P$ represents the successive change in the measured active power, which captures power variation. Under steady-state conditions, $\Delta P$ vanishes, and the feedforward path therefore remains inherently inactive except during transient events. The enhanced frequency control law is

$$\omega = \omega_{\text{set}} - \underbrace{\frac{\omega_c}{s + \omega_c}(P - P_{\text{set}})\, m_p}_{\Delta\omega} - \mathcal{D}^{\alpha}(\Delta P) \tag{6.2}$$

where $D^{\alpha}(\cdot)$ denotes the fractional-order derivative of order $0 < \alpha \leq 1$, as defined in Section 3.3. Compared with (6.1), the sole addition is the term $-D^{\alpha}(\Delta P)$, which acts as a transient damping signal. Two properties of $\Delta P$ and its fractional derivative underpin the design. First, $\Delta P$ tends toward zero; its fractional derivative therefore vanishes once the transient subsides, and the conventional droop characteristic governs the system. Second, as established in Section 3.3.4, the fractional derivative provides a frequency-domain magnitude proportional to $\omega^{\alpha}$. For $\alpha < 1$, this sub-linear growth amplifies high-frequency noise strictly less than the integer-order derivative does, which eliminates the need for additional filtering stages that would introduce phase lag. Therefore, the proposed approach provides a key advantage over conventional derivative-based damping through the introduction of a controllable phase lead. In integer-order derivatives, the phase lead remains fixed, which limits flexibility in shaping the dynamic response. In contrast, the fractional-order derivative introduces a phase lead that depends on the order α and allows continuous adjustment of the control action. Moreover, conventional derivative implementations typically require a low-pass filter to suppress noise amplification. This filter introduces additional phase delay. The fractional-order formulation avoids this requirement because the selection of α limits high-frequency gain and reduces noise sensitivity.

Upon a transient disturbance, the rapid change in power produces a non-zero $\Delta P$, and the fractional derivative $D^{\alpha}(\Delta P)$ generates a corrective signal. This action accelerates the convergence of $\omega$ toward $\omega_g$, and suppresses the resultant power oscillations. Figure 6.1 illustrates the complete architecture. The conventional droop path occupies the lower portion, where the power deviation $(P - P_{\text{set}})$ is scaled by $m_p$ and filtered to produce $\Delta\omega$, which is subtracted from $\omega_{\text{set}}$ to yield $\omega$. The proposed feedforward loop occupies the upper portion, where $\Delta P$ is passed through the fractional-order derivative block $D^{\alpha}(\cdot)$, and the resulting signal is subtracted from the frequency reference node. The corrected frequency is then integrated to produce the phase angle $\theta$ that defines the converter synchronous reference frame. The proposed loop is a non-intrusive add-on that requires no modification to the droop path, the reactive power–voltage loop, or the inner voltage and current control loops.

## 6.2 Equilibrium Point Analysis of the Proposed Fractional-Order Damping Loop

To verify that the proposed fractional-order damping mechanism does not interfere with steady-state operation, the equilibrium conditions of the augmented system must be analysed. This section establishes through formal derivation that the additional control loop remains inactive under nominal steady-state conditions and contributes only during transient events.

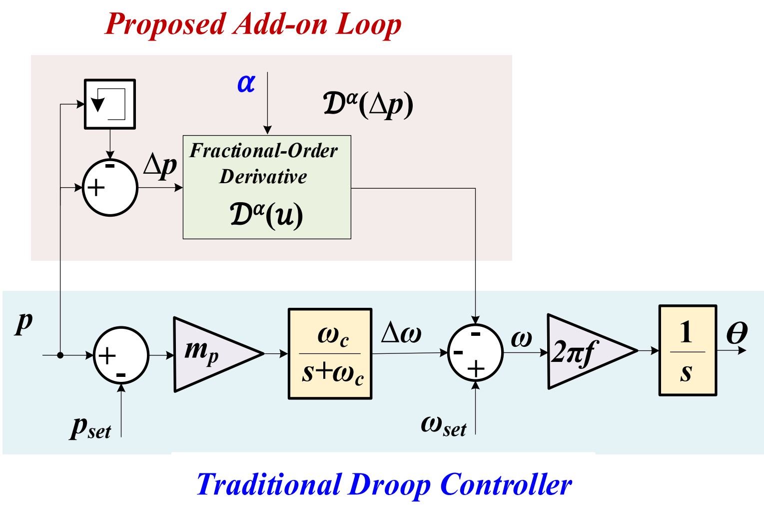


**Figure 6.1:** Block diagram of the conventional droop controller and the proposed fractional-order feedforward loop.

The dynamic behaviour of a grid-forming converter connected to an external grid is characterised through two fundamental state variables. The first is the power angle:

$$x_1 = \delta \tag{6.3}$$

which represents the phase angle difference between the converter terminal voltage phasor $\vec{V}_{\mathrm{pcc}}$ and the grid voltage phasor $\vec{V}_g$. Physically, $\delta$ quantifies the angular displacement between the converter's internally generated synchronous reference frame and the grid's reference frame. The second state variable is the frequency deviation, defined as

$$x_2 = \omega - \omega_g \tag{6.4}$$

where $\omega$ is the internal angular frequency of the converter as determined by the droop controller and the proposed feedforward loop, and $\omega_g$ is the nominal angular frequency of the grid.

The relationship between these two state variables is governed by the fundamental kinematic equation that links angular position and angular velocity. Since the power angle $\delta$ is the integral of the frequency difference between the converter and the grid, the time derivative of the first state variable is

$$\frac{dx_1}{dt} = \frac{d\delta}{dt} = \omega - \omega_g = x_2 \tag{6.5}$$

To relate the state variables to the electrical behaviour of the system, consider the simplified single-line equivalent circuit in which the converter is represented by an ideal voltage source $\vec{V}_{\mathrm{pcc}} = V_{\mathrm{pcc}}\angle\delta$ connected to the grid, represented by $\vec{V}_g = V_g\angle 0°$, through a purely inductive impedance $Z = jX_g$. The three-phase active power transferred from the converter to the grid is

$$P(\delta) = \frac{3\, V_{pcc}\, V_g}{2\, X_g} \sin(\delta) \tag{6.6}$$

The nonlinear sinusoidal dependence of $P(\delta)$ on $\delta$ makes direct analytical treatment difficult. To enable tractable equilibrium point analysis, the power transfer equation is linearised around a steady-state operating point $\delta_0$. The power angle is decomposed as

$$\delta = \delta_0 + \Delta\delta \tag{6.7}$$

where $\Delta\delta$ is a small perturbation about the equilibrium. Substitution of (6.7) into (6.6) yields

$$P(\delta_0 + \Delta\delta) = \frac{3V_{pcc}V_g}{2X_g} \sin(\delta_0 + \Delta\delta) \tag{6.8}$$

Application of the trigonometric addition formula gives

$$P(\delta_0 + \Delta\delta) = \frac{3V_{pcc}V_g}{2X_g} [\sin(\delta_0)\cos(\Delta\delta) + \cos(\delta_0)\sin(\Delta\delta)] \tag{6.9}$$

Under the small-signal assumption ( $|\Delta\delta| \ll 1$ ), the first-order approximations $\cos(\Delta\delta) \approx 1$ and $\sin(\Delta\delta) \approx \Delta\delta$ hold. Substitution into (6.9) produces

$$P(\delta) = \underbrace{\frac{3\,V_{pcc}\,V_g}{2\,X_g}\sin(\delta_0)}_{P_0} + \underbrace{\frac{3V_{pcc}V_g}{2X_g}\cos(\delta_0)}_{K_p}\Delta\delta \tag{6.10}$$

The linearised active power expression is therefore

$$P(\delta) \approx P_0 + K_p\,\Delta\delta \tag{6.11}$$

where $P_0 = \frac{3V_{pcc}V_g}{2X_g}\sin(\delta_0)$ is the steady-state active power at $\delta_0$, and $K_p = \frac{3V_{pcc}V_g}{2X_g}\cos(\delta_0)$ is the synchronising power coefficient evaluated at $\delta_0$. The coefficient $K_p$ represents the sensitivity of the active power transfer to changes in the power angle.

With the linearised power transfer relationship established, the state-space model of the grid-forming converter with the proposed fractional-order damping loop can now be derived. For the purpose of equilibrium analysis, the low-pass filter in the droop path is assumed to have reached steady state. Under this quasi-static assumption, the frequency control law from (6.2) becomes

$$\omega = \omega_{\text{set}} - (P - P_{\text{set}})\,m_p - \mathcal{D}^{\alpha}(\Delta P) \tag{6.12}$$

Two distinct signals appear in (6.12) and must be carefully distinguished. The power deviation $(P - P_{\text{set}})$ enters the conventional droop term and represents the static offset of the measured power from its reference setpoint; this quantity may assume a nonzero constant value at equilibrium if the operating point differs from the setpoint. The signal $\Delta P$ enters the fractional-order damping term and represents the incremental change in the measured active power; this quantity vanishes whenever the power reaches any constant value, regardless of whether that value equals $P_{\text{set}}$.

Substituting the control law (6.12) into the definition of $x_2$ from (6.4) gives the frequency deviation as

$$x_2 = (\omega_{\text{set}} - \omega_g) - (P - P_{\text{set}})\, m_p - \mathcal{D}^\alpha(\Delta P) \tag{6.13}$$

To linearise this expression, the measured power is written through (6.11) as $P = P_0 + K_p\, \Delta\delta$, so that the power deviation from the setpoint becomes

$$P - P_{set} = (P_0 - P_{set}) + K_p\, \Delta\delta \tag{6.14}$$

The constant offset ($P_0 - P_{\text{set}}$) is determined by the steady-state droop balance. At equilibrium, the frequency deviation must vanish ($x_2^* = 0$), and the fractional-order damping term is inactive ($D^\alpha(\Delta p^*) = 0$). Substitution of these equilibrium conditions into (6.13) gives

$$0 = (\omega_{\text{set}} - \omega_g) - (P_0 - P_{\text{set}})\, m_p \tag{6.15}$$

from which the equilibrium power is

$$P_0 = P_{\text{set}} + \frac{\omega_{\text{set}} - \omega_g}{m_p} \tag{6.16}$$

In the typical case where $\omega_{\text{set}} = \omega_g$, this reduces to $P_0 = P_{\text{set}}$ (the equilibrium power equals the setpoint exactly). Substituting (6.14) and (6.16) into (6.13) yields

$$x_2 = (\omega_{\text{set}} - \omega_g) - m_p\left(\frac{\omega_{\text{set}} - \omega_g}{m_p} + K_p\, \Delta\delta\right) - \mathcal{D}^\alpha(\Delta P) \tag{6.17}$$

The terms ($\omega_{\text{set}} - \omega_g$) cancel and yield $x_2 = -m_p\big(K_p\, \Delta\delta\big) - \mathcal{D}^\alpha(\Delta P)$

The time derivative of $x_2$ from (6.13) is

$$\frac{dx_2}{dt} = -m_p K_p\left(\frac{d(\Delta\delta)}{dt}\right) - \frac{d}{dt}\mathcal{D}^\alpha(\Delta P) \tag{6.18}$$

Since $\frac{d(\Delta\delta)}{dt} = \frac{d\delta}{dt} = x_2$ from (6.7), the first term reduces to $-m_p\, K_p\, x_2$. The state-space representation is therefore

$$\begin{bmatrix} \frac{dx_1}{dt} \\ \frac{dx_2}{dt} \end{bmatrix} = \begin{bmatrix} x_2 \\ -m_p K_p x_2 - \frac{d}{dt}\mathcal{D}^\alpha(\Delta P) \end{bmatrix} \tag{6.19}$$

At equilibrium, all state variables cease to change with time; the equilibrium conditions, therefore, require $\frac{dx_1}{dt} = 0$ and $\frac{dx_2}{dt} = 0$. From the first row of (6.19), the condition $\frac{dx_1}{dt} = 0$ requires ( $x_2^* = 0$ ).

This result states that at equilibrium, the converter's internal frequency exactly equals the grid frequency ($\omega^* = \omega_g$). This must hold regardless of the value of $\omega_{\text{set}}$, because any nonzero frequency deviation would cause the power angle $\delta$ to drift continuously. When $\omega_{\text{set}} \neq \omega_g$, the droop mechanism adjusts the equilibrium power to $P_0 = P_{\text{set}} + (\omega_{\text{set}} - \omega_g)/m_p$ as established in (6.16). This absorption of the setpoint offset drives the converter frequency to $\omega_g$.

Since the frequency is constant at equilibrium, the power angle $\delta$ is constant, the measured power $P$ is constant, and its time derivative vanishes. The incremental change $\Delta P$ therefore vanishes. The fractional derivative of a zero signal is identically zero, so $D^\alpha(\Delta P) = 0$ and consequently

$$\frac{dx_2}{dt} = -m_p K_p(0) - 0 = 0 \tag{6.20}$$

The equilibrium conditions derived are identical to those obtained from the conventional droop controller alone without the $D^\alpha(\Delta P)$ term; the steady-state frequency satisfies $\omega^* = \omega_g$, and the steady-state power is determined by the droop equation $P_0 = P_{\text{set}} + (\omega_{\text{set}} - \omega_g)/m_p$, regardless of whether the fractional-order loop is present. The proposed loop therefore contributes to the system dynamics only during transient events when $\Delta P$ varies with time. Once the system settles to a new steady state and $\Delta P$ becomes constant, the fractional-order derivative output decays to zero and the system reverts entirely to the behaviour governed by the conventional droop controller.

## 6.3 Simulation Validation of the Proposed Modified Droop Control

The proposed fractional-order damping feedforward loop is validated through time-domain simulations in MATLAB/Simulink. The test network, illustrated in Figure 6.2, comprises three interconnected grid-forming converters: GFM1 (250 MW), GFM2 (1000 MW), and GFM3 (500 MW). Two aggregate loads of 400 MW and 700 MW are supplied under normal

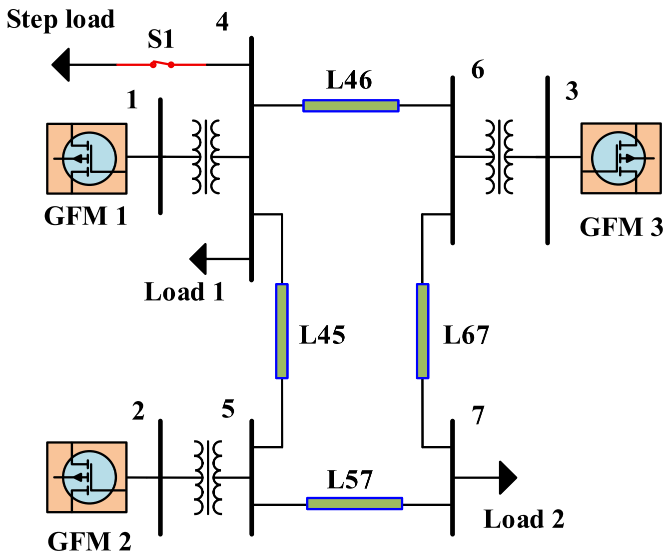


**Figure 6.2:** Schematic of the test network with three interconnected GFMs.

conditions. An additional load connection point at Bus 4, equipped with circuit breaker S1, enables controlled step-load disturbances.

To isolate the effect of the proposed method, GFM1 operates under two configurations, namely conventional droop control alone as defined in (6.1), and droop control augmented with the proposed fractional-order feedforward loop as defined in (6.2). GFM2 and GFM3 retain conventional droop controllers throughout. All parameters other than the fractional-order feedforward term remain identical across both configurations to ensure that observed performance differences are attributable solely to the proposed damping mechanism.

A 360 MW step load is applied at Bus 4 through circuit breaker S1 at t = 0.5 s and removed at t = 1.5 s. This sequence creates two transient events within a single simulation. The disturbance magnitude represents approximately 33% of the pre-disturbance total load and is directly relevant to black-start restoration, where sequential load pickup steps produce precisely this type of sudden demand change.

Figure 6.3(a) and Figure 6.3(b) present the active power and frequency under conventional droop control. At t = 0.5 s, GFM1's active power exhibits moderate overshoot followed by limited oscillation cycles before settling to the new operating point. This behaviour is a direct consequence of delayed frequency correction.

The frequency traces in Figure 6.3(b) reveal slow recovery among the three converters, with visibly different settling rates across the frequency traces, and a deep frequency nadir from which recovery requires several hundred milliseconds. A mirror-image transient accompanies load removal at t = 1.5 s. Figure 6.3(c) and Figure 6.3(d) show the responses with the proposed fractional-order loop active on GFM1. Compared with conventional droop control, the active power overshoot is reduced by approximately 57.5%. The settling time decreases from 0.39 s to 0.28 s, a 28.2% reduction. The frequency traces in Figure 6.3(d) confirm faster recovery and tighter inter-converter coordination for both events. However, a slightly larger overshoot appears due to the faster and more aggressive initial response of the proposed control. As predicted in Section 6.1.2, the rapid change in $\Delta P$ at disturbance onset causes $D^{\alpha}(\Delta P)$ to produce an immediate corrective signal. Steady-state frequency and power sharing remain identical under both configurations, which confirms the equilibrium preservation property established in Section 6.2.

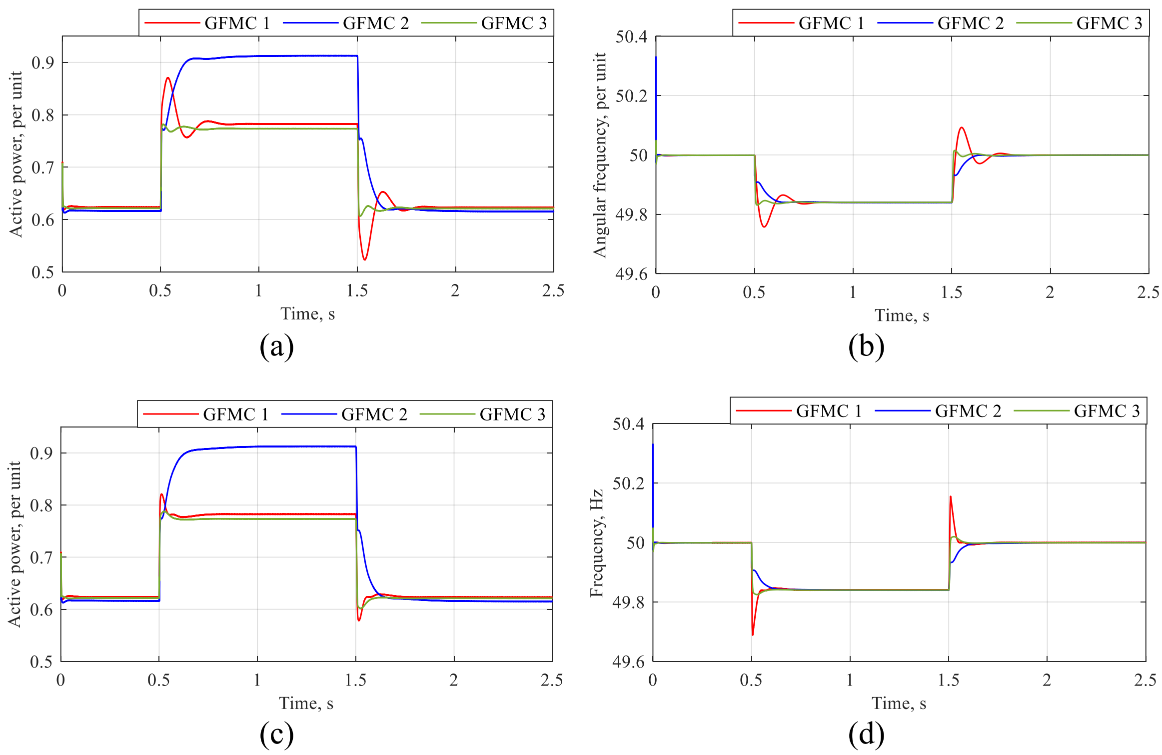


**Figure 6.3:** System performance under step-load disturbance: (a) active power under conventional droop, (b) frequency under conventional droop, (c) active power with the proposed loop, (d) frequency with the proposed loop.

Figure 6.4 plots the system trajectory in the ($\delta$, $\Delta\omega$) state space to provide a complementary geometric perspective. Under conventional droop control (blue trajectory), the system traces a wide spiral with multiple loops before it gradually converges to the equilibrium point. The large spiral radius and slow inward contraction are characteristic of an underdamped system with a low damping ratio. Under the proposed control (red trajectory), the system follows a compact path that converges rapidly with minimal oscillatory behaviour. Both trajectories converge to the same equilibrium point, a geometric confirmation that the proposed loop modifies only the transient path and not the steady-state destination.

## 6.4 Voltage Unbalance Challenge in Grid-Forming Converters

The preceding sections addressed transient damping through the proposed fractional-order feedforward loop. The present section and those that follow address the second critical challenge for grid-forming converters in low-inertia systems, which is voltage unbalance compensation at the point of common coupling. During power system restoration, reconnected loads may be unbalanced. The GB Grid Code clause CC.6.1.5(b) mandates that the voltage unbalance factor remain below 2% at the PCC under steady-state conditions, while during transients, the control objective is to restore the voltage unbalance to within this limit as rapidly as possible.

The core difficulty originates from the Park–Clarke transformation under unbalanced conditions. An unbalanced three-phase voltage decomposes into a positive-sequence component $V^+$ at angular frequency $\omega$, a negative-sequence component $V^-$ at $-\omega$, and a zero-sequence component $V^0$. In the positive-sequence synchronous dq0 frame, the positive-

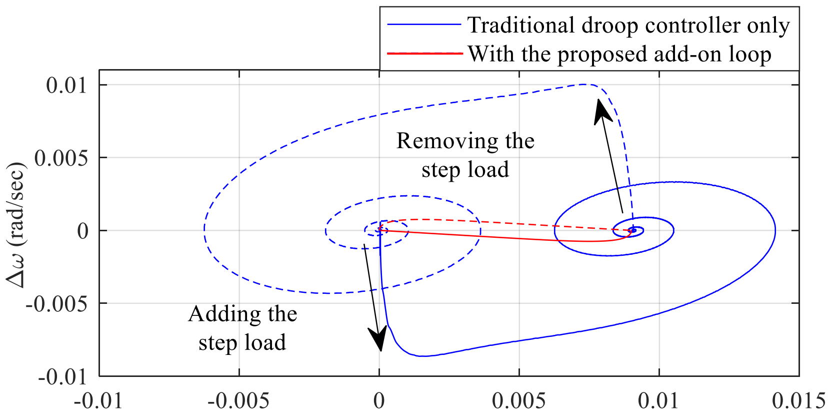


**Figure 6.4:** State-space trajectories in the ($\delta$, $\Delta\omega$) plane under conventional droop control (blue) and the proposed fractional-order damping loop (red).

sequence dq components contain the desired DC values together with an oscillatory interference from the negative sequence:

$$v^{+}_{(dq)} = \underbrace{\begin{bmatrix} v^{+}_{d} \\ v^{+}_{q} \end{bmatrix}}_{\text{DC Component}} + \underbrace{\begin{bmatrix} \cos(2\theta) & \sin(2\theta) \\ -\sin(2\theta) & \cos(2\theta) \end{bmatrix} \begin{bmatrix} v^{-}_{d} \\ v^{-}_{q} \end{bmatrix}}_{\text{2nd Harmonic Coupling}} \tag{6.21}$$

The negative-sequence dq components observed in the negative-sequence synchronous frame are similarly contaminated:

$$v^{-}_{(dq)} = \underbrace{\begin{bmatrix} v^{-}_{d} \\ v^{-}_{q} \end{bmatrix}}_{\text{DC Component}} + \underbrace{\begin{bmatrix} \cos(2\theta) & -\sin(2\theta) \\ \sin(2\theta) & \cos(2\theta) \end{bmatrix} \begin{bmatrix} v^{+}_{d} \\ v^{+}_{q} \end{bmatrix}}_{\text{2nd Harmonic Coupling}} \tag{6.22}$$

where $\theta = \omega t$ is the phase angle of the synchronous frame. This $2\omega$ interference corrupts the DC signals that the inner-loop PI controllers regulate. Since PI controllers achieve zero steady-state error only for DC inputs, they cannot reject these oscillations, which results in degraded voltage regulation, distorted currents, and phase angle estimation errors.

The most widely adopted method for separating the second-harmonic coupling is the decoupled double synchronous reference frame (DDSRF), which removes the coupling. However, the DDSRF relies on an accurate phase angle $\theta$ obtained from a PLL, which becomes unreliable under weak-grid conditions where the PCC voltage is distorted and it struggles to track the fundamental frequency.

To overcome these limitations, the following sections introduce a real-time decoupling framework based on an EM-enhanced Kalman filter (EM–K). Then, the decoupled sequence components feed an integrated voltage unbalance controller that compensates both negative-sequence and zero-sequence voltages at the PCC. Figure 6.5 illustrates the complete power circuit and proposed control architecture.

In Figure 6.5, the measured PCC voltage $v_{PCC,abc}$ is processed through Park–Clarke transformation and supplied to the EM–K estimator. The estimator outputs decoupled positive-, negative-, and zero-sequence components, which are fed into the primary controller and the unbalance controllers. The resulting modulation signals are combined in the $abc$ frame and applied to the PWM stage. The control loops are described in detail below.

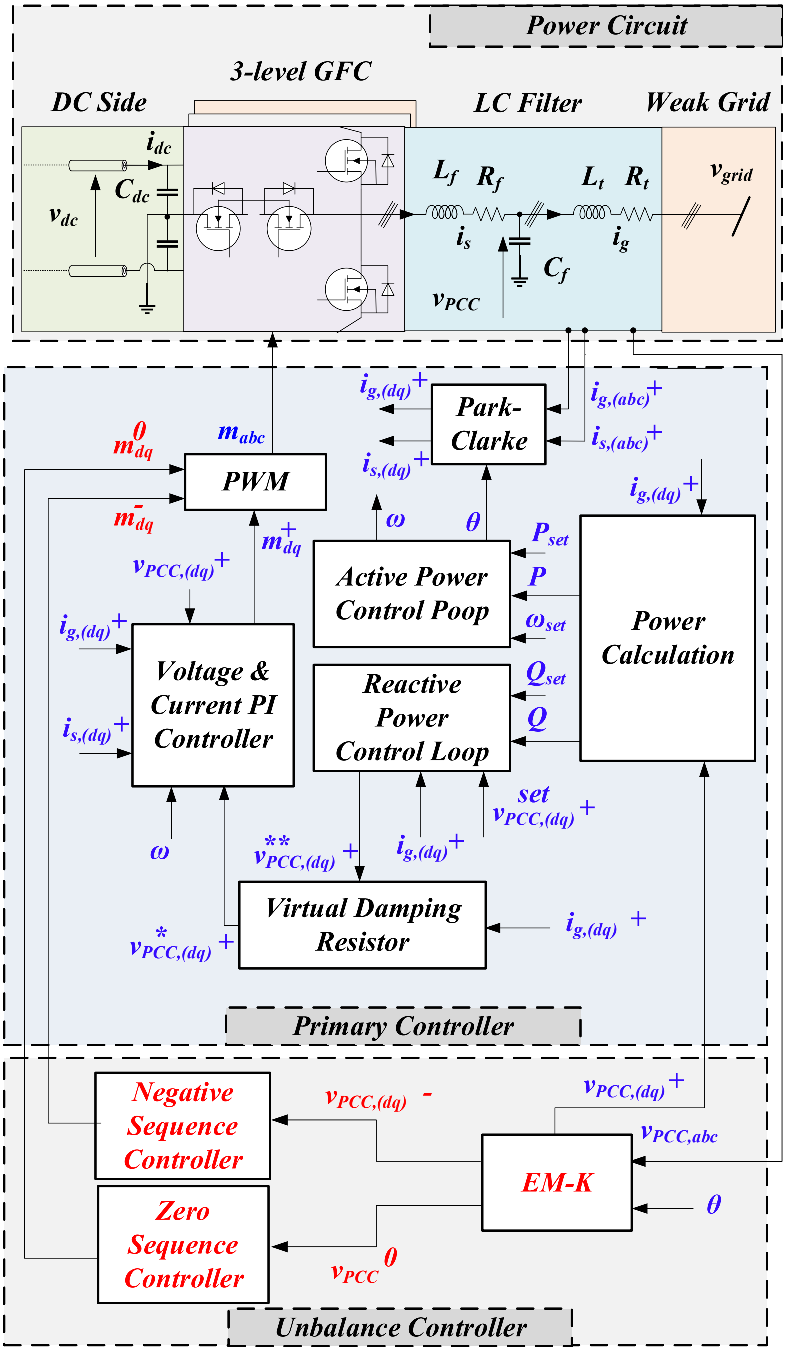


**Figure 6.5:** Complete power circuit and proposed control architecture for voltage unbalance compensation.

## 6.5 Proposed EM–K Decoupling and Unbalance Control Architecture

This section presents the complete formulation of the proposed decoupling and unbalance compensation framework for the grid-forming converter. The method integrates the discrete-time Kalman filter established in Section 3.4 with the Expectation–Maximisation algorithm introduced in Section 3.5 into a unified estimation architecture, referred to as the EM–K method. A time-varying measurement matrix that explicitly encodes the harmonic coupling physics derived in (6.21) and (6.22) enables the Kalman filter to extract clean symmetrical components from the measured PCC voltages. The EM algorithm augments the filter through iterative refinement of the noise covariance matrices, which provides robust adaptation to the variable noise environments encountered during restoration. The decoupled components then feed dedicated negative-sequence and zero-sequence controllers that actively suppress voltage unbalance at the PCC. The power circuit employs a four-wire T-type Neutral-Point-Clamped (NPC) converter connected to the weak grid through a passive LCL filter comprising an inductor $L_f$, resistance $R_f$, and a capacitor $C_f$. The four-wire T-type NPC topology is selected because its accessible neutral points are essential for zero-sequence voltage injection. Moreover, the neutral-point voltage balance of the three-level NPC converter is inherently maintained through the adopted modulation strategy, which ensures equal charge distribution between the DC-link capacitors under normal operating conditions.

The LCL filter is designed such that its resonance frequency is well separated from the operating frequency, which makes resonance excitation unlikely during normal operation. In addition, the resonance is further mitigated through the virtual damping resistor included in the primary controller. This control-based damping emulates resistive behaviour without physical losses and suppresses oscillations around the filter resonance frequency.

Although Kalman filtering has been widely applied for signal estimation in power electronic systems, the proposed method introduces two distinguishing features. First, the measurement matrix is explicitly constructed as a time-varying function $C(\theta_k)$ that embeds the physical second-harmonic coupling between sequence components, rather than treating it as a disturbance. Second, the integration of the Expectation–Maximisation algorithm enables online adaptation of the noise covariance matrices, and allows the estimator to maintain accuracy under varying noise and disturbance conditions typical of restoration scenarios.

### 6.5.1 State-Space Formulation and Measurement Matrix

The EM–K method is formulated within the discrete-time state-space framework of Section 3.4. The state vector at the $k$-th sampling instant contains the five decoupled symmetrical components of the PCC voltage:

$$x_k = \begin{bmatrix} v_d^+ & v_q^+ & v_d^- & v_q^- & v_0 \end{bmatrix}^T \tag{6.23}$$

where $v_d^+$ and $v_q^+$ are the positive-sequence dq components, $v_d^-$ and $v_q^-$ are the negative-sequence dq components, and $v_0$ is the zero-sequence component. Normally, each element (except $v_0$) is a pure DC quantity, which is precisely the form for which PI controllers achieve zero steady-state error.

The state evolution follows the general model in (3.21) with the state transition matrix set to identity, $\mathrm{A} = \mathrm{I}_{5\times5}$. This formulation reflects the physical reality that the voltages and their DC $dq$ quantities change slowly relative to the sampling rate, so the simplest linear prediction of the current state is the previous state itself. The process noise $\mathrm{w}_k \sim \mathcal{N}(0, \beta)$ captures unmodelled dynamics and inter-sample variations, with its covariance $\beta$ adaptively estimated by the EM algorithm rather than fixed a priori.

The measurement vector $\mathrm{y}_k$ comprises the dq0 components obtained from the dual standard Park–Clarke transformation of $v_{\mathrm{PCC},abc}$. The measurement equation follows (3.22), with the observation matrix replaced by a time-varying measurement matrix $\mathrm{C}(\theta_k)$ that constitutes one of the principal contributions of this work. This matrix is derived directly from the harmonic coupling relationships in (6.21) and (6.22):

$$C(\theta_k) = \begin{bmatrix} 1 & 0 & \cos(2\theta_k) & \sin(2\theta_k) & 0 \\ 0 & 1 & -\sin(2\theta_k) & \cos(2\theta_k) & 0 \\ \cos(2\theta_k) & -\sin(2\theta_k) & 1 & 0 & 0 \\ \sin(2\theta_k) & \cos(2\theta_k) & 0 & 1 & 0 \\ 0 & 0 & 0 & 0 & 1 \end{bmatrix} \tag{6.24}$$

where $\theta_k = \omega\, k\, T_s$ is the phase angle at time step k and $T_s$ is the sampling period.

The structure of this matrix encodes the complete second-order harmonic coupling between sequence components. The off-diagonal $2 \times 2$ rotation blocks that contain $\cos(2\theta_k)$ and $\sin(2\theta_k)$ represent the cross-coupling. The upper-right block captures the negative-sequence interference that appears in the positive-sequence measurements, while the lower-left block captures the reciprocal positive-sequence interference in the negative-sequence measurements. The fifth row and column correspond to the zero-sequence component, which remains decoupled from the other two sequences and therefore contains only a unity diagonal.

Although $\mathrm{C}(\theta_k)$ varies with time, the system remains strictly linear in the state variables $\mathbf{x}_k$ at each time instant, because the time variation enters only through the angle $\theta_k$. The proposed approach obtains $\theta_k$ from the active power droop controller.

The Kalman filter prediction and update recursion follows the standard form presented in Section 3.4, equations (3.24)–(3.30), with $\mathrm{A} = \mathrm{I}$ and $\mathrm{C}_k = \mathrm{C}(\theta_k)$. The prediction step simplifies to $\hat{\mathrm{x}}_{k|k-1} = \hat{\mathrm{x}}_{k-1|k-1}$ and $\mathrm{F}_{k|k-1} = \mathrm{F}_{k-1|k-1} + \beta$. The mechanism by which the filter achieves harmonic decoupling operates through the innovation defined in (3.26). Because $\mathrm{C}(\theta_k)$ explicitly encodes the second-order harmonic coupling, the predicted measurement $\mathrm{C}(\theta_k)\hat{\mathrm{x}}_{k|k-1}$ includes the expected harmonic interference based on the current state estimates. The innovation, therefore, isolates only the measurement component that cannot be explained by the known coupling structure, and the Kalman gain in (3.28) distributes this unexplained component across the state variables in proportion to the current uncertainty, as described in Section 3.4.

### 6.5.2 Adaptive Covariance Estimation using EM

The Kalman filter equipped with $\mathrm{C}(\theta_k)$ estimates second-order harmonics and decouples the sequence components, provided that the noise covariance matrices $\beta$ and M are accurately specified. As discussed in Section 3.4, misspecification of these matrices degrades the filter performance, an underestimated $\beta$ causes a slow response to real state changes, while an underestimated $M$ allows too much measurement noise to affect the estimates. In weak grids, both process noise and measurement noise vary over time, and their statistical characteristics cannot be determined in advance.

The EM algorithm established in Section 3.5 is therefore integrated with the Kalman filter to form the complete EM–K framework. The algorithm operates in two alternating steps executed periodically after every N Kalman filter iterations. During the E-step, the filter runs for N consecutive time steps with the current estimates of $\beta$ and M, and the state estimates $\hat{\mathrm{x}}_{k|k}$ and measurement vectors $\mathrm{y}_k$ are accumulated. In the subsequent M-step, the covariance matrices are updated through the closed-form expressions in (3.33) and (3.34), evaluated with $\mathrm{A} = \mathrm{I}$ and $\mathrm{C}_k = \mathrm{C}(\theta_k)$. After each M-step, the accumulated data are reset and the filter resumes operation with the updated covariance matrices.

The window length N governs the trade-off between adaptation speed and estimation accuracy discussed in Section 3.5. For the implementation considered in this work, $N = 10$ is adopted as a practical design choice. Figure 6.6 illustrates the complete EM–K framework and depicts the signal flow from the measured three-phase PCC voltages through the dual Park–Clarke transformations at angles $+\theta$ and $-\theta$, into the Kalman filter prediction and update stages, and through the EM adaptation loop that periodically refines $\beta$ and M.

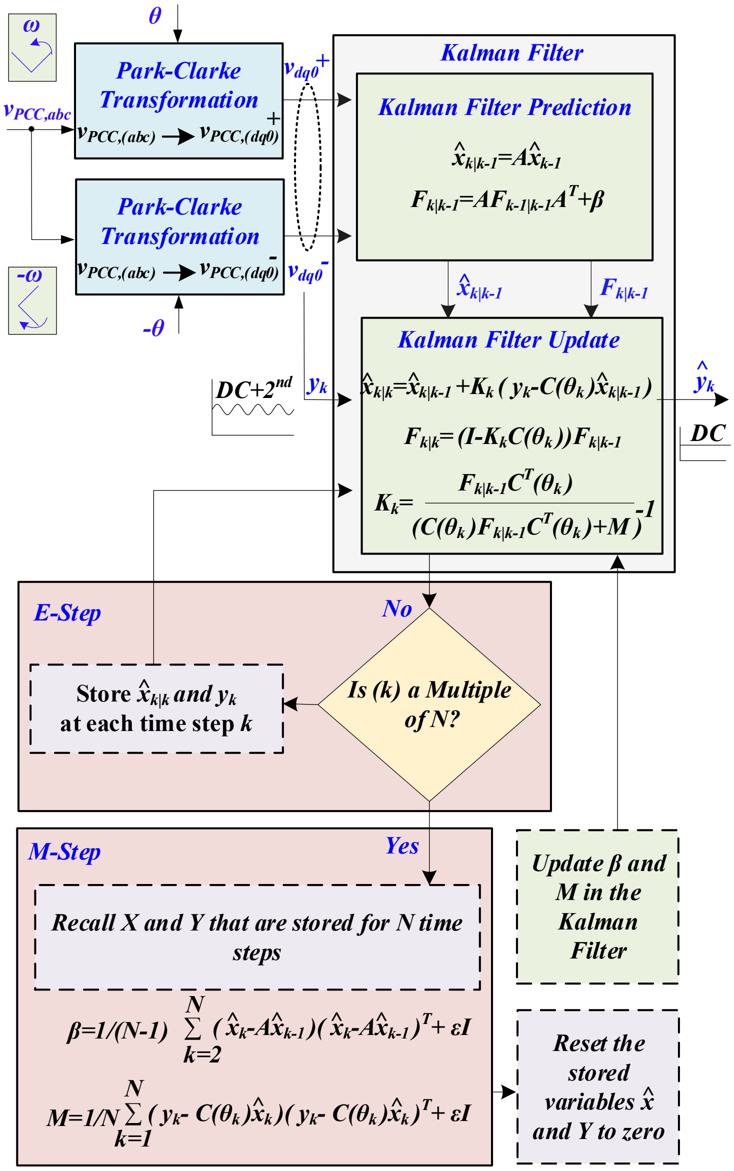


**Figure 6.6:** Framework of the proposed EM-K method.

### 6.5.3 Conventional Primary Controller of GFM

The primary controller, shown in Figure 6.5, regulates the positive-sequence voltage at the PCC and operates entirely within the positive-sequence dq frame, where all quantities appear as DC values after EM–K decoupling. The controller comprises four functional blocks: the active-power and reactive-power droop loops, followed in cascade by the virtual damping and the voltage–current PI controllers. The active power control loop employs a P–$\omega$ droop characteristic to establish the converter's output frequency $\omega$ and phase angle $\theta$ based on the active power deviation. The reactive power control loop uses a Q–V droop characteristic to determine the voltage reference magnitude $v_{\mathrm{PCC},(dq)}^{+**}$. The virtual damping processes this reference and produces the final reference $v_{\mathrm{PCC},(dq)}^{+*}$. Cascaded voltage and current PI controllers then track this reference through feedforward decoupling terms that compensate for dq-axis cross-coupling, and produce the positive-sequence modulation index $m_{abc}^{+}$. Both active and reactive power measurements are computed from the EM–K decoupled positive-sequence components, which ensures that the power calculations are free from second-order harmonic contamination. The phase angle $\theta_k$ generated by the active power loop serves the entire control architecture, which includes the Park–Clarke transformations and the measurement matrix $\mathrm{C}(\theta_k)$.

### 6.5.4 Proposed Negative-Sequence Controller

The negative-sequence controller operates in parallel with the primary controller and constitutes one of the principal contributions of this work. After EM–K decoupling, the negative-sequence dq components $v_{\mathrm{PCC},d}^{-}$ and $v_{\mathrm{PCC},q}^{-}$ appear as pure DC quantities that represent the amplitude and phase of the negative-sequence voltage. The controller drives both components to zero through dedicated PI regulators, as shown in Figure 6.7:

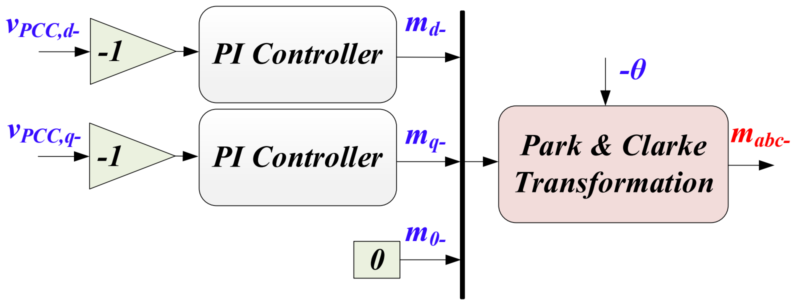


**Figure 6.7:** Proposed negative-sequence controller block diagram.

$$m_{d-} = -\left(k_{p,d-} \cdot v_{PCC,d}^{-} + k_{i,d-} \int v_{PCC,d}^{-} \, dt\right) \tag{6.25}$$

$$m_{q-} = -\left(k_{p,q-} \cdot v_{PCC,q}^{-} + k_{i,q-} \int v_{PCC,q}^{-} \, dt\right) \tag{6.26}$$

where $k_{p,d-} = 0.8$, $k_{i,d-} = 18.6$, $k_{p,q-} = 1.2$, and $k_{i,q-} = 18.6$. The modulation indices are then transformed from the negative-sequence dq frame to the abc frame through the inverse Park–Clarke transformation at angle $-\theta$:

$$m_{abc}^{-} = \mathrm{T}_{dq\rightarrow abc}(-\theta) \begin{bmatrix} m_{d-} \\ m_{q-} \\ m_{0-} \end{bmatrix} \tag{6.27}$$

The resulting three-phase modulation indices command the converter to generate a negative-sequence voltage at the PCC that is equal in magnitude but opposite in phase to the existing negative-sequence component, thereby cancelling it.

The effectiveness of this controller depends critically on the quality of the decoupled signals from the EM–K method. If $v_{\mathrm{PCC},d}^{-}$ and $v_{\mathrm{PCC},q}^{-}$ contained residual second-order harmonic contamination from the positive sequence, the PI controllers would attempt to track the 100 Hz oscillations and introduce distortion into the modulation indices. The clean DC signals provided by the EM–K method, therefore, serve as the essential prerequisite for accurate negative-sequence compensation.

### 6.5.5 Proposed Zero-Sequence Controller

The zero-sequence controller suppresses the zero-sequence voltage that arises in three-phase four-wire configurations, and the NPC topology provides the necessary neutral point access for the required zero-sequence voltage injection. The zero-sequence component presents a distinct challenge compared to the positive and negative sequences. Although the EM–K method produces a clean, noise-filtered estimate of $v_0$, this component remains a sinusoidal waveform at the fundamental frequency because the zero-sequence voltage does not rotate in the dq frame. PI controllers cannot achieve zero steady-state error for sinusoidal references, which necessitates a conversion strategy that transforms the zero-sequence signal into DC form before regulation.

A transport delay strategy accomplishes this conversion through four sequential steps, as shown in Figure 6.8. First, a time delay of exactly one quarter of the fundamental period

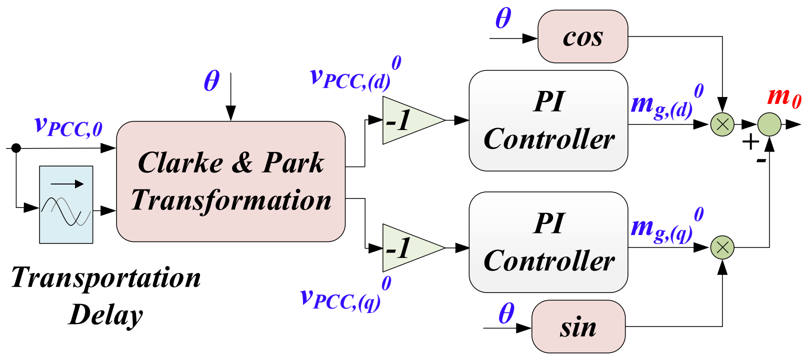


**Figure 6.8:** Proposed zero-sequence controller block diagram.

($T/4 = 5$ ms at 50 Hz) is applied to the EM–K zero-sequence output to create an orthogonal component:

$$v_{PCC,0}^{\perp}(t) = v_{PCC,0}\left(t - \frac{T}{4}\right) = V_0 \cos\left(\omega t + \phi_0\right) \tag{6.28}$$

The original signal $v_{\mathrm{PCC},0} = V_0 \sin(\omega t + \phi_0)$ and its 90°-shifted counterpart $v_{\mathrm{PCC},0}^{\perp}$ together form a quadrature pair analogous to the $\alpha\beta$ components in Clarke's transformation. Second, Park's transformation converts this pair into DC components:

$$\begin{bmatrix} v_{PCC,(d)}^{0} \\ v_{PCC,(q)}^{0} \end{bmatrix} = \begin{bmatrix} \cos\theta & \sin\theta \\ -\sin\theta & \cos\theta \end{bmatrix} \begin{bmatrix} v_{PCC,0} \\ v_{PCC,0}^{\perp} \end{bmatrix} \tag{6.29}$$

The resulting components $v_{\mathrm{PCC},(d)}^{0}$ and $v_{\mathrm{PCC},(q)}^{0}$ are DC quantities that encode the amplitude and phase of the zero-sequence voltage, entirely analogous to the dq representation of the positive and negative sequences. Third, dedicated PI controllers drive these DC components to zero:

$$m_{g,(d)}^{0} = -\left(k_{p,d0} \cdot v_{PCC,(d)}^{0} + k_{i,d0} \int v_{PCC,(d)}^{0}\, dt\right) \tag{6.30}$$

$$m_{g,(q)}^{0} = -\left(k_{p,q0} \cdot v_{PCC,(q)}^{0} + k_{i,q0} \int v_{PCC,(q)}^{0}\, dt\right) \tag{6.31}$$

where $k_{p,d0} = k_{p,q0} = 0.4$ and $k_{i,d0} = k_{i,q0} = 18.6$. Fourth, the modulated signals are transformed back to the time domain to produce the zero-sequence modulation index:

$$m^{0} = m_{g,(d)}^{0} \cos(\theta) - m_{g,(q)}^{0} \sin(\theta) \tag{6.32}$$

This single-phase modulation index shifts the neutral-point voltage without altering the line-to-line voltages, and it is added equally to all three phases.

The three modulation components generated by the primary controller and the unbalance controllers combine in the abc frame to produce the total modulation command for the converter:

$$m_{abc} = m_{abc}^{+} + m_{abc}^{-} + m^{0} \cdot \begin{bmatrix} 1 \\ 1 \\ 1 \end{bmatrix} \tag{6.33}$$

The combined modulation index $m_{abc}$ feeds the sinusoidal pulse-width modulation stage, which generates the switching signals for the converter.

## 6.6 Stability Analysis Using the Proposed Parameter-Swept Prony-Based Method

The preceding sections established the EM–K decoupling method and the complete control architecture comprising the primary controller, the negative-sequence controller, and the zero-sequence controller. Before validating this architecture experimentally, it is essential to assess whether the closed-loop system remains stable across the full range of operating conditions it is designed to accommodate, particularly as the voltage unbalance factor increases from mild to severe levels. This section introduces a novel data-driven stability assessment framework that systematically applies the classical Prony analysis of Section 3.6 across a dense grid of operating conditions parameterised by the grid unbalance factor. The proposed framework treats the entire grid-forming converter system, including the EM–K adaptive algorithm, as a black box and extracts stability information directly from the time-domain PCC voltage waveforms. This approach circumvents the fundamental limitations of conventional analytical stability methods when applied to systems containing adaptive, nonlinear, and time-varying components.

### 6.6.1 Motivation for a Data-Driven Stability Framework

The stability analysis of power electronic converters connected to weak grids has traditionally relied on linearisation-based small-signal analysis, full-state eigenvalue analysis, and Lyapunov-based energy methods. Each approach encounters specific limitations when applied to the proposed control architecture.

Linearisation-based methods construct a small-signal model around a specific operating point and examine the eigenvalues of the resulting state matrix to determine local stability. This approach is effective for conventional controllers with fixed parameters, but is fundamentally incompatible with the proposed EM–K framework shown in Figure 6.6. The process noise covariance $\beta$ and measurement noise covariance M are iteratively updated by the EM algorithm at runtime as described in Section 3.5. Each update modifies the effective Kalman gain computed in (3.28) and alters the closed-loop dynamics. A linearised model captured at one instant, therefore, becomes invalid after the next EM update cycle.

Full-state eigenvalue analysis examines the complete state matrix of the system. However, the proposed architecture contains a substantial number of states distributed across the primary controller of Figure 6.5, the unbalance controllers of Figure 6.7 and Figure 6.8, the EM–K estimator of Figure 6.6, and the physical plant. Combined with the time-varying Kalman gain updated at each EM cycle, this high state dimensionality renders full-state eigenvalue analysis impractical, because the state matrix must be reconstructed and factorised after every adaptation step.

Lyapunov-based methods require a closed-form state-space model and an appropriate energy function. The recursive and data-dependent nature of the EM algorithm violates the assumption of a fixed state-space model and renders Lyapunov analysis inapplicable without significant simplifications.

In contrast, the Prony method introduced in Section 3.6 operates directly on the simulated time-domain output of the nonlinear system and decomposes it into a sum of complex exponential modes as expressed in (3.35). Each mode is characterised by a complex pole whose real part indicates damping and whose imaginary part identifies oscillation frequency. The continuous-time parameters are recovered through (3.37). Because the method operates on the observed waveform rather than on an analytical model, it captures the net effect of nonlinearities, adaptive behaviours, and time-varying dynamics to the extent that they are observable in the output signal and can be approximated by damped exponential modes. The classical Prony method, however, provides accurate modal information only near a specific operating point. To overcome this limitation, this work proposes a parameter-swept Prony method that systematically applies the Prony decomposition across a dense grid of operating points parameterised by the grid unbalance factor D. This enables stability assessment over a broad and continuously varying operational range. The conceptual diagram of the proposed method is presented in Figure 6.9.

### 6.6.2 Proposed Parameter-Swept Prony Method

The proposed parameter-swept Prony method extends the classical single-point Prony analysis of Section 3.6 into a systematic, iterative framework that evaluates stability across a continuously varying range of operating conditions. The method consists of the following procedural steps, illustrated in Figure 6.9.

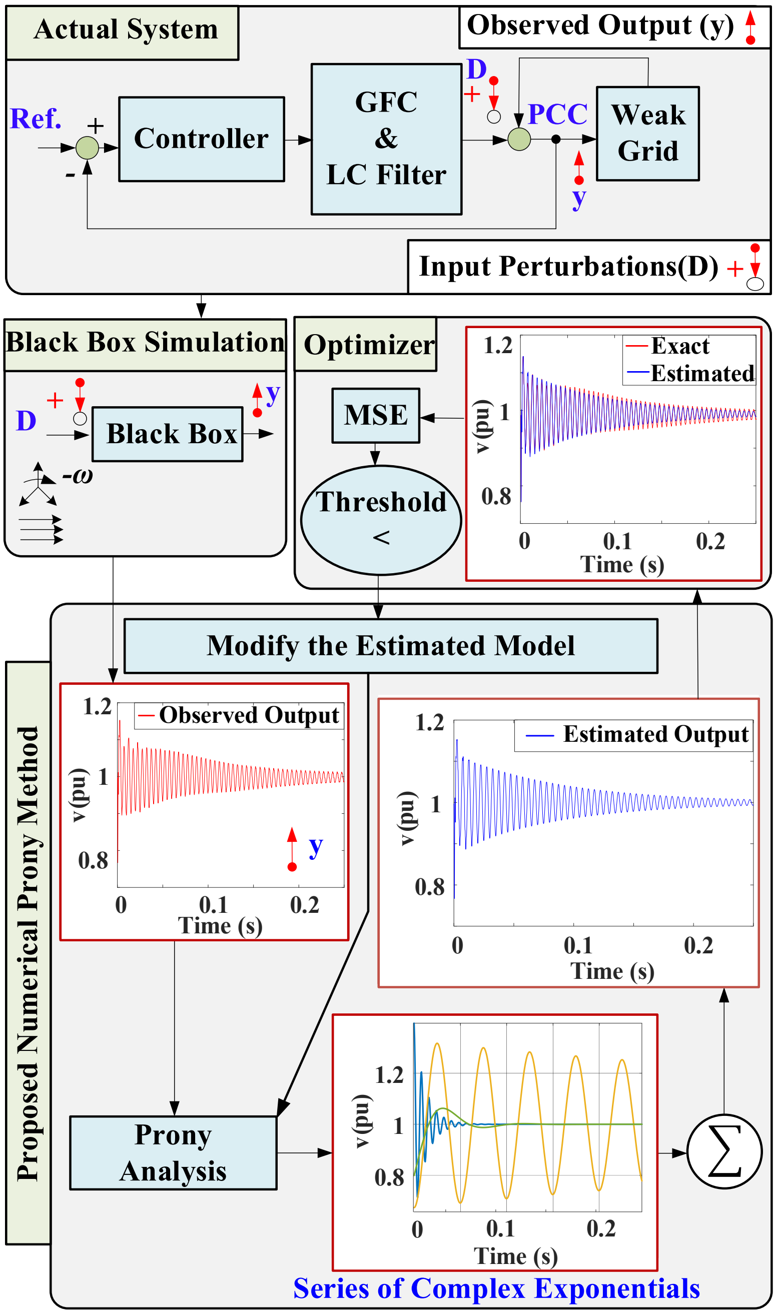


**Figure 6.9:** Conceptual diagram of the proposed parameter-swept Prony method for stability analysis.

- **Step 1 (Black-box simulation):** The complete system, comprising the power circuit (converter, LC filter, and weak grid), the primary controller, the negative-sequence and zero-sequence unbalance controllers, and the EM–K decoupling algorithm, is modelled in a simulation environment and treated as a black box. The PCC voltage $v_{\mathrm{PCC}}(t)$ is designated as the observed output y(t). The grid unbalance, quantified by the negative-sequence unbalance factor $\mathrm{UBF}_2\%$ and the zero-sequence unbalance factor $\mathrm{UBF}_0\%$, constitutes the input perturbation D. For each discrete value of D, the system is simulated, and the output signal y(t) is recorded over an observation window sufficient to capture the full response.
- **Step 2 (Prony decomposition):** The recorded output signal y(t) is decomposed into a sum of n complex exponential modes using the Prony algorithm as expressed in (3.35). The damped exponential signal model represents each sample as $y[k] = \sum_{i=1}^{n} H_i\ z_i^k$, where $H_i$ is the complex residue and $z_i$ is the discrete-time eigenvalue from which the continuous-time pole $\lambda_i = \sigma_i + j\omega_i$ is recovered through (3.37). The initial model order n is selected as a moderate value and subsequently refined through an iterative optimisation process.
- **Step 3 (Accuracy verification and order optimisation):** The mean square error between the Prony-estimated signal $\hat{y}(t)$ and the actual observed output y(t) is computed:

$$\mathrm{MSE} = \frac{1}{N_s}\sum_{k=1}^{N_s}[y(kT_s) - \hat{y}(kT_s)]^2 \tag{6.34}$$

  where $N_s$ is the number of samples. If the MSE exceeds a predefined threshold of $10^{-4}$, the iterative wrapper increases the model order n, that is, the number of complex exponential modes, and repeats the decomposition. This iterative process continues until the MSE falls below the threshold, which ensures that the decomposition captures the system's dynamic behaviour with high fidelity.

- **Step 4 (Dominant mode identification and pole extraction):** From the converged Prony decomposition, the dominant modes are identified based on the magnitude of their residues $|H_i|$. Modes with negligible residues contribute minimally to the overall signal and are discarded. The complex poles $\lambda_i$ of the dominant modes are retained as the stability-relevant eigenvalues of the system at the operating point corresponding to the current value of D. The stability criterion follows directly from Section 3.6, if $\sigma_i < 0$ for all dominant modes, the system is stable at that operating point; if $\sigma_i > 0$ for any mode, the system is unstable. The damping ratio $\zeta_i$ defined in (3.38) quantifies the rate of modal decay relative to the oscillation frequency. This analysis assumes that all stability-critical modes are observable in the PCC voltage; modes that are weakly excited or weakly observable in $v_{PCC}$ may not appear in the decomposition.

- **Step 5 (Pole locus construction):** Steps 1 through 4 are repeated for each operating point across the discretised range of D, and the extracted dominant poles are plotted in the complex plane, parameterised by D. The resulting pole locus provides a comprehensive visualisation of how the system's stability characteristics evolve as the grid unbalance increases.

While the Prony method extracts modal information from local time-domain responses, the proposed parameter-swept framework evaluates stability over a wide range of operating conditions. By systematically sweeping the operating space, the method provides a practical approximation of global stability and ensures that no unstable regions exist within the investigated range.

### 6.6.3 Stability Results and Interpretation

The proposed parameter-swept Prony method is applied to assess the stability of the complete GFM control architecture of Figure 6.5. Two analyses are performed. The first examines the Prony-extracted pole locus to verify closed-loop stability across the full range of unbalance conditions. The second evaluates the dynamic compliance of the PCC voltage unbalance factor with the GB Grid Code requirement.

The first analysis, shown in Figure 6.10, plots the eigenvalue locus for the whole system. Both $UBF_2\%$ and $UBF_0\%$ are simultaneously increased from 2.5% to 25%, which represents a severe combined unbalance scenario. All dominant poles remain firmly in the left half-plane, which confirms dominant mode stability even under severe unbalance. As the unbalance level increases, the dominant poles progressively migrate toward the imaginary axis which indicates a gradual reduction in damping margin. However, even at the extreme condition of 25% unbalance factor, all poles remain well within the stable region.

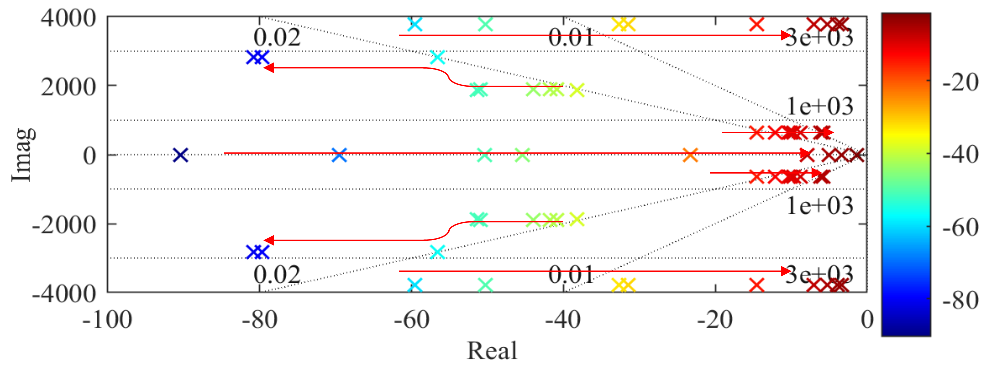


**Figure 6.10:** Principal eigenvalues of the proposed GFM controller when both $UBF_2\%$ and $UBF_0\%$ are increased from 2.5% to 25%.

Beyond the eigenvalue analysis, the dynamic compliance of the proposed controller with the GB Grid Code requirement CC.6.1.5(b) is evaluated in Figure 6.11, which stipulates that the voltage unbalance factor at the PCC shall not exceed 2%. The analysis compares three scenarios across a range of grid-side unbalance levels from 2.5% to 25%. The first scenario represents the permissible limit, shown as a constant green reference surface corresponding to the 2% UBF threshold specified by the grid code. The second scenario, shown as a red surface, represents the conventional GFM controller operating without the proposed unbalance controller. In this case the UBF at the PCC remains equal to the grid-imposed UBF, as the primary controller has no mechanism to suppress the negative-sequence voltage, and the red surface therefore lies at or above the green threshold for all grid unbalance levels exceeding 2%.

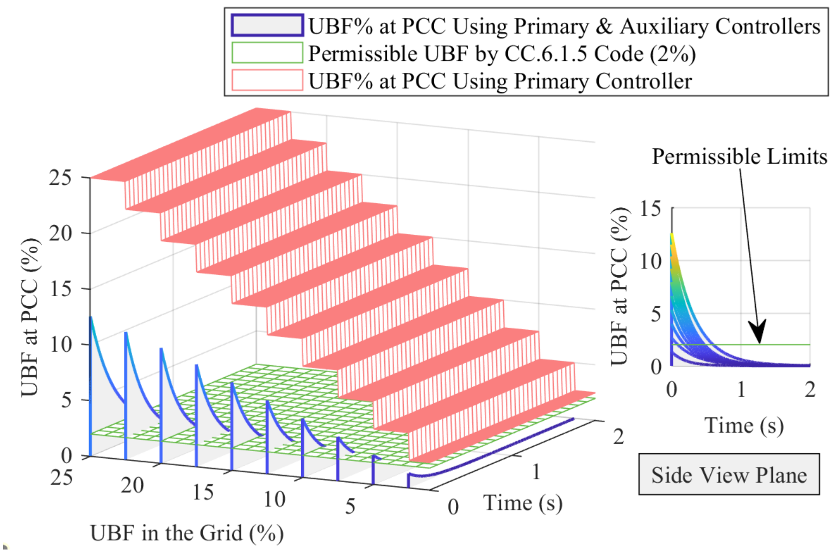


**Figure 6.11:** Performance analysis of the primary (conventional) GFM controller with and without the proposed unbalance controller support under varying $UBF\%$.

The third scenario, shown as grey surfaces, represents the primary controller operating alongside the proposed unbalance controller. In this case the UBF at the PCC is initially reduced to approximately half of the grid-imposed value and is subsequently driven below the 2% permissible limit within 0.45 seconds. This rapid suppression is achieved through the proposed suppression controllers and the clean decoupled signals provided by the EM–K method, which ensure that the PI controllers operate on accurate, sequence-decoupled feedback.

## 6.7 Validation Results of the Proposed EM–K Decoupling and Unbalance Controller

This section validates the EM–K decoupling method and the complete unbalance controller through simulation and hardware experiments on the platform described below.

The hardware platform is a 10 kVA T-Type NPC four-wire converter development kit shown in Figure 6.12. The NPC topology is a deliberate choice because its DC-bus midpoint provides the physical current return path necessary for zero-sequence voltage injection. The laboratory configuration comprises the AC grid, controllable unbalance resistor, GFM development kit with its TMS320F28379D DSP controller, graphical user interface, and oscilloscope for waveform acquisition. The entire control algorithm includes a primary controller, unbalance controllers, EM–K decoupling, Park–Clarke transformations, and SPWM modulator, executed on the DSP at 200 MHz.

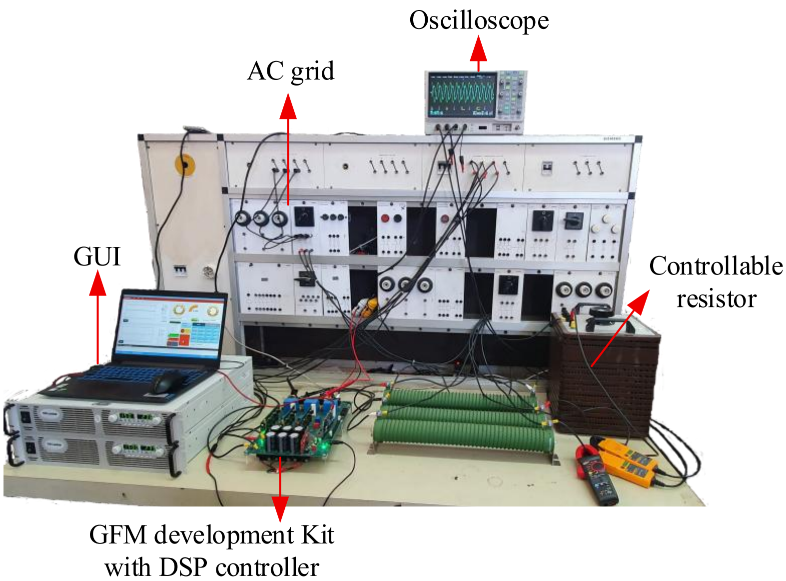


**Figure 6.12:** Experimental laboratory setup of the 10 kVA NPC converter platform.

The grid operates at 380 V line-to-line and 50 Hz, with passive filter parameters listed in Table 6.1. The voltage sensors exhibit approximately 100 dB signal-to-noise ratio. To introduce and control system unbalance, one of the phases is connected to a controllable 22-ohm resistor, either in series or between phases.

**Table 6.1:** Experimental Setup Parameters.

| Parameter | **Value** |
|---|---|
| Converter-side inductance L1 | 349 µH |
| Grid-side inductance L2 | 0.316 µH |
| Filter capacitance Cf | 10 µF |
| Switching frequency | Platform range: 5–50 kHz |
| Rated DC link voltage | Platform range: 800–1000 V |

### 6.7.1 Simulation Validation of the EM–K Method

The EM–K decoupling method and its comparative performance against the DDSRF are first validated through Simulink simulation, which permits precise control over noise injection independently of hardware constraints.

The decoupling capability is assessed through introduction of $UBF_2 = 5\%$ at $t = 1$ s while the positive- and negative-sequence dq-frame components are observed with and without the EM–K decoupling active. Figure 6.13 presents the positive-sequence results. During balanced operation before t = 1 s, all traces exhibit DC behaviour, though conventional extraction without EM–K shows visible measurement noise whereas the EM–K traces are

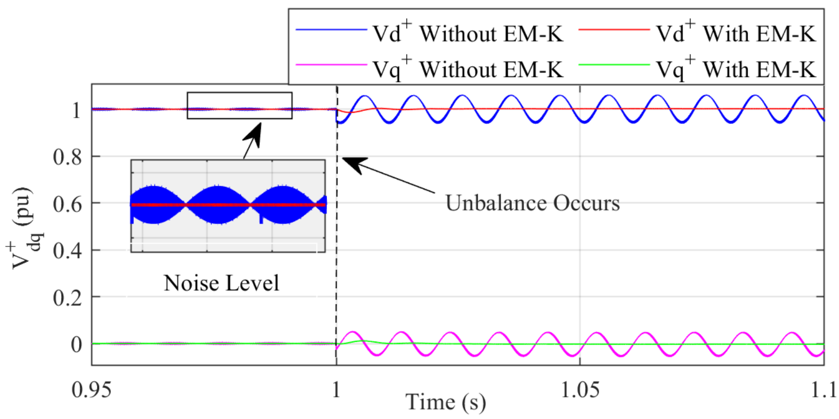


**Figure 6.13:** Positive-sequence $dq$-frame components of $v_{\mathrm{PCC}}$ with and without the EM–K method, under $UBF_2 = 5\%$.

significantly smoother. After $t = 1$ s, the positive-sequence components without EM–K develop second-harmonic oscillations at 100 Hz with a peak-to-peak magnitude of approximately 10% of the DC value, which corresponds exactly to the negative-sequence coupling amplitude. The EM–K traces remain pure DC because the Kalman filter, equipped with the time-varying measurement matrix $\mathbf{C}(\theta_k)$ defined in (6.24), attributes the 100 Hz content to the negative-sequence states and removes it from the positive-sequence estimate.

Figure 6.14 shows the complementary negative-sequence results. Without EM–K, $Vd^-$ and $Vq^-$ oscillate symmetrically between approximately −1.0 and +1.0 pu around their true DC values. With EM–K active, these oscillations vanish, and the traces settle to clean DC values that represent the true negative-sequence dq components.

The EM–K method is then benchmarked against the DDSRF through a three-stage simulation, namely, balanced operation before $t = 1$ s, introduction of $UBF_2 = 20\%$ at $t = 1$ s, and a measurement noise at t = 1.5 s. Figure 6.15 and Figure 6.16 present the positive- and negative-sequence dq components for both methods. During balanced operation, both methods achieve comparable steady-state tracking. After the 20% unbalance at t = 1 s, the EM–K method attains a lower maximum overshoot and faster stabilisation. At $t = 1.5$ s the performance divergence intensifies, the EM–K method substantially suppresses the noise to produce near-pure DC extraction, whereas the DDSRF retains residual noise content in both sequences. This superiority stems from the adaptive noise covariance estimation of the EM

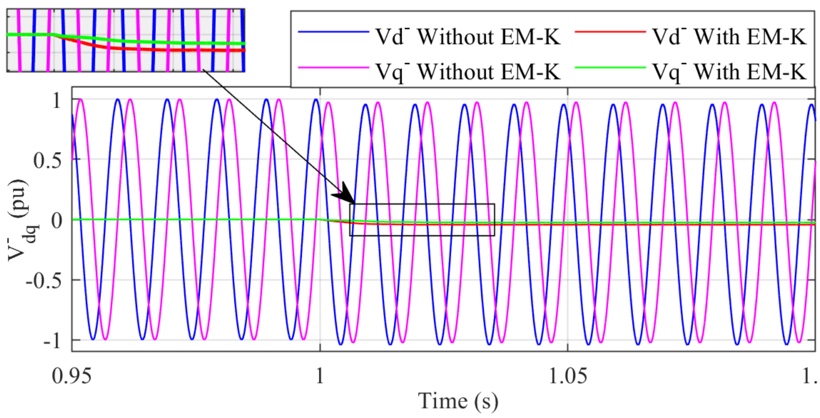


**Figure 6.14:** Negative-sequence $dq$-frame components of $v_{\mathrm{PCC}}$ with and without the EM–K method, under $UBF_2 = 5\%$.

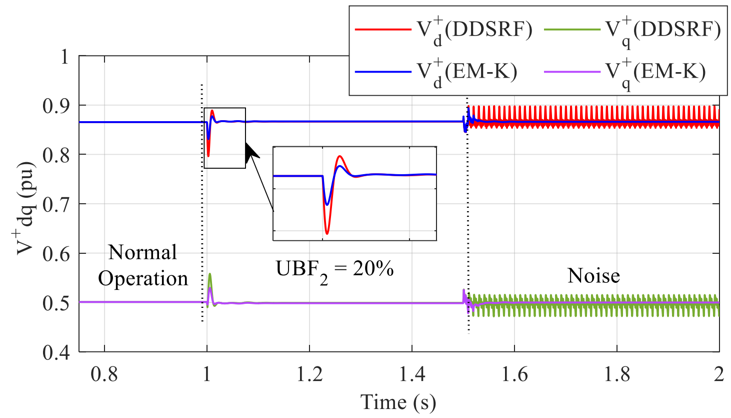


**Figure 6.15:** Positive-sequence $dq$-frame components for EM-K and DDSRF methods under various grid conditions.

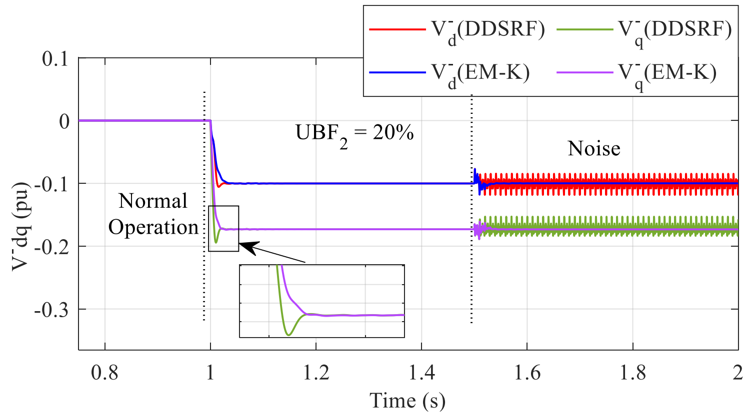


**Figure 6.16:** Negative-sequence $dq$-frame components for EM-K and DDSRF methods under various grid conditions.

algorithm, expressed through the closed-form updates in (3.33) and (3.34), which enables dynamic adjustment to deteriorated signal conditions characteristic of weak grids.

### 6.7.2 Experimental Validation of Unbalance Compensation

The hardware experiments validate the complete unbalance controller on the 10 kVA NPC platform under two four-wire conditions, namely, combined negative- and zero-sequence compensation at ($UBF_2$ = 12.5%, $UBF_0$ = 6%) and ($UBF_2$ = 2.5%, $UBF_0$ = 2.5%). Each condition is examined with and without the proposed controller.

Figure 6.17 and Figure 6.18 present the four-wire baseline with only the primary controller active. Under $UBF_2$ = 12.5% and $UBF_0$ = 6%, the three-phase PCC voltage in Figure 6.17(a) exhibits both amplitude unbalance and a common-mode shift after t = 1 s, while the corresponding normalised RMS values in Figure 6.17(b) diverge and oscillate continuously above the 2% threshold stipulated by GB Grid Code CC.6.1.5(b). The mild case ($UBF_2$ =

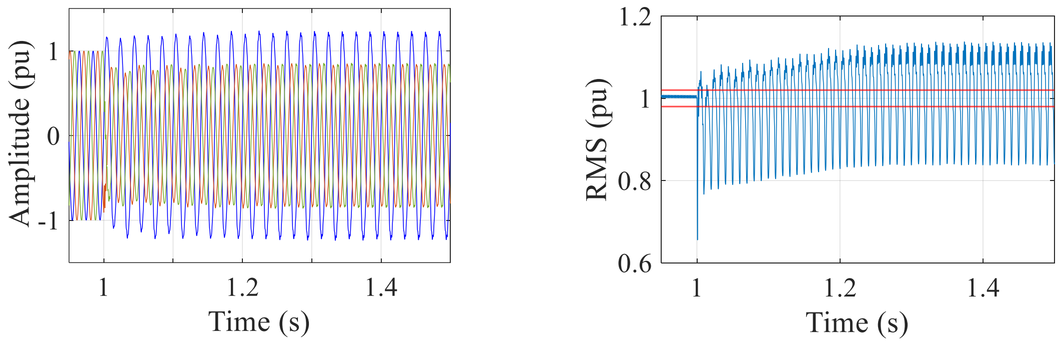


(a) (b)

**Figure 6.17:** Four-wire experimental results under $UBF_2 = 12.5\%, UBF_0 = 6\%$ without the unbalance controller: (a) three-phase $v_{PCC}$, (b) RMS value.

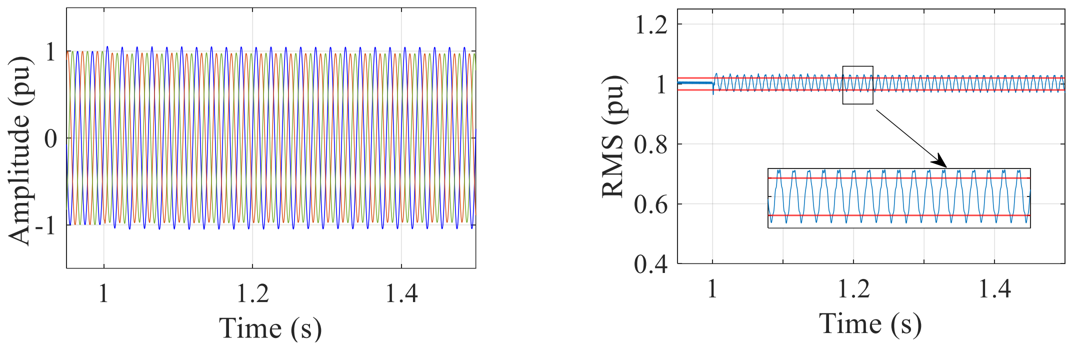


(a) (b)

**Figure 6.18:** Four-wire experimental results under $UBF_2 = 2.5\%, UBF_0 = 2.5\%$ without the unbalance controller: (a) three-phase $v_{PCC}$, (b) RMS value.

2.5%, $UBF_0 = 2.5\%$) in Figure 6.18 shows a small but persistent unbalance in both the three-phase waveform and the RMS profile, with marginal grid code violation and no tendency toward correction. These baseline experiments establish that the conventional GFM primary controller lacks the control degrees of freedom to compensate for combined negative- and zero-sequence voltage unbalance at any severity level.

Activation of the proposed controller produces consistent recovery across both conditions. Under $UBF_2 = 12.5\%$ and $UBF_0 = 6\%$, the three-phase PCC voltage in Figure 6.19(a) converges to balanced amplitudes within 0.2 s, and the normalised RMS values in Figure 6.19(b) returns below the permissible limit through a smooth, well-damped transient. The mild combined case in

Figure 6.20 confirms equivalently successful performance in both the three-phase waveform and the RMS response within the same timeframe. The recovery under both conditions, with no observable adverse interaction between negative-sequence and zero-sequence loops,

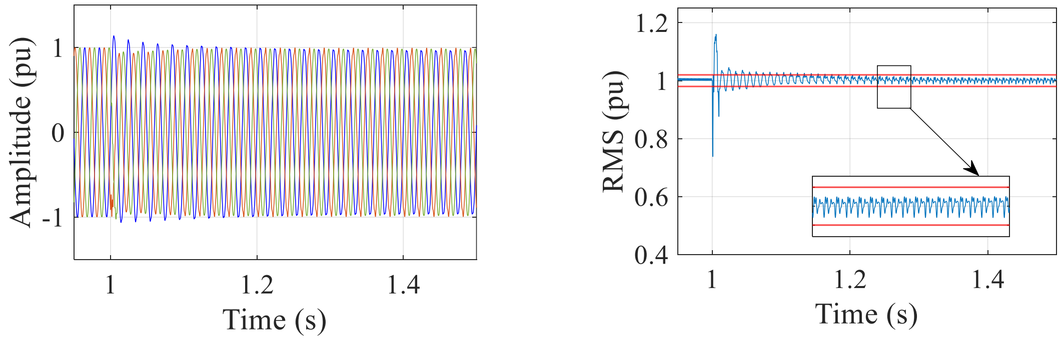


(a) (b)

**Figure 6.19:** Four-wire experimental results under $UBF_2 = 12.5\%, UBF_0 = 6\%$ with the unbalance controller: (a) three-phase $v_{PCC}$, (b) RMS value.

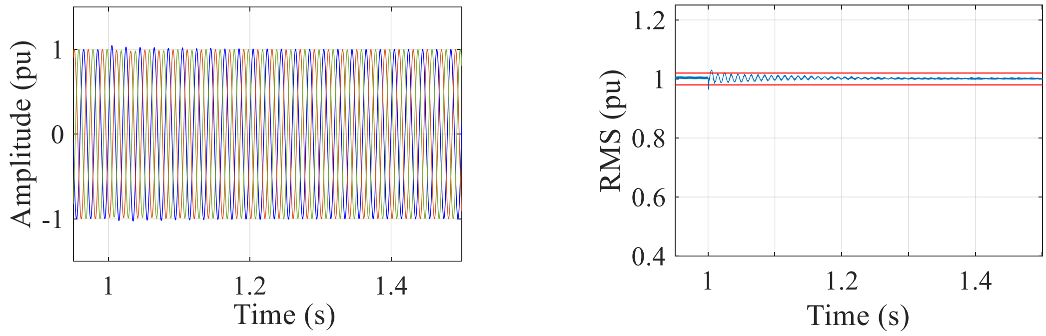


(a) (b)

**Figure 6.20:** Four-wire experimental results under $UBF_2 = 2.5\%, UBF_0 = 2.5\%$ with the unbalance controller: (a) three-phase $v_{PCC}$, (b) RMS value.

validates the modal decoupling achieved by the EM–K method and confirms full compliance with GB Grid Code CC.6.1.5(b) across the entire investigated range.

## 6.8 Summary

This chapter developed two complementary control methods for grid-forming converters in low-inertia systems, namely, a fractional-order damping feedforward loop for transient stability enhancement and an EM–K-based unbalance controller for voltage quality regulation. Both methods are designed as modular augmentations that do not modify the primary control loop.

The fractional-order damping is embedded in the primary control loop, while the unbalance controllers operate in parallel on the extracted sequence components. These control actions are applied simultaneously without any switching mechanism. The damping term improves transient response, whereas the unbalance controllers regulate sequence components independently.

The fractional-order damping method addresses the transient frequency deviation between the converter internal frequency and the grid frequency during rapid transients through application of a fractional derivative of tuneable order $\alpha \in (0, 1)$ to the active power deviation. The tunable fractional order $\alpha$ introduces an extra degree of freedom for reshaping the transient dynamics beyond what is achievable with conventional methods. Simulation results demonstrated 57.5% overshoot reduction and settling time reduction of up to 28.2% during step-load disturbances. Phase portrait analysis confirmed that the method modifies only the transient trajectory while the system converges to the identical equilibrium point as the conventional droop controller.

The EM–K method constructs a time-varying measurement matrix $C(\theta_k)$ that encodes the second-harmonic coupling between positive and negative sequences. The integrated EM algorithm refines process and measurement noise covariances online, which enables robust adaptation to variable noise environments characteristic of weak grids. Simulink validation confirmed substantial suppression of second-harmonic coupling and demonstrated clear superiority over the DDSRF. Hardware experiments on the 10 kVA NPC platform validated restoration of grid code compliance ($UBF_2$< 2% per CC.6.1.5(b)) and reduced $UBF_2$% from 12.5% to below 2% within 0.2 s.

Within the broader thesis framework, the damping method enables larger discrete load reconnection steps during black-start restoration, while the unbalance controller ensures continuous voltage quality as asymmetric loads are reconnected. Together with the inertia estimation and frequency estimation methods of Chapter 4 and Chapter 5, respectively, these contributions complete the measurement-and-control foundation for the restoration optimisation framework developed in Chapter 7.

# Chapter 7 Optimal Black-Start Restoration of Low-Inertia Distribution Networks

The preceding chapters of this thesis have developed estimation and control methods for converter-dominated power systems. Chapter 4 presented an online inertia estimation method. Chapter 5 presented a frequency estimation method. Chapter 6 presented a fractional-order damping (FOD) controller and a voltage unbalance controller for grid-forming converters. Each method has been validated independently through simulations and experimental tests. However, an important question remains unanswered, namely, how do these converter-level methods translate into quantifiable benefits at the system operation level? This chapter answers that question and bridges the gap between converter-level methods and system-level operation by introducing four confidence factors that translate the accuracy and performance of the methods developed in Chapter 4–Chapter 6 into constraint parameters of the restoration optimiser.

The remainder of this chapter is organised as follows. Section 7.1 describes the test system for black-start, including the network topology, distributed generator parameters, and load data. Section 7.2 formulates the optimal black-start restoration problem as a mixed-integer linear programme, and defines the objective function and all constraints with their embedded confidence factors. Section 7.3 presents and compares the restoration results for two scenarios, namely, a baseline scenario using conventional estimation and control methods, and a proposed scenario using the methods of Chapter 4–Chapter 6.

## 7.1 Test System Description

The formulation developed in this chapter is applied to a standalone active distribution network (ADN). This section describes the network topology, generator and load data, customer damage functions, and key system settings. The complete branch impedance data and individual load data are tabulated in Appendix A.

### 7.1.1 Network Topology

ADN is a modified IEEE 33-bus radial distribution system. The single-line diagram is shown in Figure 7.1. The network contains 33 buses numbered 0 to 32, connected by 32 normally

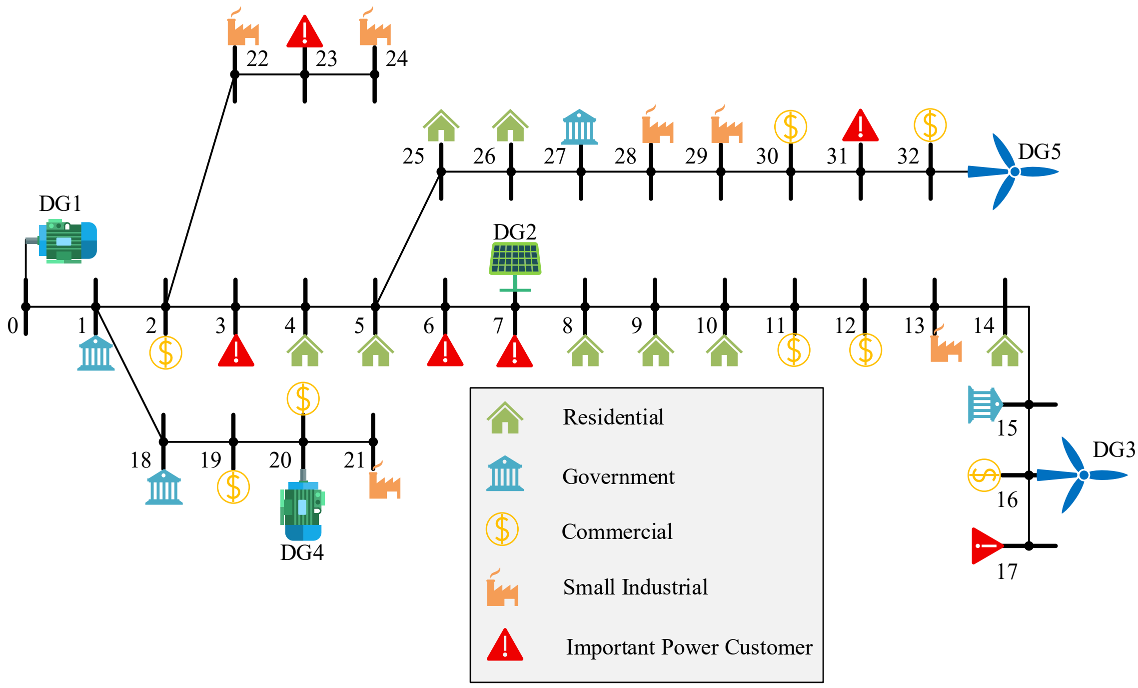


**Figure 7.1:** Single-line diagram of the ADN test system. The network is a modified IEEE 33-bus radial distribution system [70].

closed branches. Bus 0 serves as the root node and the location of the designated black-start generator. The base voltage is 12.66 kV, and the base apparent power is 10 MVA [70].

The network comprises a main feeder and three lateral feeders. The main feeder spans buses 0–1–2–3–4–5–6–7–8–9–10–11–12–13–14–15–16–17. The first lateral departs from bus 1 and extends through buses 18–19–20–21. The second lateral departs from bus 2 and extends through buses 22–23–24. The third lateral departs from bus 5 and extends through buses 25–26–27–28–29–30–31–32. The radial constraint is maintained throughout the restoration horizon. The complete branch data including resistance, reactance, and thermal ratings are listed in Table A.1 of Appendix A.

### 7.1.2 Distributed Generators

Five distributed generators supply the network. Their parameters are listed in Table 7.1. Each generator is interfaced to the network through a power electronic converter. Two converter control modes are employed, namely, grid-forming (GFM) and grid-following (GFL). Grid-forming converters establish an independent voltage and frequency reference using droop control, which enables autonomous island operation. Grid-following converters synchronise to an existing voltage and frequency reference through a PLL and therefore cannot operate until a GFM unit has established the reference on their section of the network.

**Table 7.1:** Distributed generator parameters for ADN [70].

| DG | Bus | Prime mover | Control | Black-start capability | $P_g^{\max}$ (MW) | $Q_g^{\max}$ (Mvar) | $Q_g^{\min}$ (Mvar) | $P_g^{\text{start}}$ (MW) | $t_g^{\text{DG}}$ (min) | $R_g$ (MW/min) | $K_g$ (MW/Hz) | $H_g$ (s) |
|---|---|---|---|---|---|---|---|---|---|---|---|---|
| **DG1** | 0 | Microturbine | GFM | Yes | 6.0 | 4.5 | -1.2 | 0 | 2 | 2.0 | 2.00 | 4.0 |
| **DG2** | 7 | Photovoltaic | GFL | No | 4.5 | 1.2 | -0.5 | 0.12 | 2 | 0.9 | 0.45 | 0 |
| **DG3** | 16 | Wind power (Type 3) | GFL | No | 3.5 | 1.0 | -0.4 | 0.10 | 1 | 0.7 | 0.40 | 3.0 |
| **DG4** | 20 | Microturbine | GFL | No | 7.0 | 4.0 | -1.5 | 0.20 | 4 | 2.0 | 2.00 | 4.5 |
| **DG5** | 32 | Wind power (Type 3) | GFM | No | 8.0 | 3.0 | -1.0 | 0.20 | 2 | 1.6 | 1.80 | 5.0 |

$P_g^{\max}$ is the maximum active-power capacity.

$Q_g^{\max}$ and $Q_g^{\min}$ are the maximum and minimum reactive-power limits.

$P_g^{\text{start}}$ is the minimum power required to start the unit.

$t_g^{\text{DG}}$ is the start-up time, $R_g$ is the ramp rate, $K_g$ is the frequency droop coefficient, and $H_g$ is the inertia constant.

It is important to note that the grid-forming control mode and black-start capability are two independent properties. A GFM converter can regulate voltage and frequency once it is energised; however, it cannot self-start if its prime mover depends on an external power supply for initial energisation. In this network, DG1 is the only unit that possesses both grid-forming control and black-start capability, because its microturbine prime mover can self-start without an external supply. DG5 operates in grid-forming mode but lacks black-start capability because its wind turbine prime mover requires an external supply to initiate operation. Once DG5 is energised through the restoration sequence, it contributes to voltage and frequency regulation as a grid-forming unit. The remaining three generators, DG2, DG3, and DG4, operate in grid-following mode and require an established voltage and frequency reference before they can synchronise and inject power.

### 7.1.3 Load Modelling and Customer Sectors

The network serves 32 loads located at buses 1 through 32. Bus 0 carries no load. The individual load demands are listed in Table A.2 of Appendix A. Each load is assigned to one of five customer sectors according to Table 7.2. The sector classification determines the customer damage function that applies to each load.

The customer damage function (CDF) $f_s^{\mathrm{CDF}}(\cdot)$ quantifies the economic cost of a supply interruption in \$/kW as a function of the interruption duration in minutes for each customer sector $s \in \mathcal{S} = \{1,2,\dots,5\}$. As illustrated in Figure 7.2, the CDF is specified by a set of breakpoints $(t_i, f_{s,i})$, where $t_i$ is the $i$-th duration sample point and $f_{s,i}$ is the corresponding outage cost. The breakpoint values used in this work are listed in Table 7.3 at five durations, namely 0, 1, 20, 60, and 120 minutes. Between breakpoints, the CDF is obtained by linear interpolation:

**Table 7.2:** Customer sector classification for ADN.

| Sector | Description | Bus numbers |
|---|---|---|
| **1** | Residential | 4, 5, 8, 9, 10, 14, 25, 26 |
| **2** | Governmental | 1, 15, 18, 27 |
| **3** | Commercial | 2, 11, 12, 16, 19, 20, 30, 32 |
| **4** | Small industrial | 13, 21, 22, 24, 28, 29 |
| **5** | Important power customer | 3, 6, 7, 17, 23, 31 |

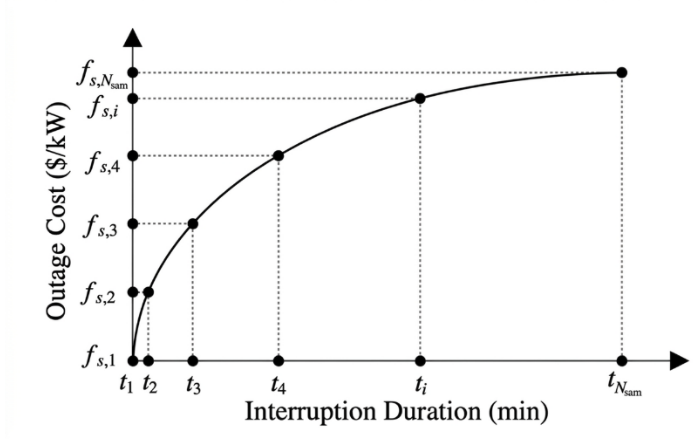


**Figure 7.2:** Linearisation of customer damage function [70].

**Table 7.3:** Sector customer damage function values in $/kW.

| Sector | 0 min | 1 min | 20 min | 60 min | 120 min |
|---|---|---|---|---|---|
| **Residential** | 0.000 | 0.004 | 0.208 | 0.747 | 1.557 |
| **Governmental** | 0.000 | 1.748 | 3.076 | 7.213 | 9.201 |
| **Commercial** | 1.371 | 1.412 | 5.386 | 14.746 | 28.787 |
| **Small industrial** | 8.516 | 8.958 | 19.759 | 34.976 | 57.802 |
| **Important power customer** | 16.703 | 75.920 | 175.677 | 229.696 | 285.163 |

$$f_s^{\mathrm{CDF}}(t) = f_{s,i} + \frac{f_{s,i+1} - f_{s,i}}{t_{i+1} - t_i}(t - t_i), \qquad t_i \le t \le t_{i+1} \tag{7.1}$$

As shown in Figure 7.2, the CDF is monotonically non-decreasing. The marginal cost per additional minute of interruption is highest during the initial minutes and gradually diminishes as the outage persists. The five sectors exhibit significantly different damage rates. The important power customer sector exhibits the steepest damage function, which reaches 285.163 $/kW at 120 minutes. The residential sector exhibits the lowest damage function and reaches 1.557 $/kW at 120 minutes. This disparity drives the optimiser to prioritise the restoration of important power customer loads over other loads.

## 7.2 Optimisation Problem Formulation

This section formulates the black-start restoration problem as an optimisation problem for a standalone active distribution network (ADN). The black-start restoration framework can be interpreted as a sequential decision-making process. At each discrete time step, the optimiser determines which components (generators, branches, and loads) should be energised, subject to physical and operational constraints. The optimisation uses: (i) network topology and component data as inputs, (ii) estimated system states such as inertia and frequency as dynamic parameters, and (iii) confidence factors derived from estimation and control performance to adjust operational limits. The objective is to minimise cumulative outage cost over the restoration horizon. The overall process can therefore be summarised as: (1) initialise system state, (2) evaluate available resources and constraints, (3) determine feasible switching actions, and (4) select the action that minimises incremental outage cost while preserving system security. Therefore, the optimisation determines the switching sequence of generators, branches, and loads over a discrete time horizon, subject to constraints on network topology, power balance, voltage limits, branch flows, and frequency stability.

### 7.2.1 Confidence Factors and Their Physical Interpretation

Four confidence factors are introduced to bridge estimation/control performance and system-level optimisation:

- $\eta_H$ (inertia confidence factor): derived from the maximum estimation error of the inertia estimator (Chapter 4), this factor reflects how much of the estimated inertia can be safely utilised.
- $\mu_R$ (RoCoF confidence factor): derived from the frequency estimation error (Chapter 5), this factor adjusts the allowable RoCoF threshold to ensure safe operation under estimation uncertainty.
- $\delta_{FOD}$ (damping enhancement factor): derived from the improvement in transient response provided by the FOD controller (Chapter 6), this factor reflects the increased effective damping support.
- $\gamma_g$ (capacity derating factor): derived from voltage unbalance control performance (Chapter 6), this factor reflects the usable fraction of converter capacity under unbalanced conditions.

These factors convert method-level accuracy into operational margins and enable the optimiser to adapt its decisions based on the reliability of system information and control capability. Therefore, a high confidence factor (close to unity) means the corresponding method provides accurate information, and the optimiser may operate close to the physical limit. A low confidence factor (significantly below unity) imposes conservatism and prevents the optimiser from operating too close to the physical limit. The level of each factor is set according to the accuracy achieved by the corresponding method, as demonstrated in its respective chapter.

The proposed control/estimation methods influence restoration in two fundamental ways: (i) they expand the feasible operating region through relaxation of conservative limits, such that higher effective inertia and droop allow larger load steps, and (ii) they alter the optimal restoration sequence to allow earlier activation of larger loads and faster generator synchronisation. Therefore, the improvement is not only in restoration speed but also in the structure of the restoration strategy.

### 7.2.2 Objective Function for Black-Start Restoration

The objective is to minimise the total customer outage cost accumulated over the restoration horizon. Because the CDF defined in (7.1) is a piecewise function, it is expressed in incremental form to obtain a linear objective:

$$\Delta f_s^{\mathrm{CDF}}(t) = f_s^{\mathrm{CDF}}(t) - f_s^{\mathrm{CDF}}(t-1), \quad s \in S, t \in T1 \tag{7.2}$$

where $T1 = \{1,2,\dots,T_{\mathrm{BS}}\}$ is the set of time steps and $T_{\mathrm{BS}} = 40$ is the total number of permissible restoration time steps. The concavity of the CDF ensures that these increments are non-negative and non-increasing, so the optimiser receives the strongest incentive to restore loads during the early time steps. The objective function is then

$$\min \sum_{k \in \mathcal{D}} \sum_{t \in T1} P_{L,k}\ \Delta f_{s(k)}^{\mathrm{CDF}}(t)\ \left(1 - u_{k,t}^{\mathrm{Load}}\right) \quad k\$ \tag{7.3}$$

where $\mathcal{D} = \{1,2,\dots,32\}$ is the set of loads; $P_{L,k}$ is the active-power demand of the load $k$ in MW; $s(k) \in S$ is the customer sector to which the load $k$ belongs; $S = \{1,2,\dots,5\}$ is the set of customer sectors; and $u_{k,t}^{\mathrm{Load}} \in \{0,1\}$ is a binary decision variable equal to 1 when load $k$ is restored at time $t$ and 0 otherwise. At each time step, every unrestored load $\left(u_{k,t}^{\mathrm{Load}} = 0\right)$ contributes an incremental cost of $P_{L,k}\,\Delta f_{s(k)}^{\mathrm{CDF}}(t)$; once restored $\left(u_{k,t}^{\mathrm{Load}} = 1\right)$, the factor $\left(1 - u_{k,t}^{\mathrm{Load}}\right)$ becomes zero, and no further cost accumulates.

### 7.2.3 Constraints for Black-Start Restoration

The constraint set comprises eleven groups, each representing a specific physical or operational requirement. Constraints (a)–(e) govern the network restoration sequencing and topology, such as initial and terminal conditions, irreversibility of restoration actions, physical prerequisites linking each component to the prior energisation of its neighbours, and the radial tree topology. Constraints (f)–(g) govern generator operation. Constraint (h) enforces power balance. Constraints (i)–(j) enforce branch-flow and voltage limits. Constraint (k) enforces frequency stability and reserve requirements.

**(a) System Initialisation Constraints**

At the initial time step $t = 0$, only the black-start generator and its host bus are available. All other components are de-energised:

$$u_{0,0}^{\text{bus}} = 1 \tag{7.4}$$

$$u_{b,0}^{\text{bus}} = 0 \;\forall\, b \in \mathcal{B} \setminus \{0\} \tag{7.5}$$

$$u_{g,0}^{\text{DG}} = \begin{cases} 1, & g \in G^{\text{BS}} \\ 0, & g \in G^{\text{NBS}} \end{cases} \tag{7.6}$$

$$u_{l,0}^{\text{line}} = 0 \;\forall\, l \in \mathcal{L} \tag{7.7}$$

$$u_{k,0}^{\text{Load}} = 0 \;\forall\, k \in \mathcal{D} \tag{7.8}$$

where $\mathcal{B} = \{0,1,\ldots,32\}$ is the set of buses; $\mathcal{L} = \{1,2,\ldots,32\}$ is the set of branches, $G = \{1,2,\ldots,5\}$ is the set of distributed generators, partitioned into the subset of black-start-capable generators $G^{\text{BS}}$ and the subset of non-black-start generators $G^{\text{NBS}} = G \setminus G^{\text{BS}}$. $G^{GFM} \subseteq G$ denotes the subset of grid-forming converters and $u_{b,t}^{\text{bus}} \in \{0,1\}$, $u_{g,t}^{\text{DG}} \in \{0,1\}$, and $u_{l,t}^{\text{line}} \in \{0,1\}$ are binary decision variables representing the restoration status of the bus $b$, generator $g$, and branch $l$ at time $t$, respectively. They take value 1 if restored and 0 otherwise.

**(b) End-of-Horizon Load Restoration Constraint**

All loads must be restored by the end of the restoration horizon:

$$u^{\text{Load}}_{k,T_{\text{BS}}} = 1 \quad \forall\, k \in \mathcal{D} \tag{7.9}$$

**(c) Restoration Irreversibility Constraints**

Once a component is restored, it remains restored for all subsequent time steps. This irreversibility reflects operational practice during black-start, under which components are not deliberately de-energised once energised:

$$u^{\text{bus}}_{b,t} \geq u^{\text{bus}}_{b,t-1} \quad \forall\, b \in \mathcal{B},\, t \in T_1 \tag{7.10}$$

$$u^{\text{line}}_{l,t} \geq u^{\text{line}}_{l,t-1} \quad \forall\, l \in \mathcal{L},\, t \in T_1 \tag{7.11}$$

$$u^{\text{DG}}_{g,t} \geq u^{\text{DG}}_{g,t-1} \quad \forall\, g \in \mathcal{G},\, t \in T_1 \tag{7.12}$$

$$u^{\text{Load}}_{k,t} \geq u^{\text{Load}}_{k,t-1} \quad \forall\, k \in \mathcal{D},\, t \in T_1 \tag{7.13}$$

**(d) Component Energisation Dependency Constraints**

These constraints enforce the physical prerequisites for restoring each component type. As illustrated in Figure 7.3, a non-black-start generator cannot become available immediately when its host bus is energised; instead, it undergoes a cranking interval of $t_g^{DG}$ time steps during which startup power is consumed and no active-power output is delivered.

Therefore, a non-black-start generator $g$ can only start after its host bus $m_g$ has been energised for at least $t_g^{\text{DG}}$ minutes:

$$u^{\text{DG}}_{g,t} = 0 \quad \forall\, g \in G^{\text{NBS}},\, t \in T_1 : t \leq t_g^{\text{DG}} \tag{7.14}$$

$$u^{\text{DG}}_{g,t} \leq u^{\text{bus}}_{m_g,\, t - t_g^{\text{DG}}} \quad \forall\, g \in G^{\text{NBS}},\, t \in T_1 : t > t_g^{\text{DG}} \tag{7.15}$$

where $m_g$ is the bus at which generator $g$ is connected and $t_g^{\text{DG}}$ is the startup time of generator $g$ in minutes, as listed in Table 7.1. Load $k$ can only be connected after its host bus is energised:

$$u^{\text{Load}}_{k,t} \leq u^{\text{bus}}_{b(k),t} \quad \forall\, k \in \mathcal{D},\, t \in T_1 \tag{7.16}$$

where $b(k)$ denotes the bus at which load $k$ is located. A branch $l$ can only be restored if at least one of its terminal buses was energised at least $t_l^{\text{line}}$ minutes earlier:

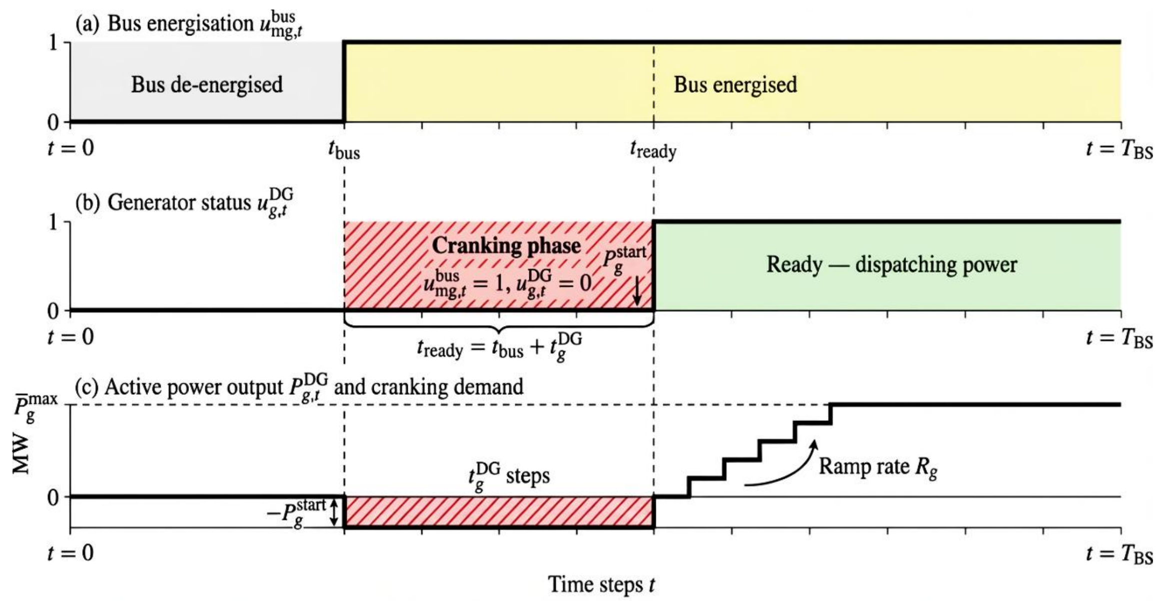


**Figure 7.3:** Representative restoration timeline of a non-black-start generator $g \in G^{NBS}$.

$$u^{\text{line}}_{l,t} - u^{\text{line}}_{l,t-1} \le u^{\text{bus}}_{\text{fr}(l),\, t-t^{\text{line}}_l} + u^{\text{bus}}_{\text{to}(l),\, t-t^{\text{line}}_l} \quad \forall\, l \in \mathcal{L},\ t \in T_1 : t \ge t^{\text{line}} + 1 \tag{7.17}$$

$$u^{\text{line}}_{l,t} = 0 \ \forall\, l \in \mathcal{L}, t \in T_1 : t < t^{\text{line}} + 1 \tag{7.18}$$

where $\text{fr}(l)$ and $\text{to}(l)$ are the sending-end and receiving-end buses of the branch $l$, and $t^{\text{line}} = 1$ min is the branch restoration time. An energised branch requires both terminal buses to be energised:

$$u^{\text{line}}_{l,t} \le u^{\text{bus}}_{\text{fr}(l),t}, u^{\text{line}}_{l,t} \le u^{\text{bus}}_{\text{to}(l),t} \ \ \forall\, l \in \mathcal{L},\ t \in T_1 \tag{7.19}$$

A bus can be energised either by a black-start generator located at that bus or by a connected energised branch:

$$u^{\text{bus}}_{b,t} \le \sum_{\substack{g \in \mathcal{G}^{\text{BS}} \\ m_g = b}} u^{\text{DG}}_{g,t} + \sum_{\substack{l \in \mathcal{L} \\ \text{fr}(l)=b \,\vee\, \text{to}(l)=b}} u^{\text{line}}_{l,t} \quad \forall\, b \in \mathcal{B},\ t \in T_1 \tag{7.20}$$

### (e) Radial Network Topology Constraint

In this thesis, a radial structure is enforced because the adopted test system is a modified IEEE 33-bus distribution network, which is inherently designed and operated as a radial system, as shown in Figure 7.1. In addition, a radial configuration is intentionally selected in this study to simplify the restoration problem and ensure a clear and tractable optimisation framework.

From a practical perspective, this requirement is consistent with standard distribution network operation. Distribution systems are typically operated radially to ensure proper coordination of protection devices, which are designed assuming unidirectional power flow. Furthermore, radial configurations facilitate straightforward fault isolation, which is critical during black-start conditions.

For a network consisting of one or more energised islands with $N_{\text{root}}$ independent source buses, radial operation requires that the number of energised branches equals the number of energised buses minus $N_{\text{root}}$. Hence, this constraint prevents the formation of loops in the restored network, as follows:

$$\sum_{l\in\mathcal{L}} u_{l,t}^{\text{line}} = \sum_{b\in\mathcal{B}} u_{b,t}^{\text{bus}} - N_{\text{root}} \; \forall\, t \in T_1 \tag{7.21}$$

where $N_{\text{root}} = 1$ for the ADN test system. Here, $N_{\text{root}}$ denotes the number of independent energised sources (grid-forming units with black-start capability), not the number of branches connected to a node. Therefore, even if a node connects multiple branches, the radiality condition remains valid as long as each energised island is supplied by a single independent source.

**(f) Generator Capacity and Output Limit Constraints**

During restoration, loads are energised sequentially and may be highly unbalanced across the three phases. At the 12 kV distribution level, the network is configured as a three-wire system; therefore, the load unbalance appears exclusively as negative-sequence current, which is supplied by the converter-based generators in $G$. Each converter is rated for a maximum per-phase current $I_{g,\text{rated}}$. Under balanced operation, the full current capacity is available for positive-sequence power delivery. Under unbalanced operation, however, the converter current contains both positive- and negative-sequence components, $I_g^+$and $I_g^-$. In the worst-case phase, these add constructively, so the peak RMS current becomes $|I_g^+| + |I_g^-|$.

To prevent the most heavily loaded phase leg from exceeding its thermal limit, the usable positive-sequence current must satisfy $|I_g^+|(1+\rho_g) \le I_{g,\text{rated}}$, where $\rho_g = \frac{|I_g^-|}{|I_g^+|}$ is the negative-sequence current ratio of converter $g$. Since active and reactive power delivery are proportional to the positive-sequence current, the available fraction of nameplate capacity is

$\gamma_g = \frac{1}{1+\rho_g}$. Moreover, managing unbalance is critical not only because it reduces converter capacity, but also because negative-sequence current introduces second-harmonic ($2\omega$) oscillations in internal variables such as instantaneous power, which may degrade performance and even threaten stability. For this reason, it is preferable to concentrate unbalance compensation in a single grid-forming converter with the capability to handle negative-sequence quantities, rather than allow the burden to spread across the entire converter fleet.

Accordingly, the value of $\rho_g$ depends on how the negative-sequence current is shared among converters, which in turn depends on whether the dual-sequence controller of Chapter 6 is deployed. Without an active unbalance controller, the negative-sequence current is shared among all $|G|$ converters through natural impedance-based current division, and for similar output impedances, all units experience the same derating. In the proposed method, the dual-sequence controller is assigned to DG5, which has the largest rating and operates in grid-forming mode. DG5 absorbs the full negative-sequence current demand, while the remaining converters see effectively balanced voltage and operate at their normal rating. The derating factor is therefore given by the following expression without the unbalance controller.

$$\gamma_g = \frac{1}{1+\rho_g} \quad \forall\, g \in G \tag{7.22}$$

With unbalance controller on DG5:

$$\gamma_g = \begin{cases} \dfrac{1}{1+|G|\rho_g}, & g = 5 \\ 1, & g \in G \setminus \{5\} \end{cases} \tag{7.23}$$

where $|G| = 5$. The effective generator limits are

$$\bar{P}_g^{\max} = \gamma_g P_g^{\max}, \bar{Q}_g^{\max} = \gamma_g Q_g^{\max}, \bar{Q}_g^{\min} = \gamma_g Q_g^{\min} \tag{7.24}$$

and the output constraints are

$$0 \le P_{g,t}^{DG} \le \bar{P}_g^{\max} u_{g,t}^{DG} \quad \forall\, g \in G,\, t \in T \tag{7.25}$$

$$\bar{Q}_g^{\min} u_{g,t}^{DG} \le Q_{g,t}^{DG} \le \bar{Q}_g^{\max} u_{g,t}^{DG} \quad \forall\, g \in G,\, t \in T. \tag{7.26}$$

where $T = \{0,1,\dots,T_{BS}\}$ is the full discrete time horizon including the initial state at $t = 0$.

**(g) Generator Active-Power Ramp-Up Constraints**

The active-power output of each generator may only increase between consecutive time steps, and the increase is bounded by the product of the ramp rate and the time-step duration:

$$0 \le P_{g,t}^{\mathrm{DG}} - P_{g,t-1}^{\mathrm{DG}} \le R_g\,\Delta t \quad \forall\, g \in G,\, t \in T_1 \tag{7.27}$$

where $R_g$ is the ramp rate of the generator $g$ in MW/min, as listed in Table 7.1, and $\Delta t = 1\,\mathrm{min}$ is the unit time step. This constraint reflects the physical limitation of generator dynamics. A generator cannot instantaneously increase its output due to mechanical and control system inertia. The ramp-rate limit ensures that the increase in active power between two consecutive time steps does not exceed the physically achievable rate. Without this constraint, the optimiser could schedule unrealistically large power changes.

**(h) Nodal Active- And Reactive-Power Balance Constraints**

Kirchhoff's current law is enforced at every bus and every time step. The active-power balance includes a term for the startup power consumed by non-black-start generators during their cranking period:

$$\begin{aligned}\sum_{\substack{g\in G\\ m_g=b}} P_{g,t}^{\mathrm{DG}} - \sum_{\substack{k\in\mathcal{D}\\ b(k)=b}} P_{L,k}\, u_{k,t}^{\mathrm{Load}} - \sum_{\substack{g\in G^{\mathrm{NBS}}\\ m_g=b}} P_g^{\mathrm{start}}\left(u_{b,t}^{\mathrm{bus}} - u_{g,t}^{\mathrm{DG}}\right) = \\ \sum_{\substack{l\in\mathcal{L}\\ \mathrm{fr}(l)=b}} P_{l,t}^{\mathrm{line}} - \sum_{\substack{l\in\mathcal{L}\\ \mathrm{to}(l)=b}} P_{l,t}^{\mathrm{line}} \quad \forall\, b \in \mathcal{B},\, t \in T\end{aligned} \tag{7.28}$$

$$\sum_{\substack{g\in G\\ m_g=b}} Q_{g,t}^{\mathrm{DG}} - \sum_{\substack{k\in\mathcal{D}\\ b(k)=b}} Q_{L,k}\, u_{k,t}^{\mathrm{Load}} = \sum_{\substack{l\in\mathcal{L}\\ \mathrm{fr}(l)=b}} Q_{l,t}^{\mathrm{line}} - \sum_{\substack{l\in\mathcal{L}\\ \mathrm{to}(l)=b}} Q_{l,t}^{\mathrm{line}} \quad \forall\, b \in \mathcal{B},\, t \in T \tag{7.29}$$

where $P_g^{\mathrm{start}}$ is the startup power consumption of the generator $g$ in MW, as listed in Table 7.1. $Q_{L,k}$ is the reactive power demand of the load $k$ in MVAr; and $P_{l,t}^{\mathrm{line}}$ and $Q_{l,t}^{\mathrm{line}}$ are continuous decision variables representing the active and reactive power flow on the branch $l$ at time $t$ in MW and MVAr, respectively. The startup-power term $P_g^{\mathrm{start}}(u_{b,t}^{\mathrm{bus}} - u_{g,t}^{\mathrm{DG}})$ is non-zero only during the interval in which the host bus of a non-black-start generator is energised $\left(u_{b,t}^{\mathrm{bus}} = 1\right)$ but the generator has not yet completed its startup sequence $\left(u_{g,t}^{\mathrm{DG}} = 0\right)$. Once the generator comes online, $u_{g,t}^{\mathrm{DG}} = 1$ and the term vanishes.

**(i) Branch Apparent-Power Flow Limit Constraints**

The circular apparent-power constraint $P_{l,t}^2 + Q_{l,t}^2 \leq (S_l^{\max})^2$ is nonlinear. It is linearised using the standard octagonal approximation, which replaces the circle by eight linear inequalities [70]:

$$-S_l^{\max} u_{l,t}^{\text{line}} \leq P_{l,t}^{\text{line}} \leq S_l^{\max} u_{l,t}^{\text{line}} \quad \forall\, l \in \mathcal{L},\, t \in T \tag{7.30}$$

$$-S_l^{\max} u_{l,t}^{\text{line}} \leq Q_{l,t}^{\text{line}} \leq S_l^{\max} u_{l,t}^{\text{line}} \quad \forall\, l \in \mathcal{L},\, t \in T \tag{7.31}$$

$$-\sqrt{2}\, S_l^{\max} u_{l,t}^{\text{line}} \leq P_{l,t}^{\text{line}} + Q_{l,t}^{\text{line}} \leq \sqrt{2}\, S_l^{\max} u_{l,t}^{\text{line}} \quad \forall\, l \in \mathcal{L},\, t \in T \tag{7.32}$$

$$-\sqrt{2}\, S_l^{\max} u_{l,t}^{\text{line}} \leq P_{l,t}^{\text{line}} - Q_{l,t}^{\text{line}} \leq \sqrt{2}\, S_l^{\max} u_{l,t}^{\text{line}} \quad \forall\, l \in \mathcal{L},\, t \in T \tag{7.33}$$

where $S_l^{\max}$ is the apparent-power thermal rating of branch $l$ in MVA. When $u_{l,t}^{\text{line}} = 0$, all eight bounds collapse to zero, which forces zero flow on a de-energised branch.

**(j) Root-Bus Reference Voltage and Branch Voltage-Drop Constraints**

The squared voltage magnitude at the root bus is fixed at the nominal value whenever the bus is energised:

$$U_{0,t} = 1.0 \cdot u_{0,t}^{\text{bus}} \quad \forall\, t \in T \tag{7.34}$$

where $U_{b,t} \geq 0$ is a continuous decision variable representing the squared voltage magnitude at bus $b$ at time $t$ in per unit. The voltage relationship along each branch is modelled using the linearised DistFlow formulation [70], in which the quadratic loss term is neglected. The big-$M$ method deactivates the constraint when the branch is open:

$$U_{\text{fr}(l),t} - U_{\text{to}(l),t} - \frac{2\left(r_l\, P_{l,t}^{\text{line}} + x_l\, Q_{l,t}^{\text{line}}\right)}{S_{\text{base}}} \leq M\left(1 - u_{l,t}^{\text{line}}\right) \quad \forall\, l \in L,\, t \in T \tag{7.35}$$

$$U_{\text{fr}(l),t} - U_{\text{to}(l),t} - \frac{2\left(r_l\, P_{l,t}^{\text{line}} + x_l\, Q_{l,t}^{\text{line}}\right)}{S_{\text{base}}} \geq -M\left(1 - u_{l,t}^{\text{line}}\right) \quad \forall\, l \in L,\, t \in T \tag{7.36}$$

where $r_l$ and $x_l$ are the resistance and reactance of branch $l$ in per unit (tabulated in Appendix A); $S_{\text{base}}$ is the system base apparent power; and $M$ is a large positive constant chosen to be sufficiently greater than the maximum possible voltage-squared difference across any branch. The squared voltage magnitude at every bus is bounded by:

$$U^{\min} u_{b,t}^{\text{bus}} \le U_{b,t} \le U^{\max} u_{b,t}^{\text{bus}} \quad \forall\, b \in \mathcal{B},\, t \in T \tag{7.37}$$

where $U^{\min} = \left(V^{\min}\right)^2 = 0.81$ and $U^{\max} = (V^{\max})^2 = 1.21$ are the squared voltage limits corresponding to the voltage magnitude limits of $V^{\min} = 0.9\ \text{p.u.}$ and $V^{\max} = 1.1\ \text{p.u.}$ The product with $u_{b,t}^{\text{bus}}$ forces $U_{b,t} = 0$ at de-energised buses, which avoids infeasibility in the voltage-drop equations for open branches.

**(k) Frequency Stability and Active-Power Reserve Constraints**

This group contains the constraints into which the confidence factors from Chapter 4–Chapter 6 are most directly embedded. These constraints govern the maximum permissible load pickup at each time step, the minimum inertial support required before any load may be energised, and the active-power reserve that must be maintained throughout the restoration process. The term "maximum allowable load pickup" refers to the upper bound on the amount of load that can be connected at a given time step without violating frequency stability limits. If this limit is exceeded, the resulting power imbalance between generation and demand may lead to excessive frequency deviation or high RoCoF, which can trigger protection mechanisms or cause instability. Therefore, this constraint ensures that load restoration is performed in a controlled and secure manner. Although increasing load pickup may, in some cases, improve system damping once sufficient generation and control support are available, during early restoration stages the system is typically inertia-limited and vulnerable to disturbances. Hence, a conservative upper bound on load pickup is required.

Each confidence factor enters the formulation as a tuneable parameter whose level is set by the accuracy demonstrated in the corresponding chapter, such that improvements in estimation or control performance directly relax specific physical constraints within the optimisation problem rather than uniformly scaling all limits.

The estimated inertia energy $\hat{E}_t$ at each time step is the sum of the stored kinetic energies of all online generators, scaled by the inertia estimation confidence factor $\eta_H$:

$$\hat{E}_t = \eta_H \sum_{g \in G} H_g\ S_g\ u_{g,t}^{DG} \ \ \forall\ t \in T \tag{7.38}$$

where $\hat{E}_t \ge 0$ is a continuous decision variable representing the estimated inertia energy of the system in MJ. Physically, the inertia energy represents the stored kinetic energy in rotating masses (or virtual inertia in converters), which determines the system's ability to resist rapid frequency changes following disturbances. $H_g$ is the estimated inertia constant of generator $g$ in seconds; $S_g$ is the apparent-power rating of generator $g$ in MVA, so that the product $H_g\, S_g$ gives the kinetic energy in megajoules at rated speed; and $\eta_H$ is the inertia estimation confidence factor, derived from the worst-case overestimation error of the wavelet-based inertia estimator developed in Chapter 4:

$$\eta_H = \frac{1}{1+\epsilon_H} \tag{7.39}$$

where $\epsilon_H$ is the maximum relative inertia estimation error. The level of $\eta_H$ is set according to the accuracy of the deployed estimator. The method of Chapter 4 achieves a worst-case error of $\epsilon_H = 6.05\%$, giving $\eta_H = 0.9430$. When a less accurate estimator is used, for example, with a benchmark error of $\epsilon_H = 10\%$, the factor reduces to $\eta_H = 0.9091$, and the optimiser perceives less inertia, which restricts load pickup. A more accurate estimator yields a higher $\eta_H$, which increases $\hat{E}_t$ and relaxes the constraints that depend on it.

The net active-power increment $\Delta P_t$ at each time step includes both the newly connected load and the change in startup-power demand:

$$\begin{aligned}\Delta P_t = \sum_{k\in D} P_{L,k}\left(u_{k,t}^{Load} - u_{k,t-1}^{Load}\right) + \\ \sum_{g\in G^{NBS}} P_g^{start}\left[\left(u_{m_g,t}^{bus} - u_{g,t}^{DG}\right) - \left(u_{m_g,t-1}^{bus} - u_{g,t-1}^{DG}\right)\right] \quad \forall\, t \in T_1\end{aligned} \tag{7.40}$$

where $\Delta P_t$ is a continuous decision variable representing the net active-power pickup at time $t$ in MW. The first summation captures the power drawn by newly energised loads. The second summation captures the change in cranking power required by non-black-start generators whose host buses are energised but whose startup sequences have not yet completed.

The frequency nadir constraint requires that the net power step must not cause the system frequency to deviate beyond the maximum allowable limit:

$$\Delta P_t \le \Delta f_{max} \sum_{g\in G} \bar{K}_g\, u_{g,t}^{DG} \quad \forall\, t \in T_1 \tag{7.41}$$

where $\Delta f_{max} = 0.5$ Hz is the maximum allowable frequency deviation, specified as a fixed regulatory threshold by the system operator. The frequency and RoCoF information are obtained locally at each converter using the estimation method described in Chapter 5. These measurements are communicated to a central restoration controller, which solves the MILP and dispatches switching decisions. Therefore, the optimisation is performed centrally, while measurements are acquired locally. Under an equivalent damping-based approximation of frequency response, the predicted frequency deviation following a net power step $\Delta P_t$ is $\frac{\Delta P_t}{\sum_{g\in G} \bar{K}_g \, u_{g,t}^{DG}}$, and constraint (7.41) requires this value not to exceed the full physical threshold $\Delta f_{max}$.

This formulation does not explicitly compute the true dynamic frequency nadir, which depends on inertia and damping interactions, but instead provides a conservative algebraic approximation suitable for MILP formulation that ensures the nadir remains within acceptable limits. The effective droop coefficient $\bar{K}_g$ incorporates the FOD damping-enhancement factor $\delta_{FOD}$ from Chapter 6:

$$\bar{K}_g = \begin{cases} (\delta_{FOD}+1)\, K_g, & g \in G^{GFM} \\ K_g, & g \notin G^{GFM} \end{cases} \tag{7.42}$$

where $K_g$ is the baseline frequency-droop coefficient of the generator $g$ in MW/Hz, as listed in Table 7.1, and $\delta_{FOD}$ quantifies the relative improvement in effective damping support provided by the fractional-order damping controller developed in Chapter 6, derived from the settling-time reduction ratio. Specifically, the simulations of Chapter 6 report a conventional settling time of $0.39$ s and a FOD-augmented settling time of $0.28$ s, which yields a response-speed ratio of $0.39/0.28 = 1.3929$. Accordingly, the equivalent enhancement factor is taken as $0.3929$, which means that GFM converters provide 39.29% more MW/Hz support. Without the FOD controller, $\delta_{FOD} = 0$, and the baseline droop coefficient is used unmodified. Therefore, the value of $\bar{K}_g$ in (7.41) directly determines the maximum load that may be picked up at each step. A more effective damping controller provides greater support for frequency deviation, thereby permitting larger load increments within the same 0.5 Hz frequency headroom.

The rate-of-change-of-frequency (RoCoF) constraint ensures that the instantaneous RoCoF at the moment of a power step does not exceed a safe operational threshold. From the swing equation, the magnitude of the initial RoCoF following a net power imbalance $\Delta P_t$ is $|\dot{f}(0^+)| = \frac{f_0 \Delta P_t}{2\hat{E}_t}$, where $f(t)$ is the system frequency in Hz, $\dot{f}(t)$ is its time derivative in Hz/s, and $0^+$ denotes the instant immediately after the disturbance. Here, $f_0$ is the pre-disturbance system frequency, which is approximated by the nominal value $50$ Hz, and $\Delta P_t$ is the net load pickup (power step) at restoration stage $t$.

Although the above formulation is based on the instantaneous RoCoF derived from the swing equation, in practical implementation, RoCoF is not measured at an exact instant but is estimated over a short time window using the frequency estimation method described in Chapter 5. Therefore, the constraint represents a conservative approximation of the peak RoCoF immediately following a disturbance.

Requiring the initial RoCoF magnitude to remain below the effective allowable threshold $\dot{f}_{max}^{eff}$ yields:

$$f_0 \Delta P_t \leq 2\dot{f}_{max}^{eff} \hat{E}_t \quad \forall\, t \in T_1 \tag{7.43}$$

The physical RoCoF withstand limit of the system, set by protection relay settings and grid-code requirements, is denoted by $\dot{f}_{max}^{phys} = 0.5\,\mathrm{Hz/s}$. This value is selected based on commonly adopted practices in modern power systems, including recent updates in the Great Britain grid code allowing RoCoF limits up to 0.5 Hz/s, although the exact limit may vary depending on system characteristics and operation requirements. This limit is a fixed design parameter rather than a measured quantity. However, during restoration, compliance with this limit must be verified in real time using an estimated RoCoF signal, and that estimate is subject to error.

Furthermore, during distribution system restoration, the network operates under low-inertia and weak-grid conditions and is more sensitive to frequency disturbances. Therefore, the choice of $f_{\max} = 0.5$Hz/s provides a realistic yet conservative upper bound that ensures secure operation during black-start and early restoration stages.

To ensure that the true RoCoF does not exceed the physical limit despite imperfect monitoring, the scheduling model enforces a more conservative operational threshold defined as

$$\dot{f}_{max}^{eff} = \mu_R \dot{f}_{max}^{phys}, \qquad \mu_R = 1 - \epsilon_R \tag{7.44}$$

where $\mu_R \in (0,1]$ is the RoCoF-detection confidence factor and $\epsilon_R$ is the relative RoCoF estimation error of the deployed fractional-order frequency estimator, as characterised in Chapter 5. Thus, $\mu_R$ reduces the admissible RoCoF threshold to provide a safety margin against underestimation of the true RoCoF. For the estimator developed in Chapter 5, $\epsilon_R = 1.47\%$, which provides $\mu_R = 0.9853$. For a less accurate conventional estimator, $\epsilon_R = 10.43\%$, which provides $\mu_R = 0.8957$.

The frequency-deviation constraint in (7.41) assumes that online generators are able to increase their active-power output through droop response when frequency declines. This response is only physically achievable if each generator retains sufficient headroom above its current dispatch. The active-power reserve constraints enforce this requirement. For each online generator, the available reserve is limited by two independent factors. The first is the remaining capacity headroom above the current dispatch level,

$$P_{g,t}^{R} \leq \bar{P}_g^{max} u_{g,t}^{DG} - P_{g,t}^{DG} \quad \forall\, g \in G,\, t \in T_1 \tag{7.45}$$

and the second is the maximum output increase that can be delivered within one time step, as determined by the ramp-rate limit,

$$P_{g,t}^{R} \leq R_g \Delta t \qquad \forall\, g \in G,\, t \in T_1 \tag{7.46}$$

where $P_{g,t}^{R} \geq 0$ is a continuous decision variable representing the active-power reserve of the generator $g$ at time $t$ in MW, and $\Delta t$ is the time-step duration in minutes. Together, (7.45) and (7.46) imply that the usable reserve of each generator is the lesser of the remaining capacity headroom and the ramp-rate-limited increment achievable within the current interval. At the system level, the total active-power reserve must cover a prescribed fraction of the total active-power demand, including both restored load and startup demand from non-black-start generators:

$$\sum_{g \in G} P_{g,t}^{R} \geq \alpha \left( \sum_{k \in D} P_{L,k}\, u_{k,t}^{Load} + \sum_{g \in G^{NBS}} P_g^{start} \left( u_{m_g,t}^{bus} - u_{g,t}^{DG} \right) \right) \; \forall\, t \in T_1 \tag{7.47}$$

where $\alpha = 0.10$ is the reserve requirement fraction. This constraint prevents the optimiser from committing all available generation to immediate load service and instead forces it to retain sufficient headroom to support post-disturbance balancing and losses.

The complete hierarchical structure of the proposed black-start restoration MILP, from the estimation and control methods that determine the confidence factors, through the five constraint groups, to the customer-outage-cost objective, is summarised in Figure 7.4.

## 7.3 Results and Discussion

This section presents the results obtained from the proposed restoration framework under two operating conditions. Scenario S1 represents the baseline configuration in which none of the four enhancement methods are activated, whereas Scenario S2 corresponds to the fully enhanced case in which all four methods are enabled simultaneously. Both scenarios are evaluated on the ADN test system comprising 33 buses, 37 lines, 5 distributed generators, and 32 loads with a total active demand of 18.575 MW and a total reactive demand of 11.5

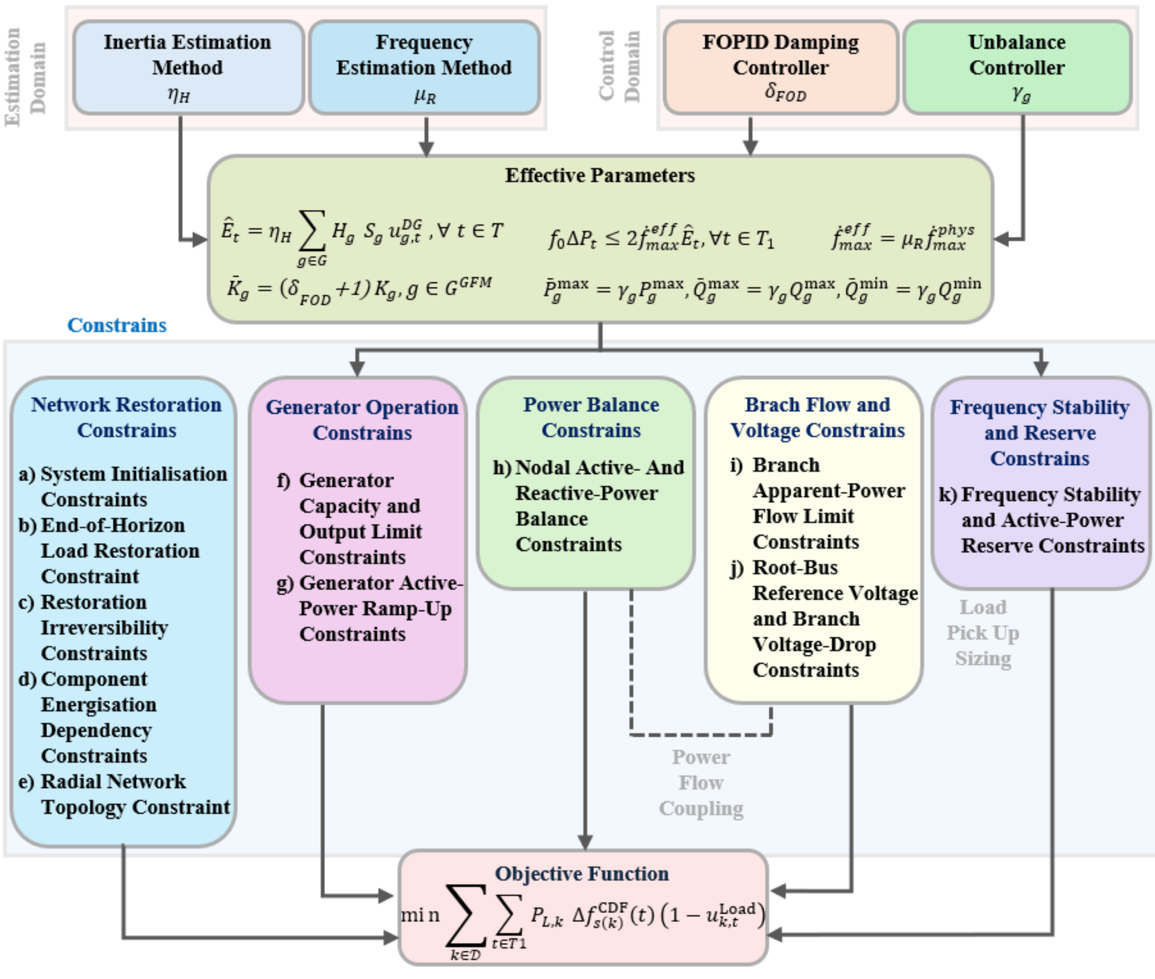


**Figure 7.4:** Hierarchical overview of the black-start restoration MILP formulation.

MVAr. The optimisation horizon spans 40 one-minute intervals, the permissible bus voltage range is 0.90 to 1.10 p.u., and the maximum allowable frequency deviation is 0.50 Hz. The MILP problem is solved using the IBM ILOG CPLEX branch-and-bound algorithm, which guarantees global optimality of the obtained solution for each scenario within the defined model, and it contains 9,465 decision variables, of which 4,387 are binary, together with 34,103 constraints.

The generator parameters show substantial differences between the two scenarios because of the proposed methods. In S1, all five generators operate with the same derating factor, with $\gamma$ equal to 0.889. This value reduces the effective capacity of each unit to about 88.9% of its rated value. In S2, the proposed unbalance control method returns the derating factor of DG1 through DG4 to unity and restores their full rated capacities. DG5, by contrast, takes responsibility for unbalance compensation and therefore operates with a lower factor, with $\gamma$ equal to 0.615. As a result, the capacity of DG5 decreases from 7.111 MW to 4.923 MW.

The FOD-based damping enhancement also changes the droop characteristics of the system. In S1, the effective droop coefficients of DG1 and DG5 are 2.000 MW/Hz and 1.800 MW/Hz, respectively. In S2, these values become 2.786 MW/Hz for DG1 and 2.507 MW/Hz for DG5.

The combined improvements in inertia estimation and frequency estimation also strengthen the frequency-security margin. In S1, the effective allowable rate of change of frequency is 0.448 Hz/s. In S2, this value rises to 0.493 Hz/s. This increase expands the feasible region of the optimisation problem by relaxing the RoCoF constraint. As a result, the optimiser can select larger load pickup steps and alter the restoration sequence, rather than only accelerating an unchanged sequence.

The minute-by-minute restoration sequence is presented in Table 7.4. In S1, the optimiser adopts a conservative strategy during the first 15 minutes, extends feeder segments, and picks up only small loads that do not exceed 0.450 MW, because DG1 alone cannot support larger load steps without violating the frequency constraint. The branch that connects to loads L23 and L24, each rated at 2.100 MW, cannot be energised until minute 16. Six loads with a total of 1.800 MW remain unserved until the final minute, namely minute 23. In S2, load L1 at bus 1 is restored at minute 2, twenty minutes earlier than in S1. After DG4 synchronises at minute 9, the optimiser picks up L7 at 1.000 MW and L27 at 0.300 MW at the same time,

**Table 7.4:** Restoration sequence for S1 and S2.

| Time (min) | S1 | S2 |
|---|---|---|
| **0** | **DG1** | **DG1** |
| **1** | — | — |
| **2** | Br0-1 | Br0-1, L1 |
| **3** | Br1-2, Br1-18, L2 | Br1-2, Br1-18, L2 |
| **4** | Br2-3, Br18-19, Br2-22, L22 | Br2-3, Br18-19, L19 |
| **5** | Br3-4, Br19-20 | Br3-4, Br19-20 |
| **6** | Br4-5, Br20-21, L21 | Br4-5, Br20-21, L21 |
| **7** | Br5-6, Br5-25, L19 | Br5-6, Br2-22, Br5-25, L22 |
| **8** | Br6-7, Br25-26, L26 | Br6-7, Br25-26 |
| **9** | Br7-8, Br26-27, L20 | **DG4**, Br7-8, Br26-27, L7, L27 |
| **10** | Br8-9, Br27-28, L18 | **DG2**, Br8-9, Br27-28, L6 |
| **11** | Br9-10, Br28-29, L27 | Br9-10, Br22-23, Br28-29, L3, L28 |
| **12** | Br10-11, Br29-30, L11 | Br10-11, Br29-30, L11, L18, L20 |
| **13** | Br11-12, Br30-31, L10 | Br11-12, Br30-31, L31 |
| **14** | Br12-13, Br31-32 | Br12-13, Br31-32, L12, L13 |
| **15** | Br13-14, L32 | Br13-14, Br23-24 |
| **16** | **DG4, DG5**, Br14-15, Br22-23, L23 | **DG5**, Br14-15, L23 |
| **17** | Br15-16, L3, L31 | Br15-16, L4, L16, L29, L32 |
| **18** | Br16-17, L6, L17 | **DG3**, L24 |
| **19** | Br23-24, L7, L28 | Br16-17, L5, L15, L17, L25, L26 |
| **20** | **DG2, DG3**, L24 | L8, L9, L10, L14, L30 |
| **21** | L13, L16, L29 | — |
| **22** | L1, L12, L15, L30 | — |
| **23** | L4, L5, L8, L9, L14, L25 | — |

with a combined step of 1.300 MW that would be infeasible in S1 at the same time because of insufficient inertia and droop.

This difference illustrates that the proposed methods change not only the speed but also the structure of the restoration sequence, and enable simultaneous energisation of multiple loads and earlier activation of high-demand branches. By minute 12, S2 has restored 7.000 MW of load compared to only 3.600 MW in S1. The full 18.575 MW is restored by minute 20 in S2, whereas S1 requires 23 minutes to reach the same level.

The voltage performance during restoration is illustrated in Figure 7.5, which shows the minimum bus voltage trajectory for both scenarios. In S1, the voltage remains relatively high during the first 15 minutes because of the light loading, then declines sharply between minutes 16 and 19 as heavy loads are energised in rapid succession, and it reaches the binding lower limit of 0.900 p.u. at bus 18 by minute 19. In S2, the earlier and more aggressive load pickup causes a faster voltage decline during the middle phase. However, the presence of DG2 at bus 7 and DG4 at bus 20 provides local reactive power support along the main feeder

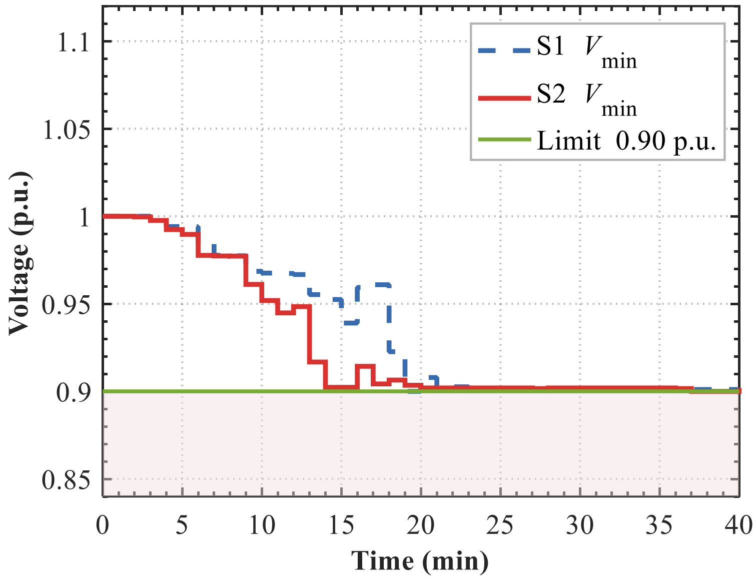


**Figure 7.5:** Minimum bus voltage profile during the 40-minute restoration horizon for Scenarios S1 and S2.

and partially mitigates the voltage depression. These results confirm that the optimiser uses the available voltage margin very effectively in both scenarios. The important observation is that S2 achieves faster restoration without violating the voltage security limit; it exploits the feasible margin more efficiently rather than exceeding it.

The frequency nadir trajectories presented in Figure 7.6 confirm that both scenarios maintain the system frequency above the minimum admissible threshold of 49.5 Hz throughout the restoration process. A representative event occurs at minute 17. In S1, a 1.75 MW load step with an aggregate droop of 5.80 MW/Hz produces a frequency nadir of approximately 49.70 Hz. In S2, a larger 2.00 MW load step occurs at a similar stage, but the higher aggregate droop of 7.74 MW/Hz limits the frequency drop to approximately 49.74 Hz. This demonstrates that the improved droop and RoCoF margin do not merely allow faster restoration, but actively reduce frequency excursions for comparable or larger disturbances.

The cumulative outage cost over restoration time is presented in Figure 7.7. This curve represents the actual economic damage incurred by all customers, computed at each minute as the sum of each load's active power weighted by its sector-specific customer damage function evaluated at the accumulated outage duration up to that instant. Both curves begin at a non-zero value because Sectors 3, 4, and 5 carry immediate interruption penalties at t =

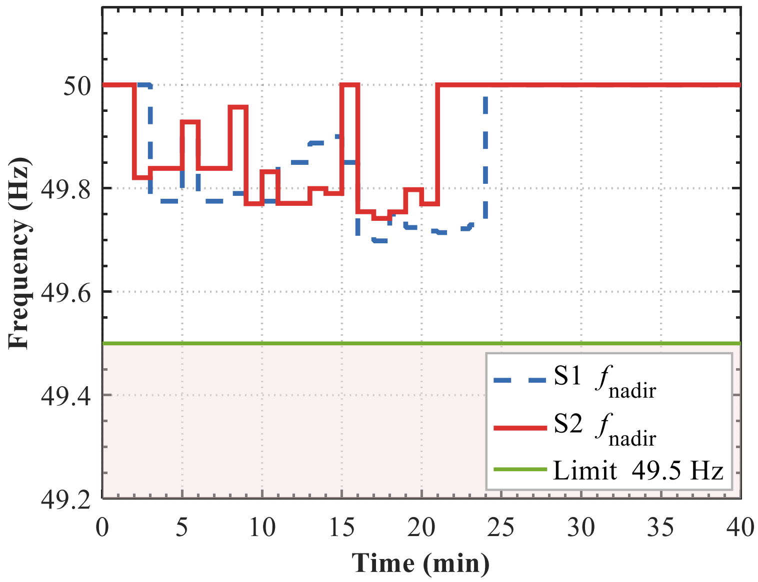


**Figure 7.6:** Frequency nadir evolution during system restoration for Scenarios S1 and S2.

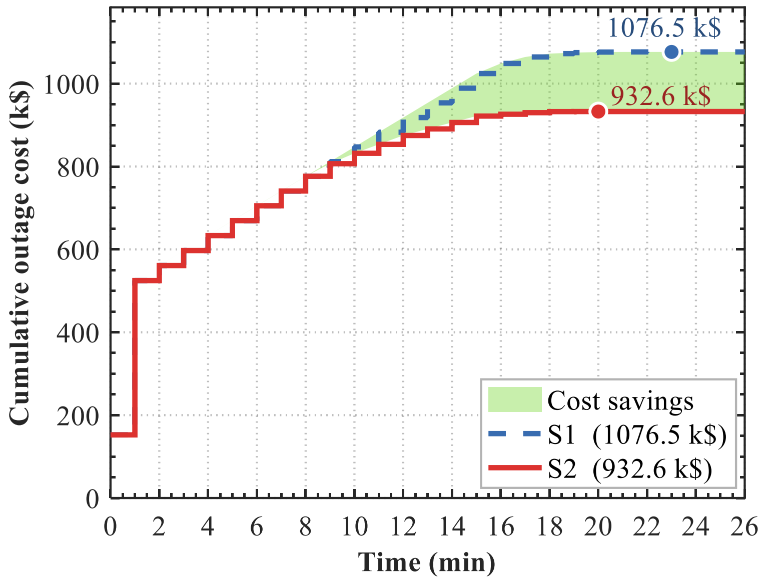


**Figure 7.7:** Cumulative outage cost for S1 and S2 during the restoration process.

0, then rise steeply while the majority of loads remain de-energised. The S2 curve flattens earlier than S1 as critical high-sector loads are restored sooner, which locks in their cost contributions before the damage functions reach their most severe values. The final cumulative outage cost reaches 1,076.46 k$ for S1 and 932.59 k$ for S2, a reduction of 143.87 k$ or 13.37%, driven predominantly by restoring the six Sector 5 loads totalling 6.200 MW on average 4.50 minutes earlier and contributing approximately 60% of the saving.

The cumulative restored load as a function of time is depicted in Figure 7.8. The restoration trajectory of S2 dominates that of S1 for nearly the entire process. The two scenarios track each other closely during the first eight minutes, with S2 maintaining a modest lead of 0.200 to 0.500 MW. The critical divergence begins at minute 9 when DG4 comes online in S2, after which the lead grows rapidly from 1.050 MW at minute 9 to a maximum of 5.775 MW at minute 19. The average restoration rate is 0.808 MW per minute for S1 over its 23-minute span and 0.929 MW per minute for S2 over its 20-minute span, which represents a 15.0% improvement in average throughput. Importantly, there are time intervals in S1 where feeder segments are energised but associated loads remain disconnected because frequency constraints prevent immediate pickup. In S2, these constraints are relaxed, so energisation and load pickup occur within the same or adjacent time steps, reducing idle network expansion and improving restoration efficiency.

The active power output trajectories of DG1 through DG5 are shown in Figure 7.9. In S1, DG1 operates as the sole generator for 16 minutes and ramps to 4.645 MW by minute 15, approaching 87.1% of its derated capacity of 5.333 MW. This heavy reliance on a single unit creates a bottleneck in which the restoration rate is directly limited by DG1's ramp capability and frequency regulation capacity. In S2, DG1 reaches only 2.62 MW by minute 8, which is 43.7% of its full rated capacity. The entry of DG4 at minute 9 and DG2 at minute 10

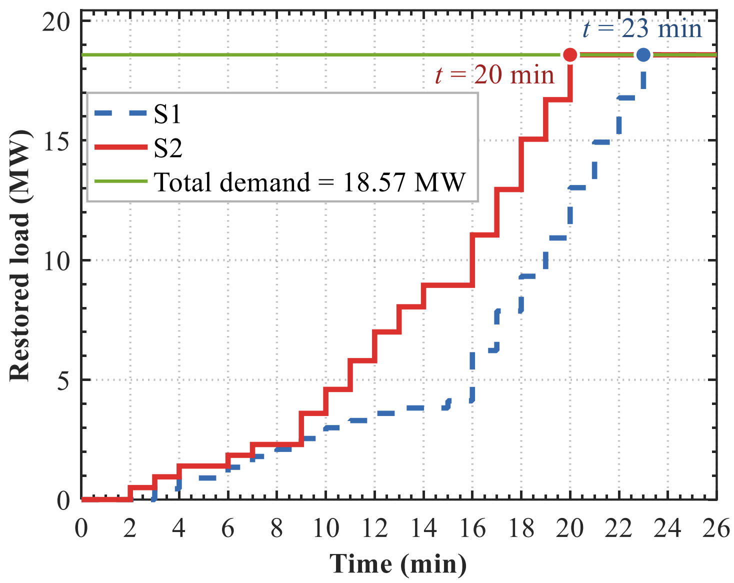


**Figure 7.8:** Restored load trajectory for S1 and S2.

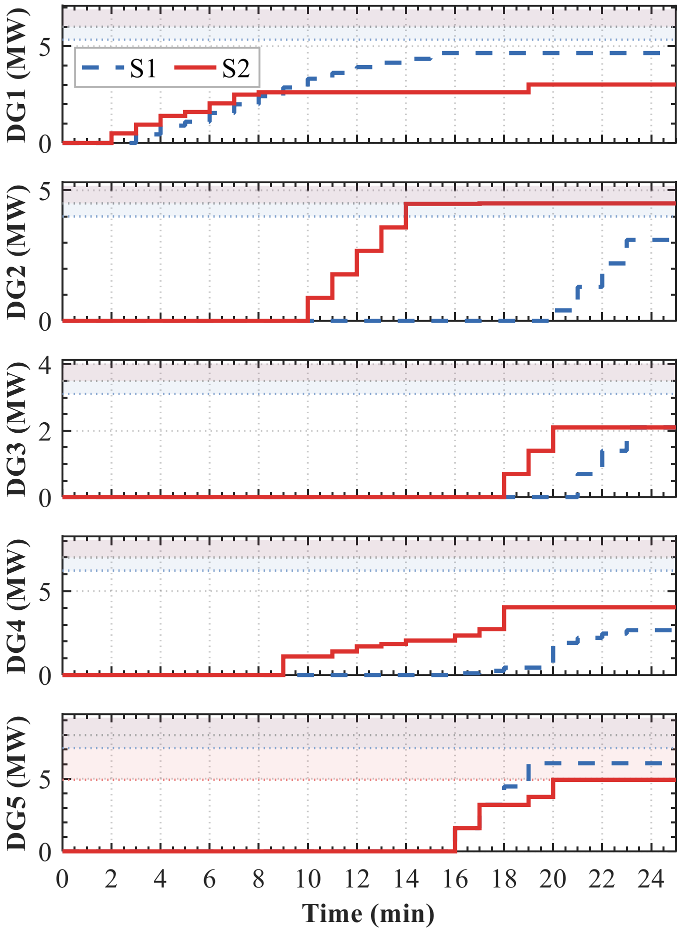


**Figure 7.9:** Active power dispatch trajectories of DG1-DG5 for Scenarios S1 and S2 during restoration.

distributes the generation burden more evenly, so that by minute 15, the combined output of DG1, DG2, and DG4 reaches 9.15 MW, nearly double the 4.645 MW available in S1 at the same time. The final steady-state dispatch in S2 features DG2 and DG4 contributing 4.500 and 4.030 MW, respectively, compared to 3.100 and 2.667 MW in S1, which yields a more balanced and operationally resilient dispatch pattern that reduces dependence on any single source during the critical recovery period.

The principal performance indicators are summarised in Table 7.5. The makespan is reduced by 3 minutes from 23 to 20, representing a 13.04% improvement. The total outage cost decreases from 1,076.46 k$ to 932.59 k$, a saving of 143.87 k$ or 13.37%. The collective evidence from the figures and tables demonstrates that S2 provides a consistently superior restoration solution across the primary performance metrics. These gains arise from the combined effect of tighter uncertainty bounds, increased effective droop, and recovery of

| **Table 7.5:** Summary of key performance indicators. | | | |
|---|---|---|---|
| **Indicator** | **S1** | **S2** | **Improvement** |
| **Makespan (min)** | 23 | 20 | 13.04% shorter |
| **Outage cost (k$)** | 1,076.46 | 932.59 | 13.37% lower |
| **Final restored load (MW)** | 18.575 | 18.575 | Identical |
| **Effective RoCoF limit (Hz/s)** | 0.448 | 0.493 | +10.0% |
| **Total effective droop (MW/Hz)** | 6.650 | 8.143 | +22.4% |
| **Average restoration rate (MW/min)** | 0.808 | 0.929 | +15.0% |
| **Loads restored earlier in S2** | — | 21 of 32 | — |
| **Loads restored at the same time** | — | 4 of 32 | — |
| **Loads restored later in S2** | | 7 of 32 | |

rated generator capacity under unbalance control. The results therefore support the proposed control and estimation methods as robust components of a decision-support framework for resilience-oriented service restoration in active distribution networks.

## 7.4 Summary

This chapter formulated the globally optimal (with respect to the MILP formulation) black-start restoration of a 33-bus active distribution network as a mixed-integer linear programme and introduced four confidence factors, namely $\eta_H$, $\mu_R$, $\delta_{\text{FOD}}$, and $\gamma_g$, that formally translate the accuracy of the inertia estimator (Chapter 4), the precision of the frequency estimator (Chapter 5), and the performance of the fractional-order damping controller and unbalance compensator (Chapter 6) into tuneable constraint parameters of the restoration optimiser.

Each factor enters the optimisation problem explicitly through constraint modification: $\eta_H$ and $\mu_R$ determine the admissible RoCoF limit, $\delta_{FOD}$ modifies the effective droop coefficients, and $\gamma_g$ scales the available generation capacity. Through these mappings, estimation accuracy and control performance directly determine which restoration actions remain feasible at each time step.

These factors affect how much damping capacity, RoCoF headroom, and converter rating the optimiser is permitted to exploit. When the proposed methods are applied, the effective damping capacity increases by 22.4% and the admissible RoCoF threshold rises by 10.0% compared with operation without the proposed methods. This gives the optimiser access to a wider yet still safe feasible region without any structural change to the MILP.

The impact of these changes is not limited to faster restoration. The enlarged feasible region alters the optimisation decisions themselves. Larger admissible load steps, earlier generator utilisation, and simultaneous load pickup become feasible, which leads to a different restoration sequence rather than a scaled version of the baseline solution. For example, load blocks that violate frequency constraints in the baseline case become admissible once droop and RoCoF limits increase, which allows earlier connection of high-demand loads.

The system-level consequences confirm that the black-start restoration quality is governed not only by the optimisation layer but equally by the estimation and control layers that feed it. With the same formulation and the same network, the proposed methods shortened the restoration makespan by 13.0%, reduced total customer outage cost by 13.4%, raised the average restoration rate by 15.0%, and enabled 65.6% of the loads to be restored earlier than in operation without the proposed methods.

These improvements arise from explicit physical mechanisms: higher damping reduces frequency deviation for a given disturbance, increased RoCoF tolerance permits larger instantaneous power imbalance, and restored generator capacity removes binding generation constraints. Each mechanism relaxes a different set of constraints, and their combined effect reshapes the feasible solution space explored by the optimiser.

The black-start problem is therefore shown to be not only an optimisation challenge, but also an integrated estimation-control-optimisation challenge, because uncertainties in estimation and the control performance of the converters directly affect the feasible operating region and, consequently, the optimisation process.

In practical deployment, the confidence factors can be calibrated offline from estimator accuracy metrics and controller performance tests, then applied within a control centre optimisation tool to support real-time restoration decision making under uncertainty.

# Chapter 8 Conclusions and Future Work

## 8.1 Conclusions

The displacement of synchronous generation by converter-interfaced resources reduces the rotational inertia and electromechanical damping that have historically maintained power system stability. This thesis addressed a central question: how converter-interfaced generation can perform black-start restoration of low-inertia distribution networks without synchronous machines.

In addition to addressing this scientific challenge, the thesis establishes a clear pathway through which converter-level intelligence translates into operational decision-making tools and therefore provides direct industrial relevance for system operators, including distribution network operators (DNOs), as well as for grid-code compliance applications.

Seven original contributions across estimation, control, and system-level optimisation were developed, validated, and integrated within a unified restoration framework. Conclusions from each domain are summarised below.

### a) Inertia and Frequency Estimation

The estimation domain addressed the two most critical variables for black-start restoration: inertia and frequency. Two complementary inertia estimation methods were developed that yield numerically stable and accurate estimates. The first is a wavelet-based method that decomposes measured frequency and power signals to extract the inertia constant of each generator. The second is an integral-based method that replaces differentiation with time-domain integration of the swing equation to recover a quantity proportional to the inertia constant and its transient evolution, while it preserves correct relative inertia ratios between generators across different disturbance locations.

**For the wavelet-based inertia estimation method:**

- Worst-case relative estimation errors were approximately 2% for electrically close generators and approximately 6% for electrically distant ones. The higher error has a physical explanation due to attenuation and dispersion of the disturbance signal across network impedance, which reduces the signal-to-noise ratio at remote measurement locations rather than indicating a limitation of the estimation method itself.

- Steady-state error bounds decreased by approximately 80% relative to the best-performing benchmark.
- Response time of approximately 20 ms represented a 50–90% reduction compared to benchmark methods.

**For the integral-based inertia estimation method:**

- The method produces a transient response profile proportional to each generator's inertia contribution, through which the relative strength of each generator and its dominance in a given disturbance can be identified.
- Estimation accuracy degrades monotonically with increased damping coefficient, where the damping-to-inertia ratio governs the sensitivity.

Two complementary frequency estimation methods were additionally developed that both exploit the oscillatory behaviour of the Park–Clarke transformation under deliberate reference frequency offset and both avoid the feedback-loop convergence delays inherent to phase-locked-loop architectures. The first is an integer-order derivative method that extracts the system frequency algebraically through a differential cross-product formulation. The second is a fractional-order derivative method that extends this principle by a tunable fractional-order derivative so that the frequency deviation appears directly in the output amplitude and enables algebraic frequency recovery without iterative convergence.

**For the integer-order derivative frequency estimation method:**

- The method requires only eight arithmetic operations per sample, which represents a computational burden approximately 60–75% lower than conventional PLL methods.
- Theoretical latency is limited to one sample period under noise-free conditions.

**For the fractional-order derivative frequency estimation method:**

- Under fast frequency dynamics, settling time improved by approximately 10–48% and root mean square error reduced by approximately 17–21% across all benchmarks.
- Phase-induced transient detection achieved approximately 1.5% error compared with approximately 10–17% for benchmark methods, which represents an improvement factor of approximately 7 to 12.
- Computational cost was approximately 58–74% lower than the two heavier benchmarks and comparable to the lightest one.
- Under unbalanced conditions, sustained oscillation was initially observed, which highlights that derivative-based estimators show sensitivity to sequence coupling;

however, this limitation was completely resolved after integration with the positive-sequence extraction stage, which confirms compatibility with practical grid conditions.

**b) Transient Damping and Voltage Unbalance Control**

The control domain addressed two critical challenges for converter-dominated networks: transient damping and voltage unbalance compensation. Two control methods were developed as modular additions that do not modify the primary converter control architecture and preserve steady-state operating characteristics.

The first is a fractional-order feedforward damping loop that augments the conventional droop controller with a fractional derivative of the incremental active power change, which provides a continuously tunable transient damping characteristic through the fractional-order parameter. The second is an Expectation–Maximisation-enhanced Kalman filter method that addresses voltage unbalance through a novel time-varying measurement matrix encoding the second-harmonic coupling between positive and negative sequence components, with online adaptation of noise covariance matrices that eliminates the need for manual tuning.

**For the fractional-order feedforward damping loop:**

- The loop is inherently inactive at steady state and does not alter the droop equilibrium point. State-space trajectory analysis confirmed convergence to the identical equilibrium point as the conventional controller, with a significantly more compact spiral path.
- Active power overshoot reduced by approximately 57.5% and settling time reduced by approximately 28.2%, which directly translate into shorter waiting times between restoration actions in practical black-start procedures.

**For the Expectation–Maximisation-enhanced Kalman filter method:**

- The method produced near-pure DC extraction under combined 20% unbalance and measurement noise, where the benchmark retained visible residual noise contamination.
- Voltage unbalance factor was reduced from 12.5% to below 2% within approximately 0.2 seconds, which ensures compliance with GB Grid Code requirements and prevents converter derating during restoration.

### c) Optimal Black-Start Restoration Integration

A mixed-integer linear programming formulation was developed that embeds the outputs of all estimation and control methods within the constraint set of an optimal black-start restoration problem through four confidence factors.

The key novelty compared to existing black-start optimisation approaches lies in the explicit coupling between converter-level performance and system-level constraints. Conventional methods assume fixed system parameters (inertia, frequency, damping), whereas the proposed framework adjusts these parameters based on real-time estimation accuracy and control performance. This transforms the optimisation problem from a static scheduling task into an adaptive, physics-informed decision process.

The proposed framework provides limited additional benefit in conventional high-inertia systems because inertia, damping, and frequency are physically well-defined quantities and do not require estimation or emulation. In such systems, restoration depends mainly on network topology and generator availability. In contrast, in converter-dominated low-inertia systems, inertia becomes virtual and uncertain and requires estimation, frequency may not be directly measurable and requires fast estimation, damping is not inherent, and must be actively controlled; moreover, voltage quality is not guaranteed, and requires active compensation. For this reason, the proposed method demonstrates its full capability in converter-dominated systems, where estimation and control directly influence system stability constraints.

Application to a 33-bus converter-dominated distribution network with five distributed generators and 32 loads demonstrated that the proposed estimation and control methods collectively:

- Shortened full restoration makespan by approximately 13.0% and reduced total customer outage cost by approximately 13.4%.
- Increased average restoration throughput rate by approximately 15.0%.
- Enabled approximately 65.6% of all loads to be restored earlier than when none of the proposed estimation and control methods were applied.

These results confirm that converter-led black-start restoration quality is governed not only by the optimisation formulation but equally by the estimation and control layers that feed it.

From an industrial perspective, this thesis provides a practical pathway for the integration of advanced converter functionalities into restoration planning tools. It enables system operators to increase safe load pickup levels, reduce outage costs, and maintain grid-code compliance in low-inertia power systems.

## 8.2 Future Work

The contributions of this thesis establish a foundation that can be extended in several directions. The following avenues are identified as the most impactful for advancing converter-led restoration of low-inertia power systems.

- The current MILP formulation assumes deterministic generator capacities. A stochastic extension that embeds generation uncertainty directly into the formulation would produce restoration plans that are robust to renewable forecast errors.
- The current formulation assumes a single sequential restoration path, where one grid-forming converter energises the network. Parallel restoration through multiple simultaneously energised islands could substantially reduce the restoration makespan but requires extension of the MILP formulation with synchronisation constraints to ensure frequency alignment prior to island interconnection.
- The fractional order is currently selected offline. An adaptive scheme that adjusts the order in real time based on evolving noise and system dynamics during restoration would maintain optimal performance throughout the process.
- The estimation methods were validated at the distribution level. Extension to transmission scale requires hierarchical architectures and the characterisation of the fractional-order estimator under inter-area oscillations.
- The current MILP formulation guarantees global optimality but scales poorly to large networks. For transmission systems with hundreds of buses, solution times may exceed practical decision windows. Development of heuristic or metaheuristic approaches capable of producing near-optimal plans within tractable computation times would be essential for large-scale deployment.
- The restoration framework operates in open loop with fixed confidence factors. Enabling estimation and control outputs to continuously update optimisation constraints would allow adaptive replanning in response to unforeseen events.

# References


[1] S. Javaid, M. Kaneko, and Y. Tan, "Safe Operation Conditions of Electrical Power System Considering Power Balanceability among Power Generators, Loads, and Storage Devices," *Energies,* vol. 14, no. 15, p. 4460, 2021. [Online]. Available: https://www.mdpi.com/1996-1073/14/15/4460.

[2] L. Meegahapola, A. Sguarezi, J. S. Bryant, M. Gu, E. R. Conde D., and R. B. A. Cunha, "Power System Stability with Power-Electronic Converter Interfaced Renewable Power Generation: Present Issues and Future Trends," *Energies,* vol. 13, no. 13, p. 3441, 2020. [Online]. Available: https://www.mdpi.com/1996-1073/13/13/3441.

[3] P. Energy, "Rate of change of frequency (ROCOF)-review of TSO and generator submissions final report," *Commission for Energy Regulation (CER),* 2013.

[4] P. Christensen *et al.*, "High penetration of power electronic interfaced power sources and the potential contribution of grid forming converters," 2020.

[5] M. AEMO and A. VIC, "Black System South Australia 28 September 2016 Final Report," Tech. Rep., Mar. 2017.[Online]. Available: https://aemo. com. au, 2017.

[6] B. E. S. Operator, "Appendices to the technical report on the events of 9 August 2019," *The British Electricity System Operator,* 2019.

[7] D. Flynn and M. Power, "Transmission planning, flexibility measures and renewables integration for ireland power system," in *2016 IEEE Power and Energy Society General Meeting (PESGM)*, 2016: IEEE, pp. 1-5.

[8] Y. Li, Y. Gu, and T. C. Green, "Revisiting Grid-Forming and Grid-Following Inverters: A Duality Theory," *IEEE Transactions on Power Systems,* vol. 37, no. 6, pp. 4541-4554, 2022, doi: 10.1109/TPWRS.2022.3151851.

[9] A. Alassi, "Black-start provision from grid-forming converters: a new network restoration paradigm," 2023.

[10] A. Alassi, Z. Feng, K. Ahmed, M. Syed, A. Egea-Alvarez, and C. Foote, "Grid-forming VSM control for black-start applications with experimental PHiL validation," *International Journal of Electrical Power & Energy Systems,* vol. 151, p. 109119, 2023/09/01/ 2023, doi: https://doi.org/10.1016/j.ijepes.2023.109119.

[11] B. Badrzadeh *et al.*, "Grid-forming inverters: Project demonstrations and pilots," *IEEE Power and Energy Magazine,* vol. 22, no. 2, pp. 66-77, 2024.

[12] A. E. M. Operator, "Application of Advanced Grid-scale Inverters in the NEM," *White Paper; Australian Energy Market Operator: Victoria, Australia,* 2021.

[13] N. ESO, "GC0137: Minimum specification required for provision of GB Grid Forming (GBGF) capability (formerly Virtual Synchronous Machine/VSM capability)," *National Grid ESO, Grid Code,* 2022.

[14] J. L. Rodríguez-Amenedo, S. A. Gómez, J. C. Martínez, and J. Alonso-Martinez, "Black-Start Capability of DFIG Wind Turbines Through a Grid-Forming Control Based on the Rotor Flux Orientation," *IEEE Access,* vol. 9, pp. 142910-142924, 2021, doi: 10.1109/ACCESS.2021.3120478.

[15] F. Milano, F. Dörfler, G. Hug, D. J. Hill, and G. Verbič, "Foundations and challenges of low-inertia systems," in *2018 power systems computation conference (PSCC)*, 2018: IEEE, pp. 1-25.

[16] P. Tielens and D. Van Hertem, "The relevance of inertia in power systems," *Renewable and sustainable energy reviews,* vol. 55, pp. 999-1009, 2016.

[17] A. Ulbig, T. S. Borsche, and G. Andersson, "Impact of low rotational inertia on power system stability and operation," *IFAC Proceedings Volumes,* vol. 47, no. 3, pp. 7290-7297, 2014.

[18] M. Abouyehia, A. Egea-Àlvarez, and K. H. Ahmed, "Evaluating inertia estimation methods in low-inertia power systems: A comprehensive review with analytic hierarchy process-based ranking," *Renewable and Sustainable Energy Reviews,* vol. 217, p. 115794, 2025.

[19] M. Liu, J. Chen, and F. Milano, "On-line inertia estimation for synchronous and non-synchronous devices," *IEEE Transactions on Power Systems,* vol. 36, no. 3, pp. 2693-2701, 2020.

[20] T. Kerdphol, M. Watanabe, Y. Mitani, and I. Ngamroo, "Inertia assessment from transient measurements: Recent perspective from Japanese WAMS," *IEEE Access,* vol. 10, pp. 66332-66344, 2022.

[21] R. K. Panda, A. Mohapatra, and S. C. Srivastava, "Online estimation of system inertia in a power network utilizing synchrophasor measurements," *IEEE Transactions on Power Systems,* vol. 35, no. 4, pp. 3122-3132, 2019.

[22] D. Zografos, M. Ghandhari, and R. Eriksson, "Power system inertia estimation: Utilization of frequency and voltage response after a disturbance," *Electric Power Systems Research,* vol. 161, pp. 52-60, 2018.

[23] P. Wall, P. Regulski, Z. Rusidovic, and V. Terzija, "Inertia estimation using PMUs in a laboratory," in *IEEE PES Innovative Smart Grid Technologies, Europe*, 2014: IEEE, pp. 1-6.

[24] L. Lugnani, D. Dotta, C. Lackner, and J. Chow, "ARMAX-based method for inertial constant estimation of generation units using synchrophasors," *Electric Power Systems Research,* vol. 180, p. 106097, 2020.

[25] X. Cao, B. Stephen, I. F. Abdulhadi, C. D. Booth, and G. M. Burt, "Switching Markov Gaussian models for dynamic power system inertia estimation," *IEEE Transactions on Power Systems,* vol. 31, no. 5, pp. 3394-3403, 2015.

[26] B. Tan, J. Zhao, V. Terzija, and Y. Zhang, "Decentralized data-driven estimation of generator rotor speed and inertia constant based on adaptive unscented Kalman filter," *International Journal of Electrical Power & Energy Systems,* vol. 137, p. 107853, 2022.

[27] J. Zhang and H. Xu, "Online identification of power system equivalent inertia constant," *IEEE Transactions on Industrial Electronics,* vol. 64, no. 10, pp. 8098-8107, 2017.

[28] M. Tuo and X. Li, "Machine learning assisted inertia estimation using ambient measurements," *IEEE Transactions on industry applications,* vol. 59, no. 4, pp. 4893-4903, 2023.

[29] D. Linaro *et al.*, "Continuous estimation of power system inertia using convolutional neural networks," *Nature Communications,* vol. 14, no. 1, p. 4440, 2023.

[30] M. Ramirez-Gonzalez, F. S. Sevilla, and P. Korba, "Power system inertia estimation using A residual neural network based approach," in *2022 4th global power, energy and communication conference (GPECOM)*, 2022: IEEE, pp. 355-360.

[31] A. K. Singh and B. C. Pal, "Rate of change of frequency estimation for power systems using interpolated DFT and Kalman filter," *IEEE Transactions on Power Systems,* vol. 34, no. 4, pp. 2509-2517, 2019.

[32] G. Escobar, L. Ibarra, J. E. Valdez-Resendiz, J. C. Mayo-Maldonado, and D. Guillen, "Nonlinear Stability Analysis of the Conventional SRF-PLL and Enhanced SRF-EPLL," *IEEE Access,* vol. 9, pp. 59446-59455, 2021, doi: 10.1109/ACCESS.2021.3073063.

[33] P. D. Achlerkar and B. K. Panigrahi, "New Perspectives on Stability of Decoupled Double Synchronous Reference Frame PLL," *IEEE Transactions on Power Electronics,* vol. 37, no. 1, pp. 285-302, 2022, doi: 10.1109/TPEL.2021.3099162.

[34] G. Liu, H. Zhang, and X. Song, "Position-Estimation Deviation-Suppression Technology of PMSM Combining Phase Self-Compensation SMO and Feed-Forward PLL," *IEEE Journal of Emerging and Selected Topics in Power Electronics,* vol. 9, no. 1, pp. 335-344, 2021, doi: 10.1109/JESTPE.2020.2967508.

[35] F. Sevilmiş and H. Karaca, "Performance enhancement of DSOGI-PLL with a simple approach in grid-connected applications," *Energy Reports,* vol. 8, pp. 9-18, 2022/04/01/ 2022, doi: https://doi.org/10.1016/j.egyr.2021.11.186.

[36] Y. F. Wang and Y. W. Li, "Grid Synchronization PLL Based on Cascaded Delayed Signal Cancellation," *IEEE Transactions on Power Electronics,* vol. 26, no. 7, pp. 1987-1997, 2011, doi: 10.1109/TPEL.2010.2099669.

[37] M. S. Reza and M. M. Hossain, "Enhanced Grid Synchronization Technique Based on Frequency Detector for Three-Phase Systems," *IEEE Transactions on Industrial Informatics,* vol. 18, no. 4, pp. 2180-2191, 2022, doi: 10.1109/TII.2021.3095295.

[38] P. Zhang, W. Du, and H. Wang, "Small-Signal Stability of Grid-Connected Converter System in Renewable Energy Systems with Fractional-Order Synchronous Reference Frame Phase-Locked Loop," *Journal of Modern Power Systems and Clean Energy,* vol. 13, no. 3, pp. 1090-1101, 2025, doi: 10.35833/MPCE.2024.000215.

[39] H. R. Chamorro, A.-J. Guel-Cortez, Y. Africano, F. Jimenez, R. Tonkoski, and W. Martinez, "Grid frequency estimation based on extended kalman filter in connected ac microgrids," in *2021 IEEE 30th International Symposium on Industrial Electronics (ISIE)*, 2021: IEEE, pp. 1-6.

[40] A. Kunac, G. Petrovic, M. Despalatovic, and P. Sarajcev, "Grid voltage amplitude and frequency real-time estimation using linear kalman filter," in *2022 7th International Conference on Smart and Sustainable Technologies (SpliTech)*, 2022: IEEE, pp. 1-6.

[41] S. Lyu, L. Zheng, and J. Song, "A second-order generalized integrator frequency locked loop with damping ratio adaptation," *IEEE Transactions on Power Electronics,* vol. 37, no. 3, pp. 2694-2704, 2021.

[42] J. Li, Z. Teng, Y. Wang, S. You, Y. Liu, and W. Yao, "A fast power grid frequency estimation approach using frequency-shift filtering," *IEEE Transactions on Power Systems,* vol. 34, no. 3, pp. 2461-2464, 2019.

[43] P. Kundur, "Power system stability," *Power system stability and control,* vol. 10, no. 1, pp. 7-1, 2007.

[44] M. Abouyehia, A. Colak, R. Nasser, A. Egea-Àlvarez, and K. H. Ahmed, "A novel fractional-order damping control method for enhancing synchronization in grid-forming converters," in *2025 13th International Conference on Smart Grid (icSmartGrid)*, 2025: IEEE, pp. 125-130.

[45] M. Ebrahimi, S. A. Khajehoddin, and M. Karimi-Ghartemani, "An Improved Damping Method for Virtual Synchronous Machines," *IEEE Transactions on Sustainable Energy,* vol. 10, no. 3, pp. 1491-1500, 2019, doi: 10.1109/TSTE.2019.2902033.

[46] S. Dong and Y. C. Chen, "Adjusting Synchronverter Dynamic Response Speed via Damping Correction Loop," *IEEE Transactions on Energy Conversion,* vol. 32, no. 2, pp. 608-619, 2017, doi: 10.1109/TEC.2016.2645450.

[47] S. Laudahn, J. Seidel, B. Engel, T. Bülo, and D. Premm, "Substitution of synchronous generator based instantaneous frequency control utilizing inverter-coupled DER," in *2016 IEEE 7th International Symposium on Power Electronics for Distributed Generation Systems (PEDG)*, 27-30 June 2016 2016, pp. 1-8, doi: 10.1109/PEDG.2016.7527020.

[48] R. Jackson, S. A. Zulkifli, N. M. B. Sham, and E. Pathan, "A self-frequency restoration control based on droop strategy for autonomous microgrid," *International Journal of Renewable Energy Research,* vol. 9, no. 2, pp. 749-756, 2019.

[49] G. Yajuan, W. Weiyang, G. Xiaoqiang, and G. Herong, "An improved droop controller for grid-connected voltage source inverter in microgrid," in *The 2nd International Symposium on Power Electronics for Distributed Generation Systems*, 16-18 June 2010 2010, pp. 823-828, doi: 10.1109/PEDG.2010.5545801.

[50] M. Karimi-Ghartemani, S. A. Khajehoddin, P. Piya, and M. Ebrahimi, "Universal Controller for Three-Phase Inverters in a Microgrid," *IEEE Journal of Emerging and Selected Topics in Power Electronics,* vol. 4, no. 4, pp. 1342-1353, 2016, doi: 10.1109/JESTPE.2016.2614956.

[51] D. Chen, Y. Xu, and A. Q. Huang, "Integration of DC Microgrids as Virtual Synchronous Machines Into the AC Grid," *IEEE Transactions on Industrial Electronics,* vol. 64, no. 9, pp. 7455-7466, 2017, doi: 10.1109/TIE.2017.2674621.

[52] L. Huang *et al.*, "A Virtual Synchronous Control for Voltage-Source Converters Utilizing Dynamics of DC-Link Capacitor to Realize Self-Synchronization," *IEEE Journal of Emerging and Selected Topics in Power Electronics,* vol. 5, no. 4, pp. 1565-1577, 2017, doi: 10.1109/JESTPE.2017.2740424.

[53] L. Zhao, Z. Jin, and X. Wang, "Small-Signal Synchronization Stability of Grid-Forming Converters With Regulated DC-Link Dynamics," *IEEE Transactions on Industrial Electronics,* vol. 70, no. 12, pp. 12399-12409, 2023, doi: 10.1109/TIE.2023.3234147.

[54] P. Rodriguez, J. Pou, J. Bergas, J. I. Candela, R. P. Burgos, and D. Boroyevich, "Decoupled Double Synchronous Reference Frame PLL for Power Converters Control," *IEEE Transactions on Power Electronics,* vol. 22, no. 2, pp. 584-592, 2007, doi: 10.1109/TPEL.2006.890000.

[55] F. Ghassemi and M. Perry, "Review of voltage unbalance limit in the GB grid code CC. 6.1. 5 (b)," *National Grid, Report,* pp. 14-58, 2014.

[56] P. Wang, W. Cao, K. Liu, and J. Zhao, "An Unbalanced Component Detection Method and Compensation Strategy Based on Second-Order Generalized Integrator (SOGI)," in *2019 IEEE Power and Energy Conference at Illinois (PECI)*, 28 Feb.-1 March 2019 2019, pp. 1-6, doi: 10.1109/PECI.2019.8698909.

[57] V. Narayanan and B. Singh, "CNISOGI and VSSMCLMS Filters for Solving Grid and Load Abnormalities for a Microgrid With Seamless Mode Transfer Capability," *IEEE Transactions on Industry Applications,* vol. 59, no. 4, pp. 4225-4237, 2023, doi: 10.1109/TIA.2023.3259387.

[58] S. R. Mohapatra and V. Agarwal, "An Advanced Voltage Support Scheme Considering the Impact of Zero-Sequence Voltage Under Microgrid Faults Using

Model Predictive Control," *IEEE Transactions on Industrial Electronics,* vol. 67, no. 10, pp. 8957-8968, 2020, doi: 10.1109/TIE.2020.2972459.

[59] Q. Zhu, Q. Li, J. Zhang, and P. Cheng, "Virtual resistor circuit-based control strategy of STATCOM during network unbalance," *The Journal of Engineering,* vol. 2017, no. 13, pp. 1804-1808, 2017.

[60] L. Wang *et al.*, "Reduction of Three-Phase Voltage Unbalance Subject to Special Winding Connections of Two Single-Phase Distribution Transformers of a Microgrid System Using a Designed D-STATCOM Controller," *IEEE Transactions on Industry Applications,* vol. 54, no. 3, pp. 2002-2011, 2018, doi: 10.1109/TIA.2017.2786707.

[61] O. P. Taiwo, R. Tiako, and I. E. Davidson, "An improvement of voltage unbalance in a low voltage 11/0.4 kV electric power distribution network under 3-phase unbalance load condition using dynamic voltage restorer," in *2017 IEEE PES PowerAfrica*, 27-30 June 2017 2017, pp. 126-131, doi: 10.1109/PowerAfrica.2017.7991211.

[62] Y. Wang, G. Zhou, and X. Li, "A voltage unbalance compensation strategy based on virtual impedance for DGs in island microgrid without sequence component separation," *International Journal of Electrical Power & Energy Systems,* vol. 127, p. 106641, 2021/05/01/ 2021, doi: https://doi.org/10.1016/j.ijepes.2020.106641.

[63] M. M. Adibi and L. H. Fink, "Power system restoration planning," *IEEE Transactions on Power Systems,* vol. 9, no. 1, pp. 22-28, 1994, doi: 10.1109/59.317561.

[64] M. M. Adibi, L. R. J. Kafka, and D. P. Milanicz, "Expert system requirements for power system restoration," *IEEE Transactions on Power Systems,* vol. 9, no. 3, pp. 1592-1600, 1994, doi: 10.1109/59.336099.

[65] J. W. Feltes and C. Grande-Moran, "Black start studies for system restoration," in *2008 IEEE Power and Energy Society General Meeting - Conversion and Delivery of Electrical Energy in the 21st Century*, 20-24 July 2008 2008, pp. 1-8, doi: 10.1109/PES.2008.4596565.

[66] H. Jain, G. S. Seo, E. Lockhart, V. Gevorgian, and B. Kroposki, "Blackstart of Power Grids with Inverter-Based Resources," in *2020 IEEE Power & Energy Society General Meeting (PESGM)*, 2-6 Aug. 2020 2020, pp. 1-5, doi: 10.1109/PESGM41954.2020.9281851.

[67] W. Sun, C. C. Liu, and L. Zhang, "Optimal Generator Start-Up Strategy for Bulk Power System Restoration," *IEEE Transactions on Power Systems,* vol. 26, no. 3, pp. 1357-1366, 2011, doi: 10.1109/TPWRS.2010.2089646.

[68] G. Patsakis, D. Rajan, I. Aravena, J. Rios, and S. Oren, "Optimal Black Start Allocation for Power System Restoration," *IEEE Transactions on Power Systems,* vol. 33, no. 6, pp. 6766-6776, 2018, doi: 10.1109/TPWRS.2018.2839610.

[69] A. Golshani, W. Sun, Q. Zhou, Q. P. Zheng, and Y. Hou, "Incorporating Wind Energy in Power System Restoration Planning," *IEEE Transactions on Smart Grid,* vol. 10, no. 1, pp. 16-28, 2019, doi: 10.1109/TSG.2017.2729592.

[70] J. Zhao, Q. Zhang, L. I. U. Z, and W. U. X, "A Distributed Black-Start Optimization Method for Global Transmission and Distribution Network," *IEEE Transactions on Power Systems,* vol. 36, no. 5, pp. 4471-4481, 2021, doi: 10.1109/TPWRS.2021.3056096.

[71] Y. Hou, C. C. Liu, K. Sun, P. Zhang, S. Liu, and D. Mizumura, "Computation of milestones for decision support during system restoration," in *2011 IEEE Power and Energy Society General Meeting*, 24-28 July 2011 2011, pp. 1-10, doi: 10.1109/PES.2011.6039162.

[72] S. Liu, R. Podmore, and Y. Hou, "System Restoration Navigator: A decision support tool for System Restoration," in *2012 IEEE Power and Energy Society General Meeting*, 22-26 July 2012 2012, pp. 1-5, doi: 10.1109/PESGM.2012.6344826.

[73] S. Toune, H. Fudo, T. Genji, Y. Fukuyama, and Y. Nakanishi, "Comparative study of modern heuristic algorithms to service restoration in distribution systems," in *2002 IEEE Power Engineering Society Winter Meeting. Conference Proceedings (Cat. No.02CH37309)*, 27-31 Jan. 2002 2002, vol. 2, p. 787 vol.2, doi: 10.1109/PESW.2002.985113.

[74] T. Nagata and H. Sasaki, "A multi-agent approach to power system restoration," *IEEE Transactions on Power Systems,* vol. 17, no. 2, pp. 457-462, 2002, doi: 10.1109/TPWRS.2002.1007918.

[75] Z. Lin, F. Wen, and Y. Xue, "A Restorative Self-Healing Algorithm for Transmission Systems Based on Complex Network Theory," *IEEE Transactions on Smart Grid,* vol. 7, no. 4, pp. 2154-2162, 2016, doi: 10.1109/TSG.2016.2539199.

[76] Z. Pan, N. Jenkins, and J. Wu, "Black start from renewable energy resources: Review and a case study of Great Britain," *Renewable and Sustainable Energy Reviews,* vol. 209, p. 115143, 2025/03/01/ 2025, doi: https://doi.org/10.1016/j.rser.2024.115143.

[77] Z. Xu, P. Yang, Q. Zheng, and Z. Zeng, "Study on black start strategy of microgrid with PV and multiple energy storage systems," in *2015 18th International Conference on Electrical Machines and Systems (ICEMS)*, 25-28 Oct. 2015 2015, pp. 402-408, doi: 10.1109/ICEMS.2015.7385067.

[78] A. I. Saichev and W. Woyczynski, "Fourier transform," in *Distributions in the Physical and Engineering Sciences, Volume 1: Distributional and Fractal Calculus, Integral Transforms and Wavelets*: Springer, 2018, pp. 75-91.

[79] C. Kuriakose, *CIRCUIT THEORY: CONTINOUS AND DISCRETE-TIME SYSTEMS, ELEMENTS OF NETWORK SYNTHESIS*. PHI Learning Pvt. Ltd., 2005.

[80] C. H. Kim and R. Aggarwal, "Wavelet transforms in power systems. I. General introduction to the wavelet transforms," *Power Engineer,* vol. 14, no. 2, pp. 81-87, 2000.

[81] R. X. Gao and R. Yan, *Wavelets: Theory and applications for manufacturing*. Springer Science & Business Media, 2010.

[82] M. Farge, "Wavelet transforms and their applications to turbulence," *Annual review of fluid mechanics,* vol. 24, no. 1, pp. 395-458, 1992.

[83] H. Alzer, "On some inequalities for the incomplete gamma function," *Mathematics of Computation,* vol. 66, no. 218, pp. 771-778, 1997.

[84] A. Ebaid and H. K. Al-Jeaid, "The mittag–leffler functions for a class of first-order fractional initial value problems: dual solution via riemann–liouville fractional derivative," *Fractal and Fractional,* vol. 6, no. 2, p. 85, 2022.

[85] I. Podlubny, "Fractional differential equations academic press, san diego, 1999," *Search in,* 1999.

[86] D. Sierociuk, "Fractional variable order derivative Simulink toolkit," *MATLAB Central File Exchange,* 2012.

[87] D. E. Catlin, *Estimation, control, and the discrete Kalman filter*. Springer Science & Business Media, 2012.

[88] Z. L. Chuan, S. M. Deni, S.-F. Fam, and N. Ismail, "The effectiveness of a probabilistic principal component analysis model and expectation maximisation algorithm in treating missing daily rainfall data," *Asia-Pacific Journal of Atmospheric Sciences,* vol. 56, no. 1, pp. 119-129, 2020.

[89] M. E. Khan and D. N. Dutt, "An expectation-maximization algorithm based Kalman smoother approach for event-related desynchronization (ERD) estimation from EEG," *IEEE transactions on biomedical engineering,* vol. 54, no. 7, pp. 1191-1198, 2007.

[90] J. F. Hauer, "Initial Results in the Use of Prony Methods to Determine the Damping and Modal Composition of Power System Dynamic Response Signals," USDOE Bonneville Power Administration, Portland, OR (United States), 1988.

[91] C. A. Floudas and X. Lin, "Mixed integer linear programming in process scheduling: Modeling, algorithms, and applications," *Annals of Operations Research,* vol. 139, no. 1, pp. 131-162, 2005.

[92] L. Meegahapola, A. Sguarezi, J. S. Bryant, M. Gu, E. R. Conde D, and R. B. Cunha, "Power system stability with power-electronic converter interfaced renewable power generation: Present issues and future trends," *Energies,* vol. 13, no. 13, p. 3441, 2020.

[93] R. Hesaraki, "Remedial action schemes for power system performance enhancement using protective relaying," Memorial University of Newfoundland, 2020.

[94] Z. Li, H. Liu, J. Zhao, T. Bi, and Q. Yang, "A power system disturbance classification method robust to PMU data quality issues," *IEEE Transactions on Industrial Informatics,* vol. 18, no. 1, pp. 130-142, 2021.

[95] T. Qoria *et al.*, "WP3-Control and Operation of a Grid with 100% Converter-Based Devices. Deliverable 3.2: Local control and simulation tools for large transmission systems," *MIGRATE Project,* pp. 1-89, 2018.

[96] G. Liu, H. Zhang, and X. Song, "Position-estimation deviation-suppression technology of PMSM combining phase self-compensation SMO and feed-forward PLL," *IEEE Journal of Emerging and Selected Topics in Power Electronics,* vol. 9, no. 1, pp. 335-344, 2020.

[97] Y. F. Wang and Y. W. Li, "Grid synchronization PLL based on cascaded delayed signal cancellation," *IEEE Transactions on Power Electronics,* vol. 26, no. 7, pp. 1987-1997, 2010.

# Appendices

## Appendix A: ADN Test System Network and Load Data

This appendix contains branch impedance data and aggregate load demand data at each bus for the 12.66 kV ADN test system described in Section 7.1. Bus 0 represents the substation slack bus and carries no load.

**Table A.1:** Branch data for ADN.

| Branch | From | To | R (Ω) | X (Ω) | Smax (MVA) | Branch | From | To | R (Ω) | X (Ω) | $S_{max}$ (MVA) |
|---|---|---|---|---|---|---|---|---|---|---|---|
| **1** | 0 | 1 | 0.0922 | 0.0477 | 20 | **20** | 19 | 20 | 0.4095 | 0.4784 | 10 |
| **2** | 1 | 2 | 0.4930 | 0.2511 | 20 | **21** | 20 | 21 | 0.7089 | 0.9373 | 10 |
| **3** | 2 | 3 | 0.3660 | 0.1864 | 20 | **22** | 2 | 22 | 0.4512 | 0.3083 | 10 |
| **4** | 3 | 4 | 0.3811 | 0.1941 | 20 | **23** | 22 | 23 | 0.8980 | 0.7091 | 10 |
| **5** | 4 | 5 | 0.8190 | 0.7070 | 20 | **24** | 23 | 24 | 0.8960 | 0.7011 | 10 |
| **6** | 5 | 6 | 0.1872 | 0.6188 | 20 | **25** | 5 | 25 | 0.2030 | 0.1034 | 12 |
| **7** | 6 | 7 | 0.7114 | 0.2351 | 20 | **26** | 25 | 26 | 0.2842 | 0.1447 | 12 |
| **8** | 7 | 8 | 1.0300 | 0.7400 | 12 | **27** | 26 | 27 | 1.0590 | 0.9337 | 12 |
| **9** | 8 | 9 | 1.0440 | 0.7400 | 12 | **28** | 27 | 28 | 0.8042 | 0.7006 | 12 |
| **10** | 9 | 10 | 0.1966 | 0.0650 | 12 | **29** | 28 | 29 | 0.5075 | 0.2585 | 12 |
| **11** | 10 | 11 | 0.3744 | 0.1238 | 12 | **30** | 29 | 30 | 0.9744 | 0.9630 | 12 |
| **12** | 11 | 12 | 1.4680 | 1.1550 | 12 | **31** | 30 | 31 | 0.3105 | 0.3619 | 12 |
| **13** | 12 | 13 | 0.5416 | 0.7129 | 12 | **32** | 31 | 32 | 0.3410 | 0.5302 | 12 |
| **14** | 13 | 14 | 0.5910 | 0.5260 | 12 | | | | | | |
| **15** | 14 | 15 | 0.5460 | 0.5450 | 12 | | | | | | |
| **16** | 15 | 16 | 0.7463 | 0.5450 | 12 | | | | | | |
| **17** | 16 | 17 | 1.2890 | 1.7210 | 12 | | | | | | |
| **18** | 1 | 18 | 0.1640 | 0.1565 | 10 | | | | | | |
| **19** | 18 | 19 | 1.5042 | 1.3554 | 10 | | | | | | |

**Table A.2:** Load data for ADN.

| Load | P (MW) | Q (MVAr) | Sector | Load | P (MW) | Q (MVAr) | Sector |
|---|---|---|---|---|---|---|---|
| **L1** | 0.500 | 0.300 | 2 | **L17** | 0.450 | 0.200 | 5 |
| **L2** | 0.450 | 0.200 | 3 | **L18** | 0.450 | 0.200 | 2 |
| **L3** | 0.600 | 0.400 | 5 | **L19** | 0.450 | 0.200 | 3 |
| **L4** | 0.300 | 0.150 | 1 | **L20** | 0.450 | 0.200 | 3 |
| **L5** | 0.300 | 0.100 | 1 | **L21** | 0.450 | 0.200 | 4 |
| **L6** | 1.000 | 0.500 | 5 | **L22** | 0.450 | 0.250 | 4 |
| **L7** | 1.000 | 0.500 | 5 | **L23** | 2.100 | 1.000 | 5 |
| **L8** | 0.300 | 0.100 | 1 | **L24** | 2.100 | 1.000 | 4 |
| **L9** | 0.300 | 0.100 | 1 | **L25** | 0.300 | 0.125 | 1 |
| **L10** | 0.225 | 0.150 | 1 | **L26** | 0.300 | 0.125 | 1 |
| **L11** | 0.300 | 0.175 | 3 | **L27** | 0.300 | 0.100 | 2 |
| **L12** | 0.300 | 0.175 | 3 | **L28** | 0.600 | 0.350 | 4 |
| **L13** | 0.600 | 0.400 | 4 | **L29** | 1.000 | 3.000 | 4 |
| **L14** | 0.300 | 0.050 | 1 | **L30** | 0.750 | 0.350 | 3 |
| **L15** | 0.300 | 0.100 | 2 | **L31** | 1.050 | 0.500 | 5 |
| **L16** | 0.300 | 0.100 | 3 | **L32** | 0.300 | 0.200 | 3 |

**Sector Key:**

1 = Residential
2 = Governmental
3 = Commercial
4 = Small-industrial
5 = Important power customer

# Appendix B: CPLEX OPL Code for the Mixed-Integer Linear Programming Restoration Model

This appendix presents the complete OPL (Optimisation Programming Language) implementation of the mixed-integer linear programming formulation developed in Chapter 7. The model is solved using IBM ILOG CPLEX Optimisation Studio and encodes the sequential service restoration problem for active distribution networks under black-start conditions.

```
 *   ADN BLACK-START RESTORATION – MILP FORMULATION
 *   RUN 1: Set all USE_Mx = 0  → Baseline (S0)
 *   RUN 2: Set all USE_Mx = 1  → Proposed (S5)
// 1. SETS & DIMENSIONS
int NB   = 33;
int NL   = 37;
int NG   = 5;
int ND   = 32;
int TBS  = 40;
int Nsec = 5;
range rB  = 0..NB-1;
range rL  = 1..NL;
range rG  = 1..NG;
range rD  = 1..ND;
range rT  = 0..TBS;
range rT1 = 1..TBS;
// 2. SYSTEM PARAMETERS
float dt        = 1.0;
float Vbase_kV = 12.66;
float Sbase     = 10.0;
float Zbase     = Vbase_kV*Vbase_kV/Sbase;
float Vmin      = 0.9;
float Vmax      = 1.1;
float Umin      = Vmin*Vmin;
float Umax      = Vmax*Vmax;
float df_max    = 0.5;
float alpha_R   = 0.1;
int   t_line    = 1;
int   Nroot     = 1;
float Mbig      = 10.0;
int USE_TIES = 0;
// 2b. METHOD SWITCHES
int USE_M1_INERTIA_EST   = 0;
int USE_M2_FREQ_EST      = 0;
int USE_M3_DAMPING_CTRL  = 0;
int USE_M4_UNBAL_CTRL    = 0;
// 3. DG DATA
int   is_BSDG  [rG] = [1,     0,     0,     0,     0    ];
int   bus_DG   [rG] = [0,     7,     16,    20,    32   ];
float Pmax_DG  [rG] = [6.0,   4.5,   3.5,   7.0,   8.0  ];
float Qmax_DG  [rG] = [4.5,   1.2,   1.0,   4.0,   3.0  ];
float Qmin_DG  [rG] = [-1.2, -0.5,  -0.4,  -1.5,  -1.0  ];
float Pstart_DG[rG] = [0.0,   0.12,  0.1,   0.2,   0.2  ];
int   tDG      [rG] = [2,     2,     1,     4,     2    ];
float R_DG     [rG] = [2.0,   0.9,   0.7,   2.0,   1.6  ];
float K_DG     [rG] = [2.0,   0.45,  0.4,   2.0,   1.8  ];
int   is_GFM    [rG] = [1,    0,    0,    0,    1    ];
```

```
float S_DG_MVA  [rG] = [7.5,  4.66, 3.64, 8.06, 8.54];
float H_DG      [rG] = [4.0,  0.0,  3.0,  4.5,  5.0 ];
// 3b. METHOD PARAMETERS
// M1: Inertia estimation confidence
float eta_H_without = 0.9091;
float eta_H_with    = 0.9430;
float eta_H = (USE_M1_INERTIA_EST == 1) ? eta_H_with : eta_H_without;
// M2: RoCoF detection confidence
float mu_R_without = 0.8957;
float mu_R_with    = 0.9853;
float mu_R = (USE_M2_FREQ_EST == 1) ? mu_R_with : mu_R_without;
// M3: FOD damping enhancement
float D_ctrl_factor = 0.39286;
float D_ctrl_KDG[g in rG] =
  (USE_M3_DAMPING_CTRL == 1 && is_GFM[g] == 1)
    ? K_DG[g] * D_ctrl_factor : 0.0;
// M4: Unbalance derating
float gamma_without = 0.8889;
float gamma_with    = 0.6154;
float gamma_eff[g in rG] =
  (USE_M4_UNBAL_CTRL == 1)
    ? ((g == 5) ? gamma_with : 1.00)
    : gamma_without;
// 3c. EFFECTIVE PARAMETERS
float f0            = 50.0;
float ROCOF_max_phys = 0.50;
float ROCOF_eff      = ROCOF_max_phys * mu_R;
float Pmax_eff [g in rG] = gamma_eff[g] * Pmax_DG[g];
float Qmax_eff [g in rG] = gamma_eff[g] * Qmax_DG[g];
float Qmin_eff [g in rG] = gamma_eff[g] * Qmin_DG[g];
float K_DG_eff [g in rG] = K_DG[g] + D_ctrl_KDG[g];
// 4. LOAD DATA
float PL[rD] = [
  0.500, 0.450, 0.600, 0.300, 0.300,
  1.000, 1.000, 0.300, 0.300, 0.225,
  0.300, 0.300, 0.600, 0.300, 0.300,
  0.300, 0.450, 0.450, 0.450, 0.450,
  0.450, 0.450, 2.100, 2.100, 0.300,
  0.300, 0.300, 0.600, 1.000, 0.750,
  1.050, 0.300
];
float QL[rD] = [
  0.300, 0.200, 0.400, 0.150, 0.100,
  0.500, 0.500, 0.100, 0.100, 0.150,
  0.175, 0.175, 0.400, 0.050, 0.100,
  0.100, 0.200, 0.200, 0.200, 0.200,
  0.200, 0.250, 1.000, 1.000, 0.125,
  0.125, 0.100, 0.350, 3.000, 0.350,
  0.500, 0.200
];
// 5. LOAD SECTORS — Table 7.2
int sector[rD] = [
  2, 3, 5, 1, 1,
  5, 5, 1, 1, 1,
  3, 3, 4, 1, 2,
  3, 5, 2, 3, 3,
  4, 4, 5, 4, 1,
  1, 2, 4, 4, 3,
  5, 3
];
// 6. CUSTOMER DAMAGE FUNCTIONS
float CDF_bp_t[1..5] = [0.0, 1.0, 20.0, 60.0, 120.0];
float CDF_bp_v[1..Nsec][1..5] = [
```

```
  [0.000,   0.004,  0.208,   0.747,   1.557 ],
  [0.000,   1.748,  3.076,   7.213,   9.201 ],
  [1.371,   1.412,  5.386,  14.746,  28.787 ],
  [8.516,   8.958, 19.759,  34.976,  57.802 ],
  [16.703, 75.920,175.677, 229.696, 285.163 ]
];
float CDF[s in 1..Nsec][t in 0..TBS];
execute INIT_CDF {
  for(var s=1; s<=Nsec; s++) {
    for(var tm=0; tm<=TBS; tm++) {
      var seg = 1;
      for(var bp=2; bp<=5; bp++) {
        if(tm > CDF_bp_t[bp]) seg = bp;
      }
      if(seg >= 5) seg = 4;
      var t0 = CDF_bp_t[seg];
      var t1 = CDF_bp_t[seg+1];
      var f0 = CDF_bp_v[s][seg];
      var f1 = CDF_bp_v[s][seg+1];
      CDF[s][tm] = f0 + (tm - t0)/(t1 - t0) * (f1 - f0);
    }
  }
}
// Incremental CDF
float dCDF[s in 1..Nsec][t in 1..TBS];
execute INIT_dCDF {
  for(var s=1; s<=Nsec; s++)
    for(var t=1; t<=TBS; t++)
      dCDF[s][t] = CDF[s][t] - CDF[s][t-1];
}
// 7. LINE DATA
int line_fr[rL] = [
  0,  1,  2,  3,  4,  5,  6,  7,  8,  9,
  10, 11, 12, 13, 14, 15, 16,
  1, 18, 19, 20,
  2, 22, 23,
  5, 25, 26, 27, 28, 29, 30, 31,
  7,  8, 11, 17, 24
];
int line_to[rL] = [
  1,  2,  3,  4,  5,  6,  7,  8,  9, 10,
  11, 12, 13, 14, 15, 16, 17,
  18, 19, 20, 21,
  22, 23, 24,
  25, 26, 27, 28, 29, 30, 31, 32,
  20, 14, 21, 32, 28
];
float R_ohm[rL] = [
  0.0922, 0.4930, 0.3660, 0.3811, 0.8190,
  0.1872, 0.7114, 1.0300, 1.0440, 0.1966,
  0.3744, 1.4680, 0.5416, 0.5910, 0.5460,
  0.7463, 1.2890,
  0.1640, 1.5042, 0.4095, 0.7089,
  0.4512, 0.8980, 0.8960,
  0.2030, 0.2842, 1.0590, 0.8042, 0.5075,
  0.9744, 0.3105, 0.3410,
  2.0000, 2.0000, 2.0000, 0.5000, 0.5000
];
float X_ohm[rL] = [
  0.0477, 0.2511, 0.1864, 0.1941, 0.7070,
  0.6188, 0.2351, 0.7400, 0.7400, 0.0650,
  0.1238, 1.1550, 0.7129, 0.5260, 0.5450,
  0.5450, 1.7210,
```

```
  0.1565, 1.3554, 0.4784, 0.9373,
  0.3083, 0.7091, 0.7011,
  0.1034, 0.1447, 0.9337, 0.7006, 0.2585,
  0.9630, 0.3619, 0.5302,
  2.0000, 2.0000, 2.0000, 0.5000, 0.5000
];
float r_pu[l in rL] = R_ohm[l] / Zbase;
float x_pu[l in rL] = X_ohm[l] / Zbase;
float Smax_line[rL];
execute INIT_SMAX {
  for(var l=1; l<=NL; l++) {
    if(l <= 7)       Smax_line[l] = 20.0;
    else if(l <= 17) Smax_line[l] = 12.0;
    else if(l <= 21) Smax_line[l] = 10.0;
    else if(l <= 24) Smax_line[l] = 10.0;
    else if(l <= 32) Smax_line[l] = 12.0;
    else             Smax_line[l] = 8.0;
  }
}
float Pmax_line[l in rL] = Smax_line[l];
float Qmax_line[l in rL] = Smax_line[l];
// 8. CONFIGURATION SUMMARY
execute PRINT_CONFIG {
  var totP = 0; var totQ = 0;
  for(var d=1; d<=ND; d++) { totP += PL[d]; totQ += QL[d]; }
  var totPG = 0;
  for(var g=1; g<=NG; g++) totPG += Pmax_DG[g];
  var scen = "S0_Baseline";
  if(USE_M1_INERTIA_EST==1 && USE_M2_FREQ_EST==1
     && USE_M3_DAMPING_CTRL==1 && USE_M4_UNBAL_CTRL==1)
    scen = "S5_Proposed";
  writeln("====================================================");
  writeln("  ADN Black-Start Restoration");
  writeln("  SCENARIO: ", scen);
  writeln("====================================================");
  writeln("  Buses=",NB," Lines=",NL," DGs=",NG," Loads=",ND);
  writeln("  TBS=",TBS," steps, dt=",dt," min");
  writeln("  Total Pd=",totP," MW, Qd=",totQ," Mvar");
  writeln("  Total DG Pmax=",totPG," MW");
  writeln("  Voltage: ",Vmin,"-",Vmax," p.u.");
  writeln("----------------------------------------------------");
  writeln("  M1 Inertia Est.   : ",
    (USE_M1_INERTIA_EST==1?"ON":"OFF"),"  eta_H=",eta_H);
  writeln("  M2 Frequency Est.: ",
    (USE_M2_FREQ_EST==1?"ON":"OFF"),"  mu_R=",mu_R);
  writeln("  M3 Damping Ctrl   : ",
    (USE_M3_DAMPING_CTRL==1?"ON":"OFF"),"  factor=",D_ctrl_factor);
  writeln("  M4 Unbalance Ctrl: ",
    (USE_M4_UNBAL_CTRL==1?"ON":"OFF"));
  writeln("----------------------------------------------------");
  writeln("  ROCOF_eff=",ROCOF_eff," Hz/s");
  writeln("----------------------------------------------------");
  for(var g=1; g<=NG; g++) {
    var gtype = (is_GFM[g]==1 ? "GFM" : " SG");
    var E_g = H_DG[g]*S_DG_MVA[g];
    writeln("  DG",g," [",gtype,"] bus=",bus_DG[g],
      " Pmax=",Pmax_DG[g],"->",Pmax_eff[g],"MW",
      " K_DG=",K_DG[g],"->",K_DG_eff[g],"MW/Hz",
      " E=",E_g,"MJ",
      " gamma=",gamma_eff[g]);
  }
  writeln("====================================================");
}
```

```
execute CPLEX_SETTINGS {
  cplex.tilim      = 300;
  cplex.epgap      = 0.02;
  cplex.mipemphasis = 1;
  cplex.threads    = 0;
  cplex.probe      = 3;
  cplex.fpheur     = 2;
  cplex.lbheur     = 1;
  cplex.mipdisplay = 2;
}
// 9. DECISION VARIABLES
dvar boolean u_bus  [rB][rT];
dvar boolean u_line [rL][rT];
dvar boolean u_DG   [rG][rT];
dvar boolean u_Load [rD][rT];
dvar float+  P_DG   [rG][rT];
dvar float   Q_DG   [rG][rT];
dvar float   P_line [rL][rT];
dvar float   Q_line [rL][rT];
dvar float+  U_bus  [rB][rT];
dvar float+  P_R    [rG][rT1];
dvar float+  E_hat  [rT];
dvar float   delta_P[rT1];
// 10. OBJECTIVE
minimize
  sum(k in rD, t in rT1)
    PL[k] * dCDF[sector[k]][t] * (1 - u_Load[k][t]);
// 11. CONSTRAINTS
subject to {
  // Tie switches locked open
  forall(l in 33..37, t in rT: USE_TIES == 0)
    u_line[l][t] == 0;
  // (a) System initialisation
  u_bus[0][0]  == 1;
  u_DG[1][0]   == 1;
  forall(b in 1..NB-1) u_bus[b][0]  == 0;
  forall(g in 2..NG)   u_DG[g][0]   == 0;
  forall(l in rL)      u_line[l][0] == 0;
  forall(k in rD)      u_Load[k][0] == 0;
  // (b) End-of-horizon
  forall(k in rD)      u_Load[k][TBS] == 1;
  // (c) Restoration irreversibility
  forall(b in rB, t in rT1)  u_bus[b][t]  >= u_bus[b][t-1];
  forall(l in rL, t in rT1)  u_line[l][t] >= u_line[l][t-1];
  forall(g in rG, t in rT1)  u_DG[g][t]   >= u_DG[g][t-1];
  forall(k in rD, t in rT1)  u_Load[k][t] >= u_Load[k][t-1];
  // (d) Component energisation dependencies
  forall(g in rG: is_BSDG[g]==0, t in rT1: t <= tDG[g])
    u_DG[g][t] == 0;
  forall(g in rG: is_BSDG[g]==0, t in rT1: t > tDG[g])
    u_DG[g][t] <= u_bus[bus_DG[g]][t - tDG[g]];
  forall(k in rD, t in rT1)
    u_Load[k][t] <= u_bus[k][t];
  forall(l in rL, t in rT1: t >= t_line+1)
    u_line[l][t] - u_line[l][t-1]
      <= u_bus[line_fr[l]][t-t_line] + u_bus[line_to[l]][t-t_line];
  forall(l in rL, t in rT1: t < t_line+1)
    u_line[l][t] == 0;
  forall(l in rL, t in rT1) {
    u_line[l][t] <= u_bus[line_fr[l]][t];
    u_line[l][t] <= u_bus[line_to[l]][t];
  }
  forall(b in rB, t in rT1)
```

```
  u_bus[b][t] <=
    sum(g in rG: is_BSDG[g]==1 && bus_DG[g]==b) u_DG[g][t]
    + sum(l in rL: line_fr[l]==b || line_to[l]==b) u_line[l][t];
// (e) Radial topology
forall(t in rT1)
  sum(l in rL) u_line[l][t]
    == sum(b in rB) u_bus[b][t] - Nroot;
// (f) Generator output limits
forall(g in rG, t in rT) {
  P_DG[g][t] <= Pmax_eff[g] * u_DG[g][t];
  Q_DG[g][t] >= Qmin_eff[g] * u_DG[g][t];
  Q_DG[g][t] <= Qmax_eff[g] * u_DG[g][t];
}
// (g) Generator ramp
forall(g in rG, t in rT1) {
  P_DG[g][t] - P_DG[g][t-1] <= R_DG[g] * dt;
  P_DG[g][t] - P_DG[g][t-1] >= 0;
}
// (h) Power balance
forall(b in rB, t in rT1)
  sum(g in rG: bus_DG[g]==b) P_DG[g][t]
  - sum(k in rD: k==b) PL[k] * u_Load[k][t]
  - sum(g in rG: bus_DG[g]==b && is_BSDG[g]==0)
      Pstart_DG[g] * (u_bus[b][t] - u_DG[g][t])
  == sum(l in rL: line_fr[l]==b) P_line[l][t]
   - sum(l in rL: line_to[l]==b) P_line[l][t];
forall(b in rB, t in rT1)
  sum(g in rG: bus_DG[g]==b) Q_DG[g][t]
  - sum(k in rD: k==b) QL[k] * u_Load[k][t]
  == sum(l in rL: line_fr[l]==b) Q_line[l][t]
   - sum(l in rL: line_to[l]==b) Q_line[l][t];
forall(b in rB) {
  sum(g in rG: bus_DG[g]==b) P_DG[g][0]
    - sum(g in rG: bus_DG[g]==b && is_BSDG[g]==0)
        Pstart_DG[g] * (u_bus[b][0] - u_DG[g][0])
    == sum(l in rL: line_fr[l]==b) P_line[l][0]
     - sum(l in rL: line_to[l]==b) P_line[l][0];
  sum(g in rG: bus_DG[g]==b) Q_DG[g][0]
    == sum(l in rL: line_fr[l]==b) Q_line[l][0]
     - sum(l in rL: line_to[l]==b) Q_line[l][0];
}
// (i) Branch flow limits
forall(l in rL, t in rT) {
  P_line[l][t] <=  Pmax_line[l] * u_line[l][t];
  P_line[l][t] >= -Pmax_line[l] * u_line[l][t];
  Q_line[l][t] <=  Qmax_line[l] * u_line[l][t];
  Q_line[l][t] >= -Qmax_line[l] * u_line[l][t];
  P_line[l][t] + Q_line[l][t] <=  1.4142*Smax_line[l]*u_line[l][t];
  P_line[l][t] + Q_line[l][t] >= -1.4142*Smax_line[l]*u_line[l][t];
  P_line[l][t] - Q_line[l][t] <=  1.4142*Smax_line[l]*u_line[l][t];
  P_line[l][t] - Q_line[l][t] >= -1.4142*Smax_line[l]*u_line[l][t];
}
// (j) Voltage
forall(t in rT) U_bus[0][t] == 1.0 * u_bus[0][t];
forall(l in rL, t in rT) {
  U_bus[line_fr[l]][t] - U_bus[line_to[l]][t]
    - 2.0*(r_pu[l]*P_line[l][t] + x_pu[l]*Q_line[l][t]) / Sbase
    <=  Mbig * (1 - u_line[l][t]);
  U_bus[line_fr[l]][t] - U_bus[line_to[l]][t]
    - 2.0*(r_pu[l]*P_line[l][t] + x_pu[l]*Q_line[l][t]) / Sbase
    >= -Mbig * (1 - u_line[l][t]);
}
forall(b in rB, t in rT) {
```

```
    U_bus[b][t] >= Umin * u_bus[b][t];
    U_bus[b][t] <= Umax * u_bus[b][t];
  }
  // (k) Frequency stability and reserve
  // Estimated inertia energy
  forall(t in rT)
    E_hat[t] == eta_H * sum(g in rG) H_DG[g] * S_DG_MVA[g] * u_DG[g][t];

  // Net power step
  forall(t in rT1)
    delta_P[t] == sum(k in rD) PL[k] * (u_Load[k][t] - u_Load[k][t-1])
                + sum(g in rG: is_BSDG[g]==0)
                    Pstart_DG[g] * ( (u_bus[bus_DG[g]][t] - u_DG[g][t])
                                   - (u_bus[bus_DG[g]][t-1] - u_DG[g][t-1]) );
  // QSS frequency limit
  forall(t in rT1)
    delta_P[t] <= df_max * sum(g in rG) K_DG_eff[g] * u_DG[g][t];
  // ROCOF constraint
  forall(t in rT1)
    f0 * delta_P[t] <= 2.0 * ROCOF_eff * E_hat[t];
  // Per-generator reserve
  forall(g in rG, t in rT1) {
    P_R[g][t] <= Pmax_eff[g] * u_DG[g][t] - P_DG[g][t];
    P_R[g][t] <= R_DG[g] * dt;
  }
  // System reserve requirement
  forall(t in rT1)
    sum(g in rG) P_R[g][t]
      >= alpha_R * (
           sum(k in rD) PL[k] * u_Load[k][t]
           + sum(g in rG: is_BSDG[g]==0)
               Pstart_DG[g] * (u_bus[bus_DG[g]][t] - u_DG[g][t])
         );
}
// 12. POST-PROCESSING
execute RESULTS {
  var prefix = "S0";
  if(USE_M1_INERTIA_EST==1 && USE_M2_FREQ_EST==1
     && USE_M3_DAMPING_CTRL==1 && USE_M4_UNBAL_CTRL==1)
    prefix = "S5";
  var cost_var = 0;
  for(var k=1; k<=ND; k++) {
    var steps_off = 0;
    for(var t=1; t<=TBS; t++)
      if(u_Load[k][t] < 0.5) steps_off++;
    cost_var += PL[k] * CDF[sector[k]][steps_off];
  }
  writeln("");
  writeln("====================================================");
  writeln("  ADN BLACK-START RESULT  [",prefix,"]");
  writeln("====================================================");
  writeln("  M1=",USE_M1_INERTIA_EST," M2=",USE_M2_FREQ_EST,
    " M3=",USE_M3_DAMPING_CTRL," M4=",USE_M4_UNBAL_CTRL);
  writeln("  eta_H=",eta_H," mu_R=",mu_R);
  writeln("  Total outage cost: ", cost_var, " k$");
  writeln("  Objective value: ", cplex.getObjValue());
  var makespan = 0;
  for(var k=1; k<=ND; k++) {
    for(var t=1; t<=TBS; t++) {
      if(u_Load[k][t] > 0.5 && (t==1 || u_Load[k][t-1] < 0.5)) {
        if(t > makespan) makespan = t;
      }
    }
```

```
}
writeln("  Makespan: ", makespan, " min");
writeln("----------------------------------------------------");
// DG schedule
writeln("  DG Schedule:");
for(var g=1; g<=NG; g++) {
  var t_on = -1;
  for(var t=0; t<=TBS; t++) {
    if(u_DG[g][t] > 0.5) { t_on = t; break; }
  }
  if(t_on >= 0) {
    var gtype = (is_GFM[g]==1 ? "GFM" : "SG ");
    writeln("    DG",g," [",gtype,"] bus=",bus_DG[g],
      " ON at t=",t_on,"min",
      " Peff=",Pmax_eff[g],"MW",
      " Keff=",K_DG_eff[g],"MW/Hz");
  }
}
// Restoration sequence
writeln("  Restoration Sequence:");
for(var t=1; t<=TBS; t++) {
  var events = "";
  for(var g=1; g<=NG; g++)
    if(t >= 1 && u_DG[g][t] > 0.5 && u_DG[g][t-1] < 0.5)
      events += " DG" + g;
  for(var l=1; l<=NL; l++)
    if(u_line[l][t] > 0.5 && u_line[l][t-1] < 0.5)
      events += " Br" + line_fr[l] + "-" + line_to[l];
  for(var k=1; k<=ND; k++)
    if(u_Load[k][t] > 0.5 && u_Load[k][t-1] < 0.5)
      events += " L" + k;
  if(events != "")
    writeln("    t=",t,": ",events);
}
// Per-sector outage cost
writeln("  Per-Sector Outage Cost:");
var sec_names = new Array("Residential","Governmental",
  "Commercial","SmallIndustrial","ImportantPower");
for(var s=1; s<=Nsec; s++) {
  var sec_cost = 0;
  var sec_count = 0;
  for(var k=1; k<=ND; k++) {
    if(sector[k] == s) {
      sec_count++;
      var soff = 0;
      for(var t=1; t<=TBS; t++)
        if(u_Load[k][t] < 0.5) soff++;
      sec_cost += PL[k] * CDF[s][soff];
    }
  }
  writeln("    ",sec_names[s-1],": ",sec_count," loads, cost=",
    sec_cost," k$");
}
// Load curve
writeln("  Load Curve (MW):");
for(var t=0; t<=TBS; t+=5) {
  var tot = 0;
  for(var k=1; k<=ND; k++)
    tot += PL[k] * (u_Load[k][t]>0.5?1:0);
  writeln("    t=",t,": ",tot," MW");
}
writeln("====================================================");
// ── Output files ──
```

```
var f;
f = new IloOplOutputFile(prefix+"_ADN_u_bus.txt");
for(var b=0; b<NB; b++) {
  for(var t=0; t<=TBS; t++) {
    f.write((u_bus[b][t]>0.5?1:0));
    if(t<TBS) f.write(" ");
  } f.writeln();
} f.close();
f = new IloOplOutputFile(prefix+"_ADN_u_line.txt");
for(var l=1; l<=NL; l++) {
  for(var t=0; t<=TBS; t++) {
    f.write((u_line[l][t]>0.5?1:0));
    if(t<TBS) f.write(" ");
  } f.writeln();
} f.close();
f = new IloOplOutputFile(prefix+"_ADN_u_DG.txt");
for(var g=1; g<=NG; g++) {
  for(var t=0; t<=TBS; t++) {
    f.write((u_DG[g][t]>0.5?1:0));
    if(t<TBS) f.write(" ");
  } f.writeln();
} f.close();

f = new IloOplOutputFile(prefix+"_ADN_u_Load.txt");
for(var k=1; k<=ND; k++) {
  for(var t=0; t<=TBS; t++) {
    f.write((u_Load[k][t]>0.5?1:0));
    if(t<TBS) f.write(" ");
  } f.writeln();
} f.close();
f = new IloOplOutputFile(prefix+"_ADN_P_DG.txt");
for(var g=1; g<=NG; g++) {
  for(var t=0; t<=TBS; t++) {
    f.write(P_DG[g][t]);
    if(t<TBS) f.write(" ");
  } f.writeln();
} f.close();
f = new IloOplOutputFile(prefix+"_ADN_Q_DG.txt");
for(var g=1; g<=NG; g++) {
  for(var t=0; t<=TBS; t++) {
    f.write(Q_DG[g][t]);
    if(t<TBS) f.write(" ");
  } f.writeln();
} f.close();
f = new IloOplOutputFile(prefix+"_ADN_P_line.txt");
for(var l=1; l<=NL; l++) {
  for(var t=0; t<=TBS; t++) {
    f.write(P_line[l][t]);
    if(t<TBS) f.write(" ");
  } f.writeln();
} f.close();
f = new IloOplOutputFile(prefix+"_ADN_U_bus.txt");
for(var b=0; b<NB; b++) {
  for(var t=0; t<=TBS; t++) {
    f.write(U_bus[b][t]);
    if(t<TBS) f.write(" ");
  } f.writeln();
} f.close();
f = new IloOplOutputFile(prefix+"_ADN_E_hat.txt");
for(var t=0; t<=TBS; t++) {
  f.write(E_hat[t]);
  if(t<TBS) f.write(" ");
} f.writeln(); f.close();
```

```
  f = new IloOplOutputFile(prefix+"_ADN_delta_P.txt");
  for(var t=1; t<=TBS; t++) {
    f.write(delta_P[t]);
    if(t<TBS) f.write(" ");
  } f.writeln(); f.close();
  f = new IloOplOutputFile(prefix+"_ADN_summary.txt");
  f.writeln("Scenario "+prefix);
  f.writeln("M1="+USE_M1_INERTIA_EST+" M2="+USE_M2_FREQ_EST
    +" M3="+USE_M3_DAMPING_CTRL+" M4="+USE_M4_UNBAL_CTRL);
  f.writeln("eta_H "+eta_H);
  f.writeln("mu_R "+mu_R);
  f.writeln("ROCOF_eff "+ROCOF_eff);
  f.writeln("Makespan "+makespan+" min");
  f.writeln("Outage_cost "+cost_var+" k$");
  f.writeln("Obj_value "+cplex.getObjValue());
  for(var g=1; g<=NG; g++) {
    var t_on2 = -1;
    for(var t=0; t<=TBS; t++) {
      if(u_DG[g][t] > 0.5) { t_on2 = t; break; }
    }
    f.writeln("DG"+g+" bus="+bus_DG[g]
      +" GFM="+is_GFM[g]
      +" ON_at="+t_on2
      +" Pmax="+Pmax_DG[g]
      +" Peff="+Pmax_eff[g]
      +" K_DG="+K_DG[g]
      +" Keff="+K_DG_eff[g]
      +" gamma="+gamma_eff[g]);
  }
  for(var k=1; k<=ND; k++) {
    var t_rest = TBS+1;
    for(var t=1; t<=TBS; t++) {
      if(u_Load[k][t] > 0.5) { t_rest = t; break; }
    }
    f.writeln("L"+k+" bus="+k+" sector="+sector[k]
      +" Pd="+PL[k]+" restored_at="+t_rest);
  }
  f.close();
  f = new IloOplOutputFile(prefix+"_ADN_params.txt");
  f.writeln("% DG_params: bus is_BSDG is_GFM Pmax Pmax_eff Qmax Qmax_eff Qmin Qmin_eff
Pstart tDG R K_DG K_DG_eff H S_MVA gamma");
  for(var g=1; g<=NG; g++) {
    f.writeln(bus_DG[g]+" "+is_BSDG[g]+" "+is_GFM[g]
      +" "+Pmax_DG[g]+" "+Pmax_eff[g]
      +" "+Qmax_DG[g]+" "+Qmax_eff[g]
      +" "+Qmin_DG[g]+" "+Qmin_eff[g]
      +" "+Pstart_DG[g]+" "+tDG[g]
      +" "+R_DG[g]+" "+K_DG[g]+" "+K_DG_eff[g]
      +" "+H_DG[g]+" "+S_DG_MVA[g]
      +" "+gamma_eff[g]);
  }
  f.writeln("% Load_params: PL QL sector");
  for(var k=1; k<=ND; k++) {
    f.writeln(PL[k]+" "+QL[k]+" "+sector[k]);
  }
  f.writeln("% System: NB NL NG ND TBS dt Vmin Vmax df_max alpha_R");
  f.writeln(NB+" "+NL+" "+NG+" "+ND+" "+TBS+" "+dt+" "+Vmin+" "+Vmax
    +" "+df_max+" "+alpha_R);
  f.writeln("% Methods: eta_H mu_R ROCOF_eff");
  f.writeln(eta_H+" "+mu_R+" "+ROCOF_eff);
  f.close();
  writeln("  Files saved with prefix: ", prefix);}
```